Understanding the cosmic abundance of 22Na : lifetime measurements in 23Mg

Chloe Fougeres

Normandie Université

THÈSE

Pour obtenir le diplôme de doctorat

Spécialité PHYSIQUE

Préparée au sein de l'Université de Caen Normandie

Understanding the cosmic abundance of 22Na: lifetime measurements in 23Mg

Présentée et soutenue par
CHLOE FOUGERES

Thèse soutenue le 03/03/2022 devant le jury composé de		
M. BERTRAM BLANK	Directeur de recherche au CNRS, UNIVERSITE BORDEAUX 1 SCIENCES ET TECHNOLOGIE	Rapporteur du jury
M. DAVID VERNEY	Directeur de recherche au CNRS, UNIVERSITE PARIS 11 PARIS-SUD	Rapporteur du jury
M. EMMANUEL CLEMENT	Chargé de recherche HDR, 14 GANIL de CAEN	Membre du jury
MME SANDRINE COURTIN	Professeur des universités, Institut Hubert Curien	Membre du jury
M. JORDI JOSÉ	Professeur des universités, Université Politècnica Catalunya Espagne	Membre du jury
MME FRANCESCA GULMINELLI	Professeur des universités, Université Caen Normandie	Président du jury
M. FRANCOIS DE OLIVEIRA SANTOS	Directeur de recherche au CNRS, 14 GANIL de CAEN	Directeur de thèse

Thèse dirigée par FRANCOIS DE OLIVEIRA SANTOS (Grand accélérateur national d'ions lourds),

UNIVERSITÉ CAEN NORMANDIE

ED 591 PSIME

GANIL spiral2 laboratoire commun CEA/DRF CNRS/IN2P3

PhD Thesis

Caen Normandie University: Physics Departement

PSIME Doctoral School

Understanding the cosmic abundance of ^{22}Na: lifetime measurements in ^{23}Mg

Author
Ms Chloé Fougères

Under the Supervision of
Dr. François De Oliveira Santos
Senior Researcher at CNRS

October 2019 - March 2022

Supervisory Committee

Dr. Bertram Blank	Senior Researcher, CENBG Gradignan *(rapporteur)*
Dr. Emmanuel Clément	Research Fellow, GANIL Caen
Prof. Sandrine Courtin	Professor, Strasbourg University
Dr. François De Oliveira Santos	Senior Researcher, GANIL Caen *(Supervisor)*
Prof. Francesca Gulminelli	Professor, Caen University
Prof. Jordi José	Professor, Catalonia Polytechnic University
Dr. David Verney	Senior Researcher, IJCLAB Orsay *(rapporteur)*

A deux infinis,
Le ciel étoilé illuminant la mer.
Je disparais devant vos airs sereins,
Aimant à contempler vos tempêtes.
C.

Acknowledgements

Le temps s'efface devant une existence plaisante, ces années de thèse me l'ont encore prouvé. Les quelques lignes qui vont suivre sont dédiées à tous ceux qui animèrent ce travail de recherche au-delà de la jeune thésarde.

Mes premiers mots vont à mon encadrant, François de Oliveira Santos, que je ne peux assez remercier. Suite à notre première discussion, tu me proposas un sujet de thèse. Ta confiance en mon travail n'a pas cessé depuis. Ta pédagogie, ton écoute, ta patience, ton calme, ta justesse, ta rigueur, tes nombreuses idées rendent ton encadrement unique et précieux. Je sens ma chance d'avoir commencé mes recherches sous ton aile, espérant que notre collaboration perdura. Tu avais réfléchi à deux domaines pour ta propre thèse, mais heureusement ton choix se porta pour la communauté d'astrophysique nucléaire. Tu arrives habilement à équilibrer entre formation et autonomie, soutien et responsabilisation. Tu as contribué à rendre cette thèse efficace et réussie. Je remercie aussi la personne humaine, qui m'accueillit, dès mon arrivée en Normandie, par un diner en famille et des observations astronomiques. Si vos pas vous ramènent un jour au cap d'Erquy, un accueil breton sera présent.

Des remerciements sont adressés aux deux rapporteurs de la présente thèse, Bertram Blank et David Verney, et aux membres du jury, Emmanuel Clément, Sandrine Courtin, Francesca Gulminelli et Jordi José. Apportant des critiques constructives, questionnant et commentant le manuscrit, leur investissement fut une aide précieuse que je tiens à remercier.

Travailler au GANIL fut un grand plaisir par la richesse scientifique et les bonnes conditions de travail. Merci à la direction et à tous les membres donnant vie aux infrastructures, aux outils expérimentaux, aux processus administratifs, aux mobilités des chercheurs... Je tiens à remercier le GANIL et la région Normandie qui ont accepté de financer cette thèse. Merci à la direction pour son implication dans la thèse. Ses conseils et critiques ont amélioré deux présentations clés de la thèse. Je souhaite aussi remercier le groupe physique qui intègre les thésards. Merci à mon comité de suivi individuel et son regard productif sur la thèse.

Si absente de l'expérience de thèse, je souhaite aussi remercier tous les collaborateurs pour la mise en place et la réalisation de ce projet expérimental qui fut un succès. Un grand merci à Caterina Michelagnoli pour avoir proposé, mené et accepté de laisser la suite de cette expérience à mes soins. C'est avec joie que j'ai pu participer aux campagnes expérimentales d'AGATA, VAMOS, MUGAST. Reconnaissante aux portes paroles et à ces collaborations pour m'avoir invitée à ces temps expérimentaux, je remercie en particulier Emmanuel Clément auprès duquel j'ai grandement appris. Les personnels techniques et scientifiques du GANIL travaillent intensément aux développements des expériences. Nombreux doivent être les soutiens et remerciements à leurs égards.

Malgré des années particulières, la thèse fut aussi un voyage vers d'autres centres, des rencontres d'équipes et de collaborateurs. Merci Fairouz Hammache et Nicolas de Séréville pour les expériences ensembles et la construction d'autres à venir... Merci Angel Miguel Sanchez Benitez et Jordi José et nos discussions espagnoles. Merci Nadia Smirnova pour l'aide théorique.

Merci à tous les collègues thésards et post-doctorants du GANIL et ailleurs : Julien, Armel, Valérian, Nishu, Abalhaian, Alejandro, Joël, Anjali, Vincent, Tom, Alexis, Pablo, Simon, Sarah, Irène,... et Sylvain, Diego, Abhi, Rikel,... Pardon pour les oublis, des pensées aussi pour tous les bons moments entre mer et montagnes : aux JRJC, au colloque du GANIL, à l'école Joliot Curie...

La thèse achevant les années d'étude, je pense avec chaleur à mes professeurs dont l'enseignement me marqua et grandit mes pensées. Mes cours à Sainte-Marie et Louis le Grand me resteront toujours en mémoire. Merci aussi pour les heures à Vienne et Orsay qui me firent découvrir l'astrophysique nucléaire.

Les dernières lignes sont pour les trésors essentiels qui toujours m'accompagnent. Ma famille me montre des étoiles terrestres. Par le confinement, mes parents, mes frère et soeur furent directement présents durant ma thèse. Qu'importe les tempêtes nous frappant, toujours la vie avec vous quatre est lumineuse. Merci. Et enfin toi, la mer sans conscience, tu éveilles en moi une infinité d'émotions. Merci.

Contents

Part I

Introduction

CHAPTER 1

Astrophysical motivations

1.1 Introduction

Contemplating a night sky will make you wonder about all theses stars and empty spaces. Celestial objects are widely observed now, from human eyes to state-of-the-art space telescopes, radio and gravitational waves. Each way teaches us about the processes behind, even being so far away. It is also possible to improve our understanding of astrophysical mechanisms by studying atomic nuclei in ground-based accelerators. The present work explains in particular how one radioelement, ^{22}Na, could help us to write the physics story of one specific astronomical object, the nova.

In this introductory chapter, the present work and its main objectives will be placed in their astrophysical context. A brief scene about the observations of nuclei in the cosmos ends on the active search for the radioelement ^{22}Na in Sec.1.2. This key actor is expected to be produced in an explosive stellar scenario: the nova presented in Sec.1.3. However, its main destruction reaction by proton capture, presented in Sec.1.4, is a very interesting plot of experimental nuclear physics which asks for new answers.

1.2 Nuclear observations in the cosmos

1.2.1 Measured abundances of the elements

What is the matter around us made of? This fundamental question of mankind has been answered qualitatively by the Greek Demokritos, two thousand five hundred years ago: the atoms, a wrongly chosen name α-$\tau o \mu \grave{o} \varsigma$ meaning "un-breakable". The past century has brought a quantitative answer: the amounts of each natural element have been determined in our solar system. These abundances, given as a function of the atomic number Z in the left of Fig. 1.1, were measured from the Sun photosphere, the Earth crust or the meteorites, illustrated on the right side. Then, these measurements were extrapolated to the whole universe.

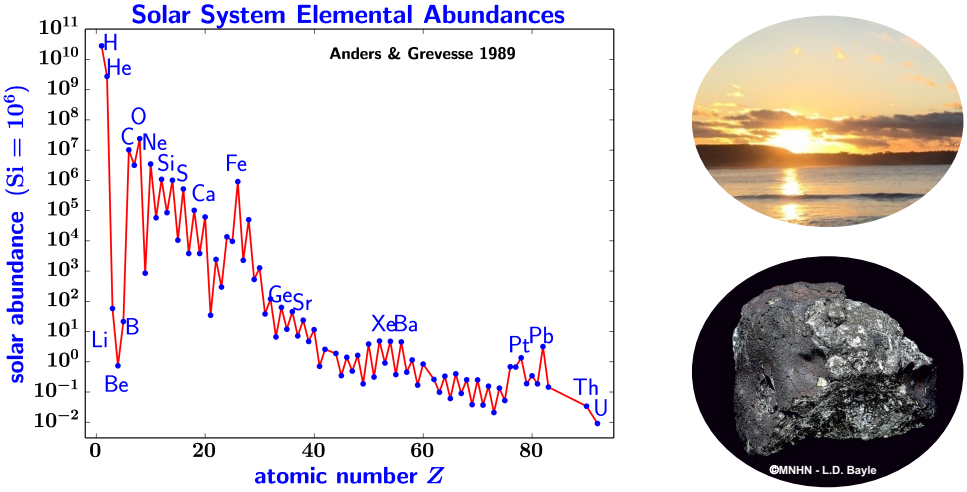

Figure 1.1: Left: measured solar abundances of elements as a function of the atomic number Z, taken from [1] by using the database of Anders & Grevesse (1989) [2]. Right: three sources to measure the elements abundances, the Sun photosphere, the Earth crust (seen from the Channel seaside) and meteorites. Picture of the meteorite from Orgueil-1864 (Muséum national d'Histoire naturelle ©MNHN - L.D. Bayle), it has a solar isotopic composition and a comet origin.

A quick look at the abundances curve of the left Fig. 1.1 points out elements more present than others: the atoms H, He, C, O, Ne, for instance. This is a hint on nuclear structure: the shell gap closures impact on the abundance of elements. There is also a decreasing tendency of the abundances with respect to Z. It is well-known that fusion above iron is endothermic contrary to fission, the inverse process. The questions of where, when and how all these elements are synthesized, are hidden behind this curve, entering then in the field of nuclear astrophysics. The light H and He elements were mainly produced during the primordial nucleosynthesis, a half-hour after the Big Bang [3]. Other nuclei are synthesized either in stellar environments or in energetic interstellar collisions, the so-called spallation processes with cosmic rays. The abundances curve is an indirect observable of the stellar evolution, see [4]. Nucleosynthesis brings constrains on stellar evolutions, being in particular the main source of stellar energy.

1.2.2 Gamma-ray astronomy of radioelements

Another cosmic footprint of nuclei comes from the γ-ray lines emitted with the β-decays of radioelements. From the 1990s, gamma-ray astronomy has searched for emissions at low-energies: the MeV scale is characteristic of nuclear transitions or of high-energy nuclear collisions. Recent reviews can be found by Dhiel *et al* [5, 6]. There are several sources of γ-rays: explosive burning stellar sites such as supernovae (SNe) and novae, high-energy collisions in stellar objects or in the interstellar space, and the 0.511 MeV annihilation line from β^+-decays (the first observed cosmic γ-ray line). The observation of nuclear decays in space can teach us about the stellar interiors and processes, the isotopic composition of specific astrophysical sites, the dynamics of thermonuclear explosions and the amount of ejected matter in the interstellar medium (ISM), the galactic chemical evolution, among others [5, 4]. A list of γ-ray lines of interest can be found in Table 1 of Ref. [5]: emissions are classified with respect to their astrophysical origin. The focus here is put on the radioactive elements, leaving aside all nuclear reactions.

Two kinds of radioelements are identified according to their lifetimes τ. First, the emissions from the long-lived nuclei (τ>Myr) are expected to be observed diffuse in the galaxy. The well-known examples are ^{60}Fe (τ=2.6 Myr) and ^{26}Al (τ=0.7 Myr). The latter, ^{26}Al with a lifetime lower than our galaxy age,

is an evidence of ongoing nucleosynthesis in the Milky Way. Its γ-ray line at E_γ=1.809 MeV has been observed by both INTEGRAL and CGRO missions. The obtained sky map from CGRO/COMPTEL instrument is shown in Fig. 1.2(a) from [7]: ^{26}Al is observed in the inner galaxy as well as in the remote regions where massive stars and core-collapse SNe are found. It agrees with the predicted map shown in Fig. 1.2(b) where these stellar sites are taken into account from Ref. [8]. Second, the emissions from the short-lived nuclei with τ of the order of one year, are short enough to ensure space-time correlation with the production site. Their γ-ray lines should be located at their astrophysical source sites, making them possible radioactive tracers. This is the case of ^{22}Na (τ=2.6 yr) and of ^{7}Be (τ=53 days) for novae sites, ^{44}Ti (τ=60 yr) for core-collapse SNe. The first one is the subject of the present work. Let's take the case of ^{44}Ti to illustrate such radioactive tracers. Indeed, its emission lines at low energies (67.9 keV, 78.4 keV) have been measured in the Cassiopeia A remnant by [9], see Fig.1.2(c). Scanning the energy spectrum with the on-board IBIS camera of INTEGRAL, the hot spot at CasA localization is well apparent when the two expected γ-ray energies are selected (images in the center). It again agrees with the simulations from [8], shown in Fig. 1.2(d), where ^{44}Ti is produced in core-collapse SNe.

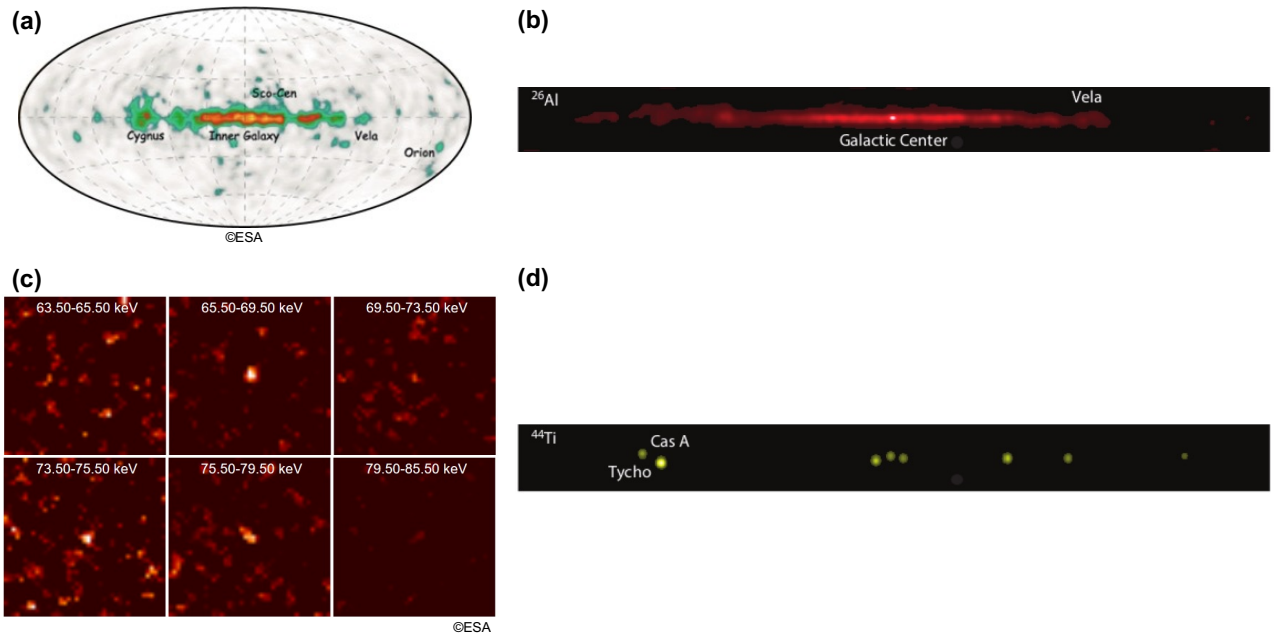

Figure 1.2: Panel (a): sky map of the Milky Way galaxy selected on the γ-rays at E_γ=1.809 MeV from the ^{26}Al β decay, from Plüschke *et al* [7]. The ten-year observation shows the emissions both in the inner galaxy and away from it, like the Cygnus and Vela regions of active stellar formation. Panel (b): simulated emissions from ^{26}Al along the galactic plane agree with the observed map in panel (a). The radioelement is mainly produced in massive stars, core-collapse SNe and novae [5]. Panel (c): flux images selected on six different energy bands, given at the top, from Renaud *et al* [9]. The low-energy emissions were observed by the mask-coded Imager on Board the INTEGRAL Satellite IBIS/ISGRI. The bright spot located at Cassiopeia A (CasA, SN remnant) is apparent in the two pictures in the center, associated with the E_γ =67.9 keV and 78.4 keV emission lines from the ^{44}Ti β decay. Panel (d): simulations of the emissions from the ^{44}Ti β decay, the production of this radioelement being predicted in core-collapse SNe events [4, 5]. The simulations are in agreement with the observations, this radioelement is observed in the form of hot spots. Panels (b, d) taken from Tomsick *et al* [8].

After this brief introduction on gamma-ray astronomy, the question arises as to how these observations are made. Due to the absorption of the MeV range by the Earth atmosphere, all instruments are obviously

required to be on-board space telescopes. Likewise laboratory instruments, they must measure the energy and the localization of the source of the γ-rays. Energies are derived from the electric signals generated by the interacting γ-rays in the detectors, in the MeV range mainly from Compton scattering and pair production. In the INTEGRAL/SPI instrument presented in Fig.1.3, germanium detector array resulted in an excellent energy resolution. But, similarly to laboratory detectors, they are submitted to a high background noise from natural cosmic γ-rays and the activation of the surrounding material like aluminium, see [5]. The signal over noise ratio was improved by using anti-coincidence shielding. But contrary to the latest ground-based γ-ray spectrometers like AGATA, based on Compton tracking algorithms, the initial angle and source of the γ-ray are usually built back by means of coded masks, at an efficiency cost, see on the right of Fig. 1.3. The angular resolutions with the mask approach are typically $\sim 2-3$ degrees [10, 11].

The last two space missions (1 MeV range) were the CGRO observatory (1991-2000) [12] from NASA and the INTEGRAL space telescope (2002 - still operative) [13] from ESA. The first one had two instruments on-board COMPTEL and OSSE, details available in [11, 14]. The COMPTEL was composed of liquid NE and NaI scintillators, and their associated photomultipliers. The energy resolution of 10 %[5] of the Compton-scattering based COMPTEL telescope limited the observation capacities to known lines and static properties of the studied astrophysical sources since Doppler effect could not be resolved. However the large active volume of the detector gave excellent efficiencies, still unequal to this day [5]. The second observatory, presented in Fig. 1.3, has also two spectrometers: SPI [10, 15] and IBIS [16]. SPI is detailed in the right side, with 19 HPGe detectors [10]. The energy resolution of 0.1% was accompanied by a sensitivity of 3.10^{-5}ph.cm^{-2}s^{-1}[5]. Beyond clear nuclear line identification, its resolution allowed lineshape analysis, based on Doppler effect, to characterize the kinematics of celestial sources. A great example is the evolution of the ^{26}Al line centroid along the galactic plane (see Fig. 14 in Ref. [5]): from a blue shift in the 4$^{\text{th}}$ quadrant (longitude $<0^{\text{o}}$) to a red shift in the 1$^{\text{st}}$ quadrant (longitude $>0^{\text{o}}$), this shows the interstellar gas motions.

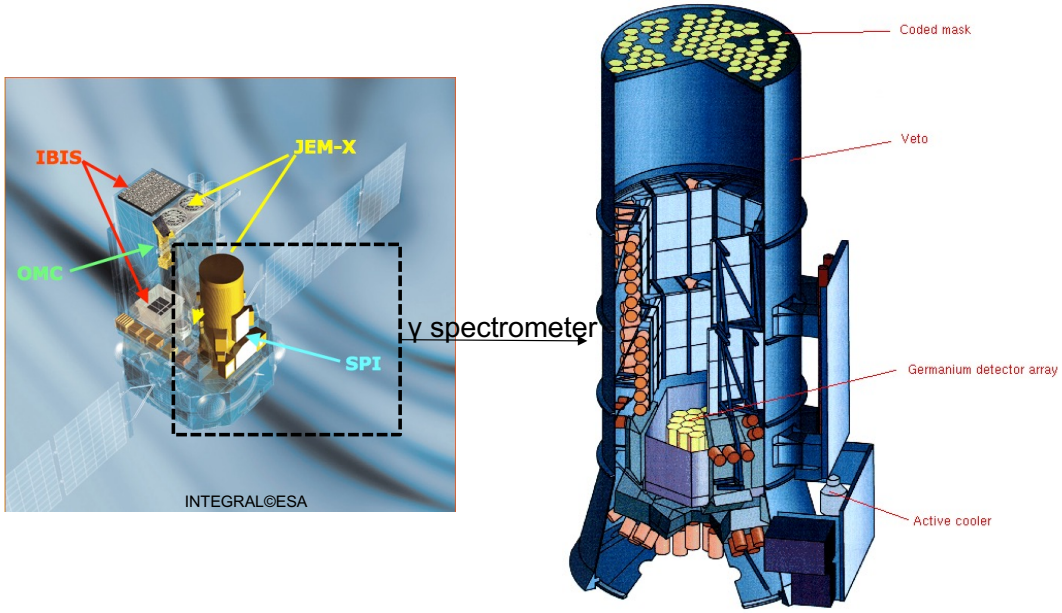

Figure 1.3: Left: layout of the INTEGRAL telescope, still operative, with the γ-ray spectrometer SPI pointed out in the black dotted square. Right: description of the SPI components, in particular the coded mask (top) to build back the γ-ray initial angle and the Ge array (bottom). Pictures taken from [13, 10].

In summary, two categories of radioelements are of interest in gamma-ray astronomy to bring con-

strains on astrophysical nucleosynthesis, at the global or local level. This branch of astronomy relies on space instruments which own similar requirements and properties as the ground-based laboratory γ-ray spectrometers.

1.2.3 Search for ^{22}Na

The present work is dedicated to one particular radioelement, ^{22}Na, which was and still is actively sought after by astrophysicists. The main reasons are presented now.

- A stellar compass

The ^{22}Na, by its lifetime τ =2.6 yr, is a radioactive tracer. The so-called ONe novae, with stable O and Ne ions, presented in Sec.1.3, are predicted to be its main astrophysical production site, argued by [17, 18, 19, 4, 20] among others. It lives long enough to cross the opaque plasma. This opaque medium prevents any observation of emissions from most of the radioelements produced in such a stellar explosion for several hours after the explosion. The ^{22}Na is thus the most promising candidate for observing nuclear γ-ray emissions from ONe novae [21].

Lines expected from the ^{22}Na β^+-decay to ^{22}Ne* are mainly at E_γ=1.275 MeV and 0.511 MeV. They have not been observed in the Milky Way over the past observation campaigns [5]. The cumulative flux for three-year observations along the galactic plane by the instrument SPI is presented on the left of Fig. 1.4 from [5]. This result was obtained by modelling the novae spatial distribution from [22] with the frequency of ONe novae events presented in Sec.1.3. The expected line at E_γ=1.275 MeV is not seen above the instrumental background noise, resulting only in an upper limit of 2.6×10^{-5} ph.cm^{-2}.s^{-1} (2σ). This limit is shown in Fig. 1.5. The cumulative measurement of the ^{22}Na emission is very relevant because its lifetime is long enough. The simulated γ-ray spectra of ONe novae, with mass of 1.15 $M_\odot$, are presented at different explosion times on the right of Fig. 1.4, taken from José [20]. In addition to the line at 1.275 MeV, the E_γ=0.511 MeV line is dominant but mainly at the earliest hours of the explosion, hence within the opaque hot plasma. Besides, all β^+ radioelements contribute to this line, contrary to the E_γ=1.275 MeV line which can be visible for months after the explosion [23].

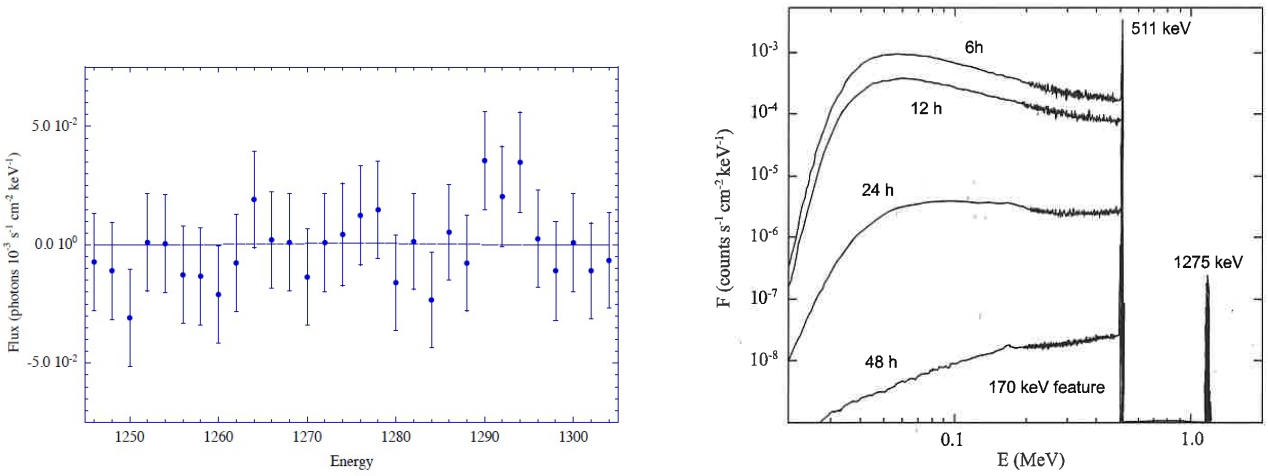

Figure 1.4: Left: the cumulative flux spectrum from SPI three-year data is derived with a spatial source distribution for novae [22]. The fitted line at 1.275 MeV led to an upper flux limit of 2.6×10^{-5} ph.cm^{-2}.s^{-1} (2σ). Spectrum from [5]. Right: simulated γ-ray spectra from an ONe nova of mass 1.15 $M_\odot$ at 1 kpc, shot (6, 12, 24, 48) hours after the explosion. From José [20].

An overview of some measured upper limits of the ^{22}Na γ-ray line at 1.275 MeV, obtained during the surveys of CGRO/COMPTEL and INTEGRAL/SPI detectors, is given with respect to the nova event in

Fig. 1.5. This non-observation is consistent with model predictions [24], see Sec.1.4.4. The measured upper limits of the ^{22}Na E_γ=1.275 MeV flux were used to estimate upper limits in the ejected amount of ^{22}Na per nova: 3.7×10^{-8} $M_\odot$ (COMPTEL) and 4.1×10^{-7} $M_\odot$ (INTEGRAL), see [24, 5]. The improvement in instrumental sensitivity over the years is also noticeable in Fig. 1.5. This is only a reduced set of the observed novae, in particular for the INTEGRAL campaign, with a zoom on the ^{22}Na case.

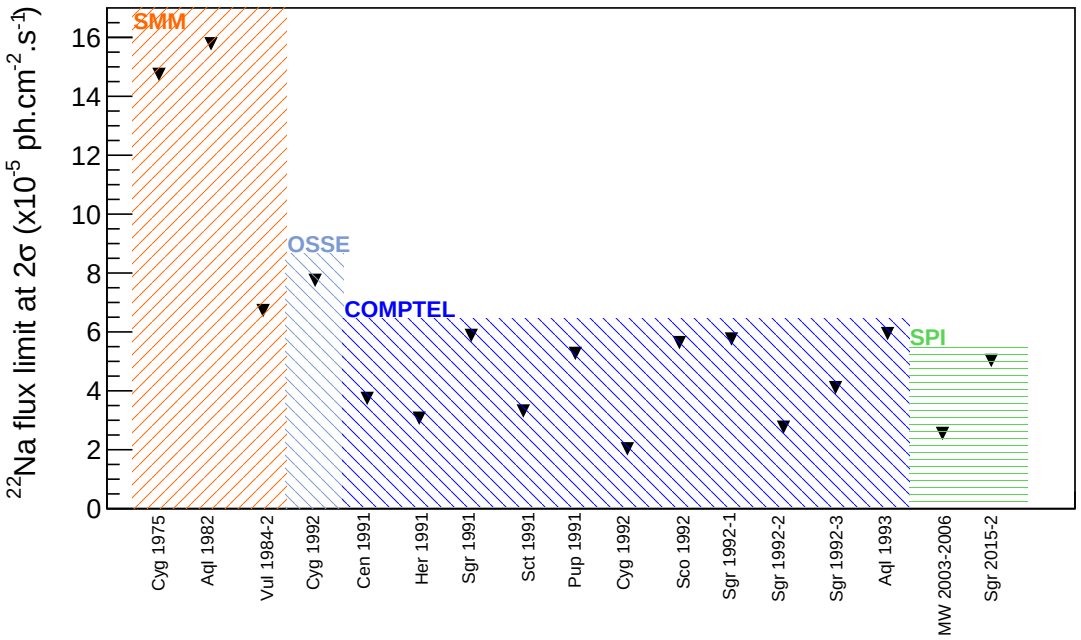

Figure 1.5: Measured upper limits in the ^{22}Na flux from some identified nova events, for almost half a century. One point represents the integrated three-year observations of the Milky Way (MW 2003-2006). Shaded regions mark the used on-board spectrometers: Solar Maximum Mission SMM (orange) from NASA [25], OSSE (light blue) and COMPTEL (dark blue) from CGRO, SPI (green) from INTEGRAL. Data of (SMM, OSSE, COMPTEL) from [26] and of SPI from [5, 27].

- Observed ^{22}Ne excess in meteoric presolar grains and cosmic rays

The radioelement ^{22}Na can be indirectly observed by measuring the over-abundance of ^{22}Ne, the daughter nucleus of ^{22}Na β-decay, compared to natural (solar) abundance of ^{22}Ne. An excess is a hint of prior ^{22}Na presence in the sample and/or astrophysical site. The preferred targets for the search for ^{22}Na, through ^{22}Ne, are the meteorite samples. Microscopic grains have been found in meteorites, with measured isotopic compositions different from solar ones [4, 20]. These presolar grains, illustrated in the left of Fig. 1.6 from scanning electron microscopy, would be material crystallized near the sites of stellar nucleosynthesis, in particular massive stars, novae and SNe. Ejected into the interstellar medium, the grains are then trapped into meteorites which sometimes reach the Earth. The presolar grains are thus another footprint of these stellar systems. The analysis of their isotopic compositions should constrain the nucleosynthesis process. Novae have been proven to be the source of presolar grains by the multiple observations of dust condensation in the ejecta, from the infra-red and ultraviolet spectra. Three types of presolar grains are considered to originate from a nova: Silicon Carbide, graphites and oxides, based on excesses of ^{22}Ne, ^{26}Mg, ^{30}Si (ONe novae) and low ^{12}C/^{13}C, ^{14}N/^{15}N (CO novae) [20]. Studies of presolar grains, presumed to originate from novae, have produced data sets on isotopic ratios, see [28, 29]. They can be compared with predictions from different models and varying nova conditions. This is illustrated

on the right of Fig. 1.6 in the case of $^{26}Al/^{27}Al$, from in-situ measured ^{26}Mg abundances [30]. The isotopic abundances of nova presolar grain candidates can be reproduced by specific conditions of the nova, here the white dwarf mass and the accretion gas composition. Such a complete study would be of high interest in the case of ^{22}Na. To our knowledge, this does not yet exist.

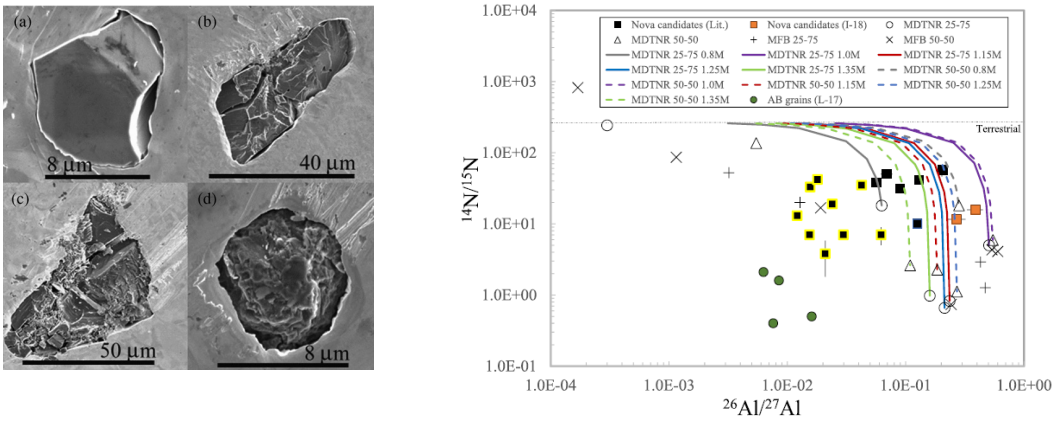

Figure 1.6: Left: scanning electron microscopy images of presolar grains. Right: measured isotopic ratios $^{14}N/^{15}N$ versus $^{26}Al/^{27}Al$ in nova presolar grains candidates. They are compared to model predictions where the white dwarf mass and the accretion gas composition are varied (color lines). Figure taken from Bose *et al* [30].

Neon noble gas is not expected to easily condense into dust grains. Hence the presence of ^{22}Ne is most likely due to the in-situ β-decay of ^{22}Na. The ratio $^{20}Ne/^{22}Ne$ is a tool to identify the nova origin of presolar grains, as well as to quantify the ratio of $^{22}Na/^{23}Na$ produced after a single nova outburst. The first excess in ^{22}Ne with respect to $^{20,21}Ne$ was observed by Black [31]. In grains of the Orgueuil meteorite, the amount of ^{20}Ne versus ^{22}Ne was found to be less than 1.5, knowing that solar abundances give a value of 9.8, i.e. (90.5 %)/(9.2 %) [4]. Deeper measurements led to $^{20}Ne/^{22}Ne<0.15$ and $^{21}Ne/^{22}Ne<0.0022$[4]. Similar excesses of ^{22}Ne were observed in galactic cosmic rays.

In summary, the ^{22}Na radioactive tracer has been actively searched to help understanding novae and to identify the presolar grains origin.

1.3 Novae

1.3.1 Sites of explosive hydrogen burning

Month-living transient stars, novae are observed as bright stars, point objects in the sky. A nova, visible in 2013 in the Delphinus constellation, is illustrated in Fig. 1.7(a). A pioneering image was obtained by the Hubble space telescope: the Nova Cygni (1992) in Fig. 1.7(b). Binary star systems are behind these events, and the observed lights come from an explosion on the surface of one of the stars. Novae outbursts are commonly understood as thermonuclear runaways on the surface of a white dwarf star accreting mainly hydrogen rich matter from the envelope of the stellar companion, most likely a main sequence star close to become a red giant [4, 20]. White dwarfs are stellar core remnants. Red giant stars have a core of helium and a shell of hydrogen burning around it, they correspond to the late stages of the stellar main sequence.

In novae, the accretion phase is modeled as a period of time when material from the companion star flows onto the other star at a speed of $[10^{-10}, 10^{-9}]$ $M_{\odot}.yr^{-1}$[20]. This material forms an accretion

disk around the white dwarf. The material gradually reaches the surface of the white dwarf, increasing the pressure and temperature of the gas. This model of classical novae is painted in Fig. 1.7(c). The composition of the accreted matter, its accretion rate and the mixing ratio with the white dwarf matter are of prime importance to understand the full story behind a nova outburst.

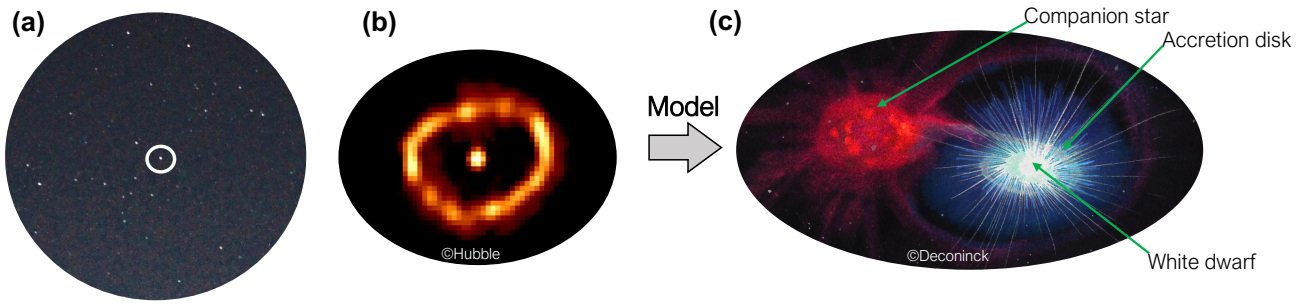

Figure 1.7: Panel (a): night sky picture in Normandy of the classical Nova Delphini event (2013), inside the white circle the star was visible to the naked eye in the constellation of the Dolphin. The event, estimated at 4.5 kpc, lasted 4 months, ©de Oliveira Santos. Panel (b): picture from the Faint Object Camera, on-board of the Hubble space telescope, of the Nova Cygni (1992) by Paresce *et al*©Hubble [32]. The expanding shell surrounding the white dwarf is clearly visible after the outburst. Panel (c): artistic view of the stellar model at the origin of a nova, Aquarellia©Deconinck.

Temperature and nuclear energy released keep increasing at the white dwarf surface. The outburst ignition triggers at a critical pressure at the surface between the core and the envelope: P_{ce}. This pressure can be derived by measuring the white dwarf mass and radius (M_{WD}, R_{WD}) and the accreted mass M_{acc} as follows from [33]

$$P_{ce} = \frac{GM_{WD}}{4\pi R_{WD}^4} \times M_{acc} \tag{1.1}$$

G being the gravitational constant. Depending on the envelope composition, it is calculated to be $P_{ce} \geq 10^{20}$ dyn.cm^{-2} (solar) or $P_{ce} \sim 10^{19} - 10^{20}$ dyn.cm^{-2} (CNO-enriched) [34, 33]. The accretion rate is currently not well measured, contrary to the transfer rate ($rate_{transfer}$). The latter is deduced by the measured orbital period (P_{orb} in hour): $rate_{transfer} = 5.1 \times 10^{-10} (\frac{P_{orb}}{4hr})^{3.2}$ ($M_\odot$.yr^{-1}) [20].

From the moment of ignition, the luminosity (emitted energy per time unit) quickly rises up to a value close or even above the Eddington limit where radiative pressure exceeds gravitational force, ejecting mass into the interstellar medium. We recall that temperature (T) can be derived from an observed luminosity (L) by the Stefan law, assuming a black body system

$$T = (\frac{L}{4\pi R_{WD}^2 \sigma})^{\frac{1}{4}} \tag{1.2}$$

where σ is the Stefan-Boltzmann constant. After the light peak, a stable period follows, with a relatively constant bolometric luminosity, maintained by the fuel from the burning of the hydrogen in the remaining matter envelope, until the system returns to its pre-nova state. The constant bolometric luminosity L_{cst} is thought to be properly given by the relation of Paczyński [35]:

$$L_{cst} = 6 \times 10^4 L_\odot (\frac{M_{WD}}{M_\odot} - 0.522) \tag{1.3}$$

where $L_\odot$ ($M_\odot$) is the the Sun luminosity (mass). From the measured nova constant bolometric luminosity, the white dwarf mass can be inferred. White dwarfs are only defined below a mass corresponding to the

Chandrasekhar limit where electron degeneracy pressure is not enough to counterbalance the gravitational collapse, and so the star collapses. This is a possible scenario for the SNe of type Ia (SNIa). There is also a low mass limit: the boundary between planets and white dwarfs is associated with a critical density where atomic structure collapses (the degenerate matter region). Overall, white dwarfs are expected with masses: $10^{-3}M_{\odot} \leq M_{WD} \leq 1.4M_{\odot}$[4]. From the minimization between kinetic (due to electron motion) and gravitational energies, the white dwarf radius is estimated from the mass [4], both in Sun unit:

$$R_{WD} = 0.01 M_{WD}^{-\frac{1}{3}} \tag{1.4}$$

Combining Eq. (1.3), (1.4) and (1.1), the observable luminosity allows us to estimate the white dwarf characteristics as well as the accreted mass. The final turn-off step of a nova is accompanied by X-ray emissions. It has been proven that the time of this last step depends on the remaining hydrogen mass in the envelope. By using the observed chemical composition from isotopic lines, the envelope mass after outburst (M_{env}) can be inferred, leading to an estimation of the ejected mass. However this derived mass is higher than model predictions [20].

$$M_{ej} = M_{acc} - M_{env} \tag{1.5}$$

The novae scenario here is a short and simplified version, key features such as energy transport, matter degeneracy have not been detailed. A complete description is available in [20].

The distance of an identified nova from Earth can be estimated by the apparent maximum magnitude m, according to

$$d \sim 10^{\frac{m-M+5}{5}} \text{[36]} \tag{1.6}$$

where the distance d is in pc and the maximum absolute magnitude M is given by the approximate relation $M \sim$ -8.3 - 10$\times$log(M_{WD})[37] (Sun unit).

Using the observed electromagnetic spectrum from ultra-violet to infra-red, important physical parameters of novae can be deduced. To quote only a few, the chemical abundances, from H to Fe, are estimated [19, 20]. Two kinds of classical novae have been pointed out: CO and ONe novae have dominant (C,O) and (O,Ne) elements at the white dwarf surface. This is illustrated in the Fig. 1.8 where the expected abundances, normalized to the solar abundances, are shown as a function of the atomic mass number, in the case of CO (blue) and ONe (black) novae. White dwarf masses of ONe novae are measured $\geq$1.1 $M_{\odot}$[20], higher than in CO novae. Furthermore, Doppler shifts of the atomic lines allow us to access the outflow velocity. Five radioelements, produced during novae outbursts, are of interest in gamma-ray astronomy: ^{13}N, ^{18}F, ^{7}Be, ^{22}Na and ^{26}Al. None of the γ-ray lines from these radioactive decays have been detected yet in the ejecta, but higher-energy emissions (>100 MeV) have been measured by the Fermi/LAT telescope in multiple events [38]. The particles acceleration in the strong outburst shocks is at the origin of these γ-rays, see more details in [23]. Moreover, it is worth mentioning that radioelements have already been measured in nova events: ^{7}Be has been measured several times through its atomic line, in particular in the near-UV spectrum of the nova V339 Del (2013) [39].

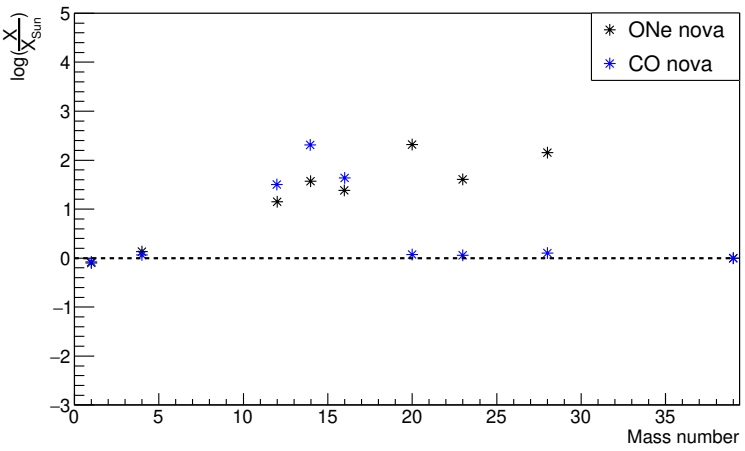

Figure 1.8: Abundances of stable ions, normalized to solar abundances [2], at the white dwarf surface in novae, from simulations with the code MESA [40]. Two kinds of novae have been calculated: ONe novae (black points) and CO novae (blue points). Ne and Na nuclei are more numerous in ONe novae while C and N nuclei are more present in CO novae.

A brief summary of the relations between observables and inferred properties of classical novae is given in Table 1.1. Exhaustive lists can be found in [19]. More details on the novae modeling will be addressed in Chapter 9.

Observables	Determinations	Model dependencies
Apparent magnitude	Distance	Eq. (1.6)
Bolometric absolute luminosity	WD mass, radius	Eq. (1.3)
	Accreted mass	Eq. (1.1), outburst critical pressure [34]
	Temperature	Eq. (1.2)
Atomic lines (IR, visible, UV)	Abundances from H to Fe [19]	
	CO or ONe novae	
	Outflow dynamics	Doppler effect
Turn-off phase time	Envelope mass	Eq. (4.14)[20]
	Ejected mass	Eq. (1.5)
Orbital period	Transfer rate	Eq. (4.2)[20]

Table 1.1: Partial list of observables and inferred physical properties of classical novae, details in text.

Novae are, after type I X-ray bursts, the most common thermonuclear explosions. The predicted rate is of 30±10 per year in the Galaxy [41]. Considering the stellar system is conserved after the outburst, most novae should be recurrent over time: several recurrent novae have been pointed out, like this summer event nova RS Ophiuchi (2021). The proportion of ONe novae is of ∼20-30 %, resulting in a frequency of 7.5 yr^{-1}[42].

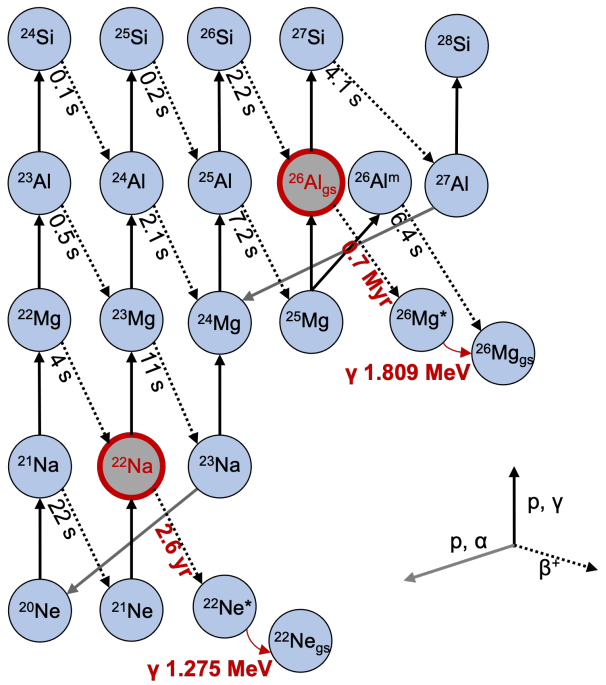

Figure 1.9: Scheme of the nucleosynthesis reaction network from Ne to Si isotopes during ONe novae, as it can be found in [4, 20]. Proton captures and β^+ decays are involved. Two radioelements, highlighted with the grey-filled red circles, are of importance for γ-ray astronomy as well as novae physics: the short-lived ^{22}Na and the long-lived ^{26}Al.

Novae are astrophysical sites of explosive hydrogen burning associated with β^+-decays. The ejected mass during the outburst is up to 10^3 smaller than during supernovae, making nova contribution to the galactic chemistry minor. Yet, novae are unique systems to study, as well as the main production sites for some elements, including ^{15}N, ^{17}O, ^{13}C, ^{22}Na [4, 20]. Focusing on ONe novae, the expected nucleosynthesis reaction network including (Ne, Na, Mg, Al, Si) isotopes is shown in Fig. 1.9. The radioelement of interest, ^{22}Na (red circle), is produced in two ways, from the ^{20}Ne seed, which depend on temperature [17, 18]. Both start with the proton capture reaction ^{20}Ne(p,γ)^{21}Na. Then it is followed by:
- ^{21}Na(β^+)^{21}Ne(p,γ)^{22}Na,
- or ^{21}Na(p,γ)^{22}Mg(β^+)^{22}Na in the hot environment.
It is transformed through the proton capture reaction ^{22}Na(p,γ)^{23}Mg. The current knowledge on the thermonuclear reaction rates influencing the ^{22}Na abundance highlights dominant uncertainties on the ^{22}Na(p,γ)^{23}Mg reaction rate at peak nova temperatures [43]. The temperature range of classical ONe novae is $[0.1, 0.4]$ GK [20, 4]. This is too low for α-capture reactions. From the accreted matter and the white dwarf seed compositions, it is clear that n-capture reactions are not significant [20]. The other key radioelement in ONe novae is ^{26}Al, also pointed out in a red circle in Fig. 1.9. The ^{25}Al(p,γ)^{26}Si reaction is targeted by nuclear experiments in order to improve the predicted contribution of novae to the ^{26}Al galactic abundance.

1.3.2 Burning questions

While novae are generally well understood, some key questions and uncertainties remain to be resolved. Better constrains on the novae contribution to galactic abundances are wanted. The relative disagreement between the predicted and estimated ejected mass from observations must be solved. Observations to test the models are wished for, such as measurements of the ^{22}Na γ-ray line. Discussions about the models include in particular:

- the accretion dynamics and composition,
- the impact of the composition of the mixture with the white dwarf,
- the stellar conditions before the accretion, such as the initial white dwarf temperature.

Increasing the collection of measured data on presolar nova grains would greatly help to improve the models. For instance, the evolution of novae as a function of the age of the Universe could be studied by analyzing the isotopic composition of presolar grains. Furthermore, the novae are certainly related to the predicted number of SNIa and to the question of the cosmic expansion. In particular, are recurrent novae the progenitors of some SNIa?

1.4 The ^{22}Na(p,γ)^{23}Mg reaction

1.4.1 The reaction through resonances

- Nuclear reaction rate

The rate of the ^{22}Na(p,γ)^{23}Mg reaction in novae, like any thermonuclear reaction in a stellar environment, is defined by the overlap between the cross section and the proton velocity distributions over energy. The cross section depends on the Coulomb barrier of the ^{22}Na nucleus for the charged proton, and thus on the quantum tunneling effect. The proton velocity distribution in stellar environment is given by the Maxwell-Boltzmann (MB) distribution, which is a function of the temperature. The resulting rate, $N_A < \sigma v >$, is

$$N_A < \sigma v >= N_A(\frac{8}{\pi \mu_{^{22}Na,p}})^{\frac{1}{2}} \times \frac{1}{(k_B T)^{\frac{3}{2}}} \times \int_0^{+\infty} \sigma(E) \exp(-\frac{E}{k_B T}) E dE \tag{1.7}$$

with k_B=8.6173×10^{-2} MeV.GK^{-1} (N_A=6.0221×10^{23} mol^{-1}) the Boltzmann (Avogadro) constant, σ(E) the cross section, T the temperature, $\mu_{^{22}Na,p}$ the reduced mass of ^{22}Na+p (amu). For a charged-particle-induced reaction, the cross section can be expressed as $\sigma(E) = \frac{1}{E} \exp(-2\pi\eta) S(E)$ where $2\pi\eta$ is equal to $31.29 Z_p Z_{^{22}Na} (\frac{\mu_{^{22}Na,p}}{E \times 10^{-3}})^{\frac{1}{2}}$ (η is the Sommerfeld parameter), and S(E) the astrophysical factor quantifying all nuclear effects.

- Gamow window

The astrophysical factor S(E) can be reasonably assumed constant over energy [4]. The product in the integrand Eq. (1.7) corresponds to the well-known Gamow peak, shown in Fig. 1.10. The calculated MB distribution at T=0.2 GK is presented over energy with the green curve, the Coulomb barrier tunneling $\exp(-2\pi\eta)$ with the blue curve. Considering S(E)=1, the product $\sigma(E) \exp(-\frac{E}{k_B T}) E$ is shown with the red curve: the Gamow peak. This depends on an effective (centroid) energy E_0 and a width ΔE_0

$$\begin{aligned} E_0 &= 0.122 (Z_p^2 Z_{^{22}Na}^2 \mu_{^{22}Na,p} T^2)^{\frac{1}{3}} \\ \Delta E_0 &= 0.2368 (Z_p^2 Z_{^{22}Na}^2 \mu_{^{22}Na,p} T^5)^{\frac{1}{6}} \end{aligned} \tag{1.8}$$

with the temperature T in GK and energies in MeV.

In the analytic expression of the reaction rate, the integrand over the full energy range can be narrowed down to the energy range associated to the Gamow peak.

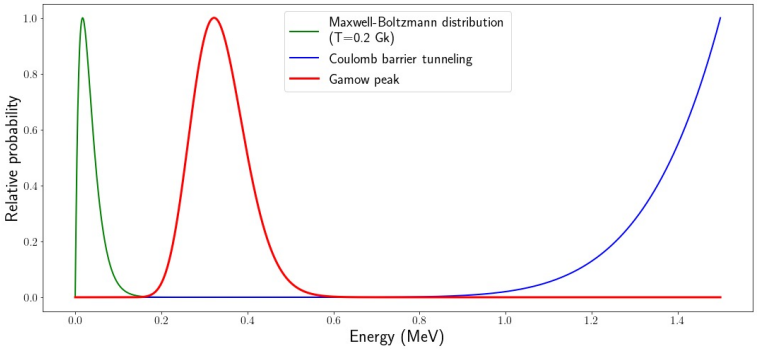

Figure 1.10: The Maxwell Boltzmann energy distribution calculated for T= 0.2 GK (green curve) and the Coulomb barrier tunneling probability for the proton capture of ^{22}Na nucleus (blue curve) are shown as a function of the kinetic energy. The red curve is the product of the MB energy distribution and the cross section. This resulting Gamow peak represents the energy window where reactions are likely to occur.

- Narrow resonances

The radiative proton capture reaction ^{22}Na(p,γ)^{23}Mg can be treated in a two-step process: the entrance channel ^{22}Na+p leads to an excited state Ex in the ^{23}Mg compound nucleus. In center of mass, Ex is equal to Ex=S_p+E_p, with E_p the proton incident energy and S_p the ^{23}Mg proton threshold (S_p=7.581 MeV). Indeed, ^{22}Na is mainly in its ground state at the temperatures of novae. Then, the excited state in ^{23}Mg* de-excites by γ-ray or proton emission. Such reaction is called a resonant reaction, where E_R is the resonance energy. The level scheme of ^{23}Mg is shown in Fig. 1.11, with the possible resonance energies which match the known Ex. This level scheme is limited to $\ell = 0$ captures, that is to say $J^{\pi}_{^{23}\mathrm{Mg}} = \frac{5}{2}^{+}$ or $\frac{7}{2}^{+}$ since the ground state spin is $J^{\pi}_{^{22}\mathrm{Na}} = 3^{+}$ and $J^{\pi}_{p} = \frac{1}{2}^{+}$. The temperatures corresponding to the maximum of the Gamow peak at each resonance energy are given in Table 1.2, after derivations using Eq. (1.8). At peak nova temperatures ($[0.1, 0.4]$ GK), the important resonances have $E_R \leq S_p$+0.5 (MeV).

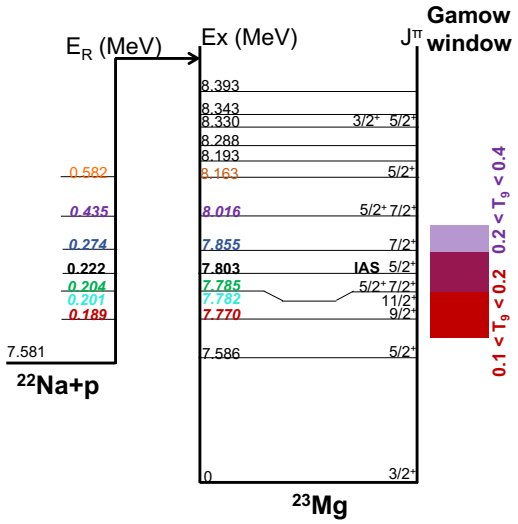

Figure 1.11: Level (Ex, J^{π}) scheme of ^{23}Mg* and the corresponding resonance energies of the proton capture reaction (E_R). The Gamow window, at peak nova temperatures ($[0.1, 0.4]$ GK), constrains the important resonance energies to be within 0.5 MeV above the proton threshold in ^{23}Mg.

E_R (MeV)	temperature (GK) of Gamow peak
0.189	0.179
0.201	0.197
0.204	0.201
0.222	0.208
0.274	0.313
0.435	0.626
0.582	0.969

Table 1.2: List of the temperatures associated with the maximum of the Gamow peak at each resonance energy E_R.

The resonant state has a width Γ assumed to be energy independent. If $\Gamma << E_R$, then the resonance is said to be narrow and the cross section can be calculated with the Breit-Wigner formula ($\sigma_{BW}(E)$)

$$\sigma_{BW}(E) = \pi \lambda\!\!\!^{-}(E)^2 \omega\gamma \times \frac{\Gamma}{(E - E_R)^2 + \frac{\Gamma^2}{4}} \quad \text{with} \quad \lambda\!\!\!^{-}(E) \sim \lambda\!\!\!^{-}(E_R) = \frac{\hbar}{\sqrt{2\mu_{(^{22}Na,p)} E_R}} \tag{1.9}$$

where $\lambda\!\!\!^{-}$ is the de Broglie wavelength and $\omega\gamma$ the resonance strength. All resonances considered in Fig. 1.11 are narrow ones. The thermonuclear rate of Eq. (1.7) can be analytically resolved by adding each resonance contribution. Then the total reaction rate is proportional to the $\omega\gamma$ of the resonances.

$$N_A < \sigma v >_{tot} = N_A \Sigma_R \left(\frac{2\pi}{\mu_{(^{22}Na,\ p)} k_B T}\right)^{\frac{3}{2}} \times \hbar^2 \times \omega\gamma \times \exp\left(-\frac{E_R}{k_B T}\right) \tag{1.10}$$

1.4.2 Experimental approaches to determine reaction rates

Different experimental methods have been developed over the years in order to determine thermonuclear rates. Three approaches can be considered: (1) the direct measurement of the rate in a plasma experiment, (2) the direct measurement of the cross section, (3) the determination of $\omega\gamma$. In the case of the ^{22}Na(p,γ)^{23}Mg reaction, the challenges to produce a ^{22}Na radioactive beam and to measure small cross sections (<<1mb) at low energies (<1MeV) do not promote the first two techniques.

Three experiments were conducted to measure the resonance strengths of interest within the nova Gamow window. In the works of [44, 45, 46], a proton beam was sent into a target with implanted ^{22}Na radioelements. The beam energy was tuned to swap the low energy range $[0.2, 0.7]$ MeV, hence passing by the different resonance energies E_R. Reaction yields were measured by counting the γ-ray emissions from the excited states in ^{23}Mg*. These yields are proportional to the resonance strengths [46]. The resonant states, close to S_p, have dominant γ-ray decays. The last experiment in TRIUMF by Sallaska *et al* [46] measured the strengths of 4 resonances, $E_R \in \{0.204, 0.274, 0.435, 0.582\}$ MeV. The resulting $\omega\gamma$ are in the range of $[1, 100]$ meV. The associated resonance rates are presented in Fig. 1.12, with the continuous coloured lines. They are in agreement with the results of [46]. The E_R=0.204 MeV resonant rate appears the highest within the whole temperature range, see the green curve. In addition, upper limits have been provided by [46] on other resonances $E_R \in \{0.189, 0.201, 0.222\}$ MeV. Dotted coloured lines in Fig. 1.12 correspond to the upper limits of the associated resonant rates.

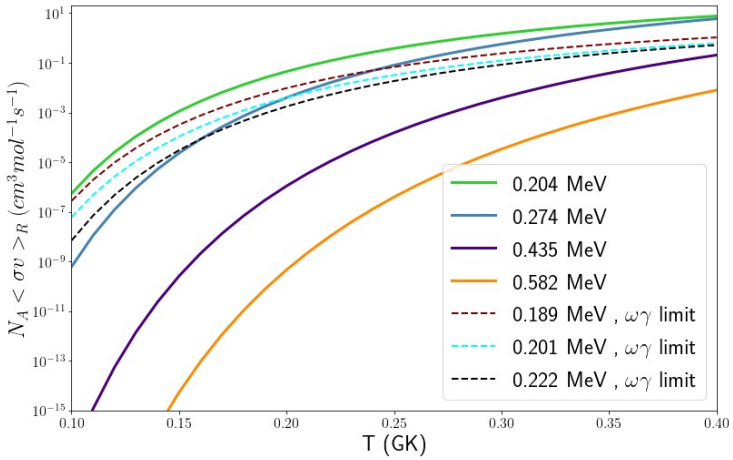

Figure 1.12: Evolution of the ^{22}Na(p,γ)^{23}Mg thermonuclear reaction rates for several resonances, as a function of the temperature. Resonance strengths taken from [46] were either finite measured values (continuous lines) or upper limits (dotted lines).

Another approach to determine $\omega\gamma$ is to measure the spectroscopic properties of the resonant states in ^{23}Mg*, i.e. spins and widths. The spin and width ratios (ω, γ) are given by

$$\omega = \frac{2J_{^{23}Mg} + 1}{(2J_{^{22}Na} + 1)(2J_{p} + 1)}$$
$$\gamma = \frac{\Gamma_{p} \times \Gamma_{\gamma}}{\Gamma_{tot}} \tag{1.11}$$

with $J_{^{23}Mg}$ the resonant state spin, Γ_{p} the resonant state proton width, Γ_{γ} the resonant state γ-ray width, and Γ_{tot} the resonant state total width.

As a summary, different experimental approaches can be used to determine the ^{22}Na(p,γ)^{23}Mg reaction rate at peak nova temperatures. The complexity of using a radioactive ^{22}Na target or beam and the small yields from low cross-sections make the indirect experimental approach of measuring ^{23}Mg* spectroscopic properties much easier.

1.4.3 The dominant resonant contribution at E_R = 0.204 MeV

As shown before, among the identified and characterized resonances of the ^{22}Na(p,γ)^{23}Mg reaction, there is a dominant resonance at peak nova temperatures. The relative resonance contributions are presented as a function of temperature in Fig. 1.13. These contributions were derived with the statistical Monte-Carlo method [47] which is presented in Chapter 8. Only contributions higher than 5% are shown. At peak nova temperatures, the E_R=0.204 MeV resonance (green curve) is well dominant, more than 60%, in agreement with [46].

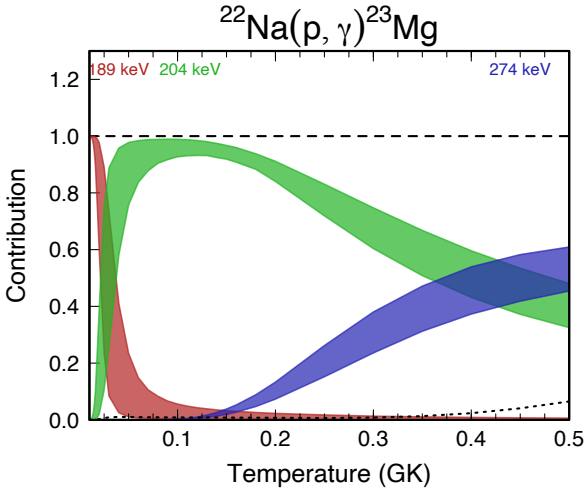

Figure 1.13: Relative contributions to the ^{22}Na(p,γ)^{23}Mg total reaction rate as a function of the temperature, using the statistical Monte Carlo approach. The experimental data from [46] point out a dominant resonance at E_R = 0.204 MeV (green curve), more than 60% of the total rate at peak nova temperatures.

However, the current status on the E_R = 0.204 MeV resonance strength, presented in Table 1.3 and Fig 1.14, brings to light a high discrepancy among the three measurements [44, 45, 46] (blue shaded region) and with the indirect determination from [48, 49]. The two measured values of [45, 46] disagree by 5σ, $\omega\gamma_{0.204MeV}$ of [46] being 4 times higher than [45]. The indirect $\omega\gamma_{0.204MeV}$ is at best 5.8 times lower than the measurement of [45].

Experiment	Ref	$\omega\gamma$ meV
Sallaska *et al* (TRIUMF, Canada)	[46]	$5.7^{+1.6}_{-0.9}$
Stegmuller *et al* (Bochum, Germany)	[45]	1.4(3)
Seuthe *et al* (Bochum, Germany)	[44]	<0.36
Indirect data	[48, 50, 51, 49, 52]	$0.27^{+0.16}_{-0.09}$

Table 1.3: Current status on the strength of the E_R=0.204 MeV resonance. Three experiments aimed at measuring it. The latest determination was obtained from the compilation of all experiments on the spectroscopy of the resonant state in ^{23}Mg*.

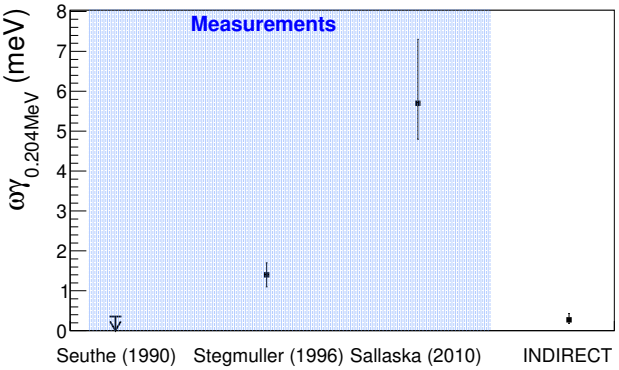

Figure 1.14: Known values on $\omega\gamma_{0.204MeV}$.

In summary, the ^{22}Na(p,γ)^{23}Mg reaction rate is expected to be dominated at peak nova temperatures by the E_R=0.204 MeV resonance. Values of this resonance strength are currently highly scattered, resulting in uncertainties greater than a factor of 4.

1.4.4 Impact on the ^{22}Na ejected mass

The uncertainties on the reaction rate impact the predicted ejected mass of ^{22}Na during a nova outburst. With the current dispersion in $\omega\gamma$ of the dominant resonance contribution, the observation of the ^{22}Na flux from a nova event would never allow us to investigate the underlying stellar physics. Indeed as shown in Ref. [46], a reduction of the total reaction rate by a factor of 3, due to a change in $\omega\gamma$ [45, 46], induces a reduced production of ^{22}Na by a factor $2-3$, depending on the nova models. We highlight here the sensitivity of the ejected mass of ^{22}Na to the $\omega\gamma$ at E_R=0.204 MeV.

The Fig. 1.15 shows the ejected mass of ^{22}Na as a function of $\omega\gamma_{0.204MeV}$. Nova simulations were achieved with the MESA code [40], considering a classical ONe nova of M_{WD}=1.2 $M_\odot$. These stellar-explosion simulations are the subject of Chapter 9. Reaction rates were determined with the Monte-Carlo method (Sec.8.3). The current data on $\omega\gamma_{0.204MeV}$ (Table 1.3) have been used, two lower values at 10 μeV and 1μeV were also tried out. Above 0.5 meV, the ejected mass of ^{22}Na was noticed that it is inversely proportional to $\omega\gamma_{0.204MeV}$. Below 0.1 meV, the predicted mass appears roughly constant with respect to the resonance strength. These two tendencies can be easily understood. When $\omega\gamma_{0.204MeV}$ is high enough that this resonance dominates at peak nova temperatures, then the amount of destroyed ^{22}Na is proportional to this dominant reaction rate and inversely proportional for the amount of ejected ^{22}Na. But if $\omega\gamma_{0.204MeV}$ is lower than 0.1 meV, then the other resonances contribute, see Fig. 1.11, 1.12. The amount of ejected ^{22}Na ions is no more dependent on this resonance strength.

The estimated detection limit of ejected mass from the COMPTEL (INTEGRAL) mission is marked with the blue (green) line in Fig. 1.15. In line with previous works [5, 20], the expected amount of ejected ^{22}Na is at best 10 times lower than these instrumental sensitivities. This explains why this radioelement has never been detected in the Universe.

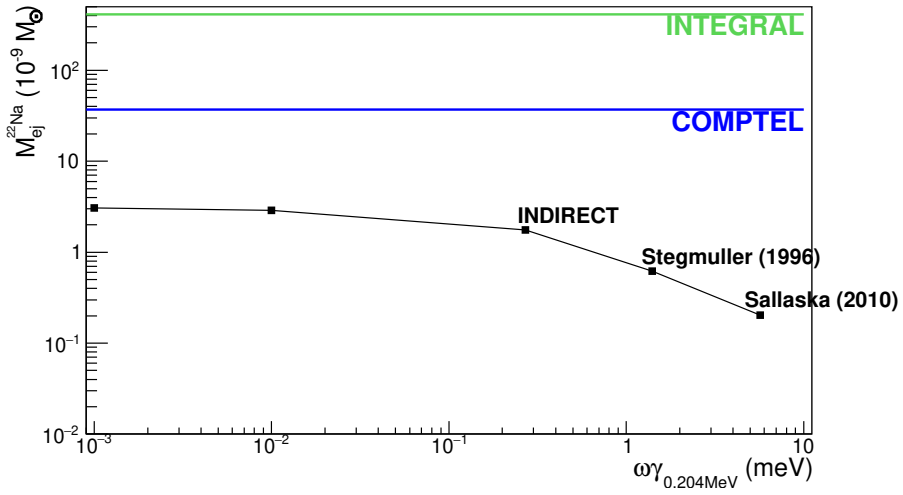

Figure 1.15: The ejected mass of ^{22}Na ($M_{ej}^{^{22}Na}$) predicted in a nova model as a function of the resonance strength at E_R=0.204 MeV ($\omega\gamma_{0.204MeV}$). Nova outbursts were calculated with the code MESA [40] and the ^{22}Na(p,γ)^{23}Mg reaction rates with the Monte Carlo method. Known values in $\omega\gamma$ were used and two lower values were also considered. Blue (green) line marks the detection limit of ejected mass estimated by the COMPTEL (INTEGRAL) mission.

In summary, the predicted amount of ^{22}Na nuclei ejected by a nova varies by a factor 10 due to the current lack of knowledge about the resonance strength at E_R=0.204 MeV. For strengths higher than 0.1 meV, this predicted mass is inversely proportional to the strength. We therefore strongly emphasize the need for new reliable nuclear data for this resonance.

1.5 Aims of the thesis

This Ph.D. work in the field of nuclear astrophysics is related to the questions around the presence of ^{22}Na in the Galaxy. To shed more lights on this key radioelement, this thesis had three well-defined goals.

1. The rate of the ^{22}Na(p,γ)^{23}Mg reaction had to be determined as accurately as possible at peak nova temperatures. We had to bring a new value of the E_R=0.204 MeV dominant resonance strength, and therefore to assess the current scattered data. This involved setting up a new nuclear experiment.

2. To know whether the next generation of γ-ray space telescopes will be able to observe the ^{22}Na line, the amount of ejected ^{22}Na, the distance and frequency of novae occurrence must be taken into account. This was achieved by means of novae simulations.

3. It was also necessary to prove that the measurement of ejected ^{22}Na would allow us to provide constrains on the nova models. We sought to find out how some uncertain physical parameters of novae might impact the production and hence the flux of ^{22}Na. In particular, the impact of an important parameter in the phases before the nova outburst, i.e. the temperature of the white dwarf and the gas accretion rate, has been investigated.

Part II

On the experimental aspects

CHAPTER 2

Selections of method and experimental parameters

2.1 Introduction

A new measurement with high accuracy is needed for the resonance strength $\omega\gamma$ of the reaction ^{22}Na(p,γ)^{23}Mg at Ex=7.785 MeV. How to bring experimentally a new brick to the question of ^{22}Na stellar synthesis? An answer will be drawn along this Chapter with the setting up of an experiment at GANIL. This Chapter will not be an extensive study of experimental approaches to get resonance strengths but a work focused on the specific case of the Ex=7.785 MeV state in ^{23}Mg*. It was in particular excluded to directly reproduce the reaction ^{22}Na(p,γ)^{23}Mg at stellar temperatures, as already done [46, 45]. The main reason was the challenges of using such radioactive target. Indirect method was so favoured: the derivation of $\omega\gamma$ through the measurements of the underlying spectroscopic parameters in ^{23}Mg*. The chosen experimental approach could also be applied a priori to other discussed resonances in nova thermonucleosynthesis, like the reaction ^{25}Al(p,γ)^{26}Si.

The resonance strength can be accessed through the measurements of the width ratio and the state spin as explained in respectively Sec.2.2.1 and Sec.2.2.4. The width ratio can be derived from the total and proton widths of the state in ^{23}Mg*. The experimental methods are overviewed in Sec.2.2.2 for the total width, and in Sec.2.2.3 for the proton one. The next Sec.2.3 specifies the experimental requirements to reach the needed sensitivity in state lifetime and proton branching ratio. Once the reaction to populate the state of interest was decided in Sec.2.3.1, with additional conditions to select the useful signals in Sec.2.3.2, the suited detection systems for the particle and γ-ray observables are considered in Sec.2.3.3. The opted experimental set-up was used at GANIL before the Ph.D. work.

2.2 Accessing the resonance strength

2.2.1 Width ratio

The strength of each resonance in the key reaction ^{22}Na(p,γ)^{23}Mg, with excited states just above the proton emission threshold, is determined by the width ratio γ. It depends on the partial and total widths of the excited state

$$\gamma = \frac{\Sigma_j \Gamma_{p,j} \times \Sigma_i \Gamma_{\gamma,i}}{\Gamma_{tot}} \tag{2.1}$$

where $\Gamma_p = \Sigma_j \Gamma_{p,j}$ ($\Gamma_\gamma = \Sigma_i \Gamma_{\gamma,i}$) is the sum over all possible proton (γ-ray) decay channels, and Γ_{tot} the total width equal to the sum of these two contributions: $\Gamma_{tot} = \Sigma_j \Gamma_{p,j} + \Sigma_i \Gamma_{\gamma,i}$. To get γ, it is sufficient to determine two of the three mentioned widths. The γ-ray decay branching of ^{23}Mg states, within the

Gamow window, are given in Fig. 2.1. Emissions of γ-rays are in principle possible towards all lower-lying states. Up to three γ-ray transitions are usually dominant, above 1% of $\Sigma_i\Gamma_{\gamma,i}$. The astrophysical Ex=7.785 MeV state presents a main transition to the first excited state, with $E_{\gamma,0}$ = 7.333 MeV and intensity $I_\gamma \geq 84\%$. This value of I_γ is debated because of the existence of another transition to the Ex=2.052 MeV state, with $E_{\gamma,0}$ = 5.734 MeV. This transition was seen in the ^{23}Al β-delayed experiment [53, 54] but not for $\gamma - \gamma$ coincidences in the comprehensive experiment with Gammasphere [49], nor in the recent indirect experiment [52]. As described later on, the second transition was not observed in the present work. The Ex=7.785 MeV state can decay by proton only towards the ground state of ^{22}Na, being 0.205 MeV above p+^{22}Na$_{gs}$ and 0.378 MeV below p+^{22}Na$^*_{1st}$ (Fig. 2.1). The proton partial width Γ_p is the product of the total width with the proton branching ratio BR_p.

$$\Gamma_p = BR_p \times \Gamma_{tot} \tag{2.2}$$

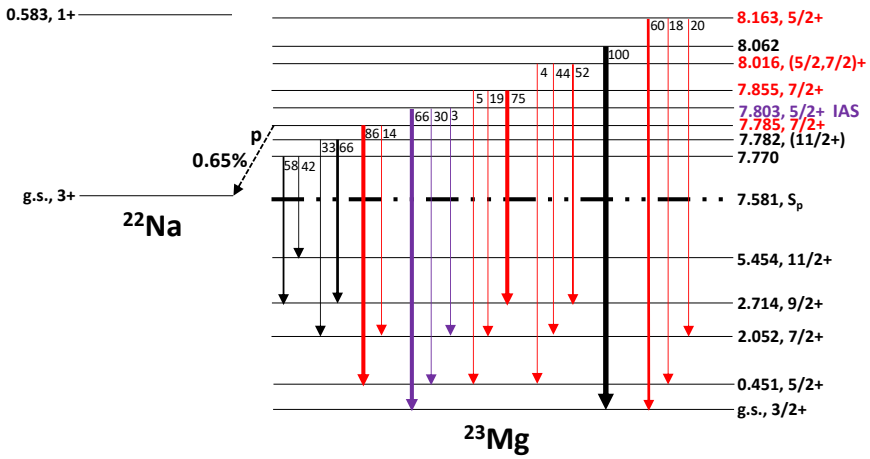

Figure 2.1: Known proton and γ-ray decay scheme of ^{23}Mg states within 500 keV above proton threshold, from [55] and BR_p [48]. Only s-captures (red written) and d-captures are shown. For the full γ-ray decay scheme see [55, 49]. The Isobaric Analog State (IAS) with ^{23}Al$_{gs}$ is indicated in purple.

Determination of γ-ray partial widths requires to know I_γ, the transition nature, magnetic or electric, and its order. It makes the experiment more complex. On the other hand, by Heisenberg's principle, the total width is simply given by

$$\Gamma_{tot} = \frac{\hbar}{\tau} \tag{2.3}$$

with τ the state lifetime. Using Eq. (2.3) and (2.2) in Eq. (2.1), the width ratio γ can be derived from the measurements of τ and BR_p

$$\gamma = BR_p(1 - BR_p)\frac{\hbar}{\tau} \tag{2.4}$$

2.2.2 Total width

Measurements of total width Γ_{tot}, or equivalently lifetime τ, have been the subject of many experiments over the past half century. Excited states with Ex $\sim$ MeV have lifetimes in the range $[10^{-16}, 10^{-6}]$ s, depending partly on the excitation energy. The unbound states, above particle emission threshold, are usually short-lived with $\tau \leq$1 fs. A brief overview of the different experimental methods to access lifetimes is given in Table 2.1. More details can be found in [56, 57].

Method	Time range (s)	Comments (pro/con with respect to the key state in ^{23}Mg*)
Resonance fluorescence	$[10^{-17}, 10^{-9}]$	only stable nuclei
Coulomb excitation	$[10^{-17}, 10^{-9}]$	difficult due to the small branching from the ground state in ^{23}Mg
Proton resonance	$[10^{-22}, 10^{-16}]$	$\tau << $ fs
Blocking	$[10^{-18}, 10^{-15}]$	$\tau << $ fs
X-ray coincidence	$[10^{-17}, 10^{-15}]$	$\tau <$ fs
Doppler shift based	$[10^{-15}, 10^{-10}]$	successful on 1$< \tau$ fs $<$20 [49, 52, 55, 58]
Recoil distance	$[10^{-12}, 10^{-8}]$	$\tau >>$ fs
Electronic timing	$[10^{-10}, 10^{-6}]$	$\tau >>$ fs

Table 2.1: Short overview of lifetime measurement techniques, commented with respect to the case of interest: the unstable Ex=7.785 MeV state in ^{23}Mg*, and with expected $\tau \sim$ fs.

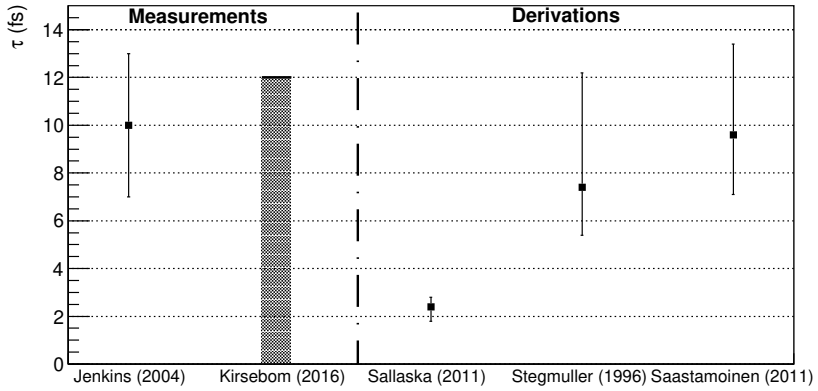

Figure 2.2: Known lifetimes of the Ex=7.785 MeV state in ^{23}Mg*. The vertical line divides results between measured and derived values. Only Jenkins *et al* [49] resulted in a finite and directly measured value.

The aimed state presenting an expected lifetime in the order of 1-10 fs, only the Doppler Shift Attenuation Method DSAM was found of interest. The past work on ^{15}O by C. Michelagnoli *et al* [58] has proven the feasibility of such resolved lifetime method with AGATA. Lifetimes measured or determined, from $\omega\gamma$ and BR_p [48], are summarized in Fig. 2.2. So we decided to use this Doppler method to determine the lifetime of the state of interest.

A moving nucleus with a velocity β emits γ-rays with an energy $E_{\gamma,0}$ in the rest frame, and shifted in the laboratory frame. This shift comes from Doppler effect, expressed in the relativistic case

$$E_\gamma = E_{\gamma,0}\frac{\sqrt{1-\beta^2}}{1-\beta\cos(\theta_{DS})} \tag{2.5}$$

where θ_{DS} is the angle between the recoil nucleus and the emitted γ-ray. This effect is illustrated in Annexes A.3.1. Two reasons, linked to the Doppler effect, favour the inverse kinematics to populate the state: faster is the recoil, higher is the energy shift and closer to beam axis is the recoil, simpler is the experiment with the detection in γ-ray energy and angle sufficient to quantify the Doppler effect. It is also interesting to look at γ-rays away from [80, 90] deg where the Doppler shift is minimal. If a degrader is inserted along the nucleus travelling path, then the state lifetime impacts the observed Doppler shift: the distribution in β-at-emission varies according to τ. Thus, the sensitivity on τ relates to the velocity of the emitting nucleus and to the stopping power of the degrading medium. With long-lived nuclei from ps

to 100 ps, the Plunger method is often used. Two layers of different thickness are used: a thin degrader placed just after the production target to slow down the nuclei and a thick stopper (the plunger) away from the target. Hence two peaks are observed, shifted for in flight emission and unshifted from nuclei stopped in the plunger. The ratio of these two components allows to derive the lifetime. The Differential Plunger [59] is however not suited for measurements of τ from fs to 10 fs since the target would have to be separated from the plunger by a few 0.1 μm, that is too small.

DSAM [57] can be used when τ is of the order of magnitude of the slowing down time of the emitter in medium. The energy losses of ^{23}Mg for typical incident energies in inverse kinematics, are presented in Annexes A.3.2. The fs accuracy is reachable with DSAM as it will be developed in Sec.2.3.1. The lifetime could be obtained from lineshape analysis, as first implemented in [60]. This is also possible through the shift of the γ-ray peak centroid as a function of backward/forward angles (fractional DSAM as [49]). Lineshape analysis implies to quantify, by a χ^2 analysis, the good matching between experimental peak and simulated peak which includes

1. reaction kinematics,
2. decay mechanisms (τ, I_γ, side feeding...),
3. slowing-down processes (properly referenced stopping powers),
4. detector response functions.

Pushing the limit to fs demanded high resolving power in the γ-ray detection, which was feasible with γ-ray tracking arrays only like the European Advanced GAmma Tracking Array (AGATA, [61]) or the American Gamma-Ray Energy Tracking In-beam Nuclear Array (GRETINA, [62]). The first one was used for this experiment. The cases of high lying excited states with small cross sections, make also such large coverage γ-ray arrays very useful.

2.2.3 Proton width

Accessing to the proton widths of states close to threshold (<300 keV) is an experimental challenge. Apart from measuring spectroscopic factors (C^2S_p), these widths may be estimated from particle branching ratios. This is commonly done in β-delayed experiments, as in [51, 50, 48, 54] for the Ex=7.785 MeV state in ^{23}Mg*. The results in BR_p of [51, 50, 48] are shown in Fig. 2.3. The measured values are not in good agreement, the value from Saastamoinen *et al* [50] is more than 3σ away from the one from Friedman *et al* [48].

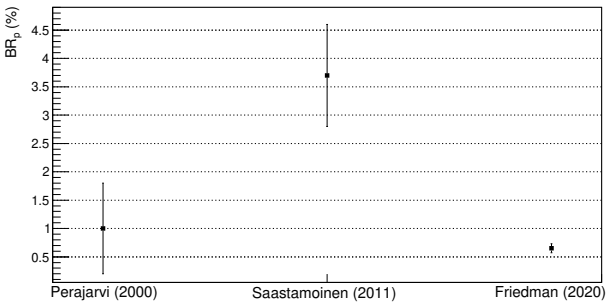

Figure 2.3: Measured proton branching ratios BR_p of the Ex=7.785 MeV state in ^{23}Mg.

The present experiment aimed also at measuring BR_p. Two methods were proposed, they will be developed in the following lines.

The first approach is based on two main steps

1. Reconstruction of the excitation energy in ^{23}Mg* from (E_p, θ_p) of the measured protons,
2. Quantification of emitted protons ($I_{Ex\&p}$) versus γ-rays ($I_{Ex\&\gamma}$).

Proton particles had first to be identified. This was done with classical ΔE-E identification plots. The used detector SPIDER measured protons properties (β_p^{lab},θ_p^{lab}) in the laboratory frame, which were used to derive the proton center-of-mass velocity. The excitation energy spectrum could be obtained from the proton center-of-mass velocity. These calculations are explained in Annexe A.1.2.

Having opted for inverse kinematics, the emitted protons were close to the beam axis (<30 deg). Due to their travels through the target and the degrader, energy losses and straggling were of importance. The measured energy of proton was corrected by the energy losses in target to reconstruct the energy at emission E_p, see Sec.5.4.1.

After identifying which excited state protons originate from, the associated branching ratio could be derived. Indeed, providing the reaction to populate this excited state is selected, BR_p is given by:

$$\begin{aligned} I_{Ex\&p} &= BR_p \times I_{Ex} = \frac{BR_p}{1 - BR_p} \\ BR_p &= \frac{1}{1 + \frac{I_{Ex\&\gamma}}{I_{Ex\&p}}} \end{aligned} \tag{2.6}$$

where I_{Ex} is the total number of counts of populated states at Ex, $I_{Ex\&p}$ ($I_{Ex\&\gamma}$) is the number of proton (γ-ray) counts in coincidence with the reaction ejectiles ^{4}He (Sec.2.3.2). From BR_p, the proton width was determined with Eq. (2.2).

The second approach is independent of the protons measurement. The particle branching ratio is estimated from the measured γ-ray branching ratio BR_γ according to

$$\begin{aligned} BR_p &= 1 - BR_\gamma \\ BR_\gamma &= \frac{I_{Ex\&\gamma}}{I_{Ex}} \end{aligned} \tag{2.7}$$

where I_{Ex} is the number of counts of the peak at Ex in the ejectiles ^{4}He spectrum. This makes the method more challenging since I_{Ex} should be estimated without coincidences to reduce the noise level. Furthermore, the difference between the estimated $I_{Ex\&\gamma}$ and I_{Ex} must be unambiguous, that is to say $I_{Ex\&\gamma} < I_{Ex}$ with the statistical uncertainties included. It implies

$$I_{Ex} \geq \left(\frac{1 + \sqrt{1 - BR_p}}{BR_p}\right)^2 \tag{2.8}$$

The minimum number of counts I_{Ex} needed to measure BR_p, from Eq. (2.8), are plotted over BR_p in Fig. 2.4. The expected $BR_p \leq 1$ %, shown with the red shaded region, requires so to measure more than 4×10^4 counts in the peak of the populated Ex=7.785 MeV state.

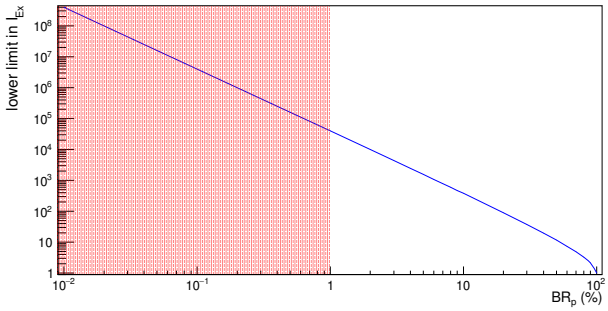

Figure 2.4: Calculated minimum number of counts in the peak of the populated Ex=7.785 MeV state, as a function of the nuclear proton branching BR_p which is estimated by measuring the γ-ray branching from counts in γ-rays and in the peak at Ex.

As a conclusion, the proton width of the key state can be estimated in the present experiment from the measured proton branching ratio by using two independent methods. Nevertheless, the approach based on protons and γ-ray detection in coincidence with ^{4}He has fewer disadvantages than the one based on γ-ray&^{4}He and ^{4}He detection alone.

2.2.4 Spin

In Jenkins *et al* [49], the spin was written to be measured at the value $\frac{7}{2}^+$ by $\gamma - \gamma$ distribution. A recent work by Kwag *et al* [63] has estimated another value $\frac{5}{2}^+$ by looking at the differential cross sections in ^{23}Mg* of the transfer ^{24}Mg(p, d) reaction. However both experiments have uncertainties making the measured spin doubtful. In the first case, the spin and parity were constrained by looking at the deexciting oriented states ratio R_{DCO}=0.89(5)[49] from the observed γ-ray transitions towards the Ex=0.451 MeV state (J=$\frac{5}{2}^+$). This found R_{DCO} value indicates a pure stretched-dipole transition. Yet the decay was identified as a mixed M1/E2 transition [49, 64]. In the second case, the resolution of the Si detector ($\sigma \sim$ 80 keV) did not allow them to well separate the Ex=7.785 MeV and 7.855 MeV states in ^{23}Mg*. They analysed the differential cross sections by only considering $\ell < 3$ transfers from ^{24}Mg$_{g.s.}$, hence intrinsically rejecting J> $\frac{5}{2}$. For the used beam energy of 31 MeV/u, the compound nucleus has a cross section of σ_{comp} =2×10^{-2} mb (from the TALYS code [65, 66]). With transfer cross sections usually of the order of ≤mb, the compound nucleus is so expected to compete with the transfer channel for ≥2%. Indeed, the $\frac{d\sigma}{d\Omega}$ distribution of the Ex = 7.788 MeV state, in Fig. 6 of Ref. [63], is observed quite flat as one expects for fusion evaporation channel. We so wanted to measure again the spin of the Ex=7.785 MeV state in ^{23}Mg*.

Different methods are at disposal to access to the spin J of a nuclear state. The observables after the state decay, here protons or γ-rays, present angular distributions function of the spin. These distributions, if statistics are sufficient, can be fitted by Legendre's polynomials to extract J. Other tools can be used according to the reaction mechanisms. In case of a dominant transfer, differential cross sections are derived from the angular distributions of the ejectiles or the recoils. They are then compared with the calculated differential cross sections with respect to the transferred orbital angular momentum ℓ, see a recent example in [63]. On the other hand, the probability of the compound nucleus formation depends on the spin, expected to be proportional to 2J+1. It is shown in Fig. 2.5 where the integrated cross sections $\sigma_{compound}$ of the fusion evaporation reaction ^{3}He(^{24}Mg,^{4}He)^{23}Mg had been calculated with the TALYS code [65, 66], based on Hauser-Feshbach calculations, and then normalized by 2J+1. This was observed constant along J, in case of the three Ex=$\{0.0, 0.451, 7.785\}$ MeV states. Thus it might be possible to determine the spin by looking at the experimental cross sections, if the state is mostly populated by fusion

evaporation reactions.

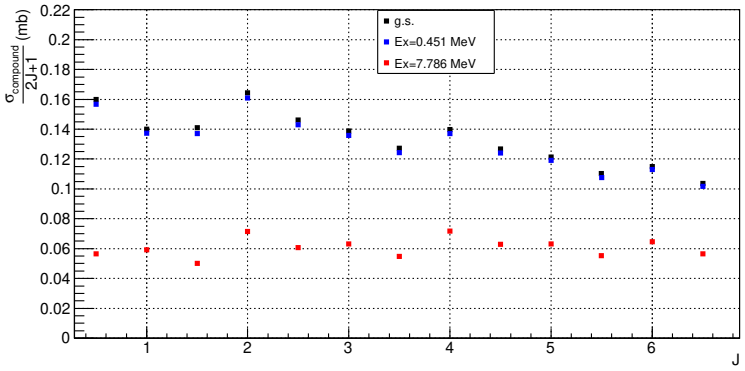

Figure 2.5: Calculated cross sections σ_{compound} for the fusion evaporation reaction ^{3}He(^{24}Mg,^{4}He)^{23}Mg as a function of the state spin J. Cross sections, obtained with TALYS code [65, 66], are normalized by 2J+1. Three states are considered: Ex=$\{0.0, 0.451, 7.785\}$ MeV. The compound cross section is proven here proportional to 2J+1, and it decreases over Ex.

In conclusion, we would like to experimentally access to state spins through the compound nucleus mechanism which favours the state populations according to 2J+1.

2.3 Principle of the experiment

Along this section, the experiment is considered with the double aims of measuring a short lifetime and a weak proton branching ratio from the Ex=7.785 MeV state in ^{23}Mg*.

2.3.1 Choice of the reaction populating states in ^{23}Mg*

The initial velocity of ^{23}Mg plays a role in both the lifetime and BR_p sensitivities. The target medium, inducing the degradation of the ^{23}Mg velocity, also governs the accessible sensitivity. This interdependence between target composition and energy at reaction is shown in Fig. 2.6. In Fig. 2.6(a) and (b), the shift of the γ-ray Doppler shift after a travel of 1 fs in the target medium is presented as a function of the ^{23}Mg initial velocity ($\beta_{^{23}\text{Mg}}$ at reaction), and of the time spent in target after reaction and before emission (t_{travel}). Two different mediums for DSAM were calculated: gold for Fig. 2.6(a) and lead for Fig. 2.6(b). Thick black lines surround the regions with a shift$\geq$1 keV, and dotted black lines the regions with a shift$\geq$2 keV. From these figures, it was possible to see that gold medium was preferred for the medium of our experiment, as already done in [52]. The "$\geq$2 keV shift" region was aimed at in the choice of the reaction and its kinematics: $\beta_{^{23}\text{Mg}} \in [0.028, 0.085]$ (Fig. 2.6(a)). Then, the proton energies in the laboratory were calculated out of target with a chosen thickness of 10 μm, in Fig. 2.6(c) for gold and in Fig. 2.6(d) for lead. Sec.2.3.2 will explain the reason of such medium thickness, due to an expected beam halo. The lower limit of E_p^{lab} $\geq$2 MeV is red marked. This is a reasonable condition for most of particle detectors in order to be away from the low energy background due to $\beta^{+/-}$ particles. It narrowed the aimed velocity range of the ^{23}Mg recoil nucleus, see Fig. 2.6(a) and (c).

$$\beta_{^{23}\text{Mg}} \in [0.071, 0.085] \quad \text{(gold target)} \tag{2.9}$$

This range of velocities corresponds to kinetic energies around 100 MeV. In this experiment, the velocity was $\beta_{^{23}\text{Mg}}$=0.077. This was well within the good range of velocities for DSAM.

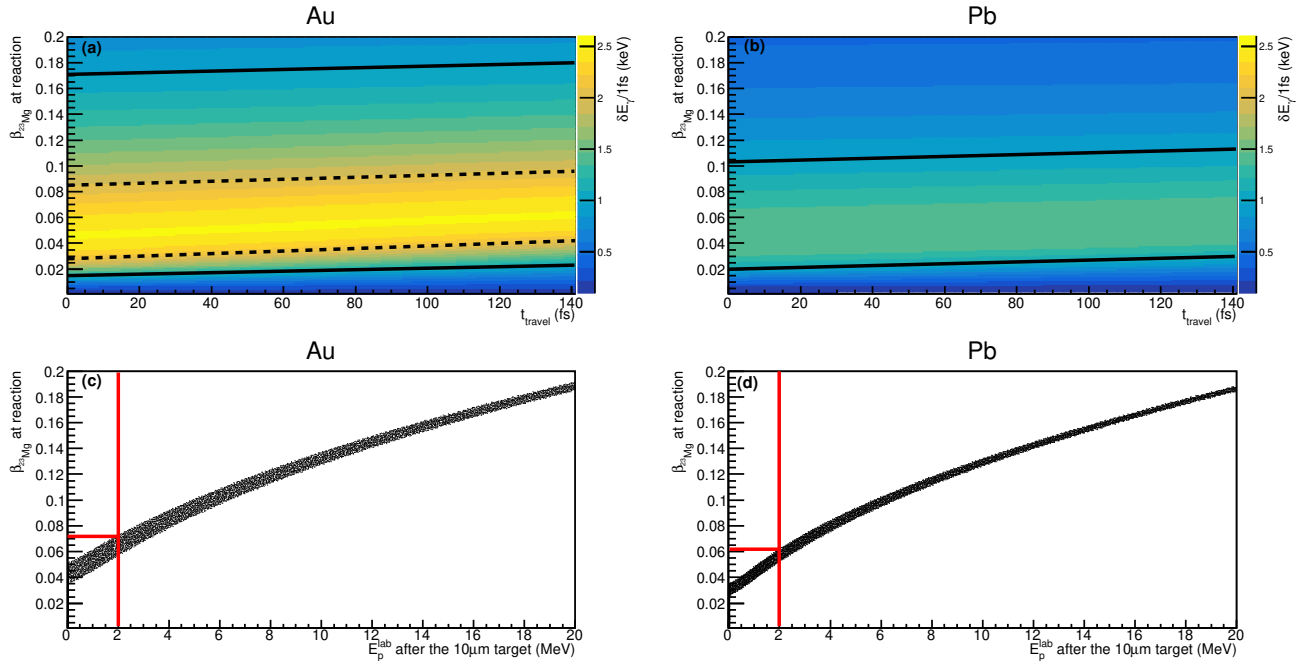

Figure 2.6: Panels (a, b): the induced shift of the Doppler shift after 1 fs in the medium, in color scale written $\delta E_\gamma/1fs$, as a function of the velocity-at-reaction of populated state in $^{23}Mg^*$ ($\beta_{^{23}Mg}$) and of the time spent in target after reaction and before emission of γ-ray (t_{travel}). Solid black lines surround the region with a shift of Doppler shift of $\delta E \geq 1$ keV, dashed black lines for $\delta E \geq 2$ keV. Panels (c, d): the proton energy out of a 10 μm target, noted E_p^{lab}, over $\beta_{^{23}Mg}$. Red lines mark the low limit of 2 MeV for proton energies. Target medium is gold for panels (a, c) and lead for panels (b, d). Doppler shifts of γ-rays were calculated for θ_γ=180 deg and energy losses of proton for θ_p=0 deg. These plots were simulated for the Ex=7.785 MeV state.

The energy losses and the straggling of protons in gold being expected important, two different target thicknesses were chosen for the experiment. The states in ^{23}Mg have been investigated many times through various reactions. The Table 2.2 presents them and their assets for the present case. The value of $\beta_{^{23}Mg}$=0.075, within Eq. (2.9), was used to estimate with LISE++ the associated kinematics. Criteria which orientated the choice of reaction were

1. the velocity of ^{23}Mg in Eq. (2.9), resulting in a feasible beam energy
2. the target composition
3. the statistics in populated ^{23}Mg from available beam intensity, cross section and target density
4. the measurement of ejectiles to select the reactions of interest.

Inverse kinematics had been privileged in Doppler effect former measurements. Direct kinematics had also been studied, but either required high energies for light beams $Z \leq 2$ with heavy ions implanted in gold, or the stable targets did not allow to reach the fs sensitivity, see Footnote A of Table 2.2. The reactions p(^{25}Mg) and p(^{24}Mg) are not a possible choice for our present experiment because of their low Q-values: the minimal β at reaction would have been out of the aimed range and the ejectile would have been hardly detectable. So the cross sections were not calculated. The reactions involving ^{22}Na are more difficult because of the low radioactive beam intensity or the unstable target. The ^{12}C+^{12}C fusion evaporation reaction would be another suitable choice as proven by the measurement [49]. However, it requires a γ-ray

coverage at forward and backward angles to maximise Doppler shift on the measured centroid (fractional DSAM). The difficulty of the ejectile detection was overcome, in Ref. [49], by $\gamma-\gamma$ coincidences thanks to the high efficiency (4π) of the used γ-ray spectrometer (Gammasphere). The cross sections, if not measured, were estimated with the nuclear codes: FRESCO [67] for transfer reaction and TALYS [65, 66] for compound nucleus formation. The higher differential cross section of ^{3}He(^{22}Na,d) by a factor 10 is not enough to compensate the lower radioactive beam intensity.

Reaction, Q (MeV)	Kinematics	Ref.	Beam	energy MeV (intensity pps)	$\frac{d\sigma}{d\Omega_\alpha}^{lab}$ (μb/sr)	Target (density at.cm^{-2})	Ejectile	E (MeV) along beam	Identification
^{3}He(^{24}Mg,α), 4.046	inverse	Present	stable	111 (>10^{10})	38±12[c]	^{3}He in Au	^{4}He	41	spectrometer [68]
		[52]		75 (>10^{10})	23	(>10^{17})		27	Si telescopes
	direct			135 (SPIRAL2...)	not calculated	^{24}Mg in Au (10^{18})[b]		131	thick Cs/Si
		[69]		8 (10^{11})	not seen	^{24}Mg (10^{19})		4	Cs/Si
p(^{25}Mg,t), -15.380	inverse		stable	142 (>10^{10}) $\beta_{^{23}Mg}\geq$0.11	not calculated	p in Au ($\leq 10^{18}$)[b]	^{3}H	<1	backward Cs/Si
	direct	[70]		229 (SPIRAL2...) 40, $\beta_{^{23}Mg}$=0.05	not calculated 140	^{25}Mg in Au ^{25}Mg[a]		200 5	thick Cs/Si Cs/Si
p(^{24}Mg,d), -14.307	inverse		stable	170 (>10^{10}) $\beta_{^{23}Mg}\geq$0.12	not calculated	p in Au ($\leq 10^{18}$)[b]	^{2}H	<1	backward Cs/Si
	direct	[63] ([71, 72])		31 (10^{11}) $\beta_{^{23}Mg}$=0.004	not calculated	^{24}Mg[a] (10^{19})		9	Cs/Si
^{3}He(^{22}Na,d), 2.087	inverse		radioactive	93 (<10^{6})	253[d]	^{3}He in Au (>10^{17})	^{2}H	23	Cs/Si, gas chamber
	direct	[73]	stable	30 (10^{11}) $\beta_{^{23}Mg}$=0.012	1.35×10^{3}	^{22}Na in C[a] (10^{18})		24	idem
p(^{22}Na), 7.581	inverse		radioactive	63 (<10^{6})	0.27[d]	p in Au ($\leq 10^{18}$)[b]	none		
^{12}C(^{12}C,n), -2.592		[49]	stable	22 (>10^{12}) $\beta_{^{23}Mg}\sim$0.03	$\sim$ 80	^{12}C[a] (2.10^{21})	n		poor resolution

[a] induced $|\delta E_\gamma|$ for (dt=1 fs, θ_γ=160 deg, $E_{\gamma,0}$ = 7.333 MeV) are {0.01:^{25}Mg, 0.04:^{24}Mg, 0.2:^{22}Na in C, 0.35:^{12}C} keV.
[b] From ion implantation experiments (^{24}Mg in copper [74], deuteron in metals [75])
[c] Calculations in Sec.3.3.2 (response function)
[d] Calculations with FRESCO [67] and TALYS [65, 66] codes.

Table 2.2: Possible reactions to populate the Ex=7.785 MeV state in ^{23}Mg* and their features with respect to (τ, BR_p) measurements. Both inverse and direct reactions are considered. LISE++ was used to estimate the required beam energy to reach the value of $\beta_{^{23}Mg}$ =0.075 at reaction, within Eq. (2.9), and the associated ejectile energy.

A special care is now given to the ^{3}He(^{24}Mg,^{4}He)^{23}Mg* reaction. The total cross section of the ^{3}He(^{24}Mg,^{4}He)^{23}Mg* reaction at Ex=7.785 MeV was calculated as a function of the beam energy ($E^{lab}_{^{24}Mg}$), and it is shown in the left of Fig. 2.7. The blue curve corresponds to the compound nucleus reaction mechanism and the red curve to the direct transfer of one neutron from ^{24}Mg to ^{3}He considering a neutron spectroscopic factor of 1, since never measured. Whatever the mechanism is, the energy range [70, 120] MeV is associated to cross sections of around 1 mb. Hence the required energy to reach best (τ, BR_p) sensitivities, i.e. $E^{lab}_{^{24}Mg}$ $\sim$100 MeV, is within the energy range associated with the maximum cross sections. The selected experimental energy is marked by a black vertical line in Fig. 2.7.

The differential cross sections in laboratory ($\frac{d\sigma}{d\Omega_\alpha}^{lab}$) were also calculated as a function of the ^{4}He ejectile angle in laboratory ($\theta^{lab}_{^{4}He}$), LISE++ was used to convert parameters from center of mass to laboratory frame, see Fig. 2.7 (right). The shaded region marks the VAMOS aperture during the experiment. The calculated $\frac{d\sigma}{d\Omega_\alpha}^{lab}$ for the compound nucleus mechanism ($\frac{d\sigma}{d\Omega_\alpha}^{lab}$ $\sim$ 200μb/sr) was found ×5.2 higher than the estimated one from the experimental data (38 μb/sr, Table 2.2). Since CS^2_n have never been measured, it is impossible to know the dominant mechanism, compound nucleus or direct transfer, for a particular state. However the direct reaction to populate the Ex=7.785 MeV state requires ℓ=4 or above for the transferred momentum. Neutrons in ^{23,24}Mg fill shells up to the 1d5/2 shell, see Fig. 7.1, the probability to find in the key state some component of the 1g9/2 shell is extremely small. Hence, the

dominant reaction mechanism for the astrophysical state is most likely the compound nucleus or multi step transfer. Lifetimes of compound nucleus formation are longer than direct transfer processes, typically $[10^{-18}, 10^{-16}]$ s compared to 10^{-22} s for direct reactions. However, the time scale of compound nucleus will not impact the slowing down of the Ex=7.785 MeV state in gold: for β=0.075, the ^{27}Si nucleus losses 0.19 MeV, that is 5×10^{-5} change in β, after traveling 10^{-16} s in gold.

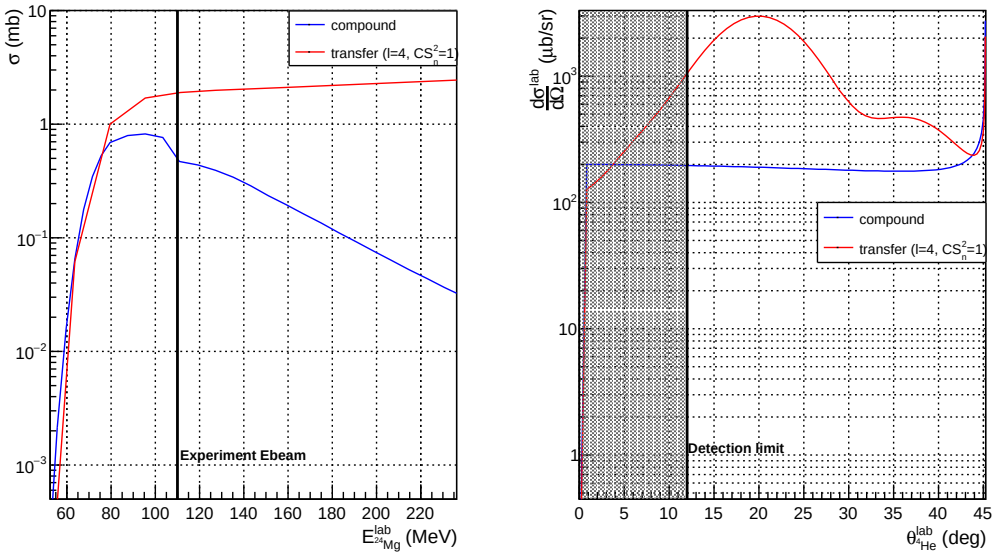

Figure 2.7: Calculated cross sections for the ^{3}He(^{24}Mg,^{4}He)^{23}Mg* reaction at Ex=7.785 MeV. On the left, the total cross section σ is plotted as a function of the laboratory beam energy. The vertical line corresponds to the beam energy of the experiment. On the right, the differential cross section, calculated for E_{beam}, is shown in the laboratory frame over the ^{4}He ejectile angle. The shaded grey region corresponds to the experiment aperture of the VAMOS spectrometer. Blue curve: the compound nucleus mechanism calculated with the TALYS code [65, 66]. Red curve: the direct transfer of one neutron calculated with the FRESCO code [67].

In conclusion on the study of the different reactions to populate ^{23}Mg states,

1. We decided to perform the inverse kinematics reaction of ^{24}Mg beam onto a target of ^{3}He implanted in gold at the incident energy of 110 MeV, already proven successful in [52]. This energy is $\times$1.5 higher than in [52] because we expected a slightly higher cross section while being within the optimum of the DSAM.

2. The dominant reaction mechanism to populate the Ex=7.785 MeV state is expected to be the compound nucleus or multi step transfer. Since the neutron spectroscopic factors are unknown, the direct transfer of one neutron may also play a part in the populations of the other states in ^{23}Mg*.

2.3.2 Improving the signal-to-noise ratio

Three main reasons demanded to increase the signal-to-noise ratio in γ-ray spectra as much as possible. First, the expected reaction cross section is only tens of μb/sr around 0 deg angle, resulting in a low statistics. Second, uncertainties in the lineshape analysis for τ could come from side-feeding by higher lying states, that was unwanted here. The quantification of proton decay events required also to reject side-feeding. Third, we wanted to measure the excitation energies in ^{23}Mg to confirm the level scheme of

^{23}Mg. These three main reasons led us to find a way to select the direct feeding of the states. This could be achieved either by measuring the recoils ^{23}Mg or the ejectiles ^{4}He in coincidence with the γ-rays or the protons. It was decided to measure the ^{4}He ejectiles, as it was done in [52].

On the one hand, the detection of the ejectiles ^{4}He was less challenging. Fusion evaporation reactions with atoms of carbon and oxygen, present in the chamber as a pollution, could contaminate the ejectiles measurement because of high amounts of produced (p, n, α) particles. This was observed during the experiment [52]. These multiple reactions channels populated nuclei close to ^{23}Mg in mass, charge and γ-rays. For instance, despite the imposed coincidence with ^{4}He, γ-rays from the Ex=6.878 MeV state in ^{28}Si* were observed overlapping the Doppler shifted γ-rays from the key state. On the other hand, the selection on recoil nuclei would have demanded to disentangle ^{23}Mg recoils from ^{24}Mg beam, both slowed down by the relative thick target. Passing through the gold target would have increased the beam charge states, making the detection of the recoil nuclei with a spectrometer more complex than the detection of the ejectiles.

Moreover, the beam presented an halo of particles which would have damaged the particle detector. Indeed, it was found impossible to put a collimator in front of the target for vacuum and mechanical reasons. For all the reasons presented before, the selection was done by measuring the ^{4}He ejectiles. As a beam collimator, a large plain gold foil was used and placed just after the target in order to stop the halo of particles and the beam. This beam and halo stopper will be referred now as the beam catcher. Its presence forced also to aim at the high velocities for ^{23}Mg at reaction in the required range Eq. (2.9). That was to reduce energy losses and straggling in target and in beam catcher for protons and ^{4}He. As an indication, ^{4}He straggling after 10 μm of gold provokes an angle dispersion around beam axis of $\pm$1.4 deg (SRIM calculations [76]). Comprehensive simulations of light particles passing through the gold {target + beam catcher } are presented in Chapter 4. The measurement of ^{4}He with kinetic energies $E_{^{4}He}$ $\sim$50 MeV should be done experimentally with an instrument having good (A, Z, E) resolutions to ensure unambiguous selections on directly populated states.

As a conclusion, in the present ^{3}He(^{24}Mg, ^{4}He)^{23}Mg* experiment, we decided to measure ^{4}He in coincidence with γ-rays and proton particles emitted from ^{23}Mg*, to improve the signal-to-noise ratio.

2.3.3 Choice of the detectors

The last century has seen different instruments and techniques to measure light particles and γ-rays. Many details about detectors for nuclear experiments can be found in the literature as [77]. The section here will focus on γ-ray spectroscopy and on proton and ^{4}He detections in the frame of the experimental goals $\delta\tau \sim$ 1fs, i.e. γ-ray energy and angle resolutions of ($\sim$ 3keV, $\sim$ 1deg), BR_p <<10% with E_p <10 MeV, and $E_{^{4}He}$ resolution of $\sim$50 MeV.

- γ-ray spectroscopy

Nuclear spectroscopic studies have been considerably helped in the past decades with the arrival of High Purity Germanium HPGe crystals and their excellent energy resolution of keV scale for the tens to thousands keV γ-rays. The never ending improvement of these γ-ray instruments has pushed furthermore the observable limits and so the discoveries of new nuclear structures and phenomena [78]. As a comparison, scintillator detectors, like NaI, have a resolution of 8% for γ-rays of 1.33 MeV. This is compensated nevertheless by an higher efficiency of 5% against 1% for coaxial HPGe [77]. Newcomers are $LaBr_3$ detectors with resolution around 2% for 1 MeV γ-rays and a slightly higher efficiency than NaI.

The quality of a HPGe array is determined by: the energy resolution, the efficiency ϵ, the peak to total ratio, the time resolution, the counting rate reachable, and the intrinsic solid angle of each detector which results in an intrinsic Doppler broadening. The quality is usually quantified by the two parameters: the sensitivity ($\frac{\text{total reaction cross section}}{\text{weakest channel reaction cross section}}$), the resolving power (peak to total ratio $\times$

$\frac{\text{mean distance between successive } \gamma\text{−ray lines}}{\text{energy resolution}}$). The signal to noise ratio is often approximated by this last parameter at the power of the amount of detectors observed in coincidence ([58]). Reducing the solid angle of each detector enables to decrease γ-ray pile-ups. The background has been drastically reduced with the use of surrounding Compton suppression shields acting as rejections when escaping photons are detected. Yet by adding these shields, it has limited the total efficiency, up to 50% for the "Ge ball" detectors (4π covering arrays). Some properties of several well-known γ spectrometers are summarized in Table 2.3.

An alternative has appeared in 1990s, 2000s with the electrical segmentation of the crystal. By dividing the external contact, like in AGATA or in GRETINA [79, 62], the path of the interacting photon inside the crystal can be observed. The developments of pulse shape analysis and Compton tracking algorithms allow us now to reconstruct the energy and the emission angle of the photon emitted in flight or at rest. The resulting resolutions ($\sim$ keV,$\sim$ deg) of AGATA likewise instrument, strongly improve the γ-ray spectroscopic sensitivity, and open new physics area in the radioactive ion beam facilities. Such Doppler highly resolved detector is suited to measure $\tau \sim$ fs on high lying excited states of radioactive elements. Coming decades will bring a new step with 4π coverage of highly efficient (AGATA, GRETA), looking at γ-ray cascades and rare nuclear state schemes.

For the goals of this experiment, the instruments AGATA and GRETINA were the only suited detectors among the γ-ray detectors shown in Fig. 2.8 and Table 2.3, i.e. the only detectors able to reach the resolution in energy and angle required for fs scale DSAM (Fig. 2.6).

We decided to perform this experiment with the AGATA detector.

Instrument	Geometry	Response function (E_γ=1.3 MeV) (resolution keV, ϵ %, P/T %)	With respect to (E_γ >6 MeV, $\tau \sim$ fs)
Coaxial HPGe crystal [77]	/	(1.9, 0.5)	Doppler broadening
GASP [80, 81]	40 crystals + Compton shields	$(2.3, 3, 60)_{\text{array}}$	out of use
EUROGAM [82]	4π + Compton shields	$(2.1, 8.5, 55)_{\text{array}}$	out of use
EUROBALL [83]	15 clusters of 7 crystals + Compton shields	$(2, 9.4, 50)_{\text{array}}$	out of use
GAMMASPHERE [84, 85]	4π, 100 crystals + Compton shields	$(2, 9, 60)_{\text{array}}$	Doppler broadening good ϵ
TIGRESS [86]	12 clovers of 4 crystals 8-fold segmented + Compton shields	(10, 0.8, 40)/clover	Doppler broadening
EXOGAM [87]	8 clovers of 4 crystals 4-fold segmented + Compton shields	(10, 0.7, 45)/clover	Doppler broadening
GRIFFIN [88]	16 clovers of 4 crystals + Compton shields	$(1.9, 19, 30)_{\text{array}}$	Doppler broadening good ϵ
AGATA [79] (2016)	32 crystals 6×6 segments + γ-ray tracking	(1.5 keV and 0.7 deg, $5.0)_{\text{array}}$	Doppler resolved
GRETINA [62] (2016)	> 28 crystals 6×6 segments + γ-ray tracking	$(1.5, 4.6)_{\text{array}}$	Doppler resolved

Table 2.3: Brief overview of γ-ray instruments based on HPGe crystals. Geometric features and referenced response function for γ-rays of 1.3 MeV are given for comparison. Last column highlights the instrumental abilities to measure or not lifetimes with fs scale from high lying states (E_γ >6 MeV).

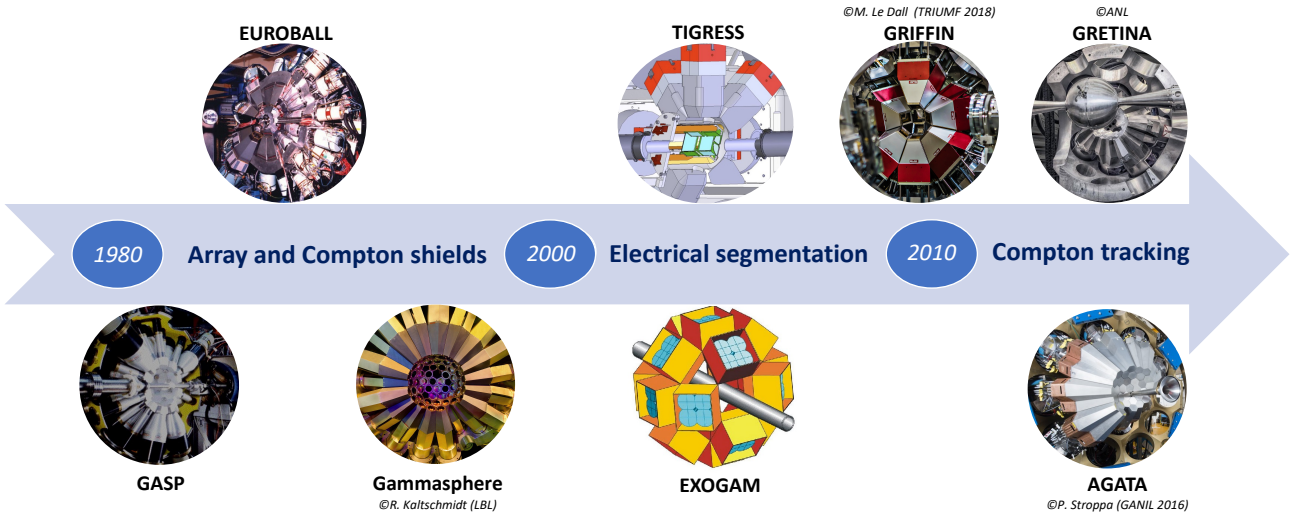

Figure 2.8: Timeline of γ-ray spectroscopic instrumentation with the three main revolutions in detection capacities.

- Charged particles detection

The detection of charged particles like protons is usually done by three categories of instrument: gaseous chambers, scintillation and semi-conductor detectors, details in [77]. The expected $BR_p \leq 3\%$ of the Ex=7.785 MeV state in $^{23}Mg^*$ called for an efficiency as high as possible. The presence of close states, less than 50 keV difference, also demanded an excellent resolution in energy and angle for the kinematics reconstruction. For these reasons, scintillation detectors were not chosen. Gaseous chambers have proven in the recent years abilities to identify and to reconstruct accurately the charge particle trajectory. The active target chambers, like the Gaseous Detector with Germanium Tagging GADGET (NSCL, [48]) or the ACtive TARget Time Projection Chambers ACTAR TPC (GANIL, [89]) are new interesting tools for measuring low energy and low statistics proton emissions. The problem is that these detectors are quite complex. Silicon based detectors were accessible and suited to be compact with the γ-ray array and for the ejectile detection. Silicon is widely used because of its operation at room temperature compared to Ge semi-conductors, and its easy access. Identification (A,Z) is obtained through ΔE-E plots with telescope detectors. The usual resolutions are of [40,50] keV and the geometric segmentation or stripping of the detection area enables the reconstruction of the emission angle with a resolution of $\sim$ deg. Silicon detectors have an efficiency of $\sim$100%.

In conclusion, we decided to use a telescope of silicon detectors to measure the protons emitted by $^{23}Mg^*$. The reaction ejectiles ^{4}He could be measured, as requested, by a large acceptance spectrometer.

2.4 Conclusion

A study of methods and experimental conditions had been done in order to measure the widths and the spin of the Ex=7.785 MeV state in $^{23}Mg^*$ The chosen experiment was performed at the heavy ion acceleration facility in Caen (GANIL). This experiment will be presented in next Chapter 3.

CHAPTER 3

Experimental set-up at GANIL

3.1 Introduction

The experiment, performed at GANIL, was based on the set-up outlined in Fig. 3.1.

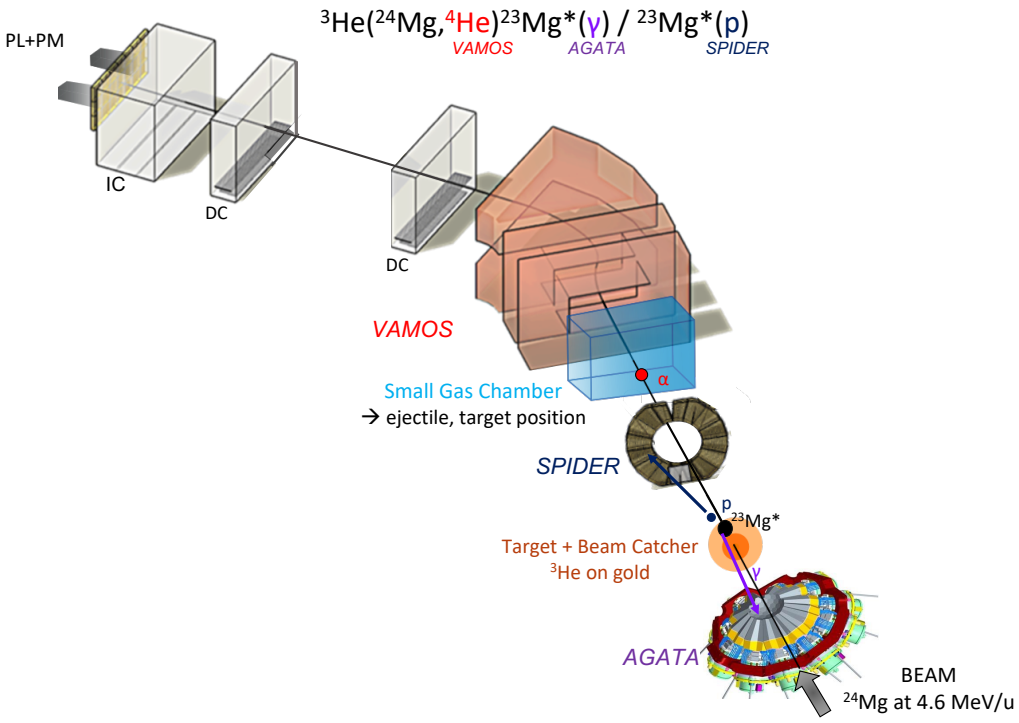

Figure 3.1: Layout of the experiment to produce and to study the Ex=7.785 MeV state in ^{23}Mg* at GANIL. The ^{3}He(^{24}Mg, ^{4}He)^{23}Mg* reactions were achieved by a 4.6 MeV/u beam onto a ^{3}He-gold target, followed by a thick gold foil to stop the beam. The reactions were selected with the ^{4}He ejectiles measured in a small gas chamber and the VAMOS spectrometer, both located downstream of target. VAMOS detectors (drift chambers DC, plastic scintillator and photomultipliers PL+PM) allowed us to reconstruct the ejectile magnetic rigidity, the charge Z and the time-of-flight. The excited state in ^{23}Mg* can decay by γ-rays, observed with AGATA located upstream of the target, or by protons measured with the silicon stripped telescope SPIDER located downstream of the target.

The state of interest was populated with a ^{24}Mg beam onto a ^{3}He-gold target. The detection system was composed of three main detectors: the VAriable MOde Spectrometer (VAMOS) for reaction channel selection, the AGATA detector for τ measurement, and the Silicon Particle Identification DEtector Ring (SPIDER) for BR_p measurement. A small gas chamber was used downstream of the target in order to have an additional ejectile path reconstruction with respect to VAMOS Drift Chambers. Indeed the Doppler resolution is improved by considering the emitter angle. The experiment took place before my Ph.D.

The experimental aspects relative to the population of the key state are presented along Sec.3.2, that is to say the beam features (Sec.3.2.1), the target composition (Sec.3.2.2) and the reaction kinematics (Sec.3.2.3). Then, Sec.3.3 focuses on the different instruments measuring charged particles in Sec.3.3.1, 3.3.3 and 3.3.4, and γ-rays in Sec.3.3.2. Each detector will be presented with its main features and the measured parameters before the data analysis.

3.2 Population of the Ex=7.785 MeV state in ^{23}Mg*

3.2.1 Beam features

The reaction ^{3}He(^{24}Mg, ^{4}He)^{23}Mg* is endothermic (Q<Ex), the chosen ^{24}Mg beam energy >>Q ensured the process to happen. The ^{24}Mg beam was accelerated by the GANIL cyclotron CSS1 after the source C02. The main ion charge state was 5^+, the beam was characterized by profilers at the entrance of the experimental room and by VAMOS. The measured properties are summarized in Table 3.1. The kinetic energy was derived from the magnetic rigidity Bρ which was reconstructed by VAMOS with a resolution of $\frac{\delta p}{p} \simeq 2.10^{-3}$ ($\frac{\delta E}{E} = 4.10^{-3}$). The exposed targets presented a burn mark in the center linked to the beam spot, shown in Fig. 3.2. This corresponded to a carbon deposit, as seen in another experiment with measured densities between 4 and 15 μg.cm^{-2}[90]. From LISE++, the energy losses of the beam, after a ^{12}C deposit of 10 μg.cm^{-2}, were estimated of 0.09 MeV. Hence, they were negligible compared to the beam energy of 110.83±0.443 MeV.

The beam spot radius was measured, it is R_{beam}=1.6(2)mm. Downstream of target, the beam catcher to protect SPIDER was located at Z=+19±1 mm. It was made of a thick gold foil of 20±0.5 μm, shown in the right side of Fig. 3.2. Such thickness was enough to stop the ^{24}Mg ions. The beam was found with a 100% purity and with the intensity varying in the tens of enA along the runs. Simulations presented in Chapter 4 are based on the measured beam features, considering Gaussian shapes with the following parameters

- energy spread 110.83±0.443 MeV
- transverse XY dispersion ($0\pm\frac{1.6}{4}$, $0\pm\frac{1.6}{4}$) mm.

Nucleus	stable ^{24}Mg
Charge	5^+
Kinetic energy $E_{beam} \pm \sigma_{E_{beam}}$	110.83±0.443 MeV
$\beta_{^{24}Mg}$	9.92 ± 0.02 %
Transverse size ($\sigma_{X_{beam}}$, $\sigma_{Y_{beam}}$)	$\pm$ ($\frac{1.6}{4}$, $\frac{1.6}{4}$) mm
Observed average intensity	$[10, 30]$ enA
	$\Leftrightarrow [1.2, 3.7]10^{10}$ pps
Purity	100 %

Table 3.1: Measured properties of the beam.

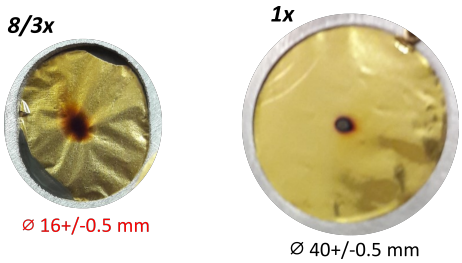

Figure 3.2: Right, picture of an used ^{3}He+gold target and left, of the gold foil. Both present a carbon deposit (burn marks). Diameters are indicated.

3.2.2 Target composition

The experimental targets, ^{3}He implanted in gold, presented two possible thicknesses: (1, 5) μm, thin ones being produced for proton measurements. This part describes how ^{3}He ions were implanted and their stability with respect to evaporation and beam exposure.

The targets were made by Helmholtz-Zentrum Dresden-Rossendorf laboratory (Dresde, Germany). Gold foils were irradiated with ^{3}He beams of two energies (5, 20) keV for one to two days. Table 3.2 summarizes the implantation as given by the producer. By changing the beam energy and the irradiation time, three different kinds of ^{3}He implantation were done. Thin targets received the same implantation of ^{3}He as thick targets (1, 2). Targets (3, 4, 5) are all 5 μm thick targets and received the same implantation. Finally, only the beam of 20 kev was used to produce the thin target 7. During the experiment, targets (3, 4, 5) were exposed 39.5 % of the beam time. Targets (1, 2) received 27 % of the beam time and targets (8, 10) 29 % of the beam time. Target 7 was not used during the experiment.

Target n^o	Au foil thickness (μm)	^{3}He density (10^{17} at.cm^{-2}) for beam at (20, 5) keV	$\frac{^3\text{He}^{5\text{keV}}}{^3\text{He}^{20\text{keV}}}$
1	5.0	(5.00, 0.55)	0.11
2	5.0	(5.00, 0.55)	0.11
3	5.0	(5.00, 3.00)	0.60
4	5.0	(5.00, 3.00)	0.60
5	5.0	(5.00, 3.00)	0.60
8	1.18	(5.00, 0.55)	0.11
10	0.9	(5.00, 0.55)	0.11
7	1.18	(0.76, 0)	0

Table 3.2: Irradiation of targets as given by the producer. Two ^{3}He beam energies were used (20, 5) keV. This resulted in three implantation profiles, shown in the last column with the predicted densities and associated ratios.

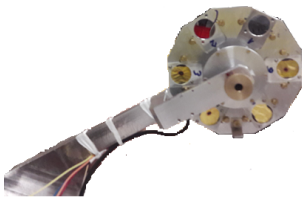

Figure 3.3: Picture of the experimental target holder.

Two analysis of the ^{3}He targets were done at Demokritos laboratory (Athens, Greece), just after the experiment in 2016, and one year after. They were achieved using the ^{3}He(d,p)^{4}He reaction with a beam of deuterium for the energy of 1.35 MeV. The α counting detector was placed at 170 deg. The cross sections from [91, 92] were used, conducting to 10 % differences. Hence, there are 10 % systematic errors in the density measurements. The ratio of the measured ^{3}He density (after the experiment) and the producer implantation ^{3}He density (Table 3.2), referred as $\frac{\text{measured}}{\text{implanted}}$, was derived and is presented in Table 3.3. The average of $29^{+8.8}_{-11}$ % (22$\pm$2.5 %) remaining ^{3}He ions after the experiment for thick (thin) targets, was found. The density ratio ($\frac{\text{measured}}{\text{implanted}}$) is presented as a function of the beam time on target (t_{beam}), in the left side of Fig. 3.4. No dependency was apparent between these two parameters. Thus, the ion evaporation during the experiment is not observed. An overall ion implantation efficiency of 25% (black line) is not surprising. Thin targets were however found less implanted and more vulnerable over beam exposure, target 10 indeed exploded online. The depth profile of implanted ^{3}He could not be measured, its effect on lifetime measurement was so tested (Chapter 4).

Target n°	measured ^{3}He density (10^{17} at.cm^{-2})	$\frac{\text{measured}}{\text{implanted}}$ (%)
1	2.1±0.21	37±4
2	1.9±0.19	34±3
3	1.5±0.15	19±2
4	2.5±0.25	31±3
5	2.2±0.22	27±3
8	1.0±0.10	18±2
10	/	/
7	0.2±0.02	26±3

Table 3.3: Analysis of the ^{3}He implanted targets by the Demokritos laboratory. The densities were measured by the ^{3}He(d,p)^{4}He reaction at 1.35 MeV. The derived ratio $\frac{\text{measured}}{\text{implanted}}$ is the measured density over the expected implanted one (Table 3.2). Target 10 was not analysed since it exploded online.

The γ-ray statistics of the Ex=4.356 MeV state in ^{23}Mg*, referred as $C_{\gamma=4.356\text{MeV}}$, was estimated from the different used targets. The counts, after background subtraction, were normalized by t_{beam}. They are presented as a function of the measured ^{3}He density, in the right side of Fig. 3.4. A linear trend is apparent between the estimated γ-ray statistics and the measured ^{3}He density, as shown by the linear fit with the red curve. The beam intensity, not properly monitored, varied of ±10 enA and the background was more important for the low ^{3}He density targets. These two points explain: *(i)* the observed scattering, *(ii)* the ordinate at origin estimated different from zero.

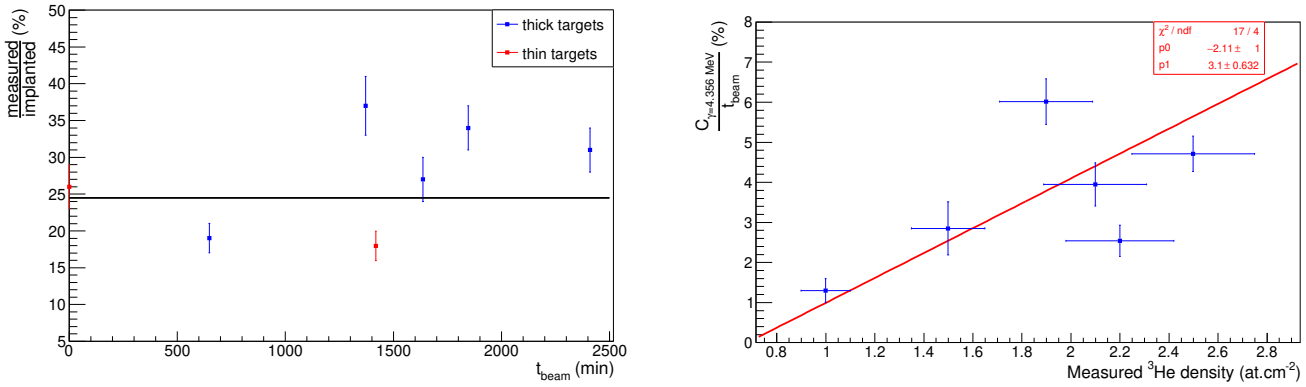

Figure 3.4: Left panel: evolution of $\frac{\text{measured}}{\text{implanted}}$ in ^{3}He density over the beam exposure time on target (t_{beam}), in case of the thick (thin) targets for the blue (red) points. Black line marks the weighted average. Right panel: the measured γ counts $C_{\gamma=4.356\text{MeV}}$, selected on the Ex=4.356 MeV state and normalized by t_{beam}, are shown over the measured ^{3}He density (Table 3.3). The linear fit is shown with the red curve.

In conclusion, two target thicknesses were used during the experiment. The target ^{3}He densities were measured after, pointing out that thin targets presented less ions than thick targets. As regard as the astrophysical Ex=7.785 MeV state in ^{23}Mg*, these thin targets could not be of use since no significant amount of γ-rays was measured above the background.

3.2.3 Reaction kinematics

For the experimental beam energy of 110.8 MeV, the reaction ^{3}He(^{24}Mg, ^{4}He)^{23}Mg* populating the Ex=7.785 MeV state was simulated with a simple Monte Carlo code, under CERN Root [93]: the crossing through the target was not included, proton decays resulted from a short-lived state (1 fs). In the laboratory frame, the kinematics of the recoil nucleus and the ejectile are respectively given in Fig. 3.5(a) and

3.5(b), the proton decay from ^{23}Mg* in Fig. 3.5(c). As a comparison, LISE++ results, shown with the black thin curves, are perfectly matching the reaction kinematics in Fig. 3.5(a) and (b).

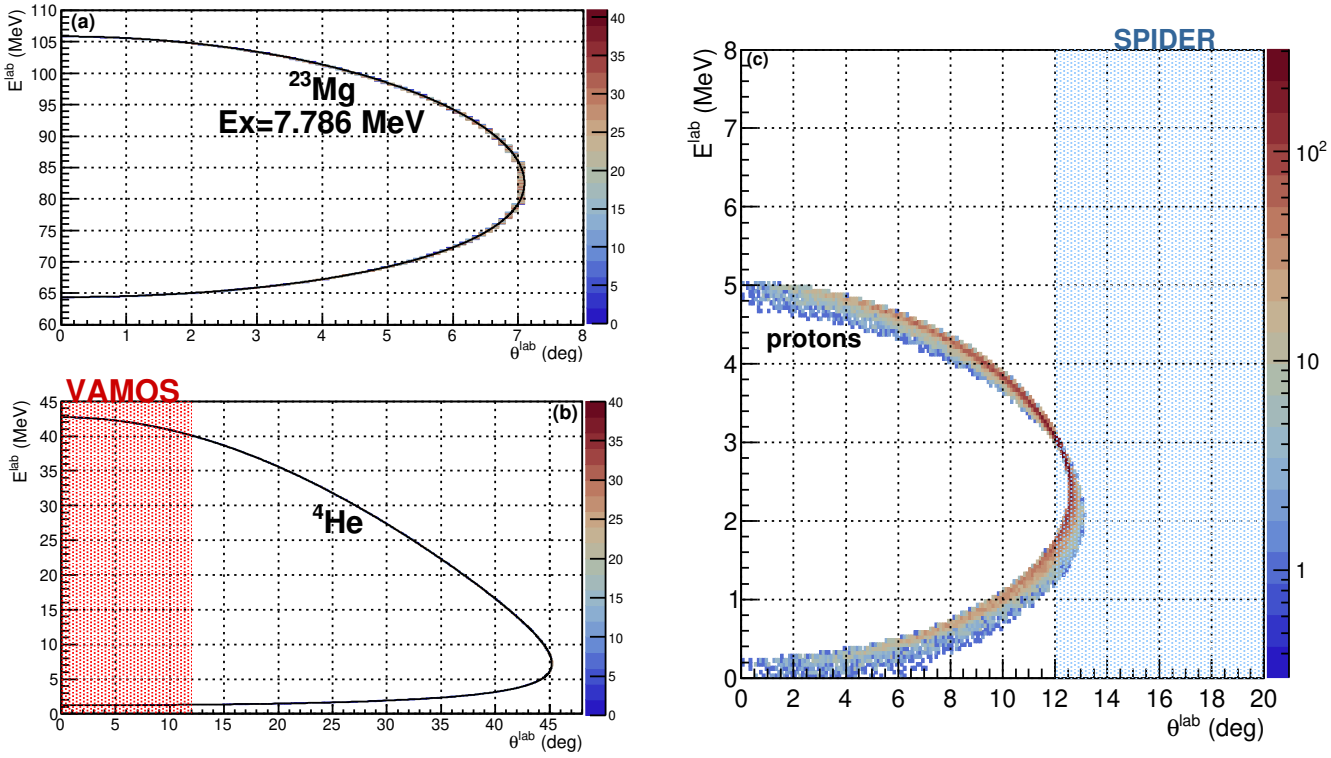

Figure 3.5: Kinematic curves of the ^{3}He(^{24}Mg, ^{4}He)^{23}Mg* reaction at Ex=7.785 MeV and a beam energy of 110.8 MeV, for the recoil nucleus in panel (a) and for the ejectile in panel (b). Black thin curves, hardly visible, come from LISE++ calculations, agreeing excellently with the present Monte Carlo code. The associated proton decay is plotted in panel (c), with an input lifetime of 10 fs. Colored regions show the acceptance of VAMOS in red and SPIDER in blue.

In conclusion, the ^{4}He ejectiles of the ^{3}He(^{24}Mg, ^{4}He)^{23}Mg* reaction at Ex=7.785 MeV, were expected with energies of [37, 40] MeV after considering energy losses due to the beam catcher. They were measured in the spectrometer VAMOS and the small gas chamber. They had $\theta^{lab} \leq 12$. This came from the mask due to the rings of SPIDER. More than 90% of emitted protons were expected in the energy range of [1, 4.5] MeV and in the angular range of [8, 13] deg. They were measured in SPIDER.

3.3 The detection systems

The study of the states in ^{23}Mg* relied on the experimental set-up, shown in Fig. 3.1, with the instruments presented now.

3.3.1 VAMOS

The detectors composing the large acceptance spectrometer VAMOS are shown in Fig. 3.6. The useful signals from these detectors are described in the following lines.

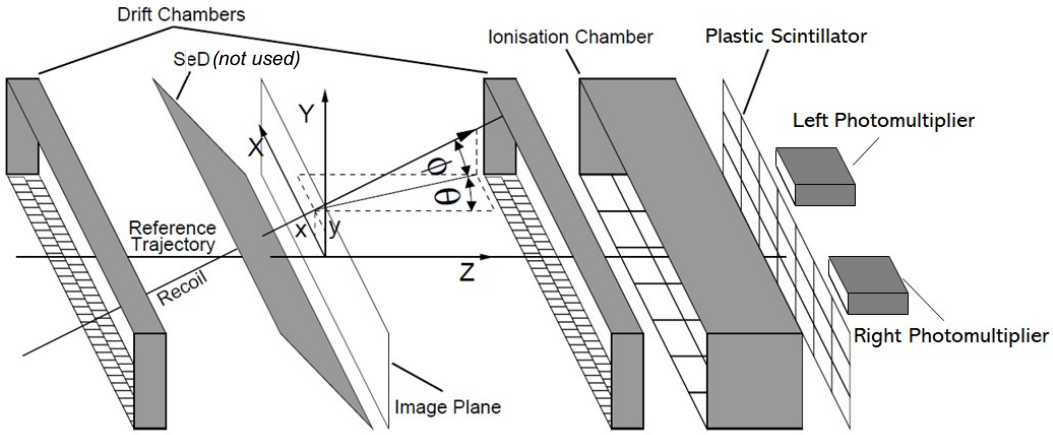

Figure 3.6: VAMOS main detectors along the schematic focal plane, adapted from Ref. [94].

As a spectrometer, VAMOS is used in general to reconstruct kinetic energy, mass, charge and angles of the nuclei passing through. Their properties are computed from the measured signals. Details on the VAMOS reconstruction algorithm in the general case can be found in Ref. [94]. The analysis specifically done for this experiment is shown with the algorithm on Fig. 3.7. During the experiment, light nuclei (Z=1, Z=2) with energies above 25 MeV were observed in VAMOS . The ionisation chambers were not used since the energy losses generated electric signals below the threshold.

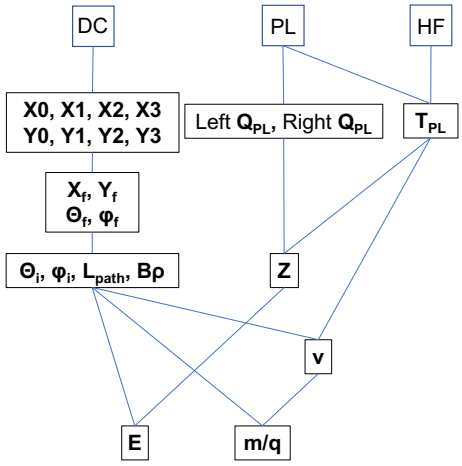

Figure 3.7: The experimental VAMOS algorithm of particles identification and characterisation. The Drift Chambers (DC) measured positions (X and Y 0 to 3) used to derive the focal plane positions (X_f, Y_f) and angles (θ_f, ϕ_f). Trajectory was computed in the target image plane characterized by (θ_i, ϕ_i), path length (L_{path}) and magnetic rigidity ($B\rho$). The plastic scintillator (PL), with the associated left and right photomultipliers, measured the collected charges Q_{PL} left and right. The cyclotron radio frequency HF was the reference time which was combined with PL to build the plastic time T_{PL}, then the Z of nuclei, the kinetic energy E, the velocity v, and the charge over mass $\frac{m}{q}$.

- Plastic charges

At the end of VAMOS, a plastic scintillator was placed with two photomultipliers, on the left and right sides of the detector. The light emission by the scintillator was electrically converted by the coupled

photomultipliers, which also ensured the signal amplification. A large variety of scintillation material exists: from organic to inorganic and from liquid to solid state, as presented in Ref. [77]. The VAMOS plastic detector was made of an organic solid. The collected charge is a function of the atomic number Z and the kinetic energy of the detected nucleus in the scintillator material. According to Ref. [95], lighter Z nuclei induce higher charge Q in the photomultipliers compared to heavier Z nuclei at the same kinetic energy. During the experiment, it was possible to separate nuclei according to Z and to kinetic energy by looking at the collected charges.

The responses of the two photomultipliers PM were checked with a ^{3}He implanted gold target and with a pure gold target, see Fig. 3.8. The majority of detected particles came from reactions with gold nuclei (^{24}Mg Coulomb and nuclear dissociation on gold) and with contaminants (^{24}Mg fusion-evaporation with ^{16}O, ^{12}C). This was demonstrated by no noticeable difference between the targets. Two separated regions were apparent, shown on the left side by the black outlines associated with left Q_{PL} <12000 and left Q_{PL} >12000. They corresponded to two different Z values as shown in the next part. Moreover, the collected charge was higher with the left PM than the right one. It is most likely due to a mismatch between the gains of the two PM, and not to the action of the magnetic field at the entrance of VAMOS. Indeed, the relative difference between the left collected charges and the right ones has not been observed correlated to the associated Bρ of the particule. Charge signal had not been calibrated since such calibration is not straightforward and not required for the analysis. The kinetic energy of nuclei was measured more accurately with the drift chambers.

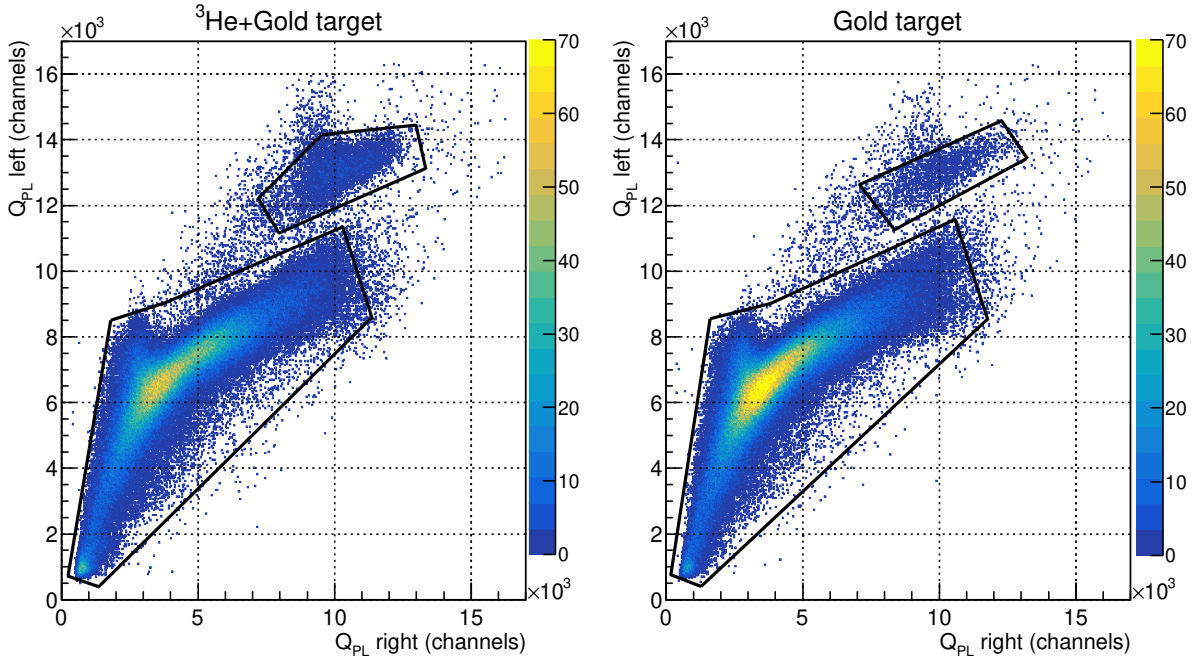

Figure 3.8: The collected charges Q_{PL} of left photomultiplier versus the right one in the VAMOS plastic scintillator. The left image was obtained with ^{3}He implanted gold target and the right image with pure gold. Quasi no difference was noticed between the two images, implying that most ejectiles came from dissociation and fusion-evaporation reactions with gold and contaminants in the target. The black surrounded regions corresponded to two different Z values expected for the ejectiles.

- Plastic time-of-flight

During the experiment, a time signal was built with the plastic detector and the cyclotron high frequency, noted HF (GANIL CSS1). Two TAC (Time to Amplitude Converter) modules were used with a START (PL) and a STOP (HF). There were one TAC with the left PM and one with the right PM. The TAC ranges were chosen larger than the HF period. With a beam frequency of 7.8456 MHz, that period was 127.46 ns. Then, a "HF propre" was defined, such as a constant delay time window, called Delay, was fixed after validated by a PM signal. It was done in order to select the closest HF to PM signal. This measured time signal $T_{PL\text{-}HFp}$ was for each PM

$$\begin{aligned} T_{PL-HFp} &= STOP_{HF} - START_{PL} \\ STOP_{HF} &= Delay + k \times T_{HF}, \quad k \in \mathbb{N} \\ START_{PL} &= T_{CSS1 \to Target} + t^* \end{aligned} \tag{3.1}$$

with the time-of-flight from target to PL detector t^*, the constant time from cyclotron to target $T_{CSS1 \to Target}$. It follows that

$$- T_{PL\text{-}HFp} + k \times T_{HF} + (Delay - T_{CSS1 \to Target}) = t^* \tag{3.2}$$

The measured T_{PL-HFp} had to be corrected by a constant $(Delay - T_{CSS1 \to Target})$ and $k \times T_{HF}$ to get the real time-of-flight. Using LISE++, the nuclei time-of-flight from target to PL was estimated less than $2 \times T_{HF}$, assuming a path of $\sim$8.5 m and light nuclei Z$\leq$2 with E$>$ 20 MeV. The measured T_{PL-HFp} is shown as a function of right Q_{PL} in Fig. 3.9(a). The events in zones (2, 2') had travelled for $\geq T_{HF}$, they were "continuous" to the zones (1, 1') but with lower Q_{PL} indicating lower kinetic energy, i.e. greater time-of-flight. The corrected time noted T_{PL}, as function of right Q_{PL} in Fig. 3.9(b), will henceforth be referred to as the plastic time

$$\begin{aligned} T_{PL} &= T_{PL-HFp} \quad \text{if} \quad T_{PL-HFp} < 1175 \text{ ns} \\ T_{PL} &= T_{PL-HFp} - T_{HF} \quad \text{if} \quad T_{PL-HFp} \geq 1175 \text{ ns} \end{aligned} \tag{3.3}$$

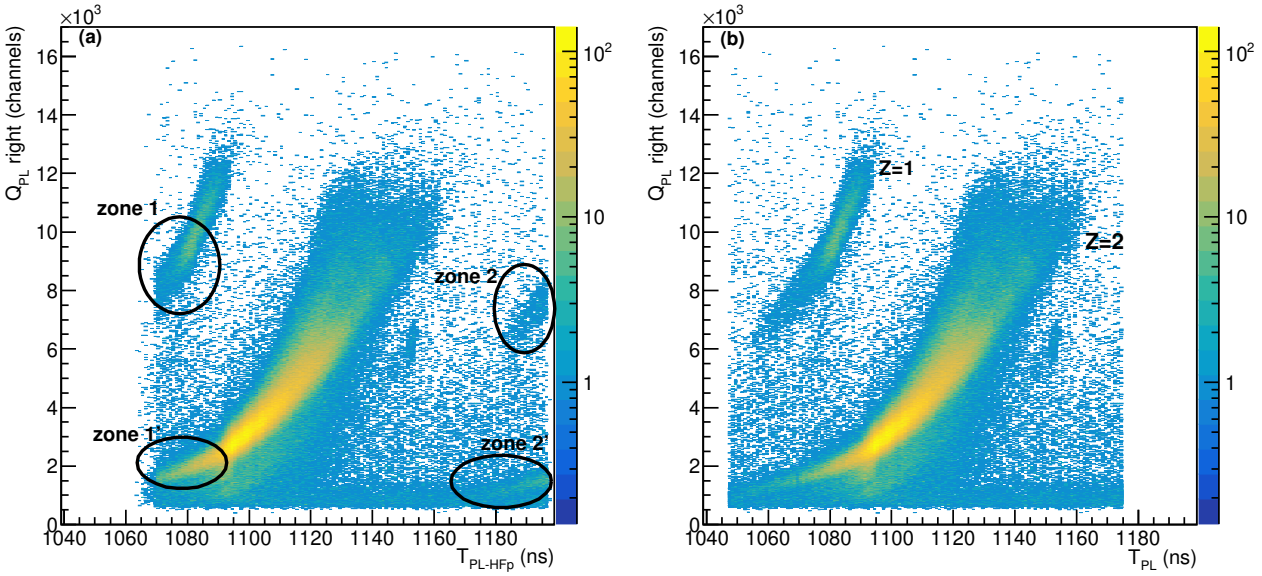

Figure 3.9: The collected right plastic charge Q_{PL} versus the time from plastic to HF. Panel (a): marked zones discussed in text. Panel (b): T_{PL-HFp} was corrected for events with time-of-flight $\geq T_{HF}$ as explained in Eq. (3.3). The two apparent curves corresponded to Z=1 and Z=2.

Hydrogen and helium ejectiles were expected to be the most abundant particles in plastic. In Fig. 3.9(b), two regions are clearly apparent. As previously said, nuclei with Z=1 generated more Q_{PL} than Z=2 nuclei for kinetic energies in [10, 60] MeV. The hydrogen Z=1 nuclei correspond so to the top region and the other region to the helium Z=2 nuclei.

The reconstruction of the real time-of-flight t* from target to PL+PM is developed in Sec.5.2.1.

- Angles and kinetic energy

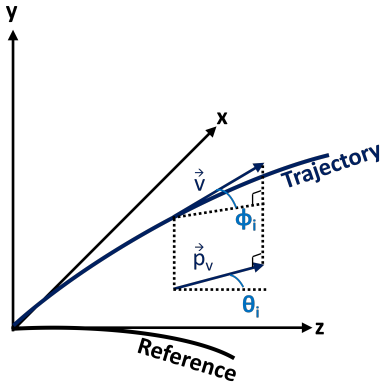

Figure 3.10: VAMOS reference frame with coordinates at the target origin. $\overrightarrow{p_v}$ is the projected particle velocity $\overrightarrow{v}$ on the horizontal plane (x,z), θ_i the angle between $\overrightarrow{p_v}$ and $\overrightarrow{z}$, ϕ_i the angle between $\overrightarrow{v}$ and $\overrightarrow{p_v}$.

The reconstruction of the particle energy and angles followed the algorithm given in Fig. 3.7. The magnetic spectrometer had four drift chambers (DC) which allowed the measurement of the position (X, Y, Z) of the ejectile. The drift chambers had 160 wires in (X, Z) plane. The position Y was derived by using the measured drift time of generated electrons in butane gas. For the chosen voltage and pressure, the drift chambers had an electron drift velocity of 5.387 cm.μs^{-1}. The position X was obtained by measuring the signals on the horizontal wires. The position Z was measured by the surveyors (Table 3.4). Then the angles (θ_f, ϕ_f) in focal plane, shown in Fig. 3.6, were reconstructed by combining two DC positions. Calling (dX, dY, dZ) the position variation either DC0-DC2 or DC1-DC3 or DC0-DC3 or DC1-DC2, angles were obtained with:

$$\begin{aligned} \tan(\theta_f) &= \frac{dX}{dZ} \\ \sin(\phi_f) &= \frac{dY}{\sqrt{dX^2 + dY^2 + dZ^2}} \end{aligned} \tag{3.4}$$

The magnetic rigidity Bρ and the path length L were calculated, knowing the imposed magnetic field of VAMOS, the target position and the reference beam trajectory. First, the measured parameters in the focal plane were transformed into the image plane which is illustrated in Fig. 3.10. This transformation depends on the target position and on the chosen VAMOS optical mode (the parameters of the optical matrix). The matrix was obtained thanks to simulations with the code Zgoubi Ref. [96]. Simulations were done on all possible trajectories for given (Bρ, L, θ_i). Then, the computed (X_f, θ_f) were compared with the measured ones to find the trajectory (Bρ, L, θ_i) best fitting. The azimuthal angle ϕ_i was differently derived due to algorithm complexity. A polynomial relation links this angle with the measured coordinates in focal plane (more details in Ref. [94]). The final step was to project in the laboratory frame the angle (θ_i, ϕ_i).

$$\begin{aligned} \theta_{lab} &= \mathrm{acos}(\cos(\theta_i) \times \cos(\phi_i)) \\ \phi_{lab} &= \mathrm{atan}\left(\frac{\sin(\phi_i)}{\cos(\phi_i) \times \sin(\theta_i)}\right) \end{aligned} \tag{3.5}$$

As explained in the VAMOS algorithm shown in Fig. 3.7, the particle velocity was derived from L and t*. Combined with $B\rho = \frac{p}{q}$, the m/q identification was obtained.

From $B\rho$, the kinetic energy of a nucleus with known mass and charge was derived. In the experiment, ^{4}He were tagged with their kinetic energy derived from $B\rho$:

$$E^{VAMOS}_{^4He} = m_{^4He}c^2\left(\frac{1}{\sqrt{1-(\frac{B\rho \times q_{^4He}}{c \times m_{^4He}})^2}} - 1\right) \quad (3.6)$$

With $m_{^4He}c^2 = 3728$ MeV, $q_{^4He} = 2 \times 1.6 \times 10^{-19}$ C, $m_{^4He} = 4 \times 1.673 \times 10^{-27}$ kg, $B\rho$ in T.m, c = 2.99×10^8 m.s^{-1}. Fig. 3.11 shows θ_f as a function of the relative rigidity $\Delta B\rho = \frac{B\rho - B\rho_{nom}}{B\rho_{nom}}$, with the nominal value $B\rho_{nom}$=0.95 T.m, in the case of a thick target (^{3}He+gold). The reconstructed $B\rho$ had a resolution of $\frac{\delta p}{p} \simeq 2.10^{-3}$ and the energy resolution was $\frac{\delta E}{E} \simeq 2 \times p \times \frac{\delta p}{p^2} = 4.10^{-3}$. For the expected ^{4}He kinetic energy within [35, 55] MeV corresponding to Ex∈[0., 9.] MeV in ^{23}Mg*, the kinetic energy resolution was 100 - 200 keV. This is shown with Gaussian fits of the first excited state, see the red curve on the bottom Fig. 3.11).

Drift Chamber	(X, Y, Z) position (mm)
DC0	(-463, -115.56, 7689.5)
DC1	(-463, -117.75, 7729.5)
DC2	(-463.3, -115.64, 8089.1)
DC3	(-463.4, -119.9, 8129.1)

Table 3.4: Geometrical configurations of the drift chambers (positions from the target origin).

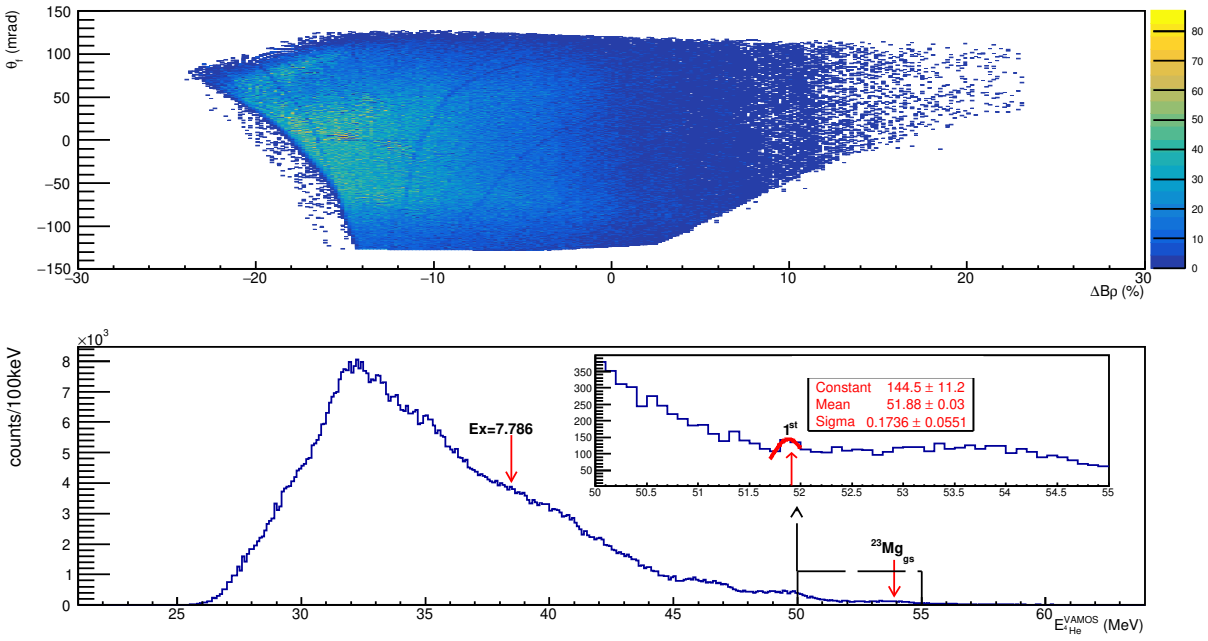

Figure 3.11: Top panel: the measured θ_f as a function of the relative rigidity $\Delta B\rho$. Bottom: the corresponding ^{4}He kinetic energy spectrum with a zoom on [50, 55] MeV. Red arrows mark the expected position of states in ^{23}Mg*: the ground, the first Ex=0.451 MeV and the astrophysical Ex=7.785 MeV state. Gaussian fits of the first excited state resulted in σ=0.17(5) MeV.

In top Fig. 3.11, some ^{4}He kinematic lines are apparent on the right side. Excitation peaks from the populated ground state and first excited state in ^{23}Mg* were also noticed in the bottom spectrum (red

arrows).

As a conclusion, using VAMOS to measure the ^{4}He ejectiles was an improvement compared to the study of [52] where they used silicon detectors. The energy resolution was so better here than in [52].

3.3.2 AGATA

The European instrument AGATA [79] is under building to a 4π array of 36-fold segmented HPGe crystals. It operates in position-sensitive mode thanks to the Pulse Shape Analysis PSA and tracking techniques. The tracking is here based on the Compton interaction of γ-rays in Ge as well as the photoelectric and pair creation interactions. The AGATA configuration and response function during the experiment will be explained in the following.

Energy losses of γ-rays in Ge medium are due to three interactions: photoelectric effect (E_γ <0.1 MeV), Compton scattering ($E_\gamma \in [0.1, 10]$ MeV), and pair e^+-e^- creation ($E_\gamma \geq 1.2$ MeV), see on the left side of Fig. 3.12. Hence, γ-ray emissions from nuclear states mainly interact through Compton scattering, that is to say an elastic collision between the γ-ray and an electron of Ge medium governed by:

$$E_{\gamma,\text{scattered}} = \frac{E_{\gamma,\text{initial}}}{1 + \frac{E_{\gamma,\text{initial}}}{m_e c^2}(1 - \cos(\theta_{\text{scattered}}))} \tag{3.7}$$

where $E_{\gamma,\text{initial}}$, $E_{\gamma,\text{scattered}}$ are energies of γ-ray respectively before and after the interaction, $\theta_{\text{scattered}}$ the scattering angle. The distance between consecutive interactions in Ge medium are at macroscopic scale, since the free mean path is $\lambda = 2.26 \pm 0.01$ cm for $E_\gamma = 1$ MeV. The right side of Fig. 3.12 shows the photon linear attenuation in Ge. With such large distances, a single γ-ray usually generates one to four interaction points per crystal. The tracking principle is to reconstruct the initial energy and angle from the deposited energy and position of all interactions measured by the detector. In principle, the source position must be known, the initial energy is the sum of the deposited energies. The tracking consists then on evaluating Eq. (3.7) for each permutation of the measured interaction energies to extract the scattered angles. These angles are also computed from the measured interaction positions. A χ^2 function of the differences between these two derivations of the scattered angles is built. The proper chronology of the γ-ray path during the event is associated with the minimum χ^2. The principle of γ-ray tracking is illustrated in Fig. 2.12 of Ref. [58]. The minimisation is not enough in practice, an empirical limit is used to discard events with incomplete deposited energies, corresponding to a soft Compton suppression of γ-ray escapes, crystal trapping-defaults,.... Due to computer time complexity and γ-ray multiplicity often greater than 1, all permutations are not considered: the practical algorithm starts with clusterisation which consists on the identification of small interaction sets associated with a single γ-ray, detailed in Sec.11.2[79]). The clusters are built according to the relative angular separation of the points, the short mean free path of γ-rays in Ge (Fig. 3.12) governs the acceptable cluster size. The AGATA tracking relies on the two codes: Mars Gamma-Ray Tracking MGT [97] and the Orsay Forward Tracking OFT [98]. Deeper explanations are found in [79, 58].

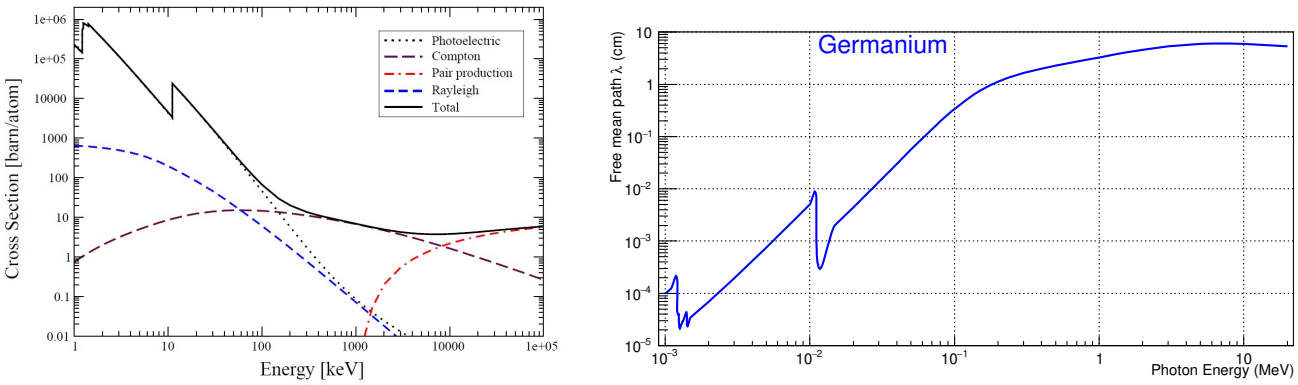

Figure 3.12: Left side: the cross-section in Ge is drawn as a function of the energy of the photon interacting by photoelectric (dashed black curve), by Compton scattering (dashed purple curve), by pair creation (dashed red curve), and by Rayleigh scattering (dashed blue curve). The total cross section, summed up on all interactions, is the solid black line. Taken from [58]. Right side: the mean free path of photon in Ge, plotted along the energy, was derived from the referenced mass attenuation coefficients [99] by using the Ge density of 5.35 g.cm^{-3}.

The layout of AGATA tracking operation is given in Fig. 3.13. Each γ-ray interaction in the crystal segments generates a current signal, digitized treatment: the so-called "traces". They are compared to a reference database in order to reconstruct the interaction point in energy and position - the PSA which is developed in the "Detector operation" point. Finally, the tracking algorithm is used to build back the initial energy and angle of the γ-ray emission. After tracking, excellent resolutions are obtained: σ_{E_γ} ~2.3 keV for 1.3 MeV γ-rays and σ_{θ_γ} ~0.7 deg. These resolutions are dominated by the intrinsic energy resolution of γ-rays in Ge and by the PSA resolution. The final energy and angular resolutions, after tracking, will be detailed in next part.

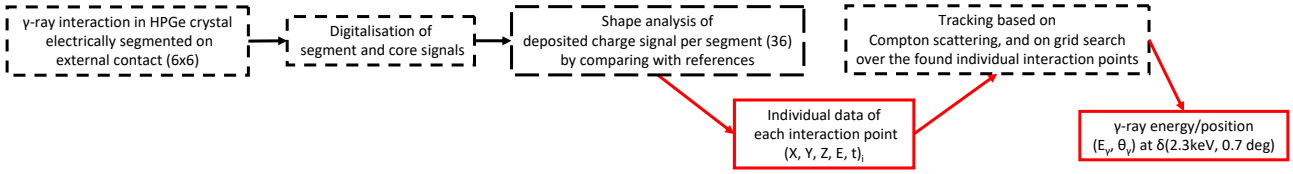

Figure 3.13: Scheme of γ-ray tracking, operated with AGATA HPGe crystals, steps detailed in text.

- Geometry

The AGATA array was located upstream of the target: for backward angles, the observed Doppler effect was redshifted. Along the beam axis, AGATA was located at -252 ± 1 mm from the target holder. The experimental components around the target, given in Fig. 3.14, were inside the chamber Charade under vacuum. Downstream of the target, SPIDER with its two Si rings and the small gas chamber were centered with respect to the beam axis, likewise the target and the beam catcher located 2 cm after. The chamber was made special for alignment between VAMOS and AGATA, thanks to a rotational sphere at the entrance where the target holder was inserted. The AGATA array consisted on 31 crystals with 36 fold-segments, each crystal with 9 cm depth and 4 cm radius at the frontside with respect to the target. The AGATA HPGe crystals are laid out in Annexe B.1. The segmentation was chosen so that the electric field balanced the effective size of segment [58]. It existed three slightly different shapes for the HPGe detectors, which were gathered in triple cluster ATC [100] sharing same cryostat. It is reminded that the energy resolution of Ge crystal at room temperatures is destroyed because of the noise from thermal

generated charge carriers, Ge having a low band gap. Hence the need of cryostat with liquid nitrogen LN_2 of 77° K to cool down the HPGe detector.

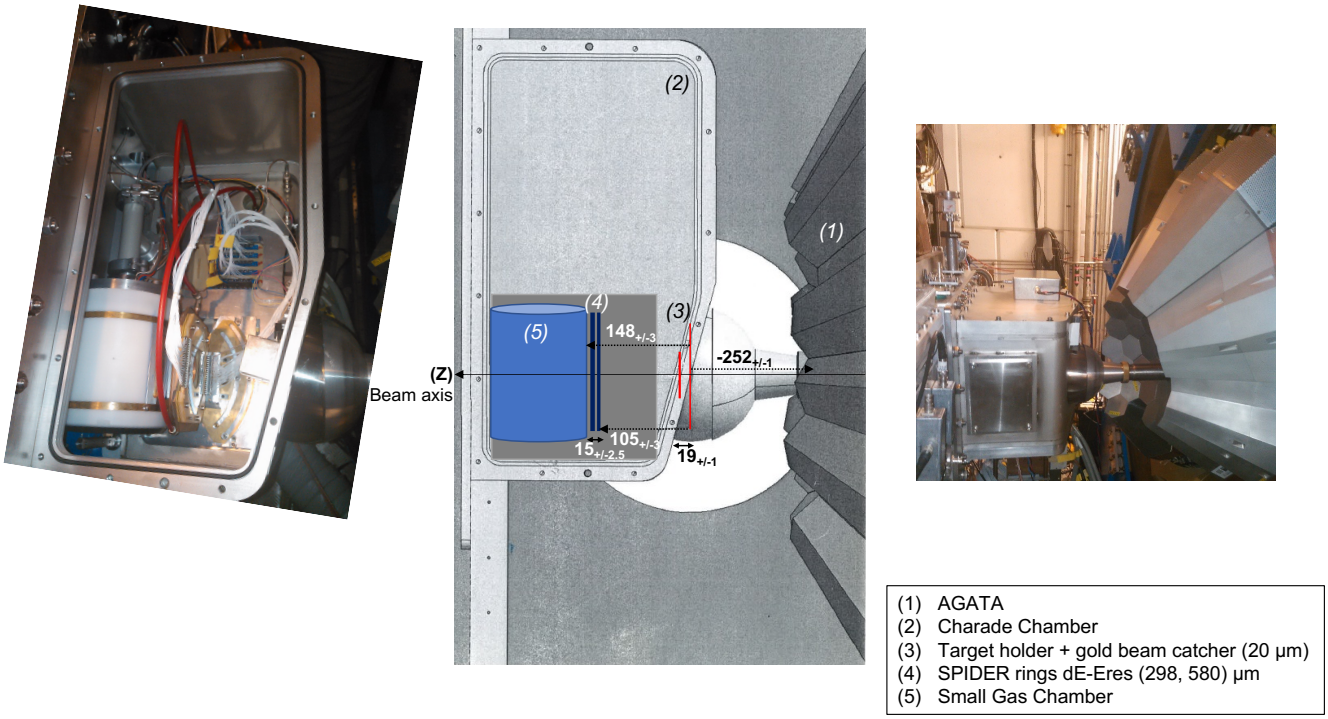

Figure 3.14: Scheme of the target chamber with the AGATA instrument. The chamber Charade included the target holder and the beam catcher (red), two Si rings for SPIDER (dark blue) and the small gas chamber (clear blue). All lengths are in mm. Pictures of the opened experimental chamber (left) and from side with AGATA (right) are also given.

The AGATA structure is pictured in Fig. 3.15 with the laboratory frame. Worth to point out that a clock like rotation of $-\frac{\pi}{2}$ was included between the AGATA tracking frame and the laboratory frame: Y_{lab} corresponded to $-X_{track}$. It was so corrected to obtain the reconstructed image $(XY)_{lab}$, after tracking, given on the right side of Fig. 3.15. The angles were derived from the tracked positions

$$\begin{aligned} \theta_\gamma &= \text{acos}\left(\frac{Z}{\sqrt{X^2+Y^2+Z^2}}\right) \\ \phi_\gamma &= \text{atan}\left(\frac{Y}{X}\right) \end{aligned} \tag{3.8}$$

The experimental coverage was $\theta_\gamma \in [120, 176]$ deg, as required to maximize Doppler effect and so to reach the fs sensitivity (Sec.2.2.2). The distance from AGATA to target strongly impacted the angular resolution and errors. It will be shown in Chapter 5 how this distance was accurately measured online, with a mm scale.

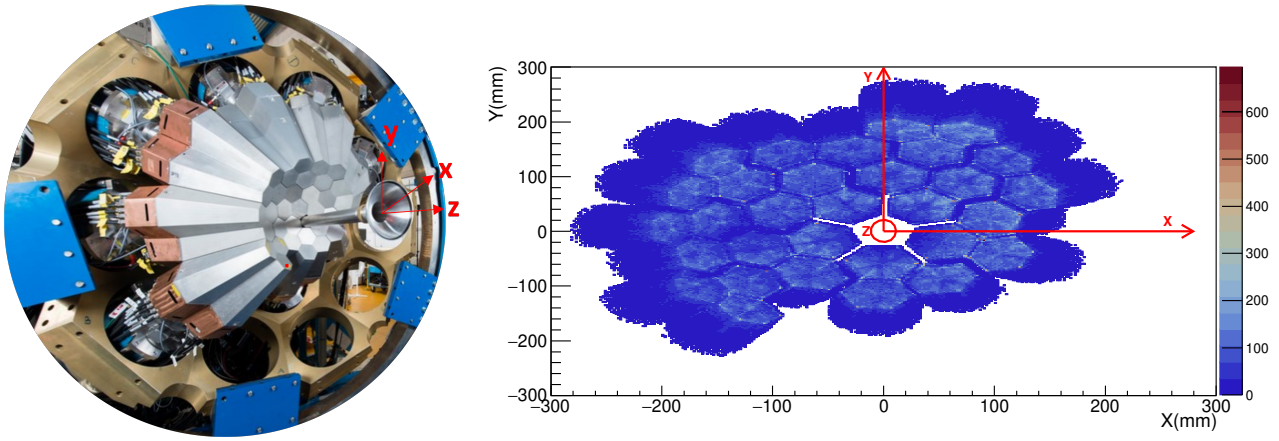

Figure 3.15: Left picture of AGATA at GANIL with the indicated laboratory frame, ©E. Clément. Right side: matrix of tracked positions in $(X, Y)_{lab}$. The experimental 31 crystals are apparent.

- Operation

The whole operation of AGATA is drawn in Fig. 3.16. It was a complex system to acquire the data from 31×(36 segments + 2 core) signals and then to analyse them.

The pulse shape analysis PSA is explained now. The γ-rays, interacting in the Ge detection volume, generated electron-hole pairs which drifted to central anodes (+) and external cathodes (-) because of the imposed electric field. The currents induced by the moving charges were measured with the cooled Field-Effect Transistors FET and the preamplifiers at each crystal backside. If the crystal owned a cylindrical symmetry, only the radial position of the deposited energy could be derived. This explains the need of an electrical segmentation of the crystals. The charge motions in one electrode, the net signal, induced signals in its neighboring segments, the transient signals. The segment where the γ-ray interaction happened was identified from the net signal, and the amplitudes of the transient signals were analyzed to determine the position inside the fired segment. To increase the position resolution, the shapes of the transient signals were compared to reference sets associated with space-defined interactions. This PSA is illustrated in Annexes B.1. To save computing time, the references were simulated ([101]) with signals calculated over position and time on a grid of (1 mm, 1 ns)[58].

The analog signals after preamplifiers were digitized. The AGATA front-end electronics, detailed in Annexes B.1, owned only optical fibre links to increase the data flow velocity and to insulate the electronic elements. The digital processing algorithms included in particular a digital trapezoidal filter of Jordanov kind to extract energy from the trace amplitudes, the principle found in [102]. The proper rise and shaping times were worked out during the calibrations before the experiment. Another algorithm -leading edge kind and CFO- extracted the time. The associated electronics were a mix between Advanced Telecommunication Computing Architecture ATCA cards [103] and the recent GGP cards. With a digitizer per crystal, the signals were 100 MHz sampled [79] and synchronized. Up to the interaction reconstruction, all crystals were dealt independently in parallel in the Local Level Processing LLP, shown in blue in Fig. 3.16. To build then a global event with the tracking algorithm, crystal data were processed together: this is referred as the Global Level Processing GLP, in purple in Fig. 3.16. The requirement of a synchronization among different elements was achieved via the distribution of a central clock Global Trigger System GTS of the same frequency 100 MHz, presented in Annexe B.1, and a timestamp to gather data in a global event with all individual interaction information hit(E, X, Y, Z, t). It was important to check the synchronization over time during the experiment. This was done by controlling the stability of the timestamp between the different crystals.

The data acquisition system of AGATA was Narval, under Linux, written in ADA. Narval [104], a program based on actor structure, ensured multiple tasks distributed in parallel on different devices. An

actor corresponded to a process along which buffers of data from previous stage were received, modified and passed to next stage. Specific C++ programs applied the undergone actions. Three types of actors were present: producer without entrance data, filter processing data from flow with output writing, and consumer writing data to disk files. Narval chain structure was user implemented through the topology configuration file. The whole Narval path is given in Fig. 3.16.

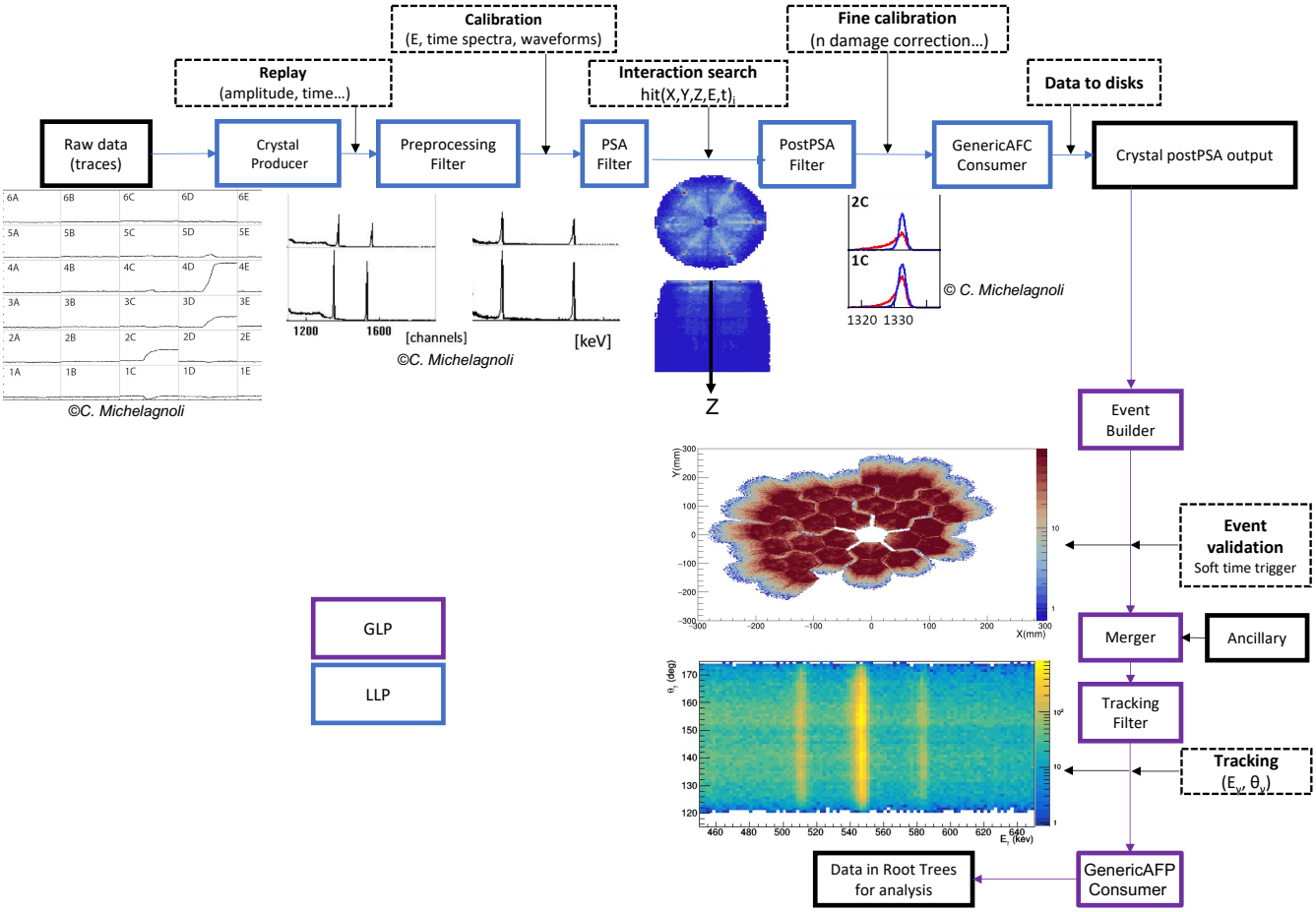

Figure 3.16: The AGATA replay processing from local level (blue) to global level (purple). Each Narval actor given in box performed operations on data, summarized in dashed boxes. Results after the actors actions are illustrated with the figures obtained from the experiment or from [58]. At the end of LLP, the individual interaction data (energy, position, time) obtained by PSA are saved to disk as "crystal outputs". They served as an entry point for GLP. The tracked results were stored in trees for later analysis. This experiment did not include ancillary detector at the merger stage.

The replay of AGATA data is described in Annexe B.1. At local level, the first energy-time calibration was done with the preprocessing filter, from a source of ^{60}Co. Cross-talks between AGATA detectors, reported in [101], were observed to be proportional to the fired segment multiplicity. In case of high energy γ-rays (E_γ >5 MeV) like in this experiment, higher segment multiplicities were expected, up to 6 [58], hence increasing the cross-talk impact. The essential correction was achieved by applying on each segment the cross-talk matrix coefficients 36×36 which were determined by sorting the energy over the segment multiplicity. The extraction of the interaction position was ensured after, by the PSA filter with the calibrated data, based on the Adaptive-Grid-Search AGS algorithm [105]. An example of obtained interactions after PSA for one crystal is shown in Fig. 3.16. Another important correction was applied with the PostPSA filter: the neutron damage correction, illustrated in Fig. 3.16 with red spectra before and blue ones after the correction. The data after the event builder were selected according to close

timestamps: a window of acceptable timestamp differences was chosen by the experimenters in the soft GTS trigger. The local AGATA fired components (segments, cores) sent trigger requests, if satisfying the GTS trigger they were validated, or if not, rejected. Online monitoring of the trigger validations and rejections was possible. The γ-ray counting rate was not expected high in the experiment. Hence, it was possible to choose the global trigger such that all local triggers were validated: this is referred as the trigger-less mode.

Tracking was implemented with the tracking filter to produce energy and angle information at emission. The matrix (E_γ, θ_γ) in Fig. 3.16 was built once the consumer GenericAFP had converted the tracked data to root trees. In the case of high energy γ-rays ($E_\gamma \in [5, 8]$ MeV), the cross section of γ-ray interactions in Ge is still dominated by Compton scattering, by more than 50% (Fig. 3.12), compared to pair creation. The single escape peak for this energy range has been measured up to 60 % of the photopeak when 12 crystals were used in AGATA, see [58]. Increasing the detection volume (the number of crystals) reduces the number of events in the escape peaks and, so, it increases the ones in the photopeak. In the present experiment, the single escape peak associated with the γ-ray transition at $E_{\gamma,0}$=7.333 MeV from the Ex=7.785 MeV state in $^{23}Mg^*$ was not clearly observed above the noise background. The reconstruction will be slightly more efficient by working on the summed segment energies with the neighboring crystals also included. But, the tracked spectrum presents higher SNR and higher resolutions in energy and angle, in comparison of the spectrum obtained by this second approach [58].

- Response function

The calibration runs were done with three sources: ^{60}Co, ^{152}Eu and AmBe(Fe). The last one, due to space congestion, could not be put at the target point. It was only used as a second energy calibration of LLP for the high γ-ray energy range (up to 8 MeV). The source data were taken before and after the experiment; thanks to its multiple well-known γ-ray peaks the runs of ^{152}Eu were used in particular to quantify the energy efficiency of AGATA. As previously said, the ^{60}Co source served for the data replay and processing before the experiment. Data analysis from the ^{152}Eu and AmBe(Fe) sources are detailed in Annexes B.1, the main results are given now. In the left bottom of Fig. 3.17, the proper energy calibration is shown with less than 0.2% relative difference between referenced $E_{\gamma,0}$ and derived E_γ^{fit} from Gaussian fits of the γ-ray peaks of ^{152}Eu. The right plot highlights the resolution of 3.4 ± 0.8keV at FWHM of γ-rays within $[0.2, 1.4]$ MeV. The slight dispersions came from two effects: the high Compton background for low energies (up to 0.5 MeV), the different intensities inducing different statistics among the peaks. The error bars, too small to be visible, were calculated from Gaussian fits, and represented only statistical uncertainties.

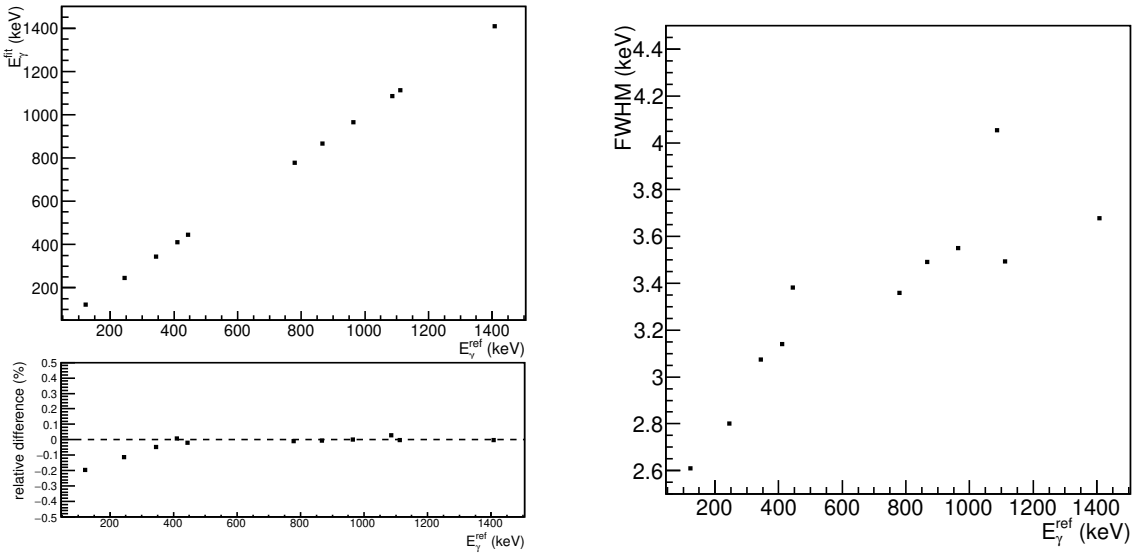

Figure 3.17: The energy resolution of AGATA from a ^{152}Eu source. Top left plot: the centroids from Gaussian fits (E_γ^{fit}) along the expected γ-ray peak energies (E_γ^{ref}) from [106]. Bottom left panel: the relative difference E_γ^{ref}-E_γ^{fit} derived, demonstrating the excellent calibration: at worst 0.2 % difference. The observed systematic differences for low γ-ray energies (E_γ <400 keV) were due to a remaining Compton background noise contribution which is usually important in the low energy region for HPGe crystals. Right panel: the evolution of the peak FWHM along the expected energy, with FWHM=2.35$\times\sigma$ from Gaussian fits.

Resolutions of AGATA over energy and angle were determined with online data, see the top Fig. 3.18. Indeed some γ-rays, with high SNR> 3, were not observed Doppler shifted. They came from 7 excited states in (^{197}Au*, ^{28}Si*, ^{22}Na*,...). These measurements of the online energy resolution are explained in Annexes B.1. The fit of the result did not allow us to derive the resolution as a function of the energy, another approach was done. After PSA with the adaptive-grid search, the position uncertainty was $\pm$4mm[79] for the FWHM of the three space directions (X, Y, Z). The dispersion due to these uncertainties in the reconstructed angle is shown in the bottom Fig. 3.18 with online data gated on γ-rays from a gold excited state. After Gaussian fits of the dispersion, the angle resolution of AGATA was found to be $\sigma_{\theta_\gamma} = 0.667\pm0.001$ deg. The measured resolutions in energy and angle have been included in the simulations of the AGATA response function, detailed in Chapter 4.

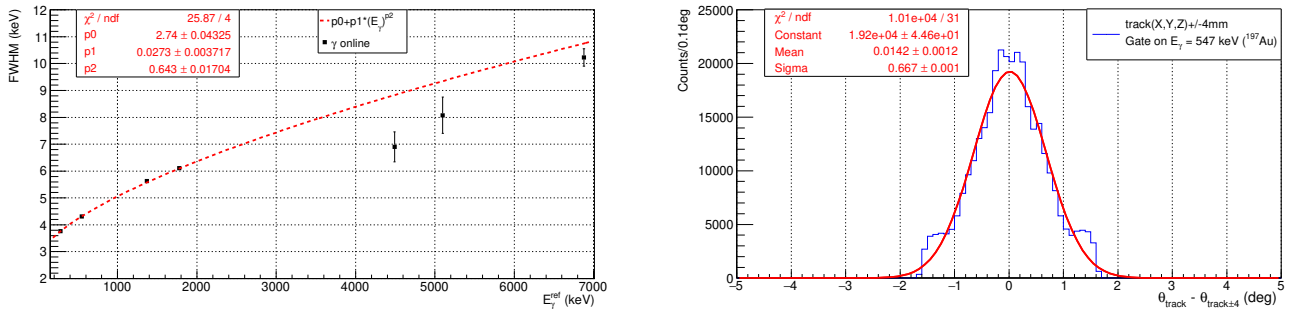

Figure 3.18: Determination of the online AGATA resolutions in energy (left) and in angle (right). The derived FWHM of 7 observed unshifted γ-ray transitions are plotted over the transition energies E_γ^{ref}. The energy resolution, measured over a large range [0,7] MeV, was fitted with a usual square root function [77], the poor fit forced us to use the measured σ instead of the fitted function, in AGATA simulations. After selecting γ-rays from the Ex=0.547 MeV state in ^{197}Au*, the position uncertainty of 4 mm[79] was included in the derivation of θ_γ from tracked coordinates ($\theta_{\text{track}\pm4}$), and compared with tracked data (θ_{track}), the blue curve in right panel. The distribution was well fitted by Gaussian function (red curve) with a dispersion of σ=0.667±0.001 deg.

The black points in Fig. 3.19 present the measured AGATA efficiency over energy with the ^{152}Eu source at the target position, using its known age and activity. The measured energy spectrum is given in Annexes B.1. Then, the AGATA efficiency was estimated by using the Geant4 AGATA code (Ref. [107]) with our experimental geometrical configuration and for the complete γ-ray energy range of use in the present analysis ($E_\gamma \in$[100, 8000] keV). As expected, a normalization of the simulated values to the measured ones was required: the normalized efficiencies are shown with the blue color in Fig. 3.19. A function was determined in Eq. (3.9) on log scales, see the bottom part of Fig. 3.19. This function allowed us to interpolate the AGATA efficiency to any energy. Such 2$^{\text{nd}}$ order polynomial functions are usual for HPGe detectors [77].

$$\epsilon = e^{-2.7+0.54\ln(E_\gamma)-0.084\ln(E_\gamma)^2} \tag{3.9}$$

with the γ-ray energy E_γ in keV.

The differential cross section to populate the Ex=7.785 MeV state, previously measured with a lower beam energy by [52], was determined in this experiment with the efficiency function. As said, the beam intensity was not accurately measured, but monitored online, see Table 3.1. Hence the derived differential cross section, within the VAMOS aperture due to the ejectile selection, was obtained with an important uncertainty. Shown in Fig. 3.5, the VAMOS laboratory aperture, corresponding to the inner hole of SPIDER rings, results in a solid angle of $d\Omega_\alpha^{\text{lab}}$=0.137 sr. The number of populated states at the energy Ex=7.785 MeV was derived from the number of measured $E_{\gamma,0}$=7.333 MeV γ-rays, after a local background noise subtraction and a correction with the expected energy efficiency from Eq. (3.9). Given in Fig. 3.4, the measured ^{3}He densities for the thick targets and the beam exposure times on target were finally taken into account to calculate the differential cross section. The measured value $\frac{d\sigma}{d\Omega_\alpha}^{\text{lab}} = 38.5^{+12.2}_{-12.1}$ μb.sr^{-1} at 4.618 MeV/u, higher than 23 μb.sr^{-1} at 3.125 AMeV [52], is in good agreement with the calculations of the total cross section over beam energy, in Fig. 2.7 (Sec. 2.3.1).

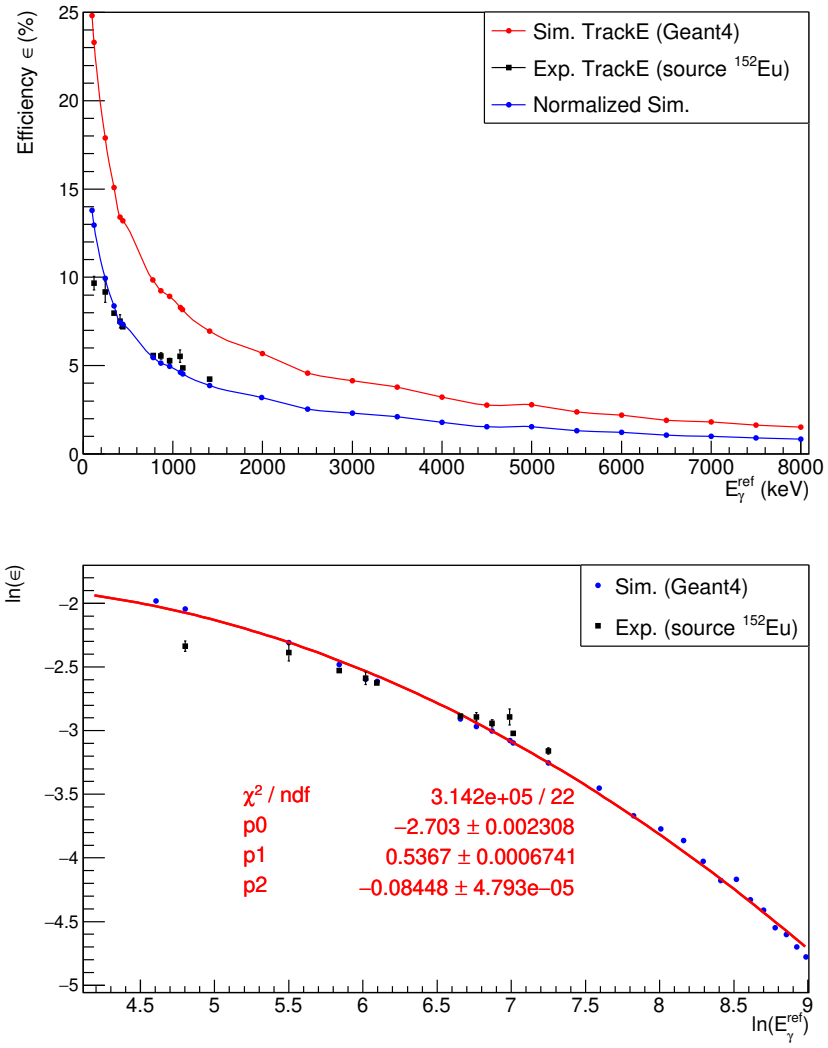

Figure 3.19: Evolution of AGATA detection efficiencies along the γ-ray energy. Top plot: absolute efficiencies were measured from a ^{152}Eu source (black points) and derived from Geant4 simulations (red curve) for $E_\gamma \in [100, 8000]$ keV. The efficiency after a normalization of the simulated efficiency to the measured one is shown with the blue curve, the normalization factor is 1.80(6). Bottom plot: the measured and normalized simulated efficiencies are shown in log scales. Simulated efficiencies were fitted by a polynomial function, given with the red curve, in order to interpolate the efficiency at any γ-ray energy. The efficiency at 1.3 MeV was found to be 4.3(1) %.

Beyond the energy efficiency, the efficiency of AGATA angle reconstruction was determined by selecting background data in the γ-ray spectrum, around the transitions of interest. The measured angle-projected distributions are presented in Fig. 3.20. The top histograms were done over $\cos(\theta_\gamma)$, and the bottom ones over θ_γ. Three ranges of energy were compared: $E_\gamma \in [1.5, 1.6]$ MeV (black histograms), $E_\gamma \in [4.2, 4.3]$ MeV (red histograms), and $E_\gamma \in [6.65, 6.75]$ MeV (blue histograms). The angular distributions were observed independent of the energy. These angular distributions are most likely proportional to the geometric total efficiency of AGATA.

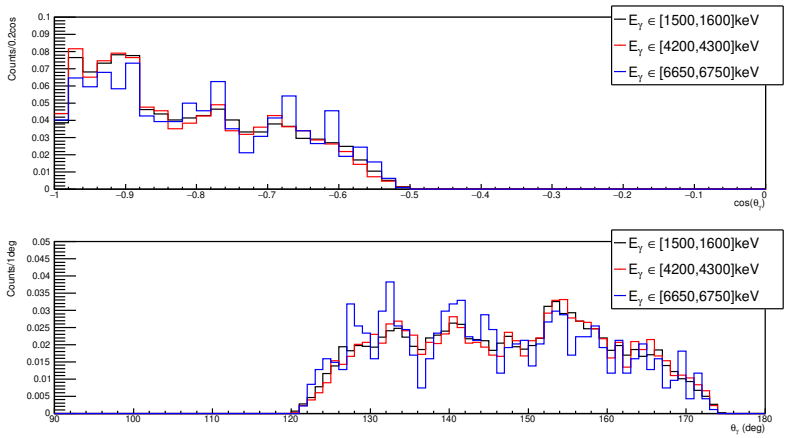

Figure 3.20: The angular distribution of AGATA γ-ray background for different energies. The measured γ-ray energies E_γ are projected on $\cos(\theta_\gamma)$ (top) and on θ_γ (bottom). The first spectrum is independent of the solid angle. Three different energy ranges in the background of the γ-ray spectrum, with a 0.1 MeV width, were selected: [1.5, 1.6] MeV (black), [4.2, 4.3] MeV (red), [6.65, 6.75] MeV (blue). It is observed that angular distributions are similar for the three energy ranges.

The stability of AGATA calibrations in energy and position as well as the crystal synchronization were checked during the full experiment. The measured γ-ray energy without Doppler correction was plotted over the experimental crystal tracked time ($\text{time}_{\text{track}}$), within two regions where γ-rays from the Ex=0.547 MeV state in ^{197}Au* (Fig. 3.21(a)) and from the Ex=6.878 MeV state in ^{28}Si* (Fig. 3.21(b)) were observed. The solid back lines mark the expected rest energy. No variation in energy was observed beyond the limit of AGATA response function from Gaussian dispersion, see Annexes B.1. Fig. 3.21(c) presents the time difference between the GANIL local HF time ($\text{time}_{\text{GANIL}}$) and the time associated with the crystal event time, along the 31 crystals. High counts within [10, 20] ns corresponded to the prompt signal. No misalignment among the crystals was noticed, supporting the stability of the clock synchronization during the experiment.

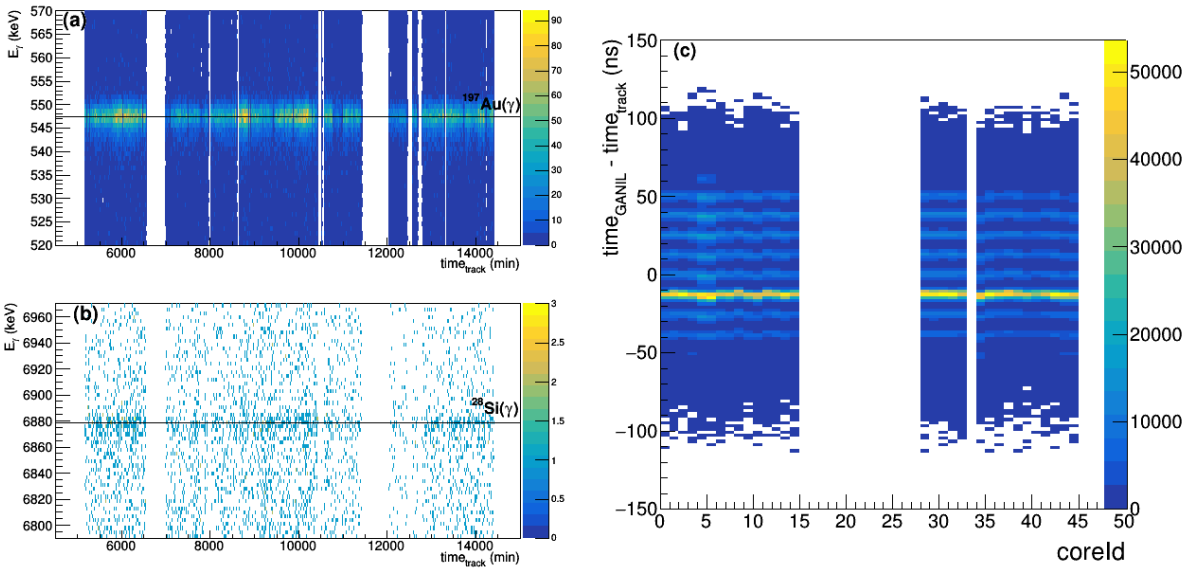

Figure 3.21: Panel a: the tracked γ-ray energy is shown as a function of experimental tracked time ($time_{track}$), the black line marking the expected rest energy from the Ex=0.547 MeV state in ^{197}Au*. Panel b: same as panel (a) but selected on the energy range associated with the γ-rays from the Ex=6.878 MeV state in ^{28}Si*. Panel c: the difference between GANIL local time and tracked time ($time_{GANIL}$-$time_{track}$) is presented over the crystal index (coreId). The stabilities, during the experiment, of the AGATA calibration, panels (a, b), and of the global synchronization, panel c, are proven.

3.3.3 SPIDER

- Geometry

The SPIDER detector was made of two silicon rings separated by 15 mm in the vacuum chamber. The first one, with respect to the target, was 300 μm thick and segmented in 16 sub-rings called strips and 16 sub-sectors, in order to measure the particle angles (θ, ϕ), see Fig. 3.22 as given by the producer. Most particles were not stopped in the first detector, hence it measured energy losses ΔE. The second silicon ring, 640 μm thick, was not segmented. It was used to stop the particles and to measure the residual energy E_{res}. A picture of that 2nd ring (E_{res}) is also shown in the bottom right of Fig. 3.22. Table 3.5 specifies the detector characteristics, in particular the angular coverage in the laboratory frame.

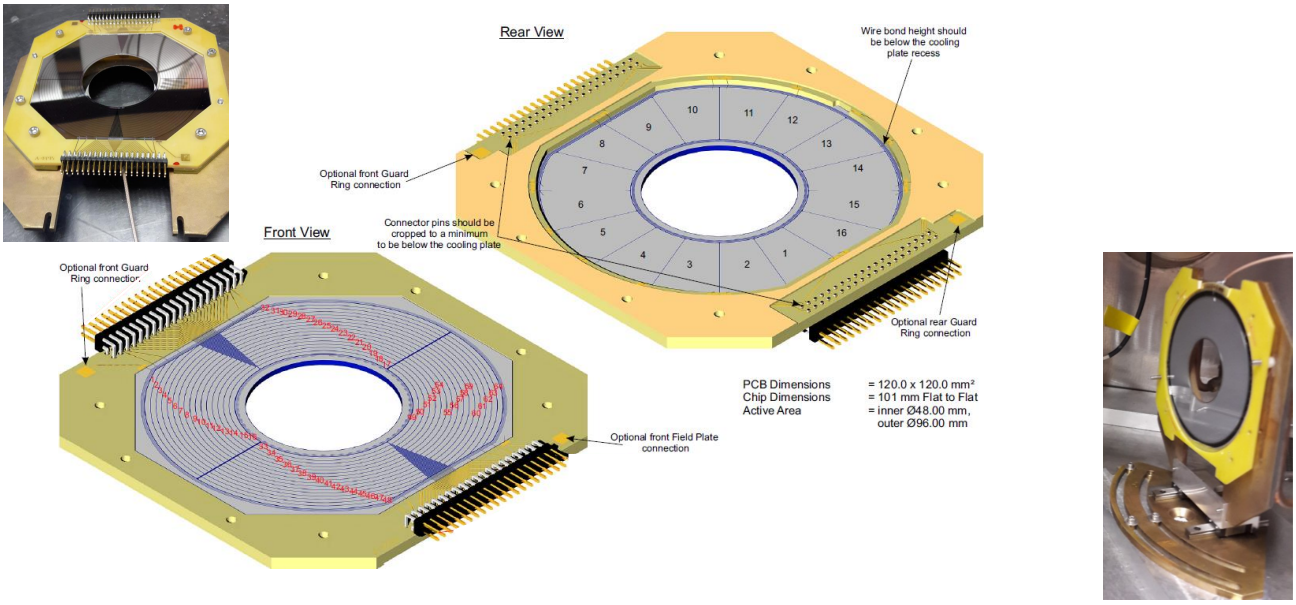

Figure 3.22: Scheme of the SPIDER 1st ring as given by the producer (MICRON technology), stripped into 16 sub-rings in the frontside and 16 sub-sectors in the backside. Top left picture: the ring mounted on its mechanical support before setting into the target chamber. Bottom right picture: 2nd ring, taken during the calibration run.

Ring	Thickness μm (Al cover μm)	Radius {inner, outer} (mm)	Segmentation	position $(XY, Z)_{lab}$ mm	Angular coverage θ_{lab} (deg)
ΔE, 1st	300±1 (0.3)	{24, 48} ± 0.5	4 quadrants (16 strips, 4 sectors)$_{quadrant}$	(0±0.3, 95±3)	strip width 1.5±0.06mm from 12.8(4) to 24.5(7)
E_{res}, 2nd	640±5	{23, 48} ± 0.5	none	(0±0.3, 110±5.5)	same

Table 3.5: Main features of SPIDER.

- Energy calibration

Isotope	Emitted α energy MeV	Intensity %
^{239}Pu	5.1566	73.4
^{241}Am	5.4856	85.2
^{244}Cm	5.8048	76.7

Table 3.6: Triple α calibration source.

The energy calibration of SPIDER was ensured by measuring α particles emitted from a known radioactive source. Such classical source presented three main isotopes of (Pu, Am, Cm) which decay by α for well referenced energies (Table 3.6). The calibration is illustrated in Fig. 3.23 for the 2nd ring. The three observed peaks in Fig. 3.23(a) were fitted with Gaussian functions and exponential functions to account for the observed left tails (at low energies). The obtained slope in Fig. 3.23(b) was used for the energy calibration. The energy resolution, shown in Fig. 3.23(c), was around 50 keV for E_{res}. The same calibration process was applied on the 16 strips of each quadrant of the 1st ring (ΔE). The calibrated α

data of the first strip, in the upper right quadrant, is illustrated in Fig. 3.24. The complete calibration is given in Annexes B.2.

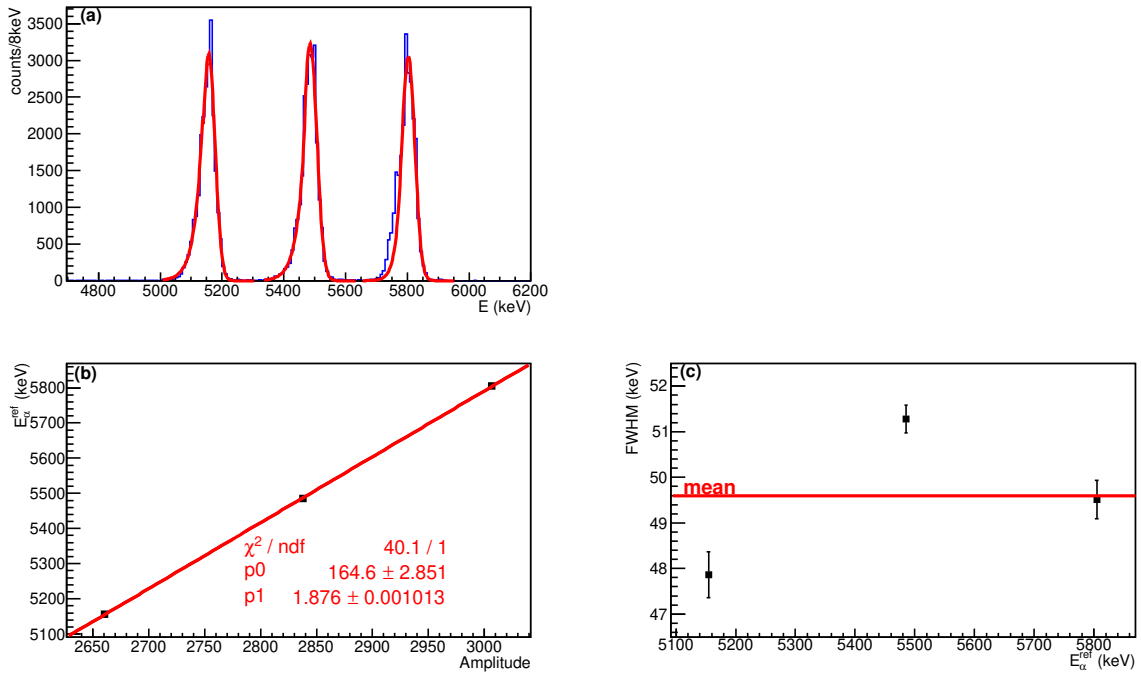

Figure 3.23: The energy calibration and resolution of the SPIDER 2nd ring (E_{res}). Panel a: energy calibration spectrum using the slope derived in panel b. Panel b: α energy (E_α^{ref}, Table 3.6) over the Gaussian centroid in the raw spectrum. Panel c: resolution, from FWHM of Gaussian fitted peaks with included exponential left tails, versus E_α^{ref}. The mean value is marked by the red line.

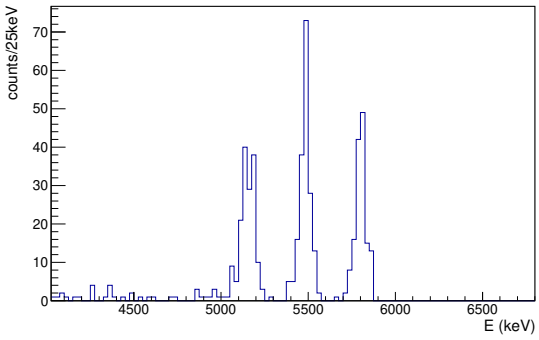

Figure 3.24: The calibrated spectrum of the first strip in the Upper Right quadrant of the SPIDER 1st ring (ΔE). Calibration done with triple α source.

All measured energy resolutions from α measurements are shown in Fig. 3.25 for 4×16 strips. The quadrants were located at upper left and upper right, down left and down right (respectively named Q1, Q2, Q3, Q4). The mean values per quadrant are shown with the red lines, only as an indication. The energy resolution was around 80 keV for ΔE. Table 3.7 summarizes the measured response functions of the two rings. Similarly to AGATA, SPIDER was simulated by Gaussian functions to predict the energy

and angle responses.

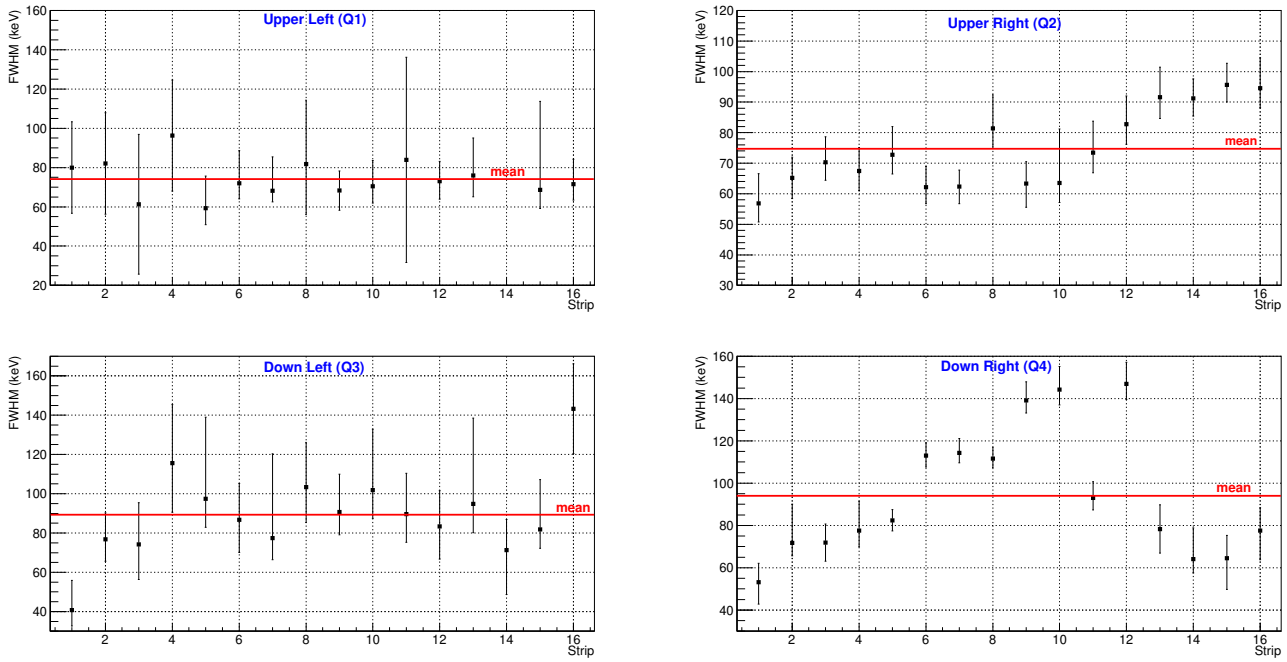

Figure 3.25: Energy resolution of SPIDER ΔE detector. It is stripped in 16 rings and 4 quadrants.

Properties	1^{st} Ring (ΔE) (UL Q1, UR Q2, DL Q3, DR Q4)	2^{nd} Ring (E_{res})
Mean FWHM energy (keV)	$(74.2^{+22.4}_{-16.8}, 74.7^{+8.9}_{-6.3}, 89.3^{+25.1}_{-15.6}, 94.0^{+9.9}_{-7.8})$	49.6(21)
$\sigma(\theta)$, $\Delta(\phi)$ (deg)	0.35, 22.5	/

Table 3.7: Response function of the SPIDER rings.

- Rejection of energy drifted events

In principle, the energy measured in the strip of the ΔE detector has to be equal to the energy measured in the corresponding sector. Yet, it was not always the case as shown in Fig. 3.26. Drifts of deposited charges were observed mainly at high energies ($\geq$ 12 MeV). Indeed the total energy losses ΔE per quadrant were higher in the sector sum (Sector ΔE) than in the strip sum (Strip ΔE). The equality condition between strip and sector was used to select cleaned events among SPIDER data.

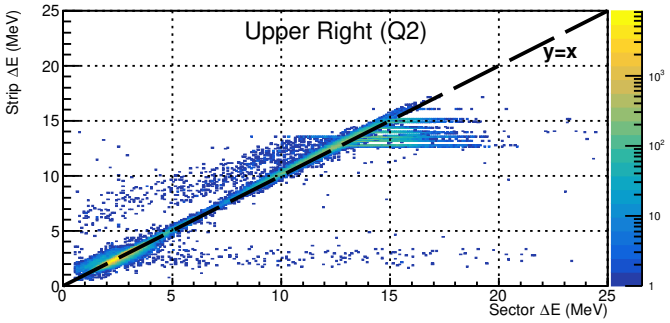

Figure 3.26: Energy losses summed up on all strips (Strip ΔE) versus the energy summed up on all sectors (Sector ΔE), shown here for the SPIDER Upper Right Q2. Dashed black line marks the y=x function. Only events along this line were selected.

- Particle identification

The particles were identified in (A, Z) by looking at ΔE-E_{res} plots with respect to energy losses calculated from stopping powers in Si (SRIM [76]). Hydrogen isotopes (^{1}H, ^{2}H) and helium isotopes (^{3}He, ^{4}He) are identified in Fig. 3.27. The few ^{3}He events could be scattered from the target or could come from fusion evaporation reactions. The apparent curve above the one of ^{2}H came from the tritium channel. Benchmarks were seen, associated to particles with too high energies to be stopped in the detector. This plot also allowed us to validate the ring thicknesses, see Table 3.5.

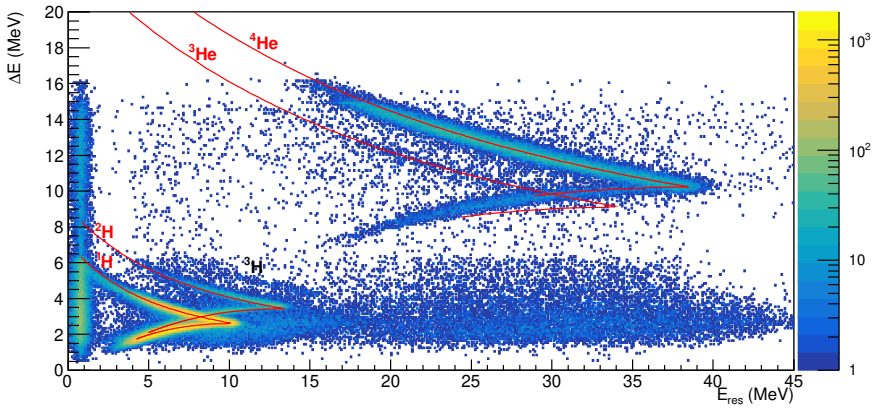

Figure 3.27: SPIDER ΔE-E_{res} matrix of particle identification. Energy losses calculated with SRIM stopping powers [76] are overlaid as red curves for (^{1}H, ^{2}H, ^{3}He, ^{4}He). The fifth noticed curve was identified as tritium events.

3.3.4 The small gas chamber

Located downstream of the target, the small gas chamber provided an additional reconstruction of the ejectile path, in order to improve the resolution and to reduce the uncertainties on the angle of the γ-ray emitter (^{23}Mg*). This detector, built at GANIL, was easily added inside the Charade chamber, see Fig. 3.14. The next lines will specify its operation, its calibration in position, and finally the angles reconstruction.

- Operation

The small gas chamber in this experiment included 4 Drift Chambers Target (DCTs), illustrated in Fig. 3.28. The drift cell has on one side conductive tap strips forming a uniform electric field. They are referred as anodes from now on. After the production of a cloud of electronic charges, the liberated electrons drift towards the anode under the effect of the imposed electric field. In the experiment, four TAC modules were used to build time signals: the start corresponded to the coincidence between the cyclotron HF and the VAMOS PL and the stop to the delayed DCT anode. As seen in Fig. 3.28, DCTs were grouped into 2 pairs along the beam axis $\overrightarrow{z}$, called DCT1 and DCT2. The first anode in DCT1 was orientated along $\overrightarrow{y}$, and the second one along $\overrightarrow{x}$. On the contrary, DCT2 had its first anode along $\overrightarrow{x}$ and its second along $\overrightarrow{y}$. Such configuration resulted in 4 raw time signals, depending on two (x, y) positions. They are referred now as ($X1^{DCT}_{raw}$, $Y1^{DCT}_{raw}$) and ($X2^{DCT}_{raw}$, $Y2^{DCT}_{raw}$).

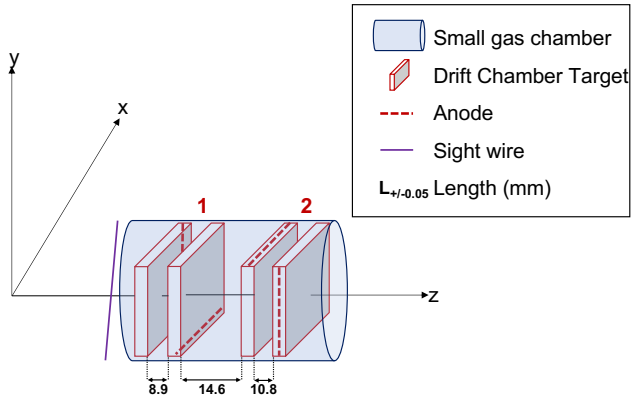

Figure 3.28: Layout of the small gas chamber. The detector was made of 4 drift chambers gathered into the two groups DCT1 and DCT2, red dashed lines showing the anode position. Positions in ($\overrightarrow{x}$, $\overrightarrow{y}$) reconstructed from the measured electron drift times, after the gas ionizations due to the crossing of charged ejectiles. The purple line shows the sight wire used for checking the anode orientation. Lengths in mm.

	Small gas chamber
Components	4 DCTs of 16 mm width side conductive strips
Gas	isobutane C_4H_{10}
Entrance	Mylar window (1.5 μm) $Z^{entrance}_{lab}$=144.4(10) mm centred w.r.t beam
DCT1 mean $Z1^{DCT}_{lab}$	170.4(10) mm
DCT2 mean $Z2^{DCT}_{lab}$	232.2(10) mm

Table 3.8: Summary of the main properties of the small gas chamber. The mean position of the DCT1 (DCT2) along beam axis, referred as $Z1^{DCT}_{lab}$ ($Z2^{DCT}_{lab}$), was used in the angle reconstruction ($\theta 1^{DCT}_{^4He}$, $\phi 1^{DCT}_{^4He}$) and ($\theta 2^{DCT}_{^4He}$,$\phi 2^{DCT}_{^4He}$). Details in text.

- Position calibration

A preliminary work was to ensure that the signals were properly associated with the anodes. To do so, the signals were compared to the orientation of anodes, as given by the designer of the chamber. A thin sight wire was put at the chamber entrance, shown with the purple line in Fig. 3.28. It was oriented with a +45 deg angle with respect to the ($\overrightarrow{x}$, $\overrightarrow{y}$) plane. The images of this wire obtained with DCT1 and DCT2 are shown in Fig. 3.29(a) and (b) respectively. The events were selected in coincidence with the detection of ^{4}He ejectiles in VAMOS (Sec.3.3.1). The image is bigger in (b) than in (a). This distortion, mostly due to the angular projection, confirmed the order of DCTs with respect to the beam direction: first DCT1 with ($X1^{DCT}_{raw}$, $Y1^{DCT}_{raw}$), then DCT2 with ($X2^{DCT}_{raw}$, $Y2^{DCT}_{raw}$). The selection of the wire position, black contour in ($X2^{DCT}_{raw}$, $Y2^{DCT}_{raw}$) of Fig. 3.29(b), is associated with the events in ($X1^{DCT}_{raw}$, $Y1^{DCT}_{raw}$) of Fig. 3.29(c). This first selection allowed us to identify the wire image in DCT1 and DCT2. The other "wire-like" shapes do not match each other. They might come from local dusts on the anodes. After the identification of the observed wire, a second selection, black contour in ($X1^{DCT}_{raw}$, $Y1^{DCT}_{raw}$) of Fig. 3.29(a), was applied to obtain the image in Fig. 3.29(d). It shows the rotation by an angle π between the two images. Let's look at the wire image in Fig. 3.29(c), its trend in X is opposite to its trend in Y, when

one increased the other decreased. The trend depends on the position of the anode in the different gas chambers, and here the measured trends are in agreement with the design drawing.

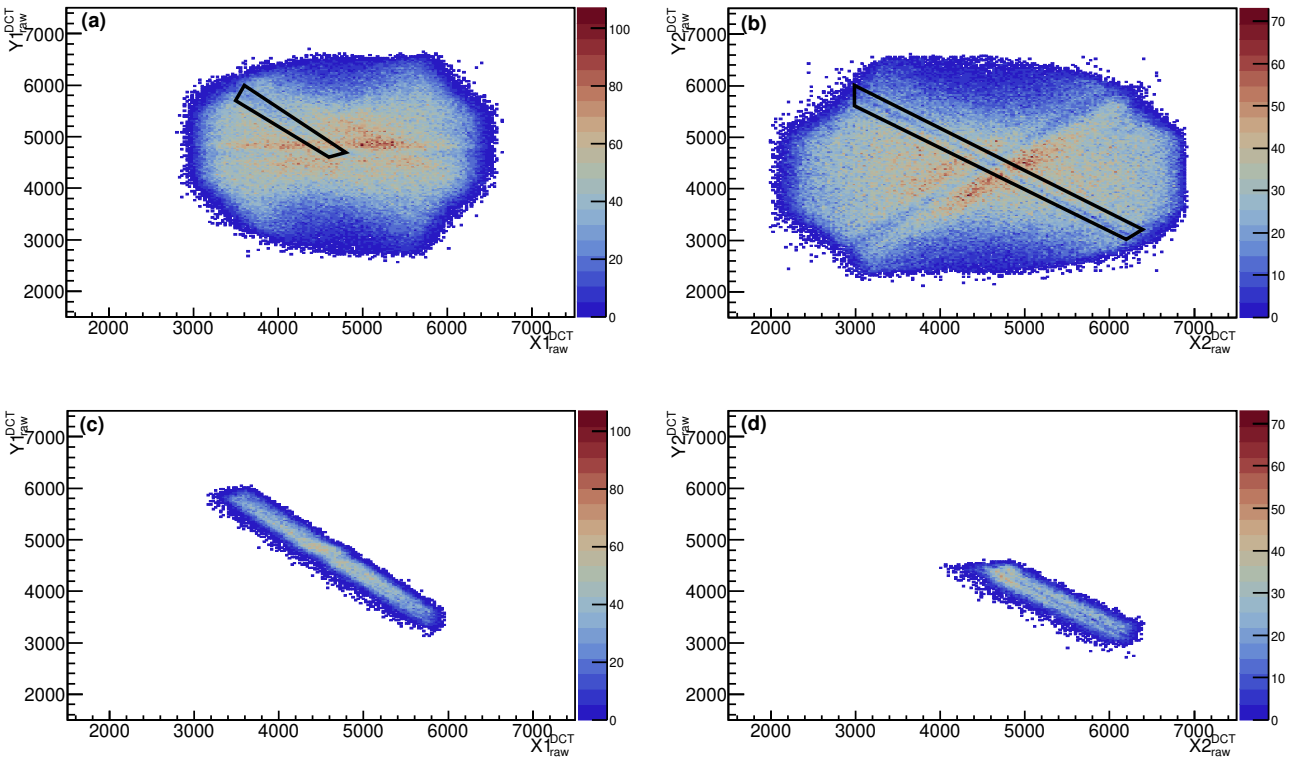

Figure 3.29: Panels (a, b): the raw signals of the drift chambers after target DCT1, $Y1_{raw}^{DCT}$ versus $X1_{raw}^{DCT}$ in (a), and of DCT2, $Y2_{raw}^{DCT}$ versus $X2_{raw}^{DCT}$ in (b). Panel (c): ($X1_{raw}^{DCT}$, $Y1_{raw}^{DCT}$) matrix in coincidence with the selection corresponding to the sight wire shadow in ($X2_{raw}^{DCT}$, $Y2_{raw}^{DCT}$), black contour in (b). The "wire-like' horizontal line in (a) does not match the diagonal wire in (b). The image of the sight wire is thus identified as the line in DCT1 (c). Panel (d): the ($X2_{raw}^{DCT}$, $Y2_{raw}^{DCT}$) matrix in coincidence with the selection on half of the sight wire in ($X1_{raw}^{DCT}$, $Y1_{raw}^{DCT}$), shown with black contour in (a). A π rotation is observed between the anodes of DCT1 and DCT2 as expected from the geometry of the small gas chamber. All events were selected in coincidence with ^{4}He ejectiles in VAMOS.

If the drift velocity of electrons in the gas is known, then the distance between the interaction point and the anode can be calculated. During the experiment, the applied tension was recorded but not the gas pressure. Another strategy was proposed to calibrate the time signals into X and Y positions. The inner hole of SPIDER, located before DCTs, acted as a mask. It allowed us to have a reference distance.

First, the TAC range, of 5 μs, was used to convert the raw signals (Xi_{raw}^{DCT}, Yi_{raw}^{DCT}) into calibrated times. Second, distances were calculated by multiplying times with approximate drift velocities for each DCT anode. Third, positions, in the laboratory frame ($\overrightarrow{x}$, $\overrightarrow{y}$), were calculated after translating the spot center to the absolute position (0, 0). The small gas chamber was indeed aligned and centered with respect to the beam direction. The obtained positions in laboratory are written ($X1_{lab}^{DCT}$, $Y1_{lab}^{DCT}$) and ($X2_{lab}^{DCT}$, $Y2_{lab}^{DCT}$). Fourth, the radii associated with the particles passing through were calculated with Eq. (3.10), and they were compared to the radius of the SPIDER inner hole corrected for the projection due to the distance between SPIDER and the DCT detector. The geometric properties of DCTs (Table 3.8) and

SPIDER (Table 3.5) were so used.

$$R^{DCTi} = \sqrt{Xi_{lab}^{DCT\,2} + Yi_{lab}^{DCT\,2}} \tag{3.10}$$

The calibrated matrices are presented in Fig. 3.30(a) and (b), in coincidence with the detection of ^{4}He ejectiles in VAMOS and γ-ray transitions in AGATA from a state in ^{23}Mg*. The red circles show the calculated images of the SPIDER inner hole. The electron drift velocities were fitted to the calculated images, see Fig. 3.30(c). The electron drift velocities obtained by this method for the two DCTs are close, of about 50 mm.μs^{-1}.

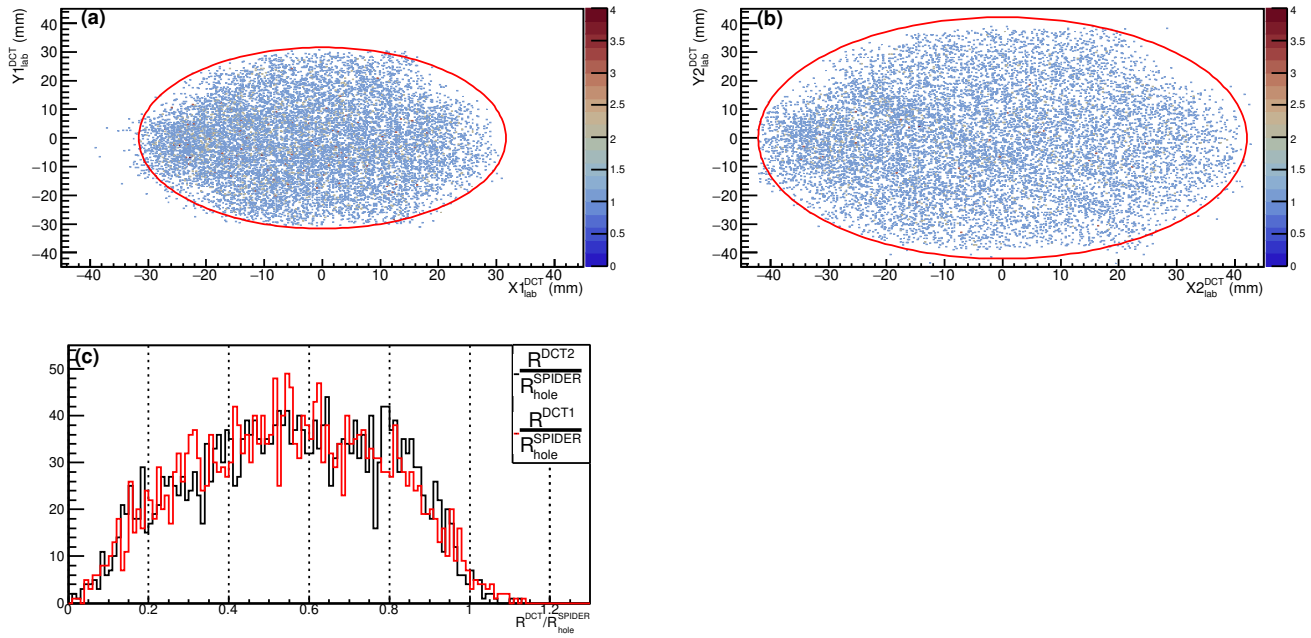

Figure 3.30: The calibrated ($X1_{lab}^{DCT}$, $Y1_{lab}^{DCT}$) of DCT1 in (a), and ($X2_{lab}^{DCT}$, $Y2_{lab}^{DCT}$) of DCT2 in (b). The events are selected in coincidence with ^{4}He ejectiles in VAMOS and γ-ray transitions in AGATA from a state in ^{23}Mg*. The image of the SPIDER inner hole is shown with the red circle, it was used to calibrate the measured time signals into distances. A prior translation of the center to (0, 0) has been applied. Panel (c): distribution of radii measured in DCT1 (DCT2), R^{DCT1} (R^{DCT2}), normalized by the radius of the SPIDER inner hole R_{hole}^{SPIDER} is presented with the red (black) histogram.

- Angles reconstruction

From the derived positions of the ejectiles ^{4}He, the associated angles (θ, ϕ) were built back. Two methods were possible

1. ($X1_{lab}^{DCT}$, $Y1_{lab}^{DCT}$) and ($X2_{lab}^{DCT}$, $Y2_{lab}^{DCT}$) can be combined,
2. ($X1_{lab}^{DCT}$, $Y1_{lab}^{DCT}$) and ($X2_{lab}^{DCT}$, $Y2_{lab}^{DCT}$) can be used independently to calculate the angles. This requires to know the positions $Z1_{lab}^{DCT}$ and $Z2_{lab}^{DCT}$.

The second method was used in order to be also sensitive to the target position. The applied formula are

$$\begin{aligned} \theta i^{DCT} &= \mathrm{acos}\left(\frac{Zi_{lab}^{DCT}}{\sqrt{Xi_{lab}^{DCT\,2} + Yi_{lab}^{DCT\,2} + Zi_{lab}^{DCT\,2}}}\right) \\ \phi i^{DCT} &= \mathrm{atan}\left(\frac{Yi_{lab}^{DCT}}{Xi_{lab}^{DCT}}\right) \end{aligned} \tag{3.11}$$

where i$\in \{1,2\}$ referred to DCT1, DCT2. The results for θ are given in Fig. 3.31(a) with $\theta 2^{\rm DCT}_{^4{\rm He}}$ along $\theta 1^{\rm DCT}_{^4{\rm He}}$, and the absolute differences in Fig. 3.31(b). The two angles differed from <0.7 deg for 90 % of the measured events. Similarly, Fig. 3.31(c) shows $\phi 2^{\rm DCT}_{^4{\rm He}}$ along $\phi 1^{\rm DCT}_{^4{\rm He}}$, the absolute differences in Fig. 3.31(d). The uncertainties on the reconstructed angles ϕ were <5 deg for 75 % of the measured events. The final value of the angles was taken as the average of the two measured values

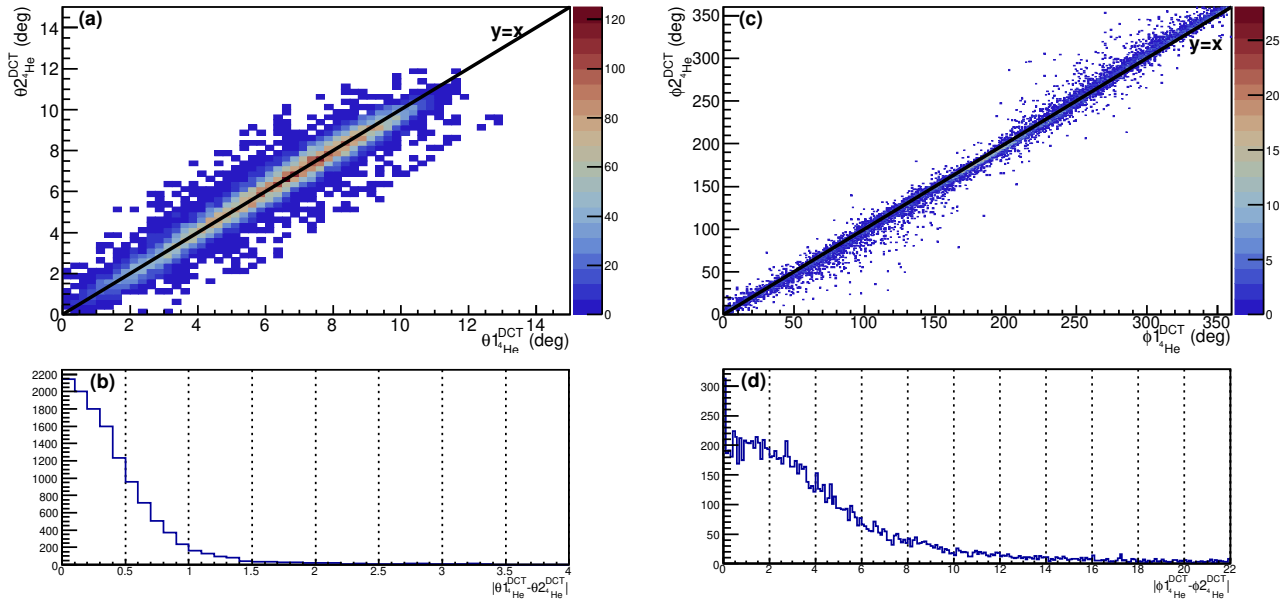

Figure 3.31: Panel (a): matrix of the reconstructed $\theta 2^{\rm DCT}_{^4{\rm He}}$ versus $\theta 1^{\rm DCT}_{^4{\rm He}}$. Black line marks the y=x function. Panel (b): distribution of the absolute differences $|\theta 1^{\rm DCT}_{^4{\rm He}} - \theta 2^{\rm DCT}_{^4{\rm He}}|$. The reconstructed angles θ agreed well: a difference of <0.7 deg is observed for 90 % of the events. Panels (c, d): same as panels (a, b) but for $\phi 1^{\rm DCT}_{^4{\rm He}}$ and $\phi 2^{\rm DCT}_{^4{\rm He}}$. The reconstructed angles ϕ appeared more dispersed than θ: 75 % of the events have a difference of <5 deg. These two limits for the angle $(\theta,\ \phi)_{^4{\rm He}}$ differences, between DCT1 and DCT2, defined the uncertainties on the final angles, and the final angle was taken as the mean value of the two measured values.

As a conclusion, the small gas chamber of the experiment allowed us, after calibration, to reconstruct the angles $(\theta,\ \phi)_{^4{\rm He}}$ of the ^{4}He ejectiles, for two positions along the beam. Mean angles were taken, noted $(\theta^{\rm DCT}_{^4{\rm He}},\ \phi^{\rm DCT}_{^4{\rm He}})$ with uncertainties of $\pm(0.7,\ 5)$ deg.

3.4 Conclusion

Along this Chapter, the experiment aiming at measuring (τ, BR$_{\rm p}$) of the Ex=7.785 MeV state in ^{23}Mg*, had been presented. The experimental parameters which contributed to the lineshapes of γ-rays and protons, were drawn: the production steps (the beam and target profiles), the particles and γ-rays properties after reaction (τ, energy losses, angles, straggling), and the detection capabilities (the instrumental response functions). How did these parameters impact the aimed physical quantities? The following Chapter 4 will present the simulations of the experiment, they helped us to quantify the sensitivity of the experiment.

Part III

On the data analysis

CHAPTER 4

Simulations of the experiment: EVASIONS code

4.1 Introduction

Experimental effects contributing to the lineshape of measured γ-rays or light particles are commonly quantified with a Monte Carlo simulation. Already existing codes can be found to simulate experiments with AGATA spectrometer, see examples built at Legnaro facility [58], at GSI facility (APCAD program [108]) as well as the AGATA Geant4 packages [107]. For several reasons mentioned here in the Chapter introduction, a new simulation code has been specifically built for this experiment during my PhD period. Beyond my desire to learn and to understand fully the simulation processes, no code was available for SPIDER, the other important detector in the experiment. All the available codes focus on γ-ray emissions and lifetime measurements, whereas the present experimental goal is the complete spectroscopy of the Ex=7.785 MeV state in ^{23}Mg*, that is to say accessing to the (τ, BR$_p$, J) parameters. The program actions and results were to be adjusted to the experimental set-up and to a physics case expected with very low statistics. Codes based on angular selected DSAM [58] or continuous-angle DSAM (APCAD [108]) cannot be reasonably applied to data with statistics lower than $\sim$30 counts per angular slice. So new analysis methods were developed in this thesis, explained in Chapters 5 and 6. They had to be implemented in a new MC simulation code. The built code has been named EVASIONS for Experimental Vamos Agata Spider Implementation On Nuclear Spectroscopy.

- Monte Carlo of the experiment

The program was written in the language C++ within the framework of ROOT (CERN [93]). Its structure is laid out in Fig. 4.1. Each main code sequence, with the name written in purple, is indeed linked to a specific section. The program inputs will be first described in Sec.4.2. The life of the states in ^{23}Mg* from their populations to their decays is presented in Sec.4.3.1. The instrument response functions are then taken into account to derive the observable γ-rays or protons, described in Sec.4.3.2. Results of MC simulations are finally given in Sec.4.4.1, and they are briefly compared with experimental data in Sec.4.4.2.

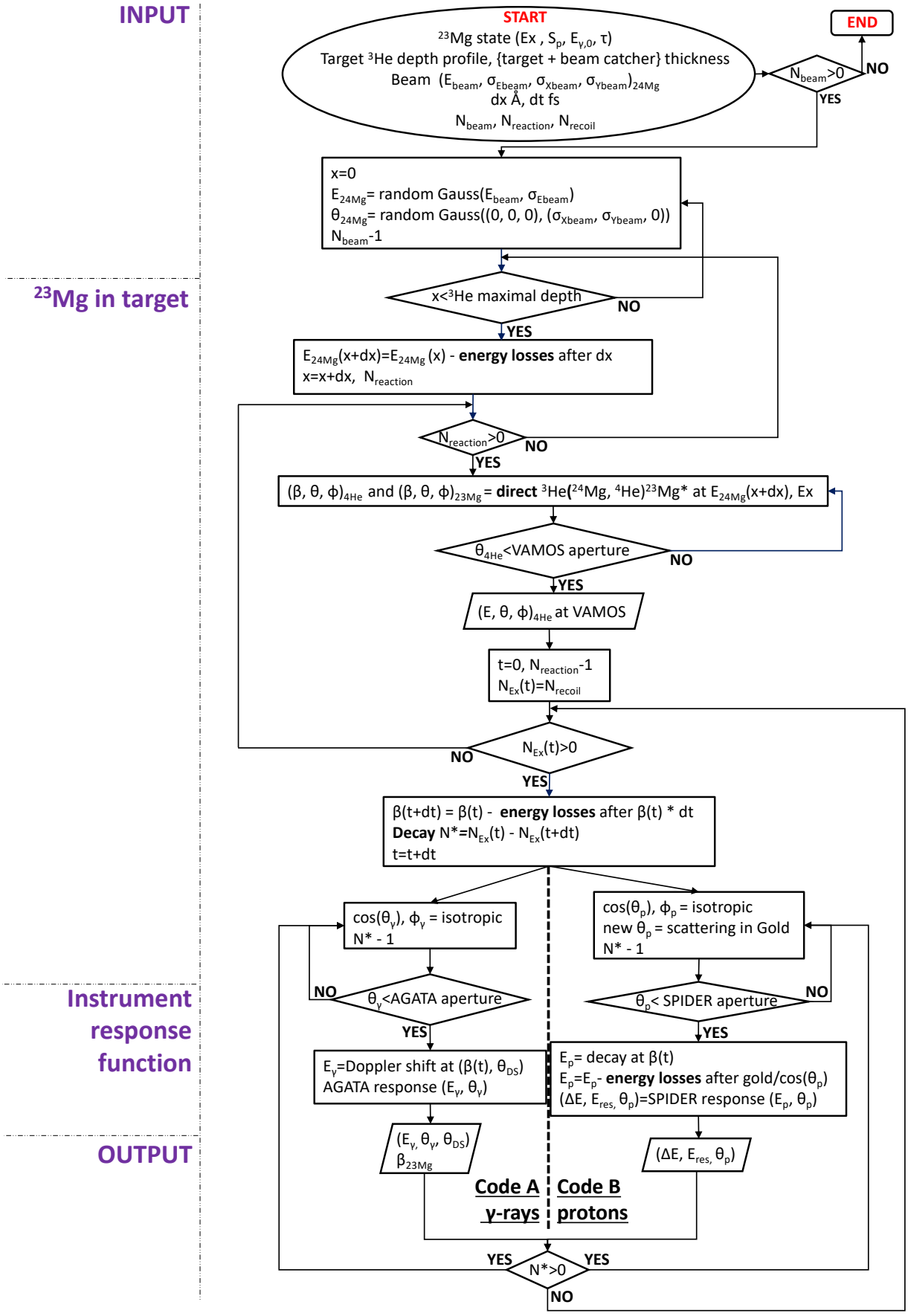

Figure 4.1: Flowchart of EVASIONS, the Monte Carlo simulation code built for the experiment on the Ex=7.785 MeV state in ^{23}Mg*. Parts in purple are described in the present Chapter sections. Due to the two different simulated emissions (γ-rays, protons), two codes, respectively (A, B), were written. They are alike until the decays of states in ^{23}Mg*. Notations are: energies E, resolutions σ, medium positions x, velocities β, angles in laboratory (θ, ϕ), numbers of beam ions N_{beam}, of reactions $N_{reaction}$, of recoil nuclei N_{recoil}, of excited states N_{Ex} and of decays N*, times from reaction populating states.

4.2 Inputs

4.2.1 Reaction initialization

Any Monte Carlo code requires some initial inputs. They encompass the spectroscopic parameters of aimed states, present reaction mechanisms and associated kinematics, beam properties and target properties. In the present EVASIONS code, these input parameters were

1. The excitation energy Ex of the state in ^{23}Mg*, its lifetime τ, the γ-ray rest energy $E_{\gamma,0}$ and the proton emission threshold S_p.
2. The two-body reaction ^{3}He(^{24}Mg, ^{4}He)^{23}Mg* with the associated masses and Z of ^{3}He, ^{24}Mg, ^{4}He, ^{23}Mg.
3. The beam profiles in energy and in space. The measured energy distribution ($E_{beam} \pm \sigma_{E_{beam}}$) and the measured transverse position ($0\pm\sigma_{X_{beam}}$, $0\pm\sigma_{Y_{beam}}$) in Table 3.1, were used.
4. The ^{3}He depth profile. We assumed a step profile from 0 to 1000 Å and the thickness of {target + beam catcher} of 25 μm. The vacum space between the target holder and the beam catcher was measured equal to 19(1) mm.

Assuming a two-body reaction in the EVASIONS code constrained the ejectile energies $E_{^4He}$ associated with the populated state. This allowed us to impose coincidences between ejectiles in VAMOS and γ-rays in AGATA (or protons in SPIDER). Thus, the excitation energy Ex of the populated state was experimentally controlled by selections on the ejectile energies. State spin was not used in the code since emissions were assumed isotropic: the experimental lineshape analysis did not need angular distribution.

In total, the code owns 24 input parameters chosen by the user to reproduce the experimental physics case. In principle, all parameters are known except one. The free parameter, i.e. the lifetime of the state, could be determined by comparison with experimental data. Along the EVASIONS code, additional parameters were given: stopping powers in medium and instrument response properties. They are detailed in Sec.4.3. The uncertainties on these external parameters contributed in fine to the lifetime uncertainties.

4.2.2 Target ^{3}He implantation profile

- Simulation of the implantation profile with SRIM

It was not possible to measure the ^{3}He implantation profile in the gold target. Special care has been taken with this issue. First, the implantation of ^{3}He ions onto gold (Table 3.2) was simulated with the SRIM Monte Carlo code [76]. Ions of ^{3}He were expected to be deeper implanted with a broader profile when using the high irradiation energy of 20 keV compared to the 5 keV one, as shown in Fig. 4.2. The thick targets were made with two different proportions of the two irradiation energies, referred as targets 1-2 for the first proportion and targets 3-4-5 for the second. Using SRIM with the two different ratios of $\frac{^{3}He^{5keV}}{^{3}He^{20keV}}$ (Table 3.2), the two implantations were simulated. The results are presented in Fig. 4.2. The profile of targets 1-2 appeared rather homogeneous between 0 Å and 1000 Å, compared to the targets 3-4-5 which peak at 250 Å. In the cases of thin targets 8 and 10, the ^{3}He ions were implanted as targets 1-2. Their depth profiles are identical to the right plot of Fig. 4.2.

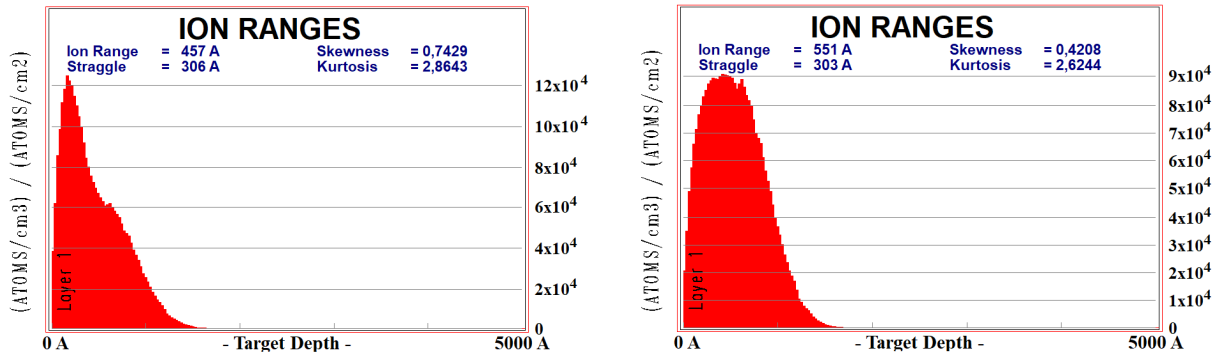

Figure 4.2: Simulations of ^{3}He implantation onto gold. Left side: targets 3-4-5 and right side: targets 1-2, associated with the producer's irradiation ratio $\frac{^3He^{5keV}}{^3He^{20keV}}$ presented in Table 3.2. From SRIM MC code [76].

- Effect of the implantation profile on γ-ray lineshape - simulations with EVASIONS

The EVASIONS code was used to evaluate the impact of the target ^{3}He implantation profile on the lifetime measurement. The energy losses of ^{24}Mg beam at 110.83(44) MeV were 0.662(1) MeV after 1000 Å of gold. Even if these losses seem low, it was important to investigate the impact of the two ^{3}He depth profiles on the observed γ-rays. Two schematic input profiles were used to evaluate the impact, they are shown in Fig. 4.3

1. T12 is a step function of ^{3}He constant concentration over gold target depth from 0 to 1000 Å, corresponding to targets 1-2.

2. T345 is a Dirac function of ^{3}He concentration at a depth of 250 Å, corresponding to targets 3-4-5.

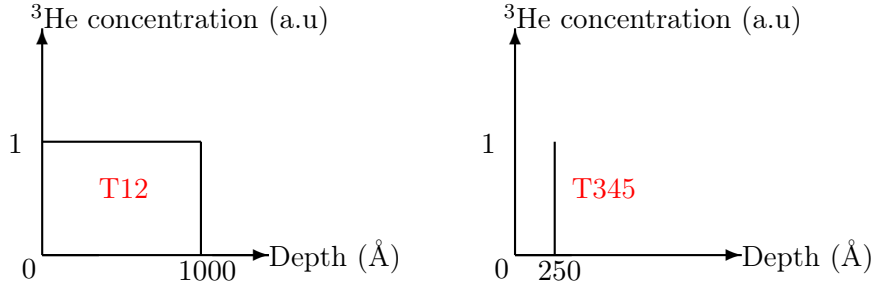

Figure 4.3: Layout of the two ^{3}He depth profiles T12 and T345, used in the EVASIONS simulation code.

To compare the impact of the two profiles, the histograms from T345 profile were normalized to the ones from T12 profile. The Fig.4.4(a) and (b) show the simulated γ-ray histograms measured by AGATA in the angular range $\theta_\gamma \in [160, 170]$ deg for the γ-ray transition $E_{\gamma,0}$=7.333 MeV from the Ex=7.785 MeV state, for two different lifetimes: τ=1 fs and τ=12 fs. Simulations of T12 profile correspond to the red curves, and T345 profile to the blue curves. Quasi no difference was noticed in the γ-ray spectra between T12 and T345 for the chosen binning of δE_γ =2 keV, which is justified by the measured energy resolution of AGATA for such high energy range $E_\gamma \geq$6 MeV.

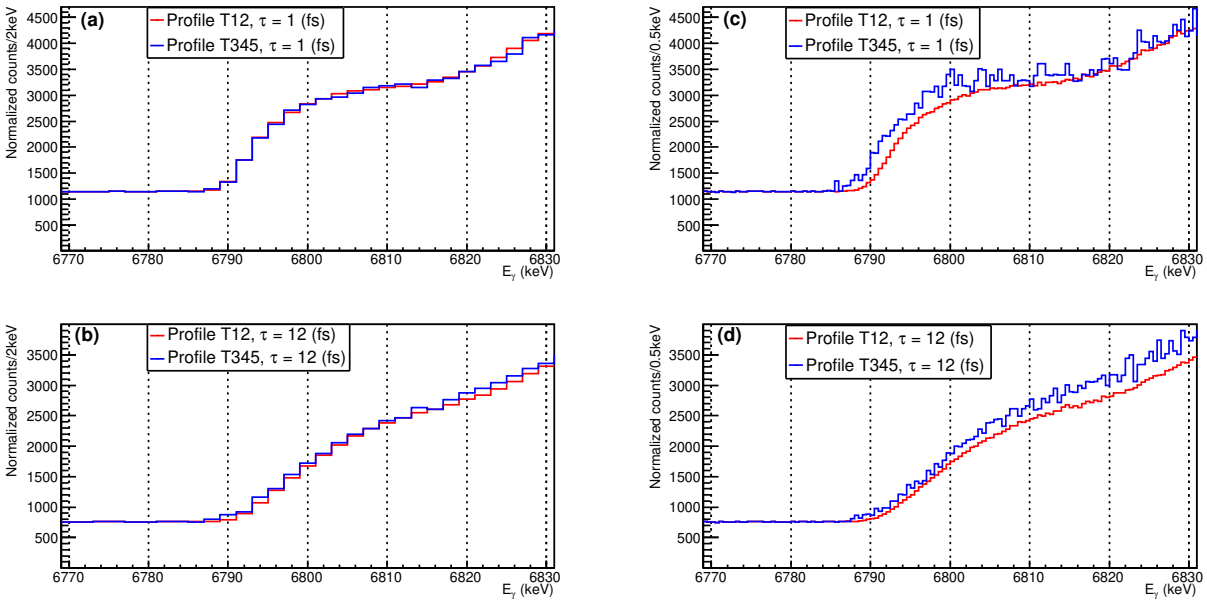

Figure 4.4: Monte Carlo simulations of the Doppler shifted γ-ray emissions (E_γ) from the (Ex=7.785 MeV, $E_{\gamma,0}$=7.333 MeV) state in ^{23}Mg*, after an angular selection in [160, 170] deg. Simulations based on the EVASIONS code were done with two input target ^{3}He depth profiles: homogeneous T12 (red curve) and peaked T345 (blue curve). Panels (a, b): the chosen binning of 2 keV corresponds to the AGATA half σ resolution for $E_\gamma \geq$6 MeV. Panels (c, d): with a 0.5 keV binning. Two different lifetimes were simulated, 1 fs in panels (a, c) and 12 fs in panels (b, d). No difference appears in panels (a, b) between T12 and T345 for the experimental resolution limit, contrary to panels (c, d) calculated with an unrealistic energy resolution of 0.5 keV.

- Effect of the implantation profile on γ-ray lineshape - calculations with LISE++

LISE++ was used in order to derive the sensitivity of the experiment. It allowed us to check the results from the EVASIONS code shown in Fig. 4.4. The calculation results are summarized in Table 4.1. First, the velocity of populated state was computed for two depths: at the entrance and at the end of the active ^{3}He region for T12 profile. The associated relative difference $\frac{\delta\beta}{\beta}$ is given in the second column. Then, the velocity was derived after two different "lifetime" travels in gold. The associated Doppler shifted γ-rays were finally calculated for the angle θ_γ=180 deg and for the experimental conditions (AGATA $\theta_\gamma^{\max}$=172 deg). The resulting relative differences $\frac{\delta E_\gamma}{E_\gamma}$ between the two reaction depths are shown in the last column. As a comparison, similar numerical estimations were done for the TRIUMF experiment [52]. It was at a lower beam energy (75 MeV) and a deeper ^{3}He implantation (depth range [0, 1500] Å) due to a target making at 30 keV. The calculations in the case of the TRIUMF experiment give the same results as shown in Table 1 of Ref. [52]: ^{3}He profile induces $\frac{\delta E_\gamma}{E_\gamma}$=0.4‰. From these numerical estimations, we can conclude that the ^{3}He depth weakly affected the velocity of ^{23}Mg and so, the γ-ray energy E_γ in the present GANIL experiment.

The effects of the target profile effects are also not sensitive to the lifetime of the state, i.e. <1‰(Table 4.1). The spreads in E_γ were obtained here in extreme conditions, i.e. between entrance and exit of the target active region. The relative spread obtained with this "extremal target model" indicates the required γ-ray energy resolution to observe effects in MC simulations

$$\min(\delta E_\gamma) = 1.89 \text{ keV at } \theta_\gamma = 172 \text{ deg} \tag{4.1}$$

In Fig. 4.4(c) and (d), the energy binning was 0.5 keV, lower than the required minimum resolution. Shifts between the two profiles (red and blue curves) can clearly be observed for the two simulated lifetimes: $\Delta E_\gamma \sim 3\times0.5$ keV with the lowest E_γ for T345. This can be understood since there is less beam energy losses with T345 than with T12, as a result the higher β at reaction the lower E_γ (for the backward angles detection). Overall, the EVASIONS simulations, presented in Fig. 4.4, agree well with the numerical estimations shown in Table 4.1. Observing differences due to the expected experimental profiles would require at least a sensitivity in γ-ray energy of <2 keV, that is to say lower than the instrumental one. The impact of the target depth profile has been studied with high statistics (>>5000 events). With the experimental statistics (<500 events), the impact of the target profile is totally negligible.

Experiment	$\frac{\delta\beta}{\beta}$ (%) after reaction	lifetime (fs) in target	$\frac{\delta\beta}{\beta}$ (%) at γ-ray emission	$\frac{\delta E_\gamma}{E_\gamma}$ (‰) at θ_γ=180 deg	θ_γ=172 deg
GANIL	0.286	1	0.389	0.28	0.28
		10	0.397	0.28	0.28
TRIUMF [52]	0.691	1	0.697	0.42	0.42
		10	0.712	0.42	0.42

Table 4.1: Numerical LISE++ estimations of the experimental effects induced by the target ^{3}He depth on the velocity β of the Ex=7.785 MeV state in ^{23}Mg* and on the associated Doppler shifted γ-rays, for lifetime $\tau \in \{1, 10\}$ fs. Present experiment and TRIUMF one [52] were considered. The differences δ are calculated between the target entrance and the ^{3}He maximum depth implantation: [0, 1000] Å (GANIL) and [0, 1500] Å (TRIUMF).

- Stopping power modification

Implantations of ^{3}He ions in gold should also affect stopping powers. Indeed, density is decreased by swelling [52]. The target composition (Table 3.2) is 1% of ^{3}He ions in 99% gold atoms. SRIM calculations were done to extract stopping powers $\frac{dE}{dx}$ with the two target compositions: pure gold and modified one by implanted ^{3}He ions. The relative differences in $\frac{dE}{dx}$ are (0.95%, 0.92%) for (^{24}Mg, ^{23}Mg) respectively.

- Conclusions

Simulations around the target ^{3}He depth profile have led to the following conclusions

1. Targets present two implantation profiles: targets 1-2 (homogeneous until 1000 Å) and targets 3-4-5 (peaked at 250 Å).
2. Comparisons of the two profiles by EVASIONS simulations and simple numerical calculations did not highlight any difference in the γ-ray spectrum at the limit of the instrumental intrinsic energy resolution of $\delta E_\gamma \sim 2$ keV.
3. Presence of ^{3}He ions in gold medium results in $\leq$1 % change in stopping powers.

4.3 Timeline of the simulation of the events

The simulation of the events is described in the following lines.

4.3.1 ^{23}Mg in target

- Beam propagation

The target was divided in spatial slices of width dx=5 Å. At each step, the energy losses of ^{24}Mg ions were locally derived, resulting in new energy $E_{^{24}Mg}(x+dx)$. Stopping powers $\frac{dE}{dx}_{^{24}Mg}$, with respect to the

nucleus energy, were taken from SRIM table [76]. An interpolation function was built in order to derive the precise $\frac{dE}{dx}_{^{24}Mg}$ value at $E_{^{24}Mg}(x)$. Using the ROOT physics library *TGenPhaseSpace* which is based on Raubold and Lynch method [109], a total of N=10000 ^{24}Mg(^{3}He, ^{4}He)^{23}Mg* reactions were generated with ^{24}Mg at the energy of $E_{^{24}Mg}(x+dx)$ and ^{3}He at rest directly populating the Ex state in ^{23}Mg*. The reaction calculations were done in center-of-mass frame then boosted to laboratory frame. The laboratory velocities and angles of recoil nucleus and ejectile were stored as respectively $(\beta,\theta,\phi)_{^{23}Mg}$ and $(\beta,\theta,\phi)_{^{4}He}$. For each event, a test of ejectile firing the VAMOS spectrometer was applied: VAMOS aperture was defined $\theta_{^{4}He} \leq$12 deg, due to the masking of higher angles by the SPIDER detector. If successful, then a new loop was started to simulate the propagation and decay of $N_{Ex}(t=0)$=50000 recoil nuclei initially at reaction $(\beta,\theta,\phi)_{^{23}Mg}$. In MC simulations, ideal statistics is often chosen as high as possible with respect to computing times.

- ^{23}Mg* propagation and decay

In this part of the EVASIONS code, a new loop on time was applied with a step of dt=0.1 fs. The energy losses of ^{23}Mg were locally derived after a distance of $\beta_{^{23}Mg}(t)\times$dt in gold. The reference $\frac{dE}{dx}_{^{23}Mg}$ were obtained from SRIM table [76] and the interpolation function was used to estimate $\frac{dE}{dx}_{^{23}Mg}$ at $\beta_{^{23}Mg}(t)$. The vacuum separation between target and beam catcher was taken into account. For the key state, all decays are expected inside the target, with a distance of $\leq$0.5 μm for $\tau \leq$10 fs. The amount of decaying states N* is governed by

$$\begin{aligned} N_{Ex}(t) &= N_{Ex}(0) \times e^{\frac{-t}{\tau}} \\ N^{*} &= N_{Ex}(t) - N_{Ex}(t+dt) \end{aligned} \tag{4.2}$$

This loop over time in target terminates either when $N_{Ex}(t) < 1$ or when the nuclei stop. In the latter case, the remaining $N_{Ex}(t)$ states deexcite at rest.

- Proton or γ-ray emissions

The direction of emission, either proton or γ-ray, was simulated isotropically through ROOT uniform random-generators of $\cos(\theta)\in[-1,1]$ and $\phi \in [0,360]$ deg. The two opened decay channels (γ-ray, proton) of the key state in ^{23}Mg* were studied. It was chosen to build two distinct EVASIONS codes: namely code A for γ-rays and code B for protons (Fig. 4.1). They differ from the considered emission.

Code A. If γ-ray fired AGATA aperture, i.e. [116, 172] deg, then simulations went to the instrument response function detailed in Sec.4.3.2, and the Doppler shift was derived at ($\beta_{^{23}Mg}$(t+dt), θ_{DS}) with Eq. (2.5).

Code B. The emitted proton underwent straggling along its path in gold. To reproduce this effect, MC simulations were done with SRIM [76] for a set of 60 initial proton conditions, at 5 MeV and different $\theta_p \in [0,30]$ deg, passing through the {target + beam catcher} foils. The two target thicknesses (1, 5) μm were simulated and the exit angular distributions were stored and analysed. An example is given in Fig. 4.5 for initial θ_p=16.4 deg. The left distribution associated with the thick target is observed 2.5$\times$ broader than the right distribution associated with the thin target. Red curves show Gaussian fits. Random functions were preferred to model the proton straggling: the exit angle "new θ_p", observable by SPIDER detector, was randomly drawn from the SRIM distributions of proton straggling in gold. If θ_p was within SPIDER aperture, i.e. [12.8, 24.6] deg, then the associated proton energy E_p was derived. Energy losses of protons were determined as previously discussed. The output variables (E_p, θ_p) were transformed with the SPIDER response function to reproduce observable signals.

The effect of the time dilatation due to the relativistic velocities of the ions was small, i.e. $\leq$ 0.2 %.

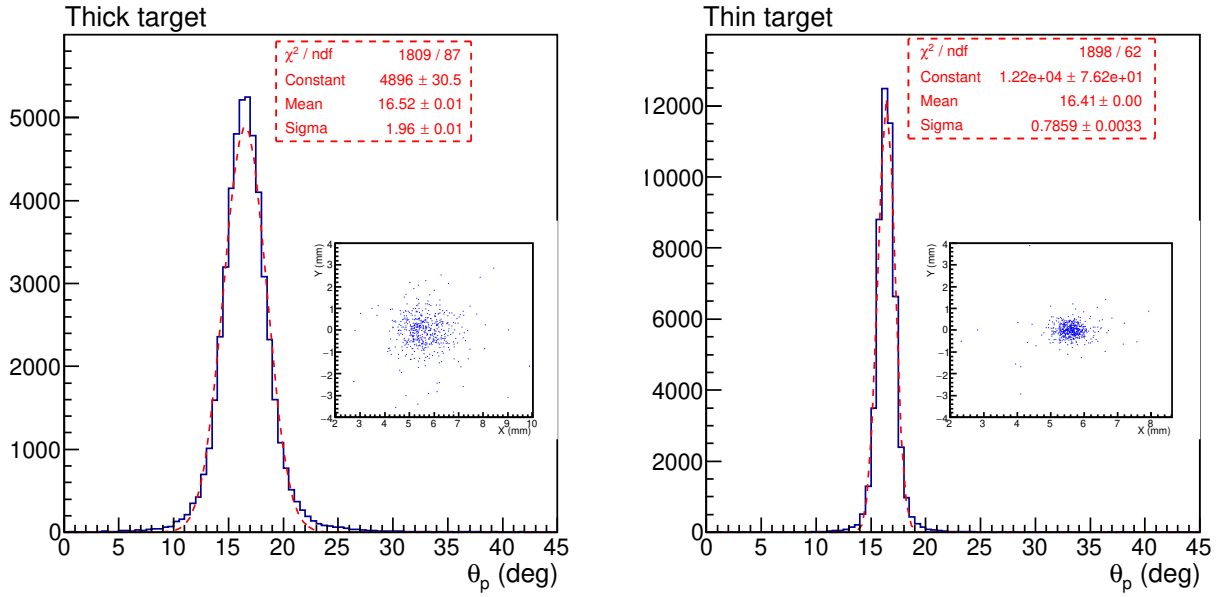

Figure 4.5: Laboratory angular distributions of protons exiting gold {target + 20 μm thick beam catcher} foils from MC simulations with SRIM code [76], the entrance parameters are (θ_p=16.4 deg, E_p=5 MeV). Gaussian fits are shown in red, and (X, Y) projections are given in the insets. Left side: 5 μm thick target, right side: 1 μm thin target.

The code also included the propagation of ^{4}He ejectiles to VAMOS, with the same calculation processes for energy losses in gold.

EVASIONS takes a reasonable time of less than one hour to simulate the experiment. It can be easily adapted to other conditions.

4.3.2 Instrument response function

Any detector induces a signal degradation mainly because of electronic noises and fluctuations in the amount of ionizations/excitations due to their random nature. The relation between entrance energies, here (E_γ, E_p=ΔE+E_{res}), and generated detector pulses is the instrument response function. Ideally, one wants to observe Dirac peak δ(E) at each energy but real peaks are usually Gaussian. The instrument response functions of SPIDER and AGATA in the EVASIONS code involved three main aspects:

1. the geometric acceptance
2. the signal resolution
3. the background noise distribution.

The geometrical acceptances of each detector were described in Chapter 3. Effects of instrument resolutions were obtained with ROOT random generators. In case of energies (E_γ, ΔE, E_{res}), it was governed by the Gaussian law:

$$\frac{1}{\sigma\sqrt{2\pi}} e^{\frac{-(E-E^{expected})^2}{2\sigma}} \tag{4.3}$$

with $\sigma = \frac{FWHM}{2.35}$ and FWHM experimentally derived . The input σ_{E_γ} came from the measured resolution of rest γ-rays which were close in energy to the γ-rays of interest, see Sec.3.3.2. The input proton energy

resolutions corresponded to the measured resolutions with the triple-α source, for each ΔE strip and E_{res} in the 2^{nd} ring, see Sec.3.3.3. Angle θ_γ also followed a Gaussian distribution from the AGATA tracking resolution which resulted in σ_{θ_γ} equal to 0.667(1) deg. In case of SPIDER, θ_p was simulated uniformly along the fired strip width (Table 3.5, Fig. 3.22). An additional calculation was done in the EVASIONS **Code B** to simulate the deposited energies (ΔE, E_{res}) in respectively SPIDER (1^{st}, 2^{nd}) rings, from the entrance E_p. The table of proton stopping powers in silicon (Ref. [76]) was used.

Background noise distribution was added to the spectra. This differed between the two EVASIONS codes. The inclusion of noise required to define a SNR parameter which was then forced to reproduce experimental SNR. This approach, similar to [52], added uncertainties on the measurement of lifetimes.
Code A. A measured noise matrix (E_γ, θ_γ) close to the aimed γ-ray window was used as a random generator function. A high statistics (>>1000) background noise matrix was generated at the γ-ray window, including as a bonus the AGATA geometry efficiency.
Code B. In the absence of beam, no noise is expected. Fusion evaporation reactions were the main sources of noise in this experiment. Simulations of the compound nuclei from ^{24}Mg reactions with ^{12}C or ^{16}O, followed by uniform emissions of light particles in the center of mass, present many possible proton decay channels. By reducing to only the nuclei mainly produced, ^{30,31}P from LISE++, the simulated background noise did not reproduce enough the measured noise from the pure gold target. Hence, a background noise subtraction was finally preferred, explained in Sec.6.3. A simple noise simulation is illustrated in this Chapter: this was generated as uniformly distributed events in SPIDER matrix (E_{res}, ΔE). They induced a continuous level in the reconstructed spectrum in Ex contrary to "good events" resulting in peaks at the states excitation energies.

As described along the section, the EVASIONS code included:

1. the instrument response function from measured data,
2. background noise reproducing the observed noise distribution.

4.4 Code results

4.4.1 Outputs

The useful observables for analysing experimental data were stored at the end of each completed step in a ROOT Tree. These variables were:

- E_γ, θ_γ, θ_{DS}, $\beta_{^{23}Mg}$ at emission (**Code A**)
- ΔE, E_{res}, θ_p (**Code B**).

Some additional outputs useful in the analysis were stored like the ejectile energies in VAMOS ($E_{^4He}$).

Fig. 4.6 shows results of EVASIONS **Code A** in case of the (Ex=7.785 MeV, $E_{\gamma,0}$=7.333 MeV) populated state in ^{23}Mg*. The simulated matrix (E_γ, θ_γ) in Fig. 4.6(a) was obtained with a lifetime of τ=1 fs. Simulations at three different τ (1 fs $\Leftrightarrow$ green curves, 6 fs $\Leftrightarrow$ red curves, 12 fs $\Leftrightarrow$ blue curves) were computed to extract both projected γ-ray energy spectra after selection on high $\theta_\gamma \in [150, 160]$ deg (Fig. 4.6(b)), and velocity at emission distributions (Fig. 4.6(c)). It is important to note here that the velocity distribution seems more sensitive to lifetime than the γ-ray spectrum.

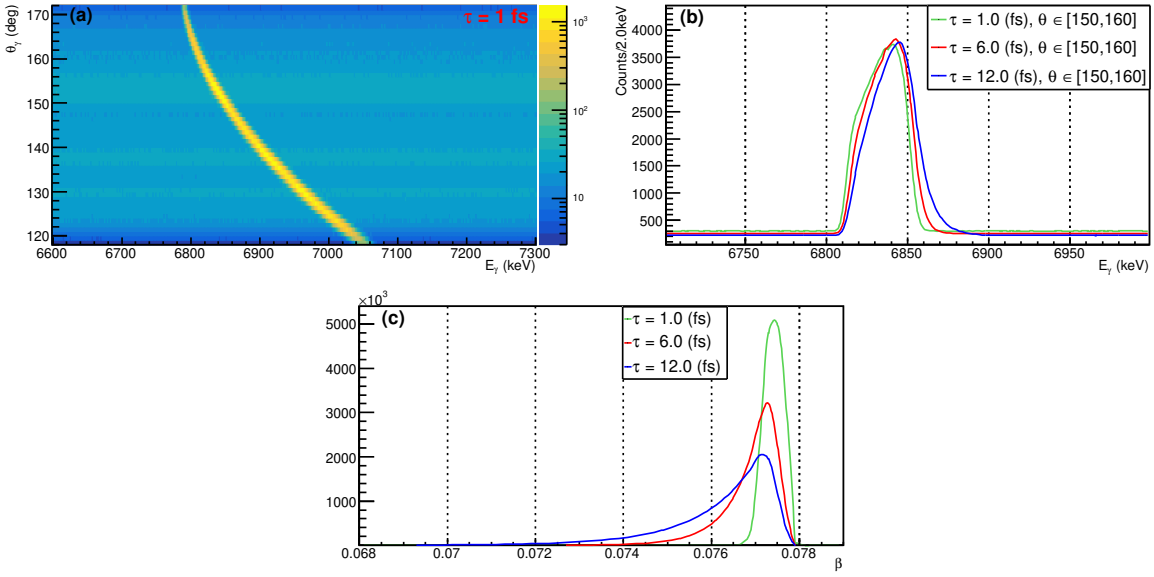

Figure 4.6: Monte Carlo simulation results of γ-ray emissions from the (Ex=7.785 MeV, $E_{\gamma,0}$=7.333 MeV) state in ^{23}Mg*, with the EVASIONS **Code A**. Panel (a): observable Doppler shifted matrix (E_γ, θ_γ) from AGATA view, with a lifetime of 1 fs. Panel (b): projections on γ-ray energies after the angular selection of $\theta_\gamma \in [150, 160]$ deg. Panel (c): velocity β distributions at γ-ray emissions. Three different simulations were done with τ=1 fs (green curves), τ=6 fs (red curves) and τ=12 fs (blue curves) in panels (b, c).

Results of EVASIONS **Code B** are presented in Fig. 4.7 for proton decays from the Ex=7.785 MeV state of interest with τ=10 fs. The SPIDER energy matrix (E_{res}, ΔE) is given in Fig. 4.7(a). These protons are stopped in the 1st ring. In Fig. 4.7(b), the simulated energy of these protons is plotted upon the angle. A kinematic line is clearly visible. The reconstructed excitation spectrum is presented in Fig. 4.7(c). The centroid of the peak, pointed by the red arrow, is Ex^{SPIDER}=7.78(4) MeV as expected. The reconstruction method was then found to work properly. Simulations were also done with τ=1 fs, the resulting proton kinematics and Ex^{SPIDER} spectrum were observed similar to those in Fig. 4.7. For our experimental conditions with an important proton straggling expected, the emitted protons distribution was not shown to be sensitive to a lifetime of few fs.

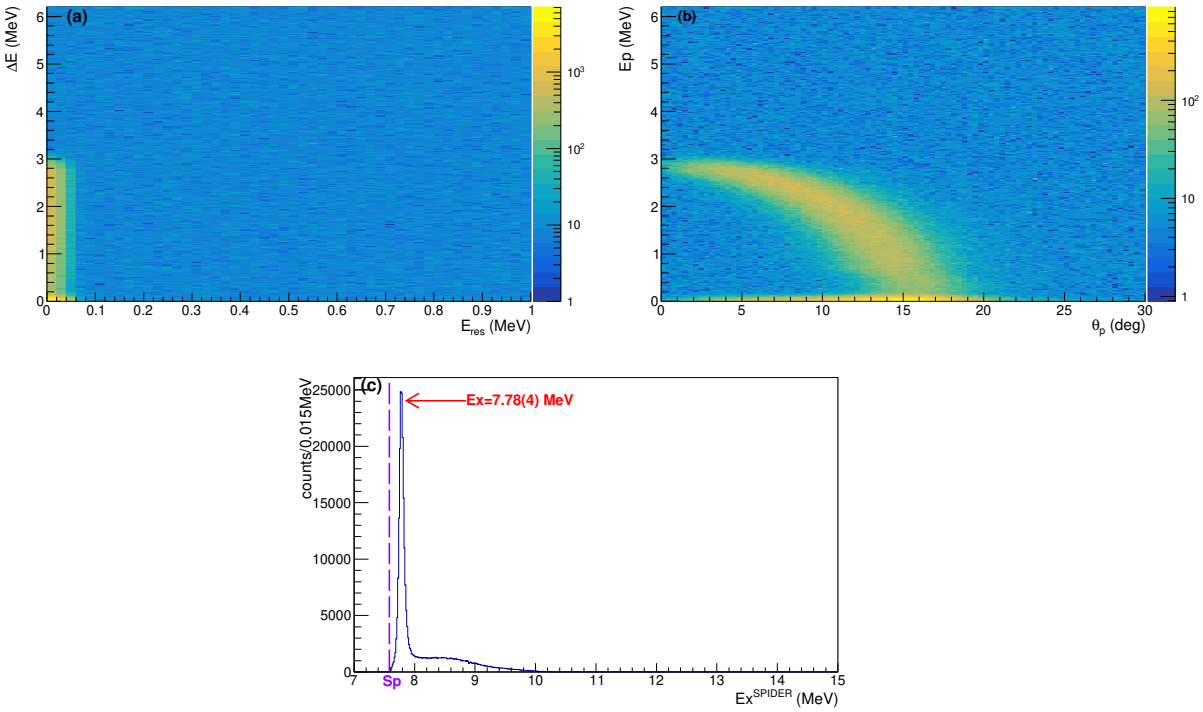

Figure 4.7: Monte Carlo simulation results of emitted protons from the state in ^{23}Mg* above threshold (Ex=7.785 MeV, S_p =7.581 MeV, τ=10 fs) with EVASIONS **Code B**. Panel (a): observable SPIDER (E_{res}, ΔE) matrix. Panel (b): reconstructed kinematics (θ_p, E_p). Panel (c): extracted excitation histogram in Ex^{SPIDER} from kinematics, the found peak centroid is marked with the red arrow (Ex=7.78(4) MeV). The purple vertical line indicates the proton threshold of ^{23}Mg.

The preliminary conclusions from the experiment simulations were:

1. the sensitivity to ∼fs for the lifetime of the key state in ^{23}Mg* is reachable with high statistics,
2. decaying protons from this state are not expected to pass through the SPIDER 1st ΔE ring.

4.4.2 Validation on experimental data

Monte Carlo simulations based on the EVASIONS code were tested with the lifetime measurement of an easy known case. Reactions between beam and chamber contaminants (^{12}C, ^{16}O) provided such case: the (Ex=6.879(1) MeV, $E_{\gamma,0}$=6.877(2) MeV)[55] long-lived state in ^{28}Si*. Its main γ-ray line, observed mainly unshifted in the high energy region of interest, was observed with ∼450 counts and SNR∼10 (black points, Fig. 4.8(c)). This spectrum was obtained after the irradiation of a thick 5 μm gold target without ^{3}He, ensuring so an unambiguous lineshape analysis without γ-ray contributions from ^{23}Mg*. The simulated reactions were fusion-evaporations ^{24}Mg+^{12}C $\Rightarrow 2\alpha + {}^{28}$Si* and ^{24}Mg+^{16}O $\Rightarrow 3\alpha + {}^{28}$Si* as measured in [52]. Lifetime published in literature is $\tau = 2.7^{+0.8}_{-0.7}$ ps[55]. The simulated γ-ray matrix as observed by AGATA is given in Fig. 4.8(a) with chosen τ=2.5 ps. The experimental γ-ray matrix in Fig. 4.8(b) shows a good agreement with the simulated result. After a selection on the full angle aperture ($\theta_\gamma \in [120, 170]$ deg), the experimental black data - projected on E_γ, were compared with simulated ones for three lifetimes in Fig. 4.8(c). The normalization of simulated spectra to the experimental data was done on the counts integral along the energy range $E_\gamma \in [6.81, 6.91]$ MeV, with the same SNR which best reproduced the observed SNR. The values of χ^2 were calculated bin to bin between the experimental spectrum and simulated ones by using the ROOT library, in the energy range $E_\gamma \in [6.84, 6.90]$ MeV. The

input τ=2.0 ps shown with the red curve is associated with the smallest χ^2. The complete χ^2 analysis resulted in a measured lifetime τ=2.0(4) ps at CL=90 %. The confidence region was determined as described in Sec.39 of Ref. [110].

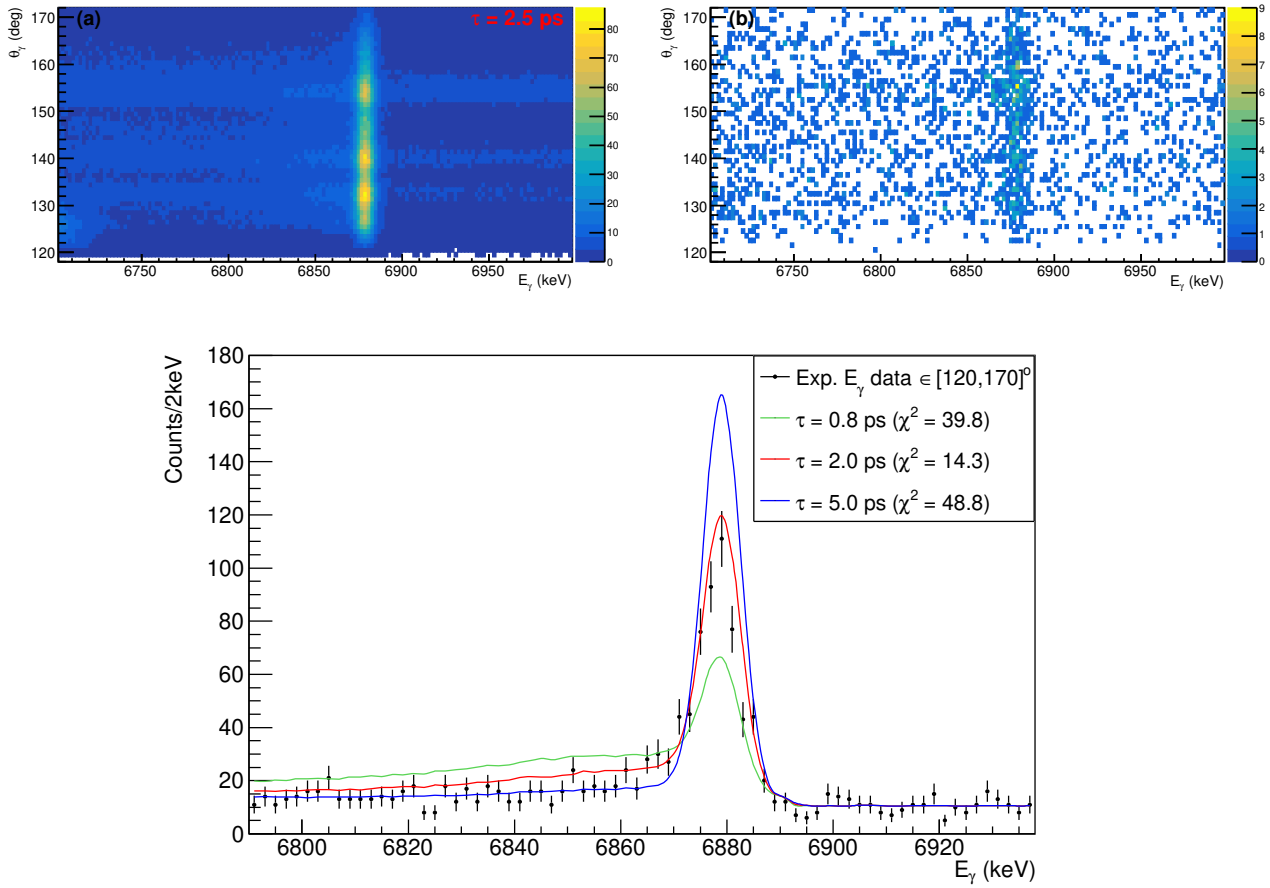

Figure 4.8: Comparison results in γ-ray analysis to extract the lifetime of the known (Ex=6.879 MeV, $E_{\gamma,0}$=6.877 MeV) state in ^{28}Si*. Panel (a): MC simulated γ-ray matrix (E_γ, θ_γ) from EVASIONS **Code A** adapted to fusion-evaporations reactions populating ^{28}Si* (^{24}Mg + ^{12}C/^{16}O). Panel (b): measured matrix (E_γ, θ_γ) from beam irradiation of a thick pure gold target, no Doppler correction applied here. Panel (c): projections on γ-ray energies after angular selection ($\theta_\gamma \in [120, 160]$ deg) of the experimental matrix (black points) in (b) and three simulated matrices with τ=0.8 ps (green curve), τ=2.0 ps (red curve) and τ=5.0 ps (blue curve). The normalization of simulated spectra to the experimental distribution was done on the spectrum integrals (along energy) with the same SNR for each simulation. The mentioned χ^2 were derived bin to bin with the ROOT library.

The obtained value for the lifetime of the Ex=6.878 MeV state in ^{28}Si* is in good agreement with literature. EVASIONS code was thus validated for this relatively long-lived state.

4.5 Conclusion

A new code of Monte Carlo simulation, EVASIONS, was written in order to include VAMOS, AGATA and SPIDER. It has been successfully tested with a first lifetime measurement of a state in ^{28}Si nucleus. The Monte Carlo tool helped at quantifying the impacts on the measurement of different experimental

uncertainties, as developed latter on. How could the raw signals be converted to physics parameters? The next Chapter will explain the reconstructions.

CHAPTER 5

The events reconstruction

5.1 Introduction

The experimental set-up described in Chapter 3 included detectors to measure the energies and angles of γ-rays and particles coming from the ^{3}He(^{24}Mg,^{4}He)^{23}Mg* reactions. In particular, the parameters (Bρ, T_{PL}, Q_{PL}, $\theta^{VAMOS}_{^{4}He}$, $\phi^{VAMOS}_{^{4}He}$) were obtained in VAMOS, ($\theta^{DCT}_{^{4}He}$, $\phi^{DCT}_{^{4}He}$) in the small gas chamber, (ΔE+E_{res}, θ_{p}) in SPIDER and (E_{γ}, θ_{γ}) in AGATA. In this Chapter, we will see how these measured parameters were used to reconstruct the physical parameters of interest in order to fully characterize the populated states in ^{23}Mg*. These physical parameters are: the ejectile masses and kinetic energy, the kinetic energy and angles of the recoil nuclei, the state excitation energy, the differential cross sections, the velocity at emission, the Doppler angle between the emitter and the γ-ray, the rest energies and intensities of γ-ray transitions. The present Chapter is dedicated to this reconstruction analysis.

The Monte Carlo EVASIONS code, presented in Chapter 4, was also used to determine the physical parameters from the observable ones. Simulations were compared with the experimental data, in order to cross check the reconstruction methods. For instance, these approaches were applied to the measured and simulated datasets in order to determine Ex from protons, β-at-emission from γ-rays.

This Chapter presents different aspects of the reconstruction analysis. First, the ejectiles masses are derived along Sec.5.2.1. Next, the ^{4}He ejectiles are identified among ^{4}He ions from fusion-evaporations reactions in Sec.5.2.2. From the measured ejectile energy and angles, the kinetic energy and angles of the ^{23}Mg recoil nuclei are derived in Sec.5.2.3. Then, the γ-ray emissions from the states in ^{23}Mg* are characterized in Sec.5.3.1. The Doppler angle is reconstructed as explained in Sec.5.3.2. Final steps are the reconstructions of the key physical parameters of the emitter states, that is to say the excitation energy Ex in Sec5.4.1, the differential cross sections in Sec.5.4.2, and the velocity β-at-emission in Sec.5.4.3.

5.2 Two-body reactions populating states in ^{23}Mg*

5.2.1 Ejectiles masses

After the beam catcher, only the light ejectiles from the reactions of transfer, fusion-evaporation and dissociation on gold were expected. The identified nuclei with SPIDER were protons, ^{2}H, ^{3}He, ^{4}He, the dominant ones being protons and ^{4}He. All these nuclei were also measured in VAMOS. Hence, the ^{4}He ejectiles of interest had to be identified among Z=2 nuclei.

First, the time-of-flight t* from target to PL+PM was obtained by combining Eq. (3.2) and (3.3),

$$t^* = \text{constant} - T_{PL} \tag{5.1}$$

The required offset constant, defined by Delay − $T_{CSS1\rightarrow Target}$ (Sec.3.3.1), was estimated with LISE++ assuming the most abundant particles were ^{4}He. The resulting time of flight t* as a function of Bρ is shown in Fig. 5.1(b). In Fig. 5.1(c), right Q_{PL} is plotted upon Bρ. The selection on Z=1 (respectively Z=2) in Fig. 5.1(a), are associated to the black (red) outlined regions in (b, c). Most of Z=1 particles had Bρ=0: their Bρ were not reconstructed. Thus, the VAMOS Bρ efficiency of Z=1 particles was found to be nearly 0. Indeed, they generated electrical signals below the drift chamber thresholds. It was not certain that Bρ was well reconstructed for the few Z=1 events shown in the black circles. If Bρ is assumed reliable, then t* matches the one of ^{4}He with equal Bρ but a higher Q_{PL}. An equal Bρ implies:

$$\begin{aligned} B\rho^{^4He} \sim B\rho^{p} \rightarrow t^{p} \sim \frac{t^{^4He}}{2} \\ B\rho^{^4He} \sim B\rho^{^2H} \rightarrow t^{^2H} \sim t^{^4He} \end{aligned} \tag{5.2}$$

According to Eq. 5.2, the few Z=1 events in black circles were identified as deuteron, if Bρ was properly reconstructed.

Some events with wrong t* are seen in the dashed black circle of Fig. 5.1(b): for low Bρ and low t*. They might be pile-up events (multiplicity ≥2) or they might have incomplete Q collections. Thus, either their Bρ were not well reconstructed since DC worked for events of multiplicity 1, or their t* were not properly calibrated due to the wrong Q_{PL}. Indeed, the correction and the calibration of T_{PL} into t* were based on Q_{PL}, see Sec.3.3.1. Only the events of the Z=2 region with well reconstructed (Bρ, t*) were selected.

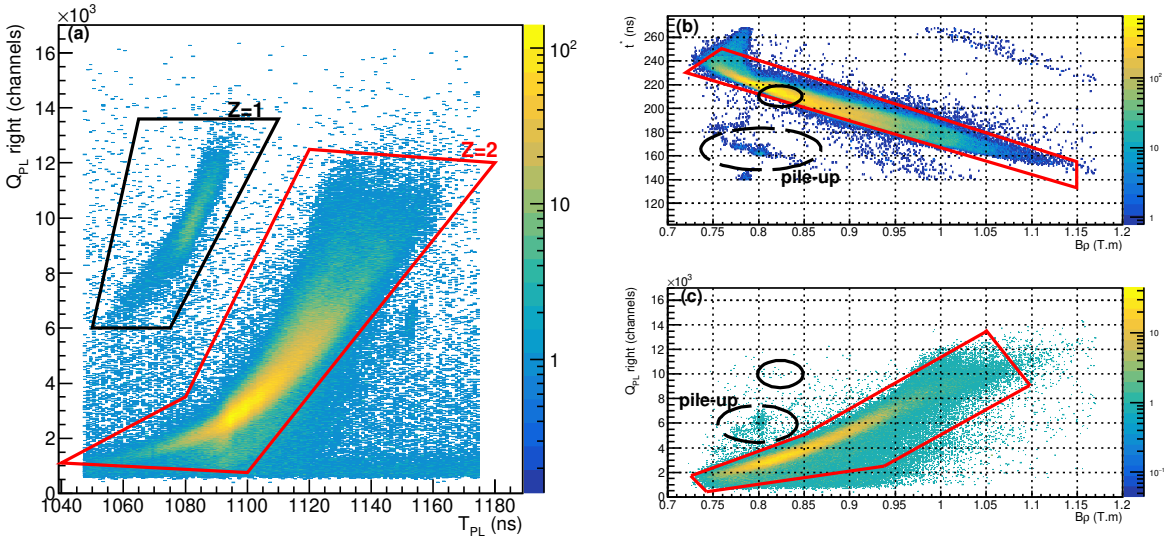

Figure 5.1: Panel (a): right Q_{PL} as a function of T_{PL}. Panel (b): time-of-flight t* versus Bρ, the time-of-flight calibrated by assuming ^{4}He. The anti-linear region, red outlined, is associated to a constant $\frac{m}{q}$. Panel (c): right Q_{PL} upon Bρ. The red outlined regions correspond to selection on the Z=2 nuclei shown in (a), the black ones to selection on the Z=1 nuclei. Possible pile-up events are noticed within the black dashed circles in (b, c).

Second, the mass over charge ratio ($\frac{m}{q}$) was derived from particle L, t* and Bρ, as explained in the VAMOS algorithm Fig. 3.7. This $\frac{m}{q}$ ratio is plotted in Fig. 5.2. The red histogram was conditioned by Z=2, B$\rho > 0$ and well reconstructed (Bρ, t*). These events with $\frac{m}{q} = 2(0.2)$ had so a mass of 4, corresponding to the ^{4}He ejectiles. The few reconstructed events selected on (B$\rho > 0$, Z=1) are associated with the black histogram with $\frac{m}{q} = 2.2(2)$. This agrees with the previous identification as deuteron.

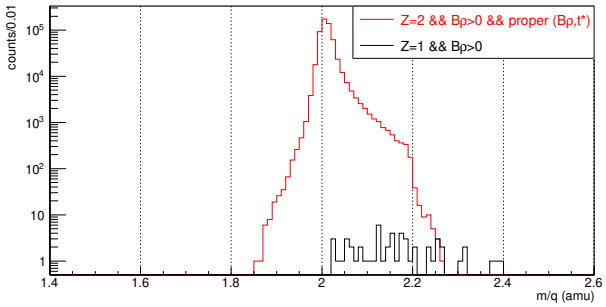

Figure 5.2: Mass over charge ratio $\frac{m}{q}$ of the reconstructed events in B$\rho > 0$. Black histogram was gated on the Z=1 selection in Fig. 5.1(a), red histogram on Z=2 and proper (Bρ, t*) in Fig. 5.1(b).

In conclusion, the reconstruction of $\frac{m}{q}$ by combining selections on Z, on Bρ and on t*, had led to the mass identification of the ^{4}He ejectiles.

5.2.2 Energy of ^{4}He ejectiles

The mass and charge reconstructions of the ejectiles in VAMOS were not enough to identify the two-body reactions populating the states in ^{23}Mg*. Fusion-evaporations reactions with the contaminants, present in the target and the chamber, also produced ^{4}He particles. Such fusion-evaporations reactions produce particles with a continuum of energies and angles overlapping. Moreover, they usually generate more than one ejectile per reaction.

The correlations between the ejectile energies and the excited states in ^{23}Mg*, directly populated by the reactions ^{3}He(^{24}Mg,^{4}He)^{23}Mg*, were identified by looking at the ^{4}He kinetic energy $E^{VAMOS}_{^4He}$ as a function of the γ-ray Doppler corrected energy E^{DC}_{γ}. The latter was calculated with a mean velocity β which was estimated with the EVASIONS code. On the top left side of Fig. 5.3, such matrix ($E^{VAMOS}_{^4He}$, E^{DC}_{γ}) is shown in the γ-ray energy region of [4200, 4500] keV. The top right side of Fig. 5.3 presents the simulated matrix with EVASIONS for the reaction ^{3}He(^{24}Mg,^{4}He)^{23}Mg* at (Ex=4.356 MeV, $E_{\gamma,0}$=4.356 MeV) and fortuitous coincidences between ^{4}He from fusion-evaporations reactions, ^{12}C(^{24}Mg,3$\times^4$He)^{28}Si* and ^{16}O(^{24}Mg,4$\times^4$He)^{28}Si*, and γ-rays which were drawn in the energy range according to the AGATA energy efficiency. These coincidences represent the apparent background noise. The black circles show the direct populations of ^{23}Mg* coinciding with γ-ray transitions. The measured ^{4}He contaminants can be observed broadly distributed in [25, 45] MeV.

The kinetic energies of ^{4}He ejectiles, associated with two-body direct populations, had been measured through the method illustrated in Fig. 5.3. On the whole, 22 states have been identified, see the bottom matrix of Fig. 5.3. The results are given in Table 5.1. The reconstructed $E^{VAMOS}_{^4He}$ are compared with the simulated ones. Experimental values are clearly in good agreement with simulations. Estimations of ^{4}He kinetic energies at the VAMOS entrance were also done with LISE++, they agreed with the experimental results.

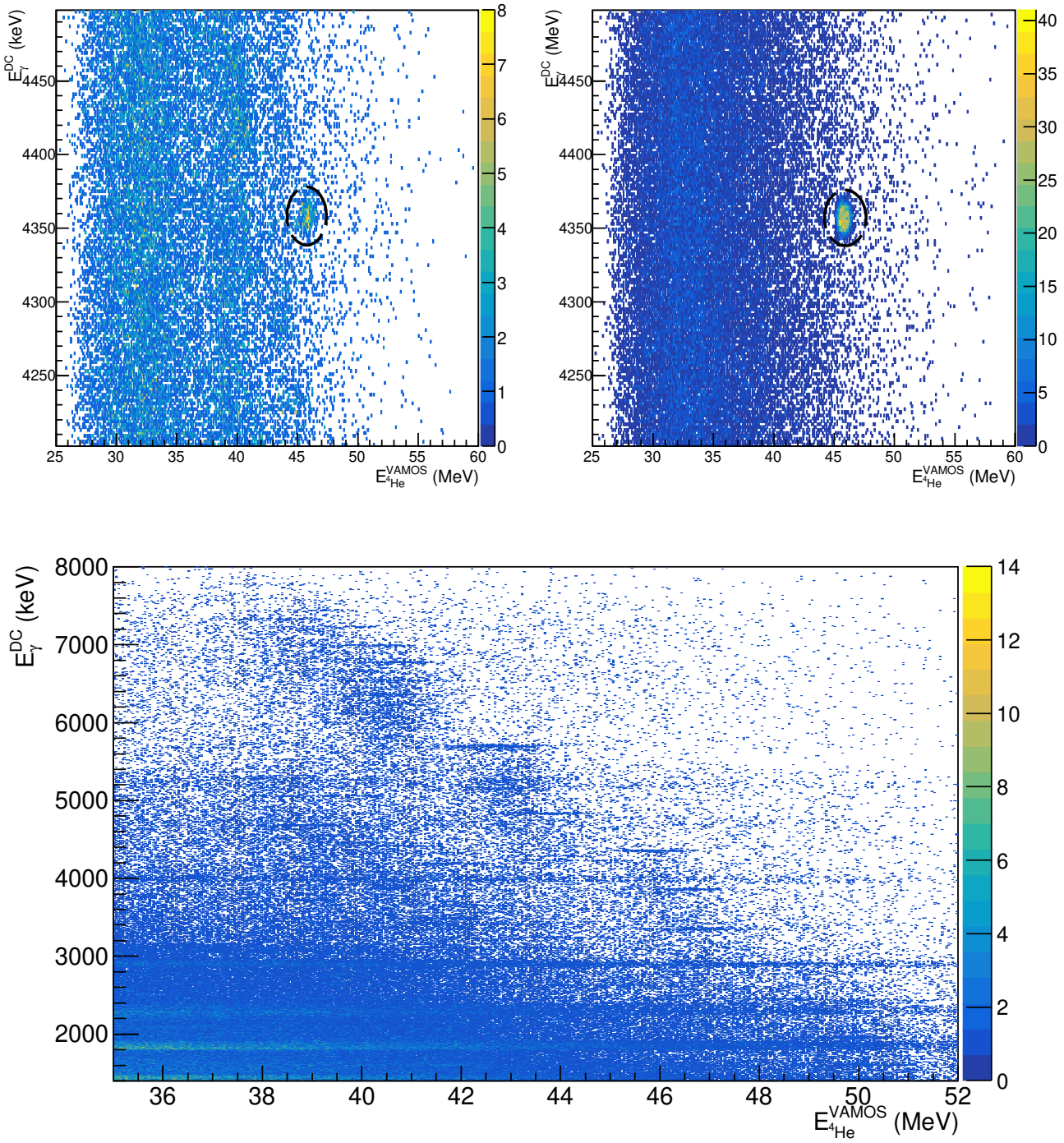

Figure 5.3: Top left: measured $E_{^4He}^{VAMOS}$ in coincidence with γ-ray Doppler corrected energy $E_\gamma^{DC}\in$[4200,4500] keV. Top right: simulated matrix ($E_{^4He}^{VAMOS}$, E_γ^{DC}) by EVASIONS. The dashed black circles surround the coincidences events in γ-rays and ^{4}He ejectiles associated with the two-body reactions populating directly the (Ex=4.356 MeV, $E_{\gamma,0}$=4.356 MeV) state in ^{23}Mg*. These events differ from the apparent background noise: the wide ^{4}He energy distribution of fusion-evaporations reactions with ^{12}C/^{16}O contaminants in fortuitous coincidences with γ-rays, see details in text. Measured $E_{^4He}^{VAMOS}\in$[45.0, 46.6] MeV for the populated state, agree with simulated $E_{^4He}^{VAMOS}\in$[44.8, 46.6] MeV. Bottom: the experimental matrix ($E_{^4He}^{VAMOS}$, E_γ^{DC}) is presented on its full size.

^{23}Mg	$E^{VAMOS}_{^4He}$ (MeV)		^{23}Mg	$E^{VAMOS}_{^4He}$ (MeV)	
(Ex, $E_{\gamma,0}$) MeV	Experiment	Simulations	(Ex, $E_{\gamma,0}$) MeV	Experiment	Simulations
(0.451, 0.451)	[51.3, 54.2]	[52.4, 54.1]	(6.240, 4.188)	[40.7, 42.5]	[41.3, 42.7]
(2.052, 1.601)	[49.5, 51.0]	[49.3, 51.1]	(6.775, 4.418)	[39.8, 41.4]	[40.1, 41.6]
(2.906, 2.455)	[47.4, 49.4]	[47.8, 49.5]	(6.908, 6.900)	[40.0, 41.0]	[40.0, 41.4]
(3.794, 3.344)	[45.5, 47.4]	[46.2, 47.6]	(6.984, 6.984)	[39.4, 41.1]	[39.9, 41.2]
(3.861, 3.861)	[45.9, 47.4]	[46.2, 47.4]	(7.112, 6.660)	[39.6, 40.6]	[39.5, 40.8]
(4.356, 4.356)	[45.0, 46.7]	[45.0, 46.6]	(7.450, 7.443)	[38.1, 39.9]	[38.8, 40.2]
(4.681, 4.230)	[44.6, 45.5]	[44.5, 45.8]	(7.584, 3.725)	[38.4, 39.8]	[38.5, 39.9]
(5.287, 3.236)	[43.3, 44.5]	[43.3, 44.7]	(7.770, 5.054)	[37.8, 39.0]	[38.1, 39.5]
(5.691, 5.690)	[42.0,43.5]	[42.4, 43.8]	(7.782, 5.067)	[37.5, 38.9]	[38.1, 39.5]
(6.132, 3.775)	[41.6, 42.4]	[41.5, 43.0]	(7.785, 7.333)	[37.5, 39.5]	[38.1, 39.5]
(6.195, 3.480)	[41.3, 42.6]	[41.3, 42.9]	(7.803, 7.801)	[37.3, 39.0]	[38.0, 39.4]

Table 5.1: Summary of the measured ejectile energies with VAMOS, $E^{VAMOS}_{^4He}$, associated with the observed γ-ray transitions at $E_{\gamma,0}$ from the directly populated Ex states in ^{23}Mg*. Data for ($E_{\gamma,0}$, Ex) taken from [55]. The $E^{VAMOS}_{^4He}$ are compared to the expected ones from the EVASIONS code.

To conclude, coincidences between ejectile energies and γ-ray transitions allowed us to extract the two-body reactions populating ^{23}Mg* states among the contaminant fusion-evaporations reactions. Agreements with simulations strengthened these identifications.

5.2.3 Energy and angles of ^{23}Mg recoil nuclei

- Energy

The kinematics of ^{23}Mg recoil nucleus was reconstructed from the measured energy and angles of ^{4}He ejectiles. The calculations are detailed in Annexes A.1.1. The kinetic energy $E_{^{23}Mg}$ was derived from

$$E_{^{23}Mg} = E^0_{^{23}Mg} \times \left(\sqrt{1 + \frac{1}{{E^0_{^{23}Mg}}^2} \times ({E^0_{^4He}}^2 \times (\gamma^2_{^4He} - 1) + {E^0_{^{24}Mg}}^2 \times (\gamma^2_{^{24}Mg} - 1) - 2 \times \cos(\theta_{^4He}) E^0_{^{24}Mg} E^0_{^4He} \times \sqrt{\gamma^2_{^4He} - 1}\sqrt{\gamma^2_{^{24}Mg} - 1})} - 1\right) \tag{5.3}$$

with $\gamma = \frac{E}{E^0} + 1$ where E is the kinetic energy and E^0 the rest mass energy. Angles were obtained with:

$$\begin{aligned} \theta_{^{23}Mg} &= \text{acos}\left(\frac{|P_{^{24}Mg}| - |P_{^4He}| \times \cos(\theta_{^4He})}{|P_{^{23}Mg}|}\right) \\ \phi_{^{23}Mg} &= \pi + \phi_{^4He} \end{aligned} \tag{5.4}$$

with the norm of impulsion vector given by $|P| = \frac{1}{c}\sqrt{E^2 + 2E^0E}$.

In Eq. (5.3) and (5.4), the ejectile energy $E_{^4He}$ is for the reaction position. The measured $E^{VAMOS}_{^4He}$ was after {target + beam catcher}. Hence energy losses have to be corrected. Using the EVASIONS code, energy losses were calculated as a function of $E^{VAMOS}_{^4He}$, shown in Fig. 5.4. Blue points are associated to the thick target and black points to the thin one. A polynomial fit of 2nd order was applied to extract a relation between $E^{VAMOS}_{^4He}$ and energy losses. In fine, from measured $E^{VAMOS}_{^4He}$, energy losses were estimated with Eq. (5.5) and added to reconstruct $E_{^4He}$ at reaction.

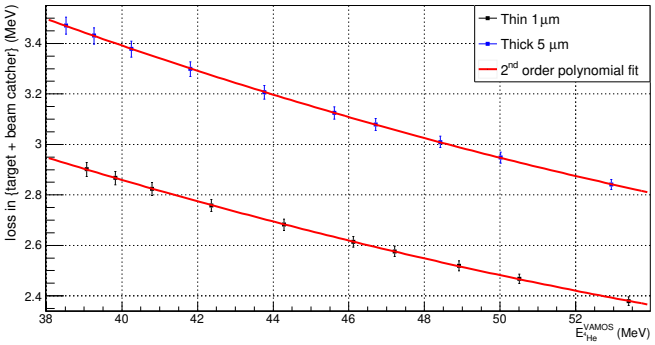

Figure 5.4: Simulated energy losses in the set {target + beam catcher} of the ^{4}He ejectiles upon the energies expected in VAMOS, obtained with the EVASIONS code. Black points correspond to a thin target and blue points to a thick target, results of 2nd order polynomial fits (red curves) in Eq. (5.5).

$$\begin{aligned} \text{loss} &= 5.52 - 8.98 \times 10^{-2} \times \mathrm{E}_{^4\mathrm{He}}^{\mathrm{VAMOS}} + 5.78 \times 10^{-4} \times \mathrm{E}_{^4\mathrm{He}}^{\mathrm{VAMOS}^2} && \text{Thin target} \\ \text{loss} &= 6.55 - 1.06 \times 10^{-2} \times \mathrm{E}_{^4\mathrm{He}}^{\mathrm{VAMOS}} - 6.89 \times 10^{-4} \times \mathrm{E}_{^4\mathrm{He}}^{\mathrm{VAMOS}^2} && \text{Thick target} \end{aligned} \tag{5.5}$$

- Angles

The ejectile angles ($\theta_{^4\mathrm{He}}$, $\phi_{^4\mathrm{He}}$) were measured both in VAMOS and in the small gas chamber. They are compared in Fig. 5.5(a) and (b) for respectively $\theta_{^4\mathrm{He}}$ and $\phi_{^4\mathrm{He}}$. The absolute differences are also given in Fig. 5.5(c) and (d). Differences of <3 deg in $\theta_{^4\mathrm{He}}$ were found for 80 % of events, and differences of <30 deg in $\phi_{^4\mathrm{He}}$ for 75 % of events. The ejectile angles $\theta_{^4\mathrm{He}}$ and $\phi_{^4\mathrm{He}}$ were taken as the mean value of ($\theta_{^4\mathrm{He}}^{\mathrm{VAMOS}}$, $\theta_{^4\mathrm{He}}^{\mathrm{DCT}}$) and ($\phi_{^4\mathrm{He}}^{\mathrm{VAMOS}}$, $\phi_{^4\mathrm{He}}^{\mathrm{DCT}}$), if the differences were <3 deg and <30 deg. If differences were higher, they were chosen to be ($\theta_{^4\mathrm{He}}^{\mathrm{DCT}}$, $\phi_{^4\mathrm{He}}^{\mathrm{DCT}}$), since the VAMOS reconstruction of ϕ was expected less reliable than the measurement with DCTs.

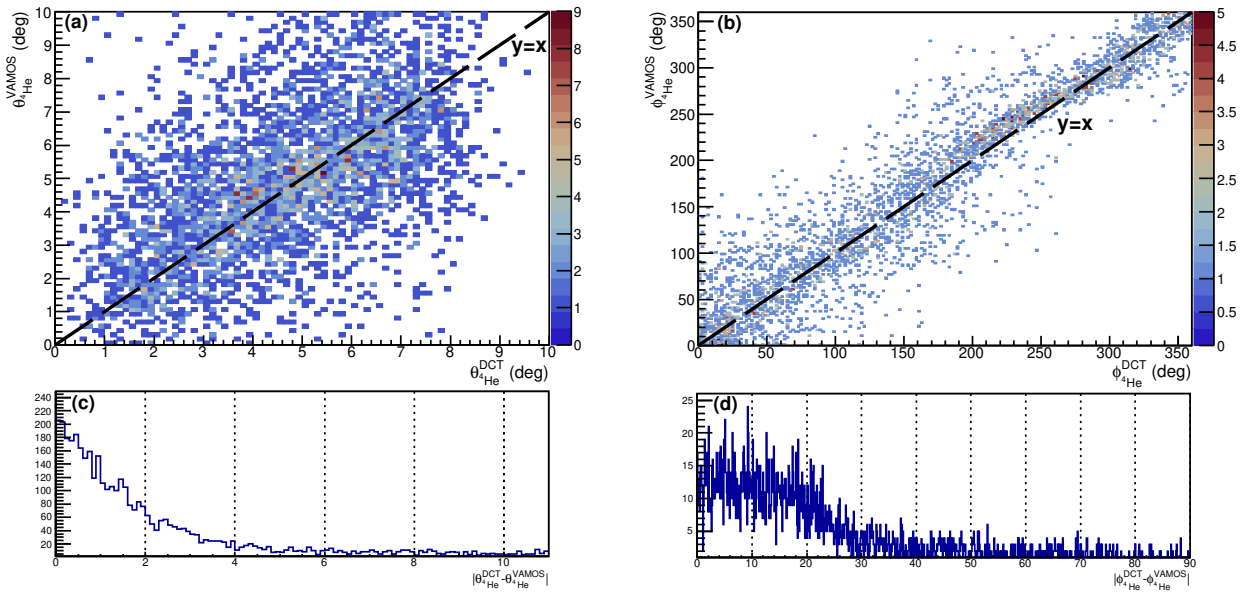

Figure 5.5: Panel (a): evolution of the ^{4}He ejectile angle $\theta^{VAMOS}_{^4He}$, from VAMOS, versus $\theta^{DCT}_{^4He}$ which is averaged from measurements in DCTs of the small gas chamber. Panel (b): $\phi^{VAMOS}_{^4He}$ versus $\phi^{DCT}_{^4He}$. The dotted black lines show the y=x function. The absolute differences between measured angles are given in panel (c) for $|\theta^{DCT}_{^4He}$-$\theta^{VAMOS}_{^4He}|$, and in (d) for $|\phi^{DCT}_{^4He}$-$\phi^{VAMOS}_{^4He}|$.

An example of the kinematics reconstructions of the ^{3}He(^{24}Mg,^{4}He)^{23}Mg* reaction is presented on the left of Fig. 5.6 for ^{4}He ejectiles in VAMOS and in DCTs. Predicted results from simulations are shown in red. The selection on the γ-ray transition with $E_{\gamma,0}$=4.356 MeV, from the Ex=4.356 MeV state in ^{23}Mg*, was applied. An additional selection on the black outlined region was implemented to calculate the kinematics of ^{23}Mg* recoil nuclei at reaction, shown on the right of Fig. 5.6.

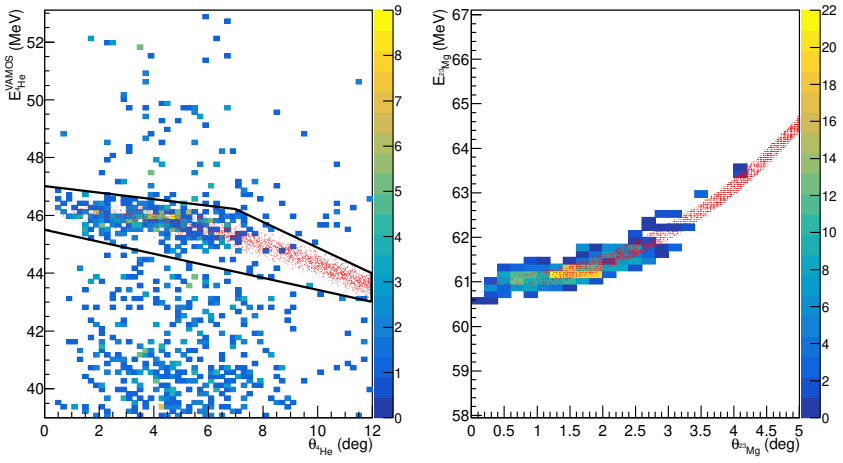

Figure 5.6: Left: measured $E^{VAMOS}_{^4He}$ in VAMOS upon $\theta_{^4He}$ determined with VAMOS and DCTs, after selections on (Z=2, $\frac{m}{q}$=2) and on γ-rays with E^{DC}_{γ}=4.356(12) MeV ($\beta = 0.075$). Right: reconstructed recoil (θ, E)$_{^{23}Mg}$, after selection on the black cut shown on the left. Predictions from EVASIONS simulations are shown with the red points.

As a conclusion, the measured ^{4}He ejectile kinematics, in the combined detectors VAMOS and DCTs, agreed greatly with predictions. From ($E^{VAMOS}_{^4He}$+loss, $\theta_{^4He}$, $\phi_{^4He}$), the ^{23}Mg* recoil nuclei were fully reconstructed in energy and angles.

5.3 γ-ray emissions from states in ^{23}Mg*

5.3.1 γ-ray transitions

- Characterization of γ-ray transitions

The ejectiles energies of Table 5.1 were used as gates to improve the signal-to-noise ratios and to suppress any top-feeding from higher-lying states in the measured matrices (E_γ, θ_γ). The example of the Ex=4.356 MeV state in ^{23}Mg* is illustrated in Fig. 5.7(a) for raw data and (b) in coincidence with ejectile energy. Doppler shifted γ-rays are well apparent in the matrix (E_γ, θ_γ) of Fig. 5.7(b), after having selected $E^{VAMOS}_{^4He}$ on [45.0, 46.7] MeV, compared to the noise dominated matrix of Fig. 5.7(a). The improvement in SNR was: SNR(b)=7.5(8) vs SNR(a)=1.1(2)(a). The γ-rays from this state, short-lived τ<11 fs[55], were observed to be Doppler redshifted as expected.

The principle of the analysis method here is to correct the Doppler effect with different values of $<\beta>$ until the γ-ray transition is observed properly corrected, that is to say observed as a vertical line with respect to θ_γ. The associated energy $E_{\gamma,0}$ is then the center of mass energy and the input value of $<\beta>$ corresponds to the mean of the β-at-emission distribution of emitters ^{23}Mg*. This method is well suited with AGATA high resolution and continuous angular coverage. It works for short-lived states, since their associated β-at-emission distributions are not too wide. In Fig. 5.7(c), the measured energies are Doppler corrected E^{DC}_γ with $<\beta>$=0.075. The γ-rays are observed as a vertical line with respect to the angles θ_γ. Hence, the corrected energies are no more dependent on θ_γ. The red dashed line marks the position of $E_{\gamma,0}$=4.356 MeV. The corrected energies are within $E^{DC}_\gamma=4.356^{+0.014}_{-0.006}$ MeV.

A shift of the γ-rays energies towards higher values than the expected rest energy can be observed for low angles θ_γ <140 deg in Fig. 5.7(c). This is most likely due to the state lifetime which is long enough to expand the β-at-emission distribution. Hence, the used mean $<\beta>$ wrongly corrected the Doppler-shifted γ-rays events emitted late during the slowing down of the nucleus in target. This effect is more apparent for angles close to 90 deg since the Doppler energy shift is less important.

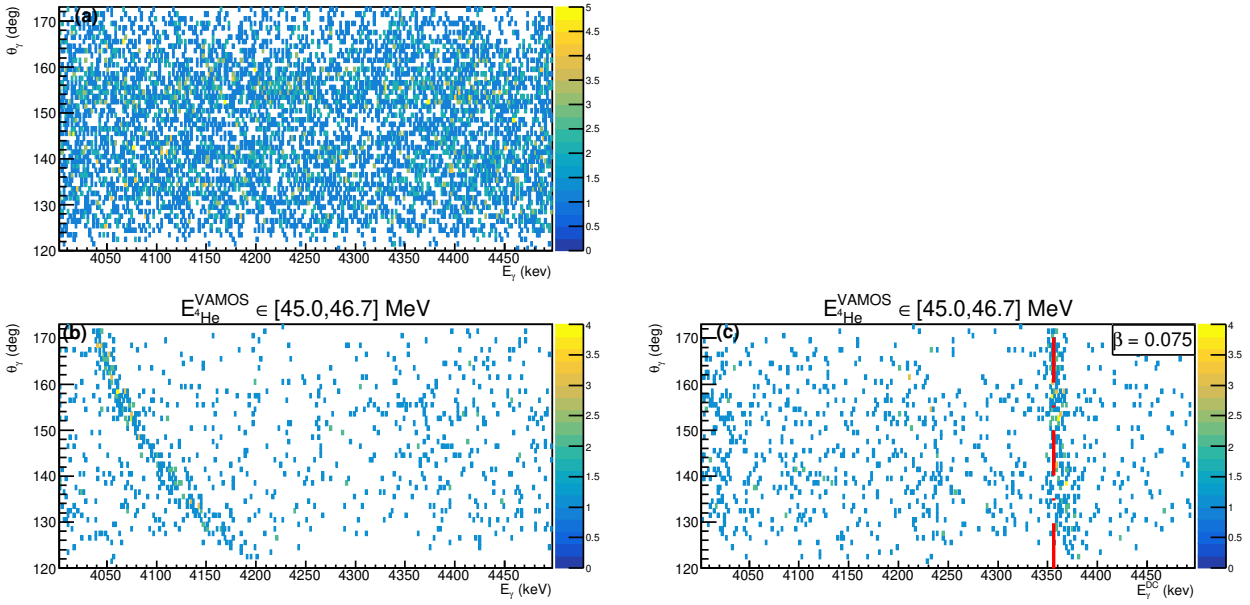

Figure 5.7: Two-dimensional (E_γ, θ_γ) spectra of γ-rays from the AGATA measurements. Panel (a): γ-ray matrix without selection on $E^{VAMOS}_{^4He}$. Panels (b, c): γ-ray matrices selected on $E^{VAMOS}_{^4He} \in [45.0, 46.7]$ MeV associated with the populated Ex=4.356 MeV state in ^{23}Mg*. Energies in panel (c) are Doppler corrected with $< \beta >$=0.075, the red dashed line marks the expected γ-ray transition of $E_{\gamma,0}$=4.356 MeV.

The intensities I_{γ_i} of γ-ray transitions γ_i, in the decay paths of states in ^{23}Mg*, were estimated for some states only. Such states must have one or two possible transitions. Due to the large uncertainties on the beam intensity and the unknown cross-sections, I_{γ_i} were not directly calculated from the observed counts in γ_i. Nonetheless, if the state can decay by two different transitions (γ_1, γ_2), then the associated intensities are

$$I_{\gamma_1} = \frac{\frac{C_{\gamma_1}}{C_{\gamma_2}}}{1 + \frac{C_{\gamma_1}}{C_{\gamma_2}}} = \frac{C_{\gamma_1}}{C_{\gamma_2} + C_{\gamma_1}} \qquad (5.6)$$
$$I_{\gamma_2} = 1 - I_{\gamma_1}$$

with C_{γ_1} the observed counts in γ_1, and C_{γ_2} in γ_2. These counts were obtained after correcting from the energy efficiency of AGATA (Eq. (3.9)). The results on well identified transitions of low-lying states are given in Table 5.2. Except for the Ex=5.287 MeV last state, the measured intensities agreed with known values within <10 %.

Ex (MeV)	$E_{\gamma,0}$ (MeV)	Experiment I_γ (%)	Literature I_γ [55] (%)
2.906	2.455	63(7)	60(2)
	2.908	37(7)	40(1)
3.794	3.344	98(2)	93(1)
	3.794	2(2)	7(2)
5.287	3.236	28(6)	52(3)
	4.836	72(6)	48(1)
7.785	5.734	<3	14(2)[a]
	7.785	>97	86(1)

[a] only observed in the ^{23}Al β-delayed experiment [53].

Table 5.2: Results in the estimated γ-ray transition intensities I_γ by using Eq. (5.6). Among the 22 identified states in ^{23}Mg*, the ones having only two first transitions in their decay paths were considered. The referenced intensities, from ^{12}C(^{12}C,nγ) experiments [55], agree within <10 %, except for the Ex=5.287 MeV state. For the Ex=7.785 MeV key state, the $E_{\gamma,0}$=5.734 MeV transition, observed only once [53], was not seen above background noise in the experiment, resulting in a lower limit of I_γ.

- Impact of fusion-evaporations reactions with contaminants

The γ-ray transitions of the Ex=7.785 MeV astrophysical state in ^{23}Mg* have been similarly studied. The Fig. 5.8(a) shows the matrix (E_γ, θ_γ) without selection, and Fig. 5.8(b) with $E^{\mathrm{VAMOS}}_{^4\mathrm{He}}$ gated. A Doppler shifted line emerges hardly from background noise. The Fig. 5.8(c) corresponds to the Doppler corrected matrix. The dashed line marks the expected $E_{\gamma,0}$=7.333 MeV energy. A projection onto E^{DC}_γ is shown in Fig. 5.9. The observed peak at $7.334^{+0.011}_{-0.005}$ MeV confirmed that the Doppler shifted γ-ray transition, observed in Fig. 5.8(b), originated from the Ex=7.785 MeV state in ^{23}Mg*. In Fig. 5.8(a), a straight line is visible with the energy E_γ=6.879 MeV corresponding to the γ-rays emitted from the Ex=6.879 MeV state in ^{28}Si*. This state was produced in fusion-evaporations reactions with the ^{12}C or ^{16}O contaminants. In Fig. 5.8(b), the ^{28}Si and ^{23}Mg lines overlap in the region shown with the purple circle. In this region, it is not possible to separate the two contributions. These events have to be rejected from the analysis.

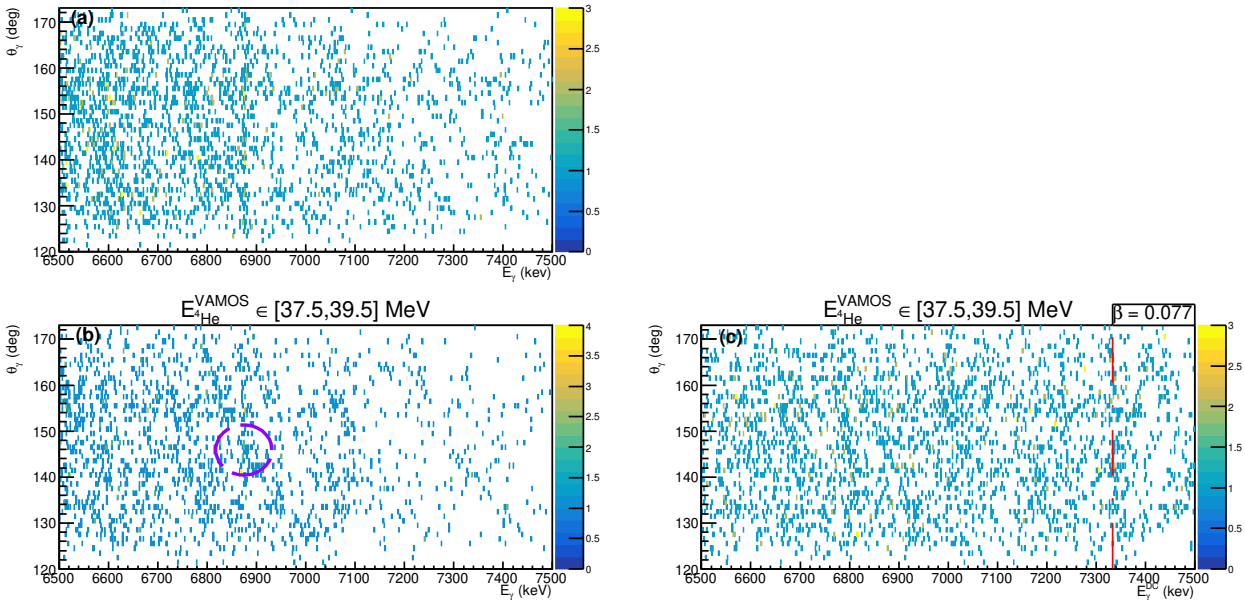

Figure 5.8: Two-dimensional (E_γ, θ_γ) spectra of γ-rays from the AGATA measurements. Panel (a): raw data. Panels (b, c): γ-ray matrices selected on $E^{VAMOS}_{^4He} \in [37.5, 39.5]$ MeV associated with the Ex=7.785 MeV populated state in ^{23}Mg*. Energies in panel (c) are Doppler corrected with $<\beta>$=0.077, the red dashed line marks the expected γ-ray transition with $E_{\gamma,0}$ = 7.333 MeV. The purple circle in (b) shows the region of overlap between γ-ray transitions from the Ex=6.879 MeV state in ^{28}Si*, emitted at rest $E_{\gamma,0}$=6.879 MeV, and from the Ex=7.785 MeV state in ^{23}Mg*.

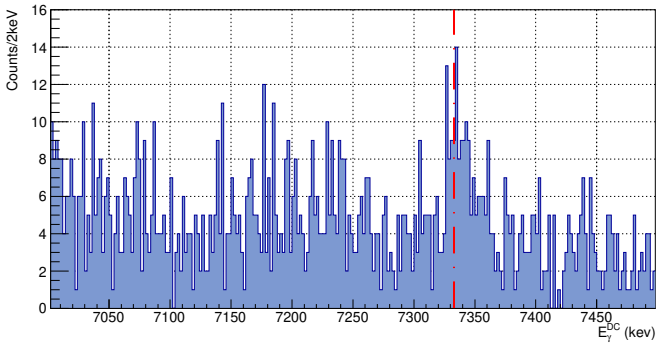

Figure 5.9: Histogram of the projection onto Doppler corrected E^{DC}_γ of the γ-ray matrix in Fig. 5.8(c). The expected γ-ray transition is shown with the red dashed line at E^{DC}_γ=7.333 MeV.

As it is shown in Fig. 5.9, the statistics of the experiment is quite low. This is in agreement with expectations after calculating the differential cross section for this Ex=7.785 MeV state, see Table 2.2 and Fig. 2.7 (Sec.2.3.1). Two other transitions were looked for, around $E_{\gamma,0}$=5.734 MeV and $E_{\gamma,0}$=7.785 MeV, as discussed in Sec.2.2.1 (Fig. 2.1). The first one was not observed above the background noise, similarly to the study [52]. It resulted in an upper limit for the associated I_γ in Table 5.2. The second possible transition to the ground state was searched due to the debate around the state spin. Nor was it observed above background noise. Hence, only one γ-ray transition was observed from the astrophysical state, with $E_{\gamma,0}$=7.333 MeV.

In conclusion, the following points were obtained

1. As wanted, the signal-to-noise ratios of γ-ray transitions from states in ^{23}Mg* were highly improved thanks to coincidences and gates with the ^{4}He ejectiles energies.

2. The method based on Doppler correction was used to estimate $E_{\gamma,0}$ and a mean velocity $< \beta >$ at emission of states in ^{23}Mg*, benefiting from AGATA angular continuous coverage and its excellent resolutions in energy and angle.

3. Events were rejected if they were inside the (E_γ, θ_γ) region of overlap between γ-rays lines from the Ex=7.785 MeV state in ^{23}Mg* and the Ex=6.879 MeV state in ^{28}Si*.

5.3.2 Doppler angle

Doppler energy shift is function of the excited nucleus velocity and the Doppler angle defined between the γ-ray and the nucleus momentum. This last parameter $\theta_{\rm DS}$ was reconstructed from the measured angles $(\theta,\ \phi)_\gamma$ and the reconstructed $(\theta,\ \phi)_{^{23}{\rm Mg}}$. In the laboratory frame, $\theta_{\rm DS}$ is equal to the scalar product of the γ-ray vector and the ^{23}Mg* momentum vector

$$\cos(\theta_{\rm DS}) = \sin(\theta_\gamma)\sin(\theta_{^{23}{\rm Mg}}) \times (\cos(\phi_\gamma)\cos(\phi_{^{23}{\rm Mg}}) + \sin(\phi_\gamma)\sin(\phi_{^{23}{\rm Mg}})) + \cos(\theta_\gamma)\cos(\theta_{^{23}{\rm Mg}}) \qquad (5.7)$$

From Eq. 5.7, one can easily check that if ^{23}Mg* is close to the beam axis then $\theta_{\rm DS} \sim \theta_\gamma$. This is the usual assumption which has not been used in our experiment analysis where the ^{23}Mg emitter angles were taken into account to build back $\theta_{\rm DS}$.

In order to improve the resolution on the measured lifetimes, the reconstructed Doppler angles $\theta_{\rm DS}$, from the γ-ray and ^{23}Mg* angular parameters, were used in all calculations involving Doppler effect.

5.4 Key properties of the emitting state in ^{23}Mg*

5.4.1 Excitation energy Ex

The excitation energy of the emitting state in ^{23}Mg* was reconstructed from both the emitted protons and the ^{4}He ejectiles.

- From protons in SPIDER

It is possible to express Ex as a function of $(E,\ \theta)_{\rm p}$ at emission, see Sec.2.2.3 and Annexes A.1. The measured proton energy $\Delta E{+}E_{\rm res}$ in the rings of SPIDER was corrected for the energy losses in the {target + beam catcher} foils, shown in Fig. 3.14. Simulations with EVASIONS were done to estimate $E_{\rm p}$ as a function of the measured $\Delta E{+}E_{\rm res}$, at each $\theta_{\rm p}$ associated with a SPIDER strip. An example at $\theta_{\rm p}$=13.0(5) deg is shown in Fig. 5.10, the black curve for thin target and the blue curve for thick target. Polynomial functions were fitted on these curves.

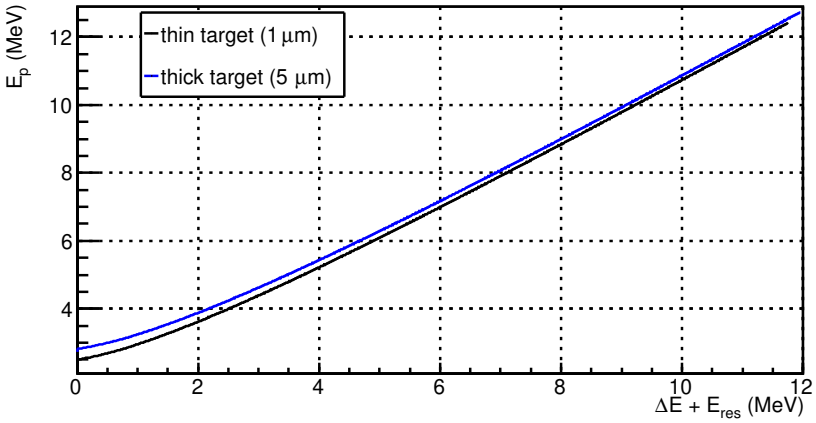

Figure 5.10: Evolution of the proton energy E_p at the time of emission as a function of the SPIDER ΔE+E_{res} energy, simulated with the EVASIONS code. That plot was obtained for the first strip of SPIDER detector with respect to beam axis, associated with θ_p=13.0(5) deg. The black curve corresponds to thin target, and the blue curve to thick target.

The excitation energies of proton emitting states in ^{23}Mg* were obtained from the measured protons in SPIDER, they are presently called Ex^{SPIDER}. The measured Ex^{SPIDER} are compared to simulated results in Fig. 6.14 of Sec.6.3 where these Ex^{SPIDER} spectra have been used to derive the proton branching ratios of emitting states in ^{23}Mg*.

- From ^{4}He in VAMOS

Simulations with EVASIONS allowed us to plot $E^{VAMOS}_{^4He}$ as a function of Ex as shown in Fig. 5.11, for thick target in blue and for thin target in black. A total of 10 states with Ex∈[0.4, 7.9] MeV were simulated. These points were well fitted with 2nd order polynomial functions, given in Eq. (5.8). The same approach as for the protons in SPIDER could also have been used: an analytic resolution with a correction included for the ^{4}He energy losses in gold to build back Ex from the measured ^{4}He ejectiles. The first method is less expensive in terms of computer time to select, event by event, coincidences between the aimed γ-ray transitions and populated states in ^{23}Mg*.

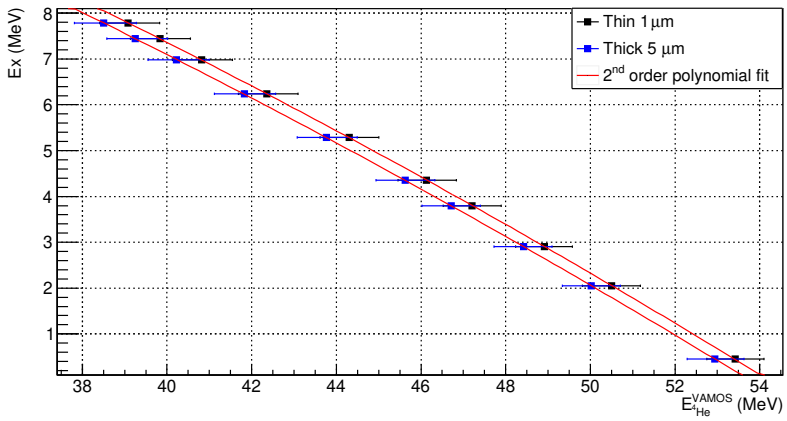

Figure 5.11: Evolution of the excitation energy Ex of states in ^{23}Mg* over the ^{4}He ejectile energy $E^{VAMOS}_{^4He}$ measured in VAMOS, obtained with EVASIONS simulations. Black points correspond to a thin target and blue ones to a thick target. The results of the 2nd order polynomial fits are shown with the red curves.

$$\begin{aligned} \mathrm{Ex}^{\mathrm{VAMOS}} &= 20.43 - 0.185 \times \mathrm{E}_{^4\mathrm{He}}^{\mathrm{VAMOS}} - 3.54 \times 10^{-3} \times \mathrm{E}_{^4\mathrm{He}}^{\mathrm{VAMOS}\,2} \quad \text{Thin target} \\ \mathrm{Ex}^{\mathrm{VAMOS}} &= 20.20 - 0.187 \times \mathrm{E}_{^4\mathrm{He}}^{\mathrm{VAMOS}} - 3.51 \times 10^{-3} \times \mathrm{E}_{^4\mathrm{He}}^{\mathrm{VAMOS}\,2} \quad \text{Thick target} \end{aligned} \tag{5.8}$$

The coincidences between the observed γ-ray transitions, after Doppler correction, and the reconstructed excitation energies $\mathrm{Ex}^{\mathrm{VAMOS}}$ were studied. As an illustration, two matrices ($\mathrm{Ex}^{\mathrm{VAMOS}}$, $\mathrm{E}_\gamma^{\mathrm{DC}}$) are presented in Fig 5.12 for two γ-ray energy windows, on the left with [3000, 5000] keV and on the right with [6800, 7500] keV. The red circles bring to light some identified populated states, including the astrophysical one, i.e. the middle one on the right.

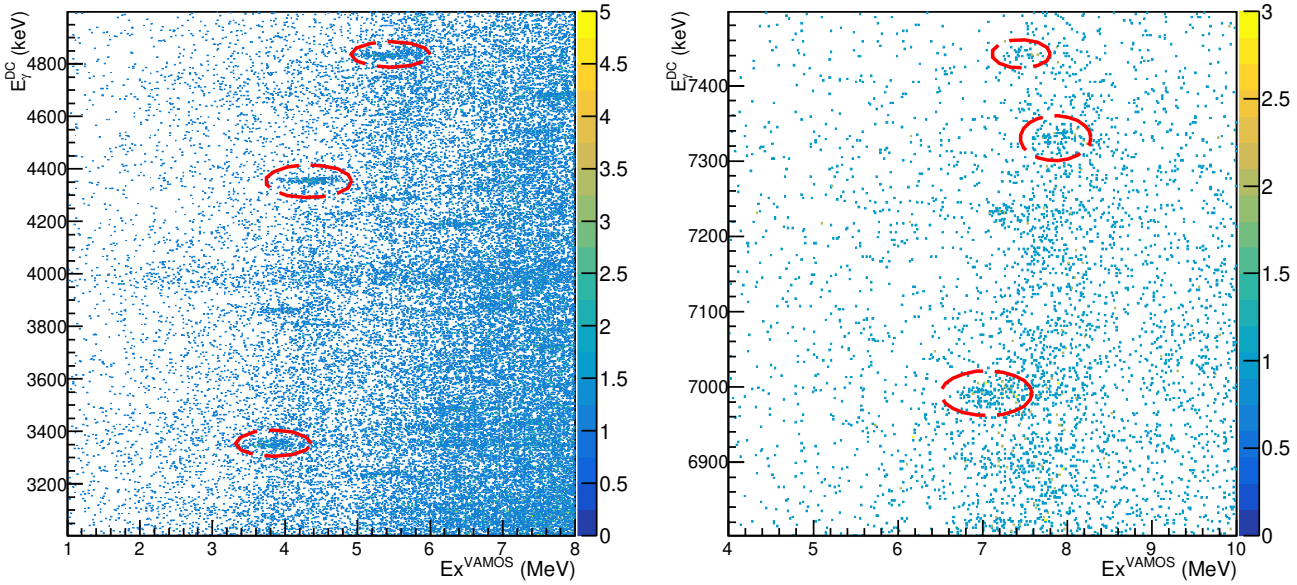

Figure 5.12: The Doppler corrected energy $\mathrm{E}_\gamma^{\mathrm{DC}}$ is plotted over the calculated excitation energy $\mathrm{Ex}^{\mathrm{VAMOS}}$ in ^{23}Mg*. Two γ-ray energy windows are presented: $\mathrm{E}_\gamma^{\mathrm{DC}}$ $\in$[3000, 5000] keV (left) and $\mathrm{E}_\gamma^{\mathrm{DC}}$ $\in$[6800, 7500] keV (right). Red circles mark some directly populated states in ^{23}Mg*.

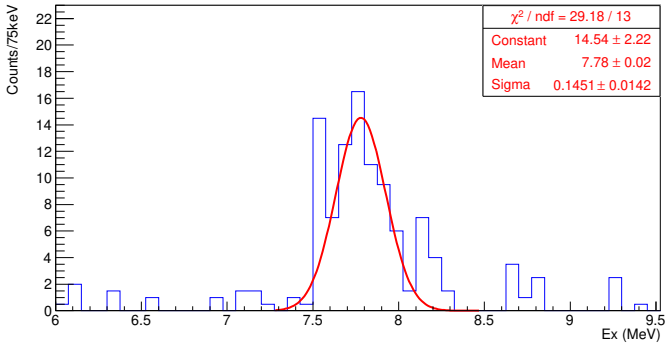

Figure 5.13: Projection histogram onto $\mathrm{Ex}^{\mathrm{VAMOS}}$ of the right matrix ($\mathrm{Ex}^{\mathrm{VAMOS}}$, $\mathrm{E}_\gamma^{\mathrm{DC}}$) in Fig. 5.12, after the selection on $\mathrm{E}_\gamma^{\mathrm{DC}}$ $\in$[7.318, 7.348] MeV and the subtraction of the local mean background noise (explained in A.2). The Gaussian fit of the observed excitation peak is shown in red.

After projection of slices onto Ex^{VAMOS}, the excited state peaks were observed. Then local background noise subtractions were proceeded. The background noise was evaluated on both sides of the excitation peak, described in Annexes A.2. Finally, the noise-subtracted excitation peaks were fitted by Gaussian functions, allowing us to estimate the measured excitation energies Ex^{VAMOS} associated with the populated states and their resolutions. In Fig. 5.13, the Ex=7.785 MeV astrophysical state was correctly found with Ex^{VAMOS}=7.78(15) MeV, using a slice of γ-ray energy of $E_\gamma^{DC} \in [7.318, 7.348]$ MeV. The results of the 22 identified states in ^{23}Mg* are listed in Table. 5.3. The measured resolutions in Ex^{VAMOS} do not appear to be correlated with the excitation energy, it is rather dominated by statistics fluctuations and residual noises.

^{23}Mg (Ex, $E_{\gamma,0}$) MeV	Ex^{VAMOS} (MeV) $\pm\sigma$	^{23}Mg (Ex, $E_{\gamma,0}$) MeV	Ex^{VAMOS} (MeV) $\pm\sigma$
(0.451, 0.451)	0.46(0.5) ±0.08	(6.240, 4.188)	6.24(0.8)±0.17
(2.052, 1.601)	2.10(1) ±0.20	(6.775, 4.418)	6.78(2)±0.18
(2.906, 2.455)	2.95(1)±0.28	(6.908, 6.900)	6.85(6)±0.22
(3.794, 3.344)	3.79(1)±0.27	(6.984, 6.984)	6.99(1)±0.17
(3.861, 3.861)	3.85(8) ±0.30	(7.112, 6.660)	7.05(5)±0.10
(4.356, 4.356)	4.35(1)±0.19	(7.450, 7443)	7.44(8)±0.31
(4.681, 4.230)	4.67(1) ±0.16	(7.584, 3.725)	7.57(1)±0.16
(5.287, 4.836)	5.25(2)±0.16	(7.770, 5.054)	7.74(2)±0.08
(5.691, 5.690)	5.71(1)±0.21	(7.782, 5.067)	7.78(2)±0.08
(6.132, 3.775)	6.15(3) ±0.14	(7.785, 7.333)	7.78(2)±0.15
(6.195, 3.480)	6.19(2) ±0.21	(7.803, 7.801)	7.80(1)±0.1

Table 5.3: Experimentally estimated excitation energies Ex^{VAMOS} of ^{23}Mg* states, after a selection on E_γ^{DC} around γ-ray transition at $E_{\gamma,0}$ [55] and the subtraction of the local mean background noise. The associated uncertainties σ come from Gaussian fits of the observed excitation peaks. The results written in red correspond to the states highlighted in Fig. 5.12.

To summarize, the excitation energies of states in ^{23}Mg* were obtained from two independent measurements of: first, the decaying protons with SPIDER (Ex^{SPIDER}), second, the ^{4}He ejectiles with VAMOS (Ex^{VAMOS}) in coincidence with γ-rays. The resolution of Ex^{VAMOS}, $\sigma \sim 0.2$ MeV, is better than the Ex^{SPIDER} resolution, mainly because of the proton straggling in gold.

5.4.2 Differential cross sections of populated states

For each excitation energy identified, the differential cross section associated with ^{4}He in laboratory ($\frac{d\sigma}{d\Omega_\alpha}^{lab}$) was estimated. First, the number of observed γ-ray counts for each transition measured in coincidence with $E_{^4He}^{VAMOS}$ was corrected from the instrument response functions:

1. Each γ-ray transition was isolated by using a selection cut in the ejectile energy $E_{^4He}^{VAMOS}$.
2. The local noise, measured from both sides in E_γ^{DC}, was subtracted (Annexes A.2).
3. The simulated efficiency of AGATA, given by Eq. (3.9), and its associated errors, from the normalization to the ^{150}Eu source measurements, were taken into account.
4. The noise and efficiency of VAMOS were taken into account. The background noise distribution in $E_{^4He}^{VAMOS}$ was measured with the beam irradiation onto the pure gold target.

Then, the referenced γ-ray transition intensities I_γ, or the measured ones from Table 5.2, were used to determine the population of each state. Already mentioned, the measured $\frac{d\sigma}{d\Omega_\alpha}^{lab}$ for the Ex=7.785 MeV state, after taking into account an averaged beam intensity and the targets concentrations, agrees with

previous experiment [52]. The ratio of the measured Ex=7.785 state population over its $\frac{d\sigma}{d\Omega_\alpha}^{lab}$, was used to estimate $\frac{d\sigma}{d\Omega_\alpha}^{lab}$ for all states. The ^{23}Mg state $\frac{d\sigma}{d\Omega_\alpha}^{lab}$ in the angular range coverage of the present experiment, $\theta^{lab}_{^4He} < 12$ deg, are shown in Fig. 5.14 as a function of excitation energy. It can be seen that the differential cross sections decrease as a function of the excitation energy, varying overall from 8×10^2 μb/sr to 4 μb/sr.

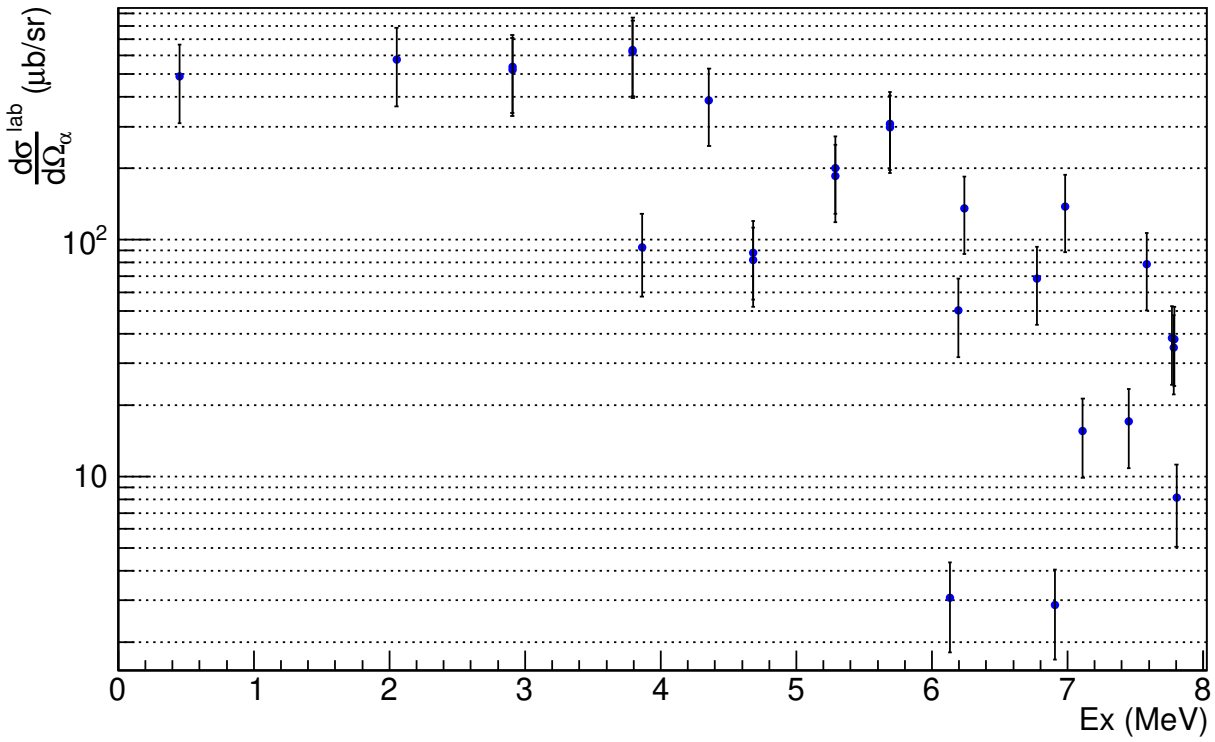

Figure 5.14: Estimated differential cross section of each state in ^{23}Mg*, during the experiment, plotted over the associated excitation energies. See details about the calculations in text.

5.4.3 Velocity β

From the measurement of the Doppler shifted γ-ray energy and the Doppler angle θ_{DS}, the velocity β of the emitter ^{23}Mg* can be derived for each photon. Indeed, β can be isolated in the Doppler Eq. (2.5)

$$(1 + R^2\cos(\theta_{DS})^2) \times \beta^2 - 2R^2\cos(\theta_{DS}) \times \beta + R^2 - 1 = 0 \tag{5.9}$$

with R= $\frac{E_\gamma}{E_{\gamma,0}}$. This 2nd polynomial equation can be solved to extract β, the discriminant being

$$\Delta = -4 \times (R^2 - R^2\cos(\theta_{DS})^2 - 1) \tag{5.10}$$

For AGATA backward angles, R$\leq$ 1, hence $\Delta \geq 0$. With $\cos(\theta_{DS}) \leq 0$, only one solution is physical, that is to say $\beta > 0$,

$$\beta = \frac{R^2\cos(\theta_{DS}) + \sqrt{1 + R^2\cos(\theta_{DS})^2 - R^2}}{R^2\cos(\theta_{DS})^2 + 1} \tag{5.11}$$

Using Eq. (5.11), the β distributions associated with the measured γ-rays, selected on $E^{VAMOS}_{^4He}$, were reconstructed. Three examples are presented in Fig. 5.15 from the γ-ray transitions of three states in

^{23}Mg*: Ex$\in$ $\{3.794, 4.356, 7.785\}$ MeV shown with respectively black, blue and red points. The sensitivity in β was given by the AGATA high precision in energy and angle, i.e. $\sim$(2 keV, 1 deg), and by the uncertainties in the reconstructed ($\theta_{^4\mathrm{He}}$, $\phi_{^4\mathrm{He}}$)$\lesssim$(3, 30) deg. It was noticed that the mean value of the β distributions increased with respect to Ex. This observation was confirmed by LISE++ predictions, shown in Annexes C.2. The lower Ex=3.794 MeV state has τ=41(6) fs[52] whereas the other two have τ<12 fs. As expected, the β black distribution, from the Ex=3.794 MeV state, has a more important left tail than the other two β distributions. The slowdown in the target of this longer-lived state is therefore clearly observed. This demonstrates that it is possible to determine lifetimes with an analysis of this spectrum. The great advantages of this method are that the spectrum is easily obtained and that it condenses all the statistics into a single spectrum.

The angles of the γ-ray emitting nucleus ^{23}Mg* were included in the β-at-emission reconstruction, see Eq. (5.7) for θ_{DS}. Thus, the reconstructed β-at-emission distributions are independent of the ^{23}Mg* angular distribution which depends on the reaction mechanism.

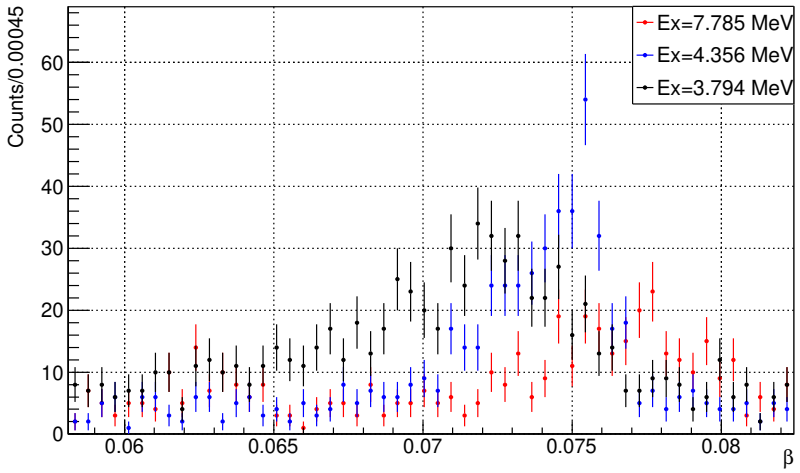

Figure 5.15: Reconstructed β distributions from the measured γ-ray transitions from three excited states in ^{23}Mg*: Ex=7.785 MeV in red, Ex=4.356 MeV in blue and Ex=3.794 MeV in black. The lifetime of the Ex=3.794 MeV state is τ=41(6) fs[52] whereas they are τ<12 fs for the other two states.

In conclusion, a new analysis method has been developed to extract the velocity β distribution at γ-ray emission and ultimately state lifetimes. To our knowledge, this is the first time this method is proposed. It was noticed that β distributions depend mainly on the Ex and τ parameters.

5.5 Conclusion

In this Chapter, the reconstruction procedures of the physical parameters have been presented. It has led to the determination of the differential cross sections, the velocity β-at-emission and the excitation energies Ex in ^{23}Mg*. These physics quantities are central to the spectroscopic analysis of the identified states in ^{23}Mg*. How to access J, τ and BR$_\mathrm{p}$ from $\frac{\mathrm{d}\sigma}{\mathrm{d}\Omega_{^4\mathrm{He}}}$, β and Ex? Answers will be given in the next Chapter 6.

Part IV

On the experimental results and interpretation

CHAPTER 6

Spectroscopic properties of states in ^{23}Mg*

6.1 Introduction

The goal of the experiment was to determine the three spectroscopic parameters ($\Gamma_{\rm tot}$, $\Gamma_{\rm p}$, J) of the astrophysical state in ^{23}Mg*. This will be addressed in the present Chapter. Each analysis method to measure a state constant, τ or $BR_{\rm p}$ or J, is first described with illustrative test state(s). Then, the Ex=7.785 MeV state is studied. On one hand, all identified states with their γ-ray transitions have been investigated in (τ, J). On the other hand, the states relevant for the nova energy window have been studied through their proton decays. Their associated $BR_{\rm p}$ have been looked for.

The analysis to access to $\Gamma_{\rm tot}$ is presented along Sec.6.2. Three methods were used to get lifetimes: the classical DSAM in Sec.6.2.2, a new method based on β distribution in Sec.6.2.3, and the method using Doppler-corrected γ-ray lineshapes in Sec.6.2.4. The systematic uncertainties originating from experimental conditions are developed in Sec.6.2.5. The final results in (τ, $\Gamma_{\rm tot}$) are given in Sec.6.2.6. Then, the partial proton widths $\Gamma_{\rm p}$ of states close to $S_{\rm p}$ were investigated by measuring their $BR_{\rm p}$ in Sec.6.3. The spin determination is developed in Sec.6.4. Our main experimental results regarding the spectroscopy of the Ex=7.785 MeV key state are summarized in the conclusive section Sec.6.5.

6.2 Total width

6.2.1 Introduction

The total widths of excited states in ^{23}Mg* were experimentally accessed by measuring the associated lifetimes. Lifetime measurements were based on quantifying the goodness of fit between the experimental and simulated lineshapes with χ^2 test. Simulations were done with the EVASIONS code. They were normalized to the experimental spectra on the counts integral along the same energy range for each input free parameter (lifetime, γ-ray rest energy). These energy ranges were chosen such the peak and the noise from both sides were included. The χ^2 values were computed with the ROOT histogram library [93] on the maximum likelihood option. Statistical uncertainties of the measured values were taken at 1σ equal to 68 % confidence levels (CL). The associated changes in χ^2, written $\Delta\chi^2$, depend on the amount of free parameters (m). They are listed in Table 6.1 from [110].

CL (%)	$\Delta\chi^2$		
	m=1	m=2	m=3
68	0.99	2.29	3.53
95	3.84	5.99	7.82

Table 6.1: Changes in χ^2 ($\Delta\chi^2$) over confidence levels CL depend on the free parameters m, source [110].

The amount of free parameters was m=2: the state lifetime and the γ-ray rest energy in Sec.6.2.2, 6.2.3 and 6.2.4, the lifetime and the target position in Sec.6.2.5. Besides, two analysis parameters (SNR, binning) were used in the lineshape analysis. The systematic uncertainties from these analysis parameters were observed negligible compared to statistical ones. The systematic uncertainties originating from experimental conditions, developed in Sec.6.2.5, were included in the EVASIONS simulations. Finally, the uncertainties of the measured lifetimes correspond to statistical uncertainties only.

6.2.2 Doppler-Shift Attenuation Method DSAM

- Principle and examples

The classical Doppler-Shift Attenuation Method DSAM consists on analyzing the γ-ray lineshape selected on an angle slice. The observed Doppler-shifted E_γ spectrum is compared with simulated spectrum at a given τ. Lifetime measurements with DSAM and AGATA are well illustrated in Michelagnoli *et al* [58] in the case of ^{15}O and ^{15}N. Here as an example, the DSAM method applied to the Ex=2.052 MeV state in ^{23}Mg* is shown in Fig. 6.1. The observed γ-ray lineshape, selected on high $\theta_{DS} \in [149, 157]$ deg, is compared in Fig. 6.1(a) to three simulated lineshapes at τ=50 fs (green curve), τ=75 fs (red curve) and τ=150 fs (blue curve). A similar comparison is presented in Fig. 6.1(b) for a selection on a lower angle slice ($\theta_{DS} \in [127, 135]$ deg). The normalized χ^2/ndf are given. In both cases, the red curves are associated with the minimal χ^2. The overall χ^2 obtained as a function of the input (τ, $E_{\gamma,0}$) are given in Fig. 6.1(c) for $\theta_{DS} \in [149, 157]$ deg and in Fig. 6.1(d) for $\theta_{DS} \in [127, 135]$ deg. Red marks point out the 68 % CL. Minimums in χ^2 are well apparent, allowing us to measure the state lifetime and the γ-ray rest energy. Final results are listed in Table 6.2. The weighted average value over the angle slices τ_{DSAM}=78(19) fs ($E_{\gamma,0}$=1601.8(11) keV) is in agreement with the known value τ=94(17) fs ($E_{\gamma,0}$=1601.4(13) keV)[55].

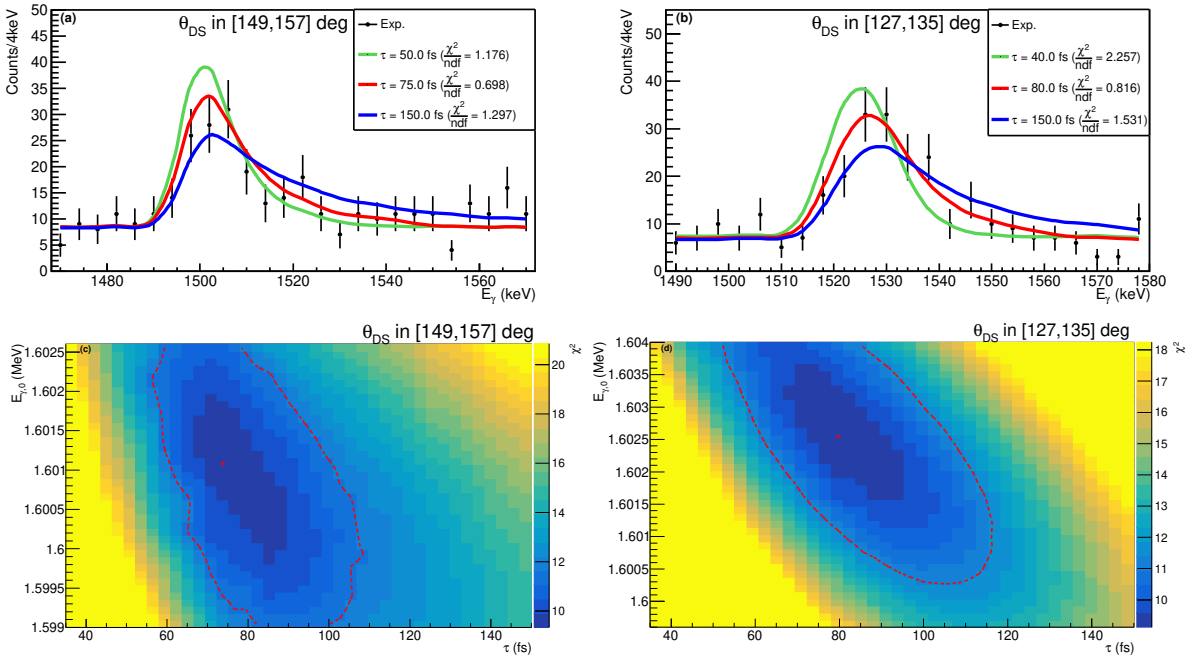

Figure 6.1: The DSAM lifetime measurement of the Ex=2.052 MeV state in ^{23}Mg*. Panel (a): experimental Doppler-shifted γ-rays E_γ spectrum (black points) compared to three simulated profiles with τ=50 fs (green curve), τ=75 fs (red curve) and τ=150 fs (blue curve), after a selection on the angle slice $\theta_{DS}\in$[149, 157] deg. Panel (b): similar comparison between experiment and simulations, with τ=40 fs (green), τ=80 fs (red) and τ=150 fs (blue), after another selection on the lower angle slice $\theta_{DS}\in$[127, 135] deg. The normalized χ^2/ndf are indicated. Panels (c, d): the derived χ^2 in color scale as a function of the lifetime τ and the γ-ray rest energy $E_{\gamma,0}$, for the selection on $\theta_{DS}\in$[149, 157] deg (c) and on [127, 135] deg (d). Red dashed lines correspond to the 1σ limit (68 % CL). The red curves in (a, b) correspond to the χ^2 minimal value (red cross). Panel (c): $\tau = 75^{+28}_{-13}$ fs, $E_{\gamma,0} = 1601^{+1.5}_{-1.7}$ keV. Panel (d): $\tau = 80^{+27}_{-14}$ fs, $E_{\gamma,0} = 1602.5^{+1.3}_{-1.5}$ keV.

Focusing on the Ex=7.785 MeV key state in ^{23}Mg*, the experimental lineshape selected on high angles $\theta_{DS}\in$[154, 162] deg is compared in Fig. 6.2(a) to three simulated ones with τ=2 fs (green curve), τ=14 fs (red curve) and τ=20 fs (blue curve). The obtained χ^2/ndf were far from 1. This showed that the chosen binning of the spectrum, from the instrumental AGATA resolution of 4 keV/bin, was too low for the available statistics. Experimental points were too much scattered. The binning was increased up to 12 keV/bin in order to reach χ^2/ndf$\sim$1, the results are presented in Fig. 6.2(b). The χ^2 values calculated over the (τ, $E_{\gamma,0}$) parameters are given in Fig. 6.2(c). Since the energy sensitivity had to be degraded to get reasonable statistics, the sensitivity in τ was also decreased. With 95 % CL as in Ref. [52], only an upper limit could be obtained: $\tau_{DSAM}<$17 fs. It should be noted that the lineshape analysis for other angle slices are not presented since the associated statistics were even lower.

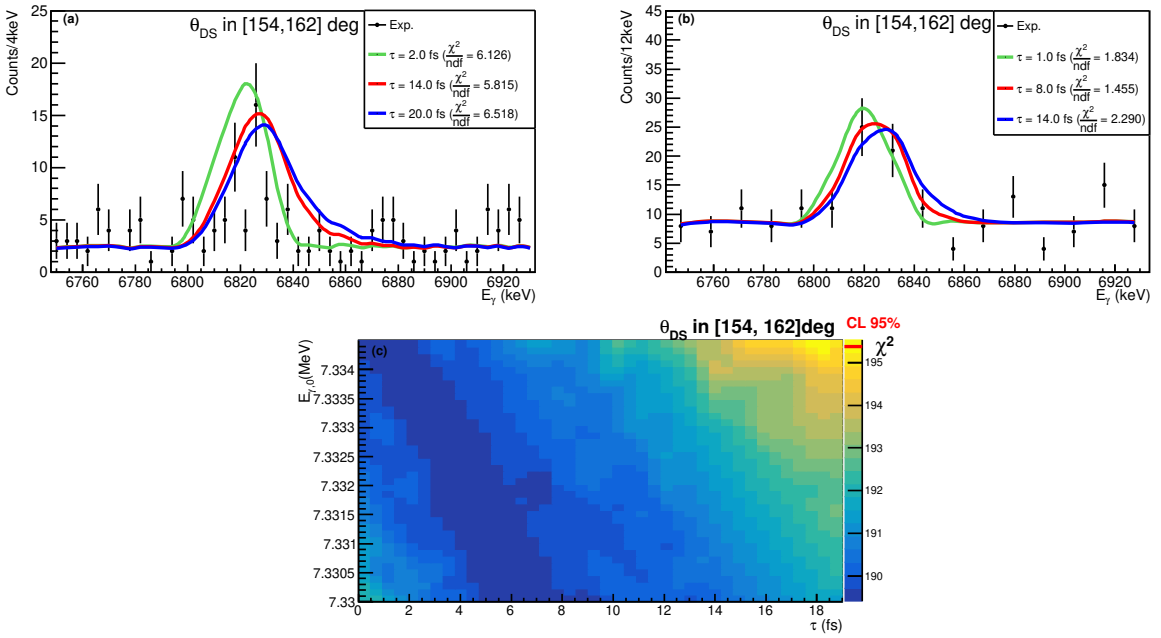

Figure 6.2: The DSAM lifetime study of the Ex=7.785 MeV state in ^{23}Mg*. Panel (a): experimental Doppler-shifted γ-rays spectrum (black points) compared to three simulated profiles for τ=2 fs (green curve), τ=14 fs (red curve) and τ=20 fs (blue curve) after a selection on the angles $\theta_{\mathrm{DS}} \in [154, 162]$ deg. The χ^2/ndf are much higher than 1 which is the expected value when the compared spectra are alike. Panel (b): similar comparison but after increasing the E_γ binning width to 12 keV, instead of 4 keV. The derived χ^2/ndf were closer to 1, and the experimental spectrum less scattered. Simulations shown with τ=1 fs (green curve), τ=8 fs (red curve) and τ=14 fs (blue curve). Panel (c): the χ^2 matrix as a function of (τ, $E_{\gamma,0}$) in case of the 12 keV binning. There is no observed minimum in χ^2, the sensitivity in τ being degraded when binning is increased. Here, the DSAM sensitivity is dominated by $E_{\gamma,0}$. At the known $E_{\gamma,0}$=7333 keV[55], estimated upper limit τ_{DSAM}<17 fs (95 % CL).

- Results

The results obtained with the DSAM method for (τ, Γ_{tot}, $E_{\gamma,0}$) of the identified states in ^{23}Mg* are listed in Table 6.2.

As a conclusion,

1. Independent lifetime measurements were obtained with the classical DSAM method by looking at different angle slices. The γ-ray rest energies were also measured.

2. Despite an expected experimental sensitivity of 1 fs, only an upper limit of the lifetime of the key state was obtained with DSAM, due to limited statistics in angle slices.

Ex MeV	$E_{\gamma,0}$ keV Ref. [55]	$E_{\gamma,0}$ keV This study	τ fs Ref. [55, 52]	τ fs This study	Γ_{tot} meV This study
0.451	450.7(15)	451.0(5)	1.66(12) ps	1.62(35) ps	$0.41^{+0.11}_{-0.07}$
2.052	1601.4(13)	1601.8(11)	94(17)	78(19)	$8.4^{+2.7}_{-1.7}$
2.906	2454.6(7)	$2454.5^{+1.0}_{-1.5}$	15(3)	14^{+5}_{-6}	47^{+35}_{-12}
3.794	3343.9(13)	/	41(6)	<44	>15
3.861	3861.0(7)	/	12(3)	<22	>30
4.356	4356.0(20)	/	<11	<14	>47
4.681	4230(1)	/	10(3)	<16	>41
5.287	3236(1)	/	5(2)	<10	>66
5.691	5690(1)	/	∅	<24	>27
6.132	3775(1)	/	∅	<20	>33
6.195	3480(1)	/	17(3)	<25	>26
6.240	4188(1)	/	<40	<28	>24
6.775	4418(1)	/	∅	<32	>21
6.908	6900(3)	/	<10	<18	>37
6.984	6984(5)	/	∅	<45	>15
7.112	6660(1)	/	∅	<14	>47
7.450	7443(3)	/	<14	<18	>36
7.584	3725(6)	/	∅	<10	>66
7.770	5054.8(6)	/	2(1)	/	/
7.782	5067.1(11)	/	<1	/	/
7.785	7333.2(11)	/	10(3)	<17	>39
7.801	7801.3(6)	/	∅	<20	>33

Table 6.2: Results in lifetimes τ and associated total widths Γ_{tot} of states in $^{23}Mg^*$ by using the DSAM method. Uncertainties are 68 % CL, upper limits in τ are taken at 95 % CL as in Ref. [52]. Upper limits were derived if the γ-ray rest energies were known, allowing us to constrain the χ^2 matrices. The γ-ray rest energies $E_{\gamma,0}$ were also measured if finite values for τ were obtained.

6.2.3 Emitter velocity Method βM

- Principle and examples

A new method was developed to overcome the statistics limitation shown with the DSAM method. Thanks to the high capabilities of the detection set-up AGATA+VAMOS+DCT, the emitter velocity β-at-emission was extracted from measured E_γ and reconstructed θ_{DS} in Eq. (5.11). Like in DSAM, lifetimes can be measured by lineshape analysis between experimental and simulated β distributions. This method has the advantage to produce a much higher statistics spectrum. This method, proposed for the first time in this thesis, is referred as βM. It is illustrated with the Ex=4.356 MeV state in Fig. 6.3. On the left, black points correspond to the experimental β distribution and color lines to the simulated profiles with τ=2 fs (green curve), τ=9 fs (red curve) and τ=18 fs (blue curve). Normalized χ^2/ndf are given. The χ^2 matrix depending on (τ, $E_{\gamma,0}$) is shown on the right. From the visible minimum in χ^2, the state lifetime was measured for the first time: $\tau_{\beta M}=9^{+4}_{-2}$ fs. It agrees with the known upper limit τ<11 fs[52]. The measured γ-ray rest energy is also in agreement with known value: 4357.0(8) keV vs 4356.4(20) keV[55].

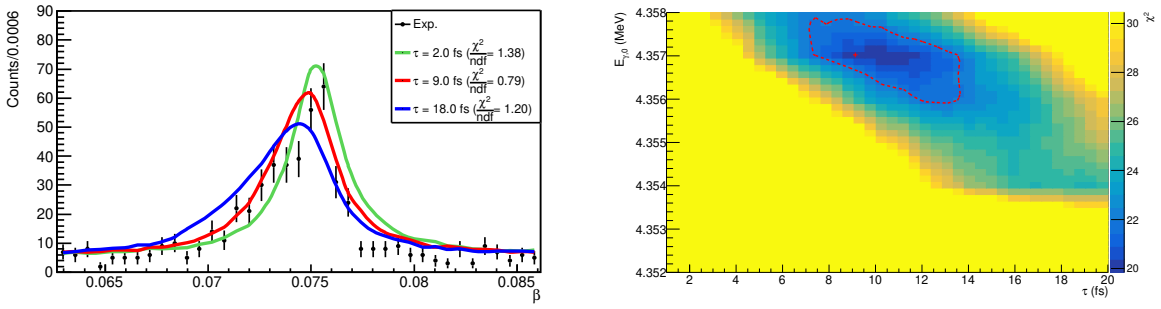

Figure 6.3: The βM lifetime measurement of the Ex=4.356 MeV state in ^{23}Mg*. On the left: the reconstructed experimental β distribution for $E_{\gamma,0}$=4357 keV is compared to three simulated profiles with τ=2 fs (green curve), τ=9 fs (red curve) and τ=18 fs (blue curve). On the right: the resulting χ^2 over the parameters (τ, $E_{\gamma,0}$) points out a minimum associated with the red curve on the left plot. The χ^2 minimum is shown by the red cross, the 68 % CL by the red dashed line. The first time measured lifetime is $\tau_{\beta M} = 9^{+4}_{-2}$ fs with $E_{\gamma,0}$ =4357.0(8) keV.

The results obtained with the βM method in the case of the Ex=7.785 MeV state are presented in Fig. 6.4. On the left, the experimental distribution is compared to three simulated lifetimes, red curve being associated with the minimum χ^2. On the right, the χ^2 matrix shows a minimum for $\tau_{\beta M}$=11^{+6}_{-4} fs. The measured finite lifetime agrees with the past measurement τ=10(3) fs[49] as well as with the previous limit τ_{DSAM}<17 fs. The measured $E_{\gamma,0}$=$7333.0^{+1.2}_{-0.4}$ keV also agrees with the known value 7333.2(11) keV[55].

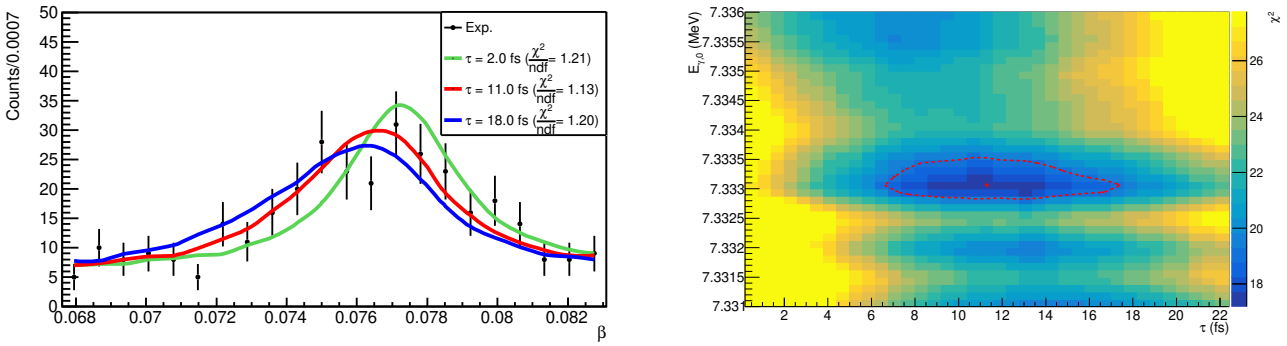

Figure 6.4: The βM lifetime measurement of the Ex=7.785 MeV state in ^{23}Mg*. On the left: the experimental β distribution at $E_{\gamma,0}$=7333 keV is compared to simulated profiles with τ=2 fs (green curve), τ=11 fs (red curve) and τ=18 fs (blue curve). On the right: χ^2 over the (τ, $E_{\gamma,0}$) parameters points out a minimum corresponding to the left red curve. The optimum value is $\tau_{\beta M} = 11^{+6}_{-4}$ fs with $E_{\gamma,0}$ =$7333.0^{+1.2}_{-0.4}$ keV. The χ^2 minimum is shown by the red cross, the 68 % CL by the red dashed line.

To confirm the previous result, it is necessary to validate the βM method with a short-lived state. The velocity distribution of the Ex=7.785 MeV state has been compared with the one from a state with lifetime expected shorter, of the order of ∼1 fs. The experimental results are shown in Fig. 6.5: black points for the Ex=7.785 MeV key state and blue points for the Ex=$\{7.770, 7.782\}$ MeV states located very close to the key state. These two states have their main γ-ray transitions too close in energy, $E_{\gamma,0}$=5.055 MeV vs 5.067 MeV, to be disentangled in the Doppler-shifted γ-rays spectra. A distribution was built back with the energy $E_{\gamma,0}$ =5.067 MeV, for the γ-rays from both Ex=$\{7.770, 7.782\}$ MeV states, see blue points in Fig. 6.5. The apparent broadening for high β>0.079 is thus caused by the wrongly reconstructed events which correspond to emissions from the Ex=7.770 MeV state. The same reconstruction approach was

simulated with EVASIONS for a lifetime τ=0 fs (3 fs) of the Ex=7.782 MeV (7.770 MeV) state, resulting in the blue curve in Fig. 6.5. This simulated curve is in good agreement with the experimental data. The profile with $\tau_{\beta M}$=11 fs of the astrophysical state, shown with the black continuous curve, presents an important left tail for β<0.076, as expected if lifetime is longer than 1 fs. This low lifetime of 1 fs is shown with the black dashed curve. For comparative purposes, the statistics of the blue spectrum, associated with the Ex=$\{7.770, 7.782\}$ MeV states, was normalized to the statistics of the black spectrum. The comparison between the blue and black spectra, for two states close in excitation energy but differing in lifetime, made it clear to us that the key state has a longer lifetime than ∼1 fs, such low lifetime was argued by [48, 63]. In other words, the observed shift in velocity between the two peaks demonstrates that this experiment is capable, via the βM method, to measure lifetimes of the order of 1 fs, and that the astrophysical state has a lifetime much longer than 1 fs.

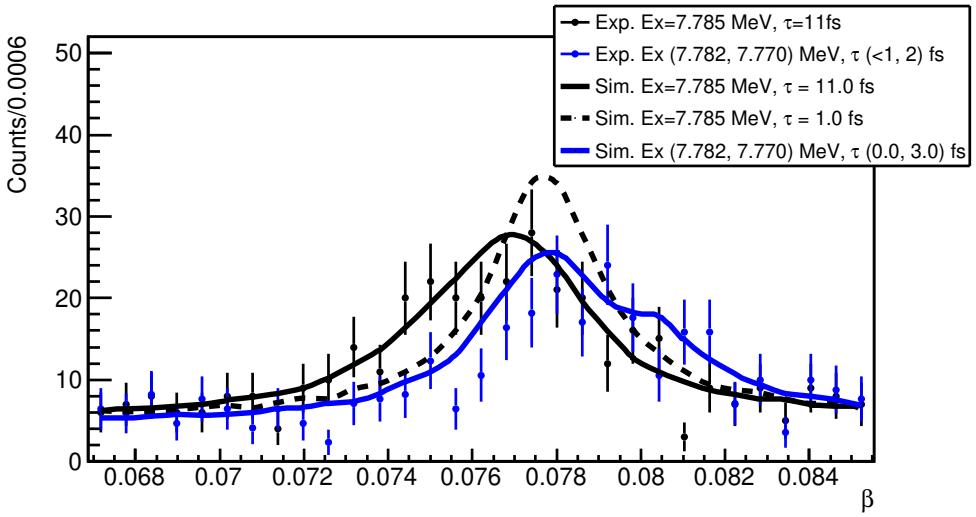

Figure 6.5: Lifetime sensitivity study with the βM method for the high-lying states in ^{23}Mg*. Points correspond to experimental β distributions: black points to the $E_{\gamma,0}$=7333 keV γ-rays from the Ex=7.785 MeV state, blue points to the $E_{\gamma,0}$=5067 keV γ-rays from the Ex=$\{7.782, 7.770\}$ MeV mixed states. Each peak is compared to simulations with: $\tau_{\beta M}$=11 fs (black continuous curve), τ=1 fs (black dashed curve), and τ=$\{0, 3\}$ fs (blue curve) for the expected shorter living Ex=$\{7.782, 7.770\}$ MeV states (Table 6.2). This second simulation included the E_γ mixing. This mixing explains the broadening of the blue peak. Statistics of blue spectra normalized to statistics of black spectra. The observed shift in velocity between the two peaks demonstrates that this experiment is capable, via the βM method, to measure 1 fs lifetimes.

- Results

Final values in (τ, Γ_{tot}, $E_{\gamma,0}$) of the identified states in ^{23}Mg* are listed in Table 6.3 for the βM method. They are compared to previous results obtained with DSAM.

In conclusion, about the new method to access to lifetimes,

1. This approach gathered all experimental data into a single spectrum, contrary to the classical DSAM with measurements at reduced angle slices. Hence, the βM method is well suited for states observed with low statistics.

2. The sensitivity in τ of the βM method is of ∼1 fs.

3. The method allowed us to obtain a finite lifetime of the astrophysical state in ^{23}Mg*, as well as unprecedented measurements for other short-lived states.

4. The γ-ray transition energies $E_{\gamma,0}$ can also be measured, they were found to be consistent with previous results.

	$E_{\gamma,0}$ keV			τ fs			Γ_{tot} meV	
Ex	Ref.	This study		Ref.	This study		This study	
MeV	[55]	DSAM	βM	[55, 52]	DSAM	βM	DSAM	βM
0.451	450.7(15)	451.0(5)	$451.5^{+0.2}_{-0.1}$	1.66(12) ps	1.62(35) ps	1.60(11) ps	$0.41^{+0.11}_{-0.07}$	0.41(3)
2.052	1601.4(13)	1601.8(11)	$1601.2^{+0.3}_{-0.5}$	94(17)	78(19)	85(15)	$8.4^{+2.7}_{-1.7}$	$7.7^{+1.7}_{-1.2}$
2.906	2454.6(7)	$2454.5^{+1.0}_{-1.5}$	2454.9(3)	15(3)	14^{+5}_{-6}	12(5)	47^{+35}_{-12}	55^{+39}_{-16}
3.794	3343.9(13)	/	3345.3(3)	41(6)	<44	40^{+6}_{-7}	>15	$16^{+3.5}_{-2.1}$
3.861	3861.0(7)	/	$3861.4^{+1.2}_{-0.4}$	12(3)	<22	19(6)	>30	35^{+16}_{-8}
4.356	4356.0(20)	/	4357.0(8)	<11	<14	9^{+4}_{-2}	>47	73^{+21}_{-23}
4.681	4230(1)	/	4231.2(8)	10(3)	<16	12(8)	>41	55^{+110}_{-22}
5.287	3236(1)	/	$3241.6^{+0.4}_{-0.3}$	5(2)	<10	4^{+1}_{-3}	>66	165^{+494}_{-33}
5.691	5690(1)	/	$5690.3^{+0.3}_{-0.2}$	∅	<24	28^{+4}_{-5}	>27	24^{+5}_{-3}
6.132	3775(1)	/	$3775.7^{+0.4}_{-0.6}$	∅	<20	18(9)	>33	37^{+37}_{-12}
6.195	3480(1)	/	$3479.2^{+0.4}_{-0.6}$	17(3)	<25	19^{+3}_{-5}	>26	35^{+12}_{-5}
6.240	4188(1)	/	$4188.8^{+0.2}_{-0.4}$	<40	<28	20(3)	>24	33^{+6}_{-4}
6.775	4418(1)	/	$4418.5^{+0.7}_{-0.2}$	∅	<32	16^{+6}_{-3}	>21	41^{+9}_{-11}
6.908	6900(3)	/	$6900.8^{+0.4}_{-0.5}$	<10	<18	8^{+5}_{-2}	>37	82^{+27}_{-32}
6.984	6984(5)	/	$6983.3^{+0.2}_{-0.4}$	∅	<45	30(8)	>15	22^{+8}_{-5}
7.112	6660(1)	/	$6660.0^{+0.8}_{-0.4}$	∅	<14	7^{+5}_{-4}	>47	94^{+125}_{-39}
7.450	7443(3)	/	$7443.7^{+0.2}_{-0.4}$	<14	<18	6^{+8}_{-4}	>36	110^{+219}_{-63}
7.584	3725(6)	/	/	∅	<10	<2	>66	>329
7.770	5054.8(6)	/	5054.4(15)	2(1)	/	3(3)	/	$219^{+(>219)}_{-109}$
7.782	5067.1(11)	/	/	<1	/	<2.5	/	>263
7.785	7333.2(11)	/	$7333.0^{+1.2}_{-0.4}$	10(3)	<17	11^{+6}_{-4}	>39	60^{+34}_{-21}
7.801	7801.3(6)	/	/	∅	<20	<3.5	>33	>188

Table 6.3: Measured properties of states in ^{23}Mg* with the βM method are compared with DSAM results.

6.2.4 Doppler-Corrected Lineshape Method DCLM

- Principle and examples

The new βM method has been validated by measuring lifetimes in agreement with known values, see Table 6.3. Another cross-check of the measured lifetimes was to compare the measured values using another method based on the Doppler-corrected lineshapes: E_γ^{DC} generated from all available angles. Employing a different approach allowed us to strengthen the measured lifetimes. This third method, referred now as DCLM, is explained in the following lines.

1. The Doppler-shifted γ-ray matrices (E_γ, θ_{DS}), as observed by AGATA, were simulated for the chosen state in ^{23}Mg* and its associated spectroscopic parameters: τ and (Ex, $E_{\gamma,0}$).

2. The experimental γ-rays (and simulated ones) were Doppler-corrected, event by event, with the mean velocity written β_{DC}, as given in Eq. (6.1). The parameter β_{DC} was computed from a simulated velocity distribution with the lifetime τ.

$$E_\gamma^{DC} = E_\gamma \frac{1 - \beta_{DC}\cos(\theta_{DS})}{\sqrt{1-\beta_{DC}^2}} \quad \text{with} \;\; \beta_{DC} = \text{mean}(\beta^{\text{Sim.}}(\tau)) \tag{6.1}$$

3. The goodness of fit with χ^2 test was derived between the experimental and simulated Doppler-corrected spectra.

The DCLM method is illustrated with the Ex=6.195 MeV state in Fig. 6.6. The calculated χ^2 is shown as a function of (τ, $E_{\gamma,0}$) in Fig. 6.6(c). It points out a minimum at τ=15 fs and $E_{\gamma,0}$=3486.3 keV. The experimental Doppler-corrected γ-rays (black points) are compared to the simulated profile (red curve) in Fig. 6.6(a) for τ=15 fs. The experimental spectrum and the simulated Doppler-corrected one with τ=1 fs, presented in Fig. 6.6(b), disagree: the found χ^2/ndf is higher than the 1σ uncertainties. The measured $\tau_{\mathrm{DCLM}} = 15^{+3}_{-1}$ fs of the Ex=6.195 MeV state agrees with the previous measurement $\tau_{\beta\mathrm{M}}$=19^{+3}_{-5} fs.

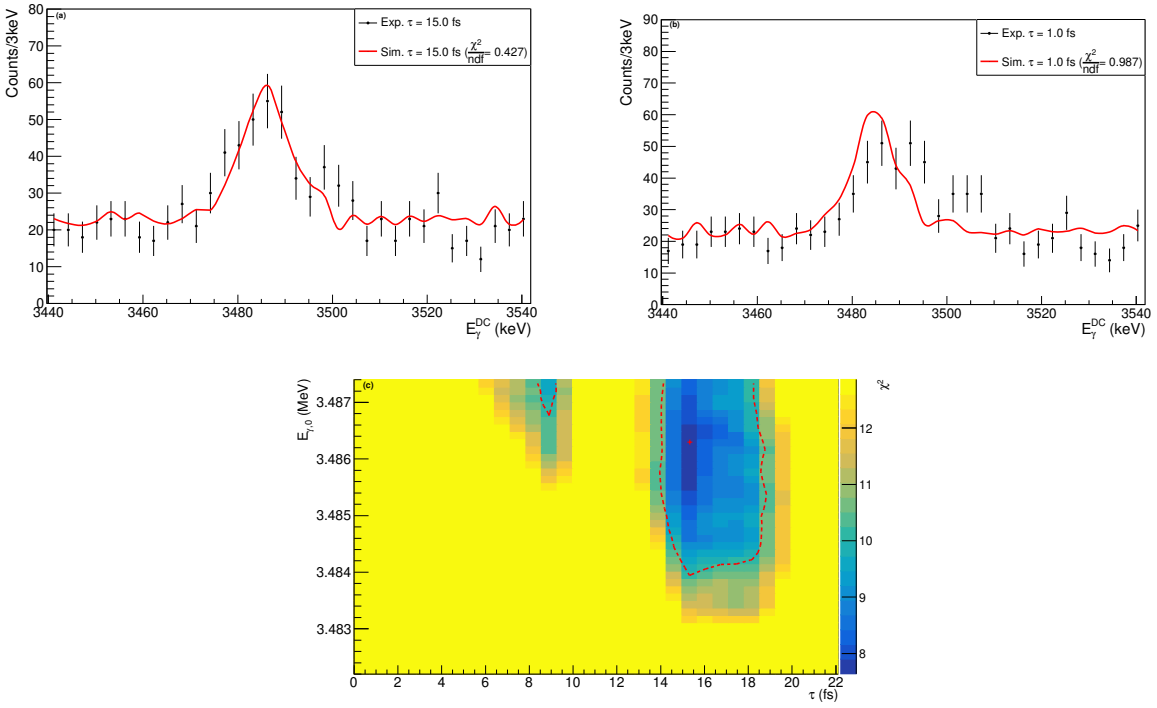

Figure 6.6: Illustration of the DCLM lifetime measurement, here in the case of the Ex=6.195 MeV state in ^{23}Mg*. Panel (c): the χ^2 matrix as a function of the (τ, $E_{\gamma,0}$) parameters presents a minimum at τ=15 fs. The χ^2 minimum is shown by the red cross, the 68 % CL by the red dashed line. The measured lifetime of the Ex=6.195 MeV state is $\tau_{\mathrm{DCLM}} = 15^{+3}_{-1}$ fs with $E_{\gamma,0}$ =3486.3(21) keV. Panels (a, b): the Doppler-corrected experimental γ-rays (black points) are compared to simulated profiles (red curves) with τ=15 fs (a) and τ=1 fs (b).

The results with the DCLM method for the Ex=7.785 MeV key state are presented in Fig. 6.7. A minimum at τ=9.5 fs is apparent in the χ^2 matrix shown in Fig. 6.7(c). The experimental Doppler-corrected γ-rays are compared with the simulated Doppler-corrected spectrum (red curve), at the optimum value τ=9.5 fs in Fig. 6.7(a) and at a poor value τ=1 fs in Fig. 6.7(b). The finite measured τ_{DCLM}=$9.5^{+4.5}_{-2.0}$ fs agrees with the previous measurement $\tau_{\beta\mathrm{M}}$=11^{+6}_{-4} fs.

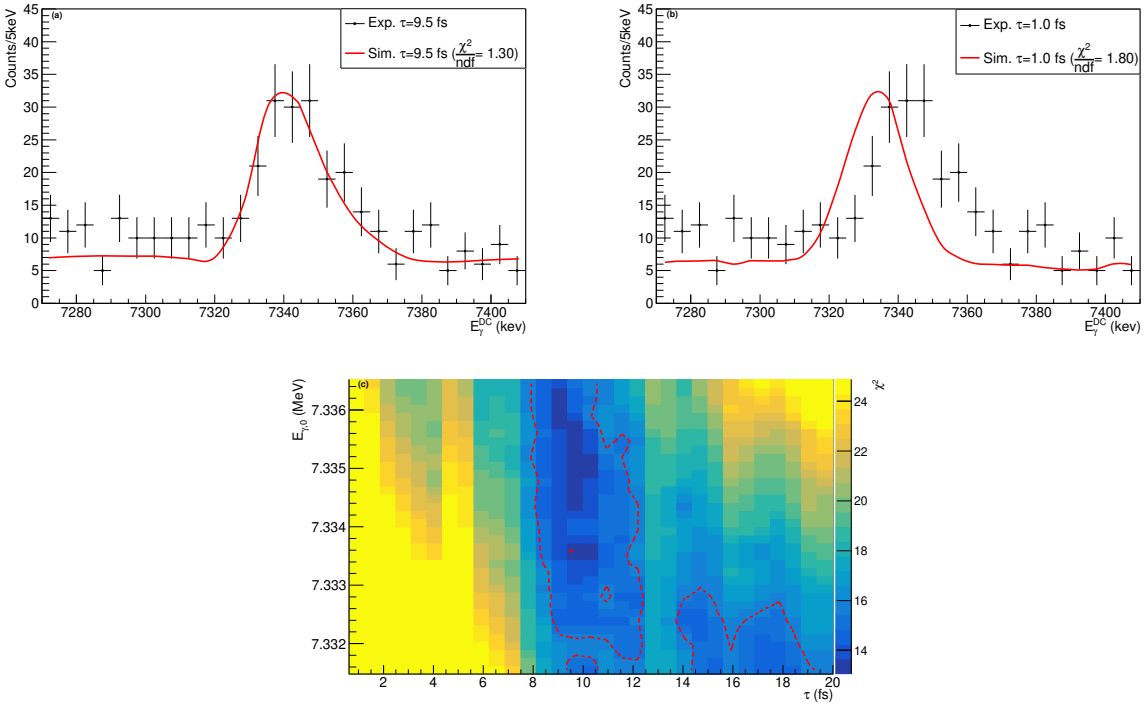

Figure 6.7: The DCLM lifetime measurement of the Ex=7.785 MeV state in ^{23}Mg*. Panel (c): χ^2 matrix as a function of (τ, $E_{\gamma,0}$) points out a minimum at τ=9.5 fs. The measured lifetime is $\tau_{\mathrm{DCLM}} = 9.5^{+4.5}_{-2.0}$ fs with $E_{\gamma,0}$ =7333.5$^{+3.5}_{-2.0}$ keV. Panels (a, b): comparison between the experimental γ-rays and the simulated profiles (red curves) with τ=9.5 fs (a) and with τ=1 fs (b).

- Results

The measured lifetimes τ_{DCLM} with the DCLM method for the identified states in ^{23}Mg* are given Table 6.4 and compared to previous results obtained by the DSAM and βM methods. The relative differences between the measured lifetimes τ_{DCLM} and the measured ones $\tau_{\beta\mathrm{M}}$ with the βM method were derived to check if there were systematic errors with either of these two approaches. The resulting relative differences $\frac{\tau_{\mathrm{DCLM}}-\tau_{\beta\mathrm{M}}}{\tau_{\beta\mathrm{M}}}$ are shown in Fig. 6.8. They were observed to be evenly distributed around 0 which means the methods had no systematic errors.

	$E_{\gamma,0}$ keV				τ fs				Γ_{tot} meV		
Ex	Ref.	This study			Ref.	This study			This study		
MeV	[55]	DSAM	βM	DCLM	[55, 52]	DSAM	βM	DCLM	DSAM	βM	DCLM
0.451	450.7(15)	451.0(5)	$451.5^{+0.2}_{-0.1}$	$451.4^{+0.6}_{-0.4}$	1.66(12)ps	1.62(35)ps	1.60(11)ps	$1.35^{+0.31}_{-0.25}$ps	$0.41^{+0.11}_{-0.07}$	0.41(3)	$0.49^{+0.11}_{-0.09}$
2.052	1601.4(13)	1601.8(11)	$1601.2^{+0.3}_{-0.5}$	$1600.3^{+0.7}_{-0.5}$	94(17)	78(19)	85(15)	90(10)	$8.4^{+2.7}_{-1.7}$	$7.7^{+1.7}_{-1.2}$	$7.3^{+0.9}_{-0.7}$
2.906	2454.6(7)	$2454.5^{+1.0}_{-1.5}$	2454.9(3)	$2453.6^{+1.2}_{-1.0}$	15(3)	14^{+5}_{-6}	12(5)	14^{+3}_{-2}	47^{+35}_{-12}	55^{+39}_{-16}	47(8)
3.794	3343.9(13)	/	3345.3(3)	$3344.8^{+0.8}_{-1.0}$	41(6)	<44	40^{+6}_{-7}	35^{+5}_{-2}	>15	$16^{+3.5}_{-2.1}$	19^{+1}_{-2}
3.861	3861.0(7)	/	$3861.4^{+1.2}_{-0.4}$	3862.5(20)	12(3)	<22	19(6)	16^{+2}_{-1}	>30	35^{+16}_{-8}	41^{+3}_{-5}
4.356	4356.0(20)	/	4357.0(8)	4356.7(9)	<11	<14	9^{+4}_{-2}	$9.5^{+4.5}_{-2.5}$	>47	73^{+21}_{-23}	69^{+22}_{-31}
4.681	4230(1)	/	4231.2(8)	$4230.3^{+1.2}_{-1.8}$	10(3)	<16	12(8)	12^{+4}_{-2}	>41	55^{+110}_{-22}	55^{+11}_{-14}
5.287	3236(1)	/	$3241.6^{+0.4}_{-0.3}$	3240.5(15)	5(2)	<10	4^{+1}_{-3}	6(3)	>66	165^{+494}_{-33}	110^{+110}_{-37}
5.691	5690(1)	/	$5699.3^{+0.3}_{-0.2}$	5699.3(9)	∅	<24	28^{+4}_{-5}	$26^{+2.0}_{-2.5}$	>27	24^{+5}_{-3}	25^{+3}_{-2}
6.132	3775(1)	/	$3775.7^{+0.4}_{-0.6}$	3774.8(20)	∅	<20	18(9)	19^{+2}_{-3}	>33	37^{+37}_{-12}	35^{+7}_{-3}
6.195	3480(1)	/	$3479.2^{+0.4}_{-0.6}$	3486.3(21)	17(3)	<25	19^{+3}_{-5}	15^{+3}_{-1}	>26	35^{+12}_{-5}	44^{+3}_{-7}
6.240	4188(1)	/	$4188.8^{+0.2}_{-0.4}$	4189.5(7)	<40	<28	20(3)	19^{+4}_{-3}	>24	33^{+6}_{-4}	35^{+7}_{-6}
6.775	4418(1)	/	$4418.5^{+0.7}_{-0.2}$	4419.2(11)	∅	<32	16^{+6}_{-3}	14(2.5)	>21	41^{+9}_{-11}	47^{+10}_{-7}
6.908	6900(3)	/	$6900.8^{+0.4}_{-0.5}$	$6903.8^{+4}_{-3.8}$	<10	<18	8^{+5}_{-2}	10^{+7}_{-3}	>37	82^{+27}_{-32}	66^{+28}_{-27}
6.984	6984(5)	/	$6983.3^{+0.2}_{-0.4}$	$6984.8^{+1.4}_{-1.0}$	∅	<45	30(8)	31(4)	>15	22^{+8}_{-5}	21^{+3}_{-2}
7.112	6660(1)	/	$6660.0^{+0.8}_{-0.4}$	6669.5(15)	∅	<14	7^{+5}_{-4}	10^{+1}_{-2}	>47	94^{+125}_{-39}	66^{+16}_{-6}
7.450	7443(3)	/	$7443.7^{+0.2}_{-0.4}$	7442.4(6)	<14	<18	6^{+8}_{-4}	4(3)	>36	110^{+219}_{-63}	165^{+494}_{-71}
7.584	3725(6)	/	/	/	∅	<10	<2	<4	>66	>329	>165
7.770	5054.8(6)	/	5054.4(15)	5054.5(2)	2(1)	/	3(3)	2^{+4}_{-2}	/	$219^{+(>219)}_{-109}$	$329^{+(>329)}_{-219}$
7.782	5067.1(11)	/	/	/	<1	/	< 2.5	<3	/	>263	>21
7.785	7333.2(11)	/	$7333.0^{+1.2}_{-0.4}$	$7333.5^{+3.5}_{-2.0}$	10(3)	<17	11^{+6}_{-4}	$9.5^{+4.5}_{-2.0}$	>39	60^{+34}_{-21}	60^{+18}_{-22}
7.801	7801.3(6)	/	/	/	∅	<20	<3.5	<2.5	>33	>188	>263

Table 6.4: Measured properties of states in ^{23}Mg* by the DCLM method, and comparisons with the DSAM results and the βM results.

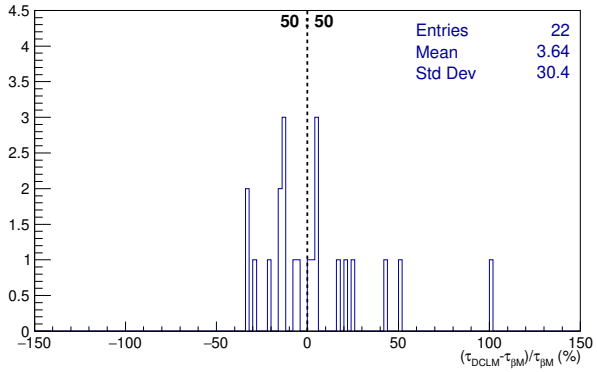

Figure 6.8: Distribution of the relative differences $\frac{\tau_{\mathrm{DCLM}}-\tau_{\beta\mathrm{M}}}{\tau_{\beta\mathrm{M}}}$ between the measured lifetimes using the DCLM method with respect to the measured ones with the βM method. The count halves were observed on both sides of 0, showing that the methods did not present any systematic errors.

In conclusion, the DCLM lifetime and γ-ray energy measurements agree with the βM results.

6.2.5 Systematic uncertainties

- Target position

The target position is of importance for the lifetime analysis. The γ-ray lineshape is strongly influenced by this parameter. The reconstruction of the target position is usually not required in usual analysis. Here, its position as well as the detectors ones were measured by surveyors before the experiment took place. However, during the analysis, a systematic error was found in the measured γ-rays from states in ^{23}Mg* with well-known lifetimes. While doing an exhaustive study of the different possible origins of this error, the target position along the beam axis was built back with some contradictory results. Thus, two methods were proposed to independently measure the target position.

First, it is possible to accurately measure the target position with the analysis of a well known state in ^{23}Mg*. For short-lived states, the γ-ray emissions happened inside the target. In the EVASIONS code, the position of AGATA with respect to target (Z^{AGATA}) was varied, as well as the state lifetime. The derived χ^2 as a function of (Z^{AGATA}, τ) with DCLM are shown in Fig. 6.9(a) for the Ex=3.794 MeV state, in Fig. 6.9(b) for the Ex=5.287 MeV state and in Fig. 6.9(c) for the Ex=2.906 MeV state. Minimums in χ^2 are noticed. The results in Z^{AGATA} and τ_{DCLM} are listed Table 6.5 for these three example states.

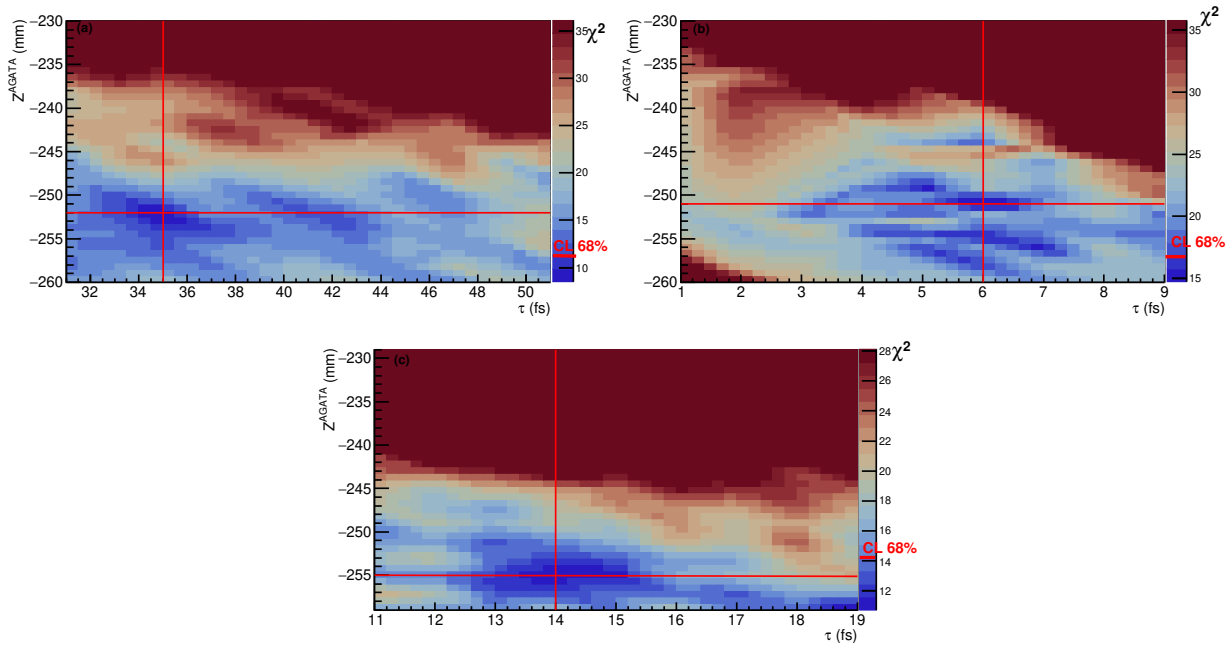

Figure 6.9: Measurement of the target distance with respect to the AGATA reference point by the DCLM lifetime measurements on known lifetime states. Results in χ^2 are shown as a function of the AGATA position (Z^{AGATA}) from the target and of the state lifetime τ. Panel (a): the Ex=3.794 MeV state with expected τ=41(6) fs [55]. Panel (b): the Ex=5.287 MeV state with τ=5(2) fs [55]. Panel (c): the Ex=2.906 MeV state with τ=15(3) fs [55].

Ex MeV	τ fs, Ref. [55]	τ_{DCLM} fs	Z^{AGATA} mm
2.906	15(3)	14^{+3}_{-2}	$-255^{+4.5}_{-2.5}$
3.794	41(6)	35^{+5}_{-2}	-252^{+1}_{-2}
5.287	5(2)	6(3)	$-251^{+1.5}_{-5.5}$

Table 6.5: Results in the measured AGATA positions Z^{AGATA} by using DCLM on known lifetime states.

The three independent measured positions of AGATA, see Fig. 6.9 and Table 6.5, were averaged to get the final value with a high resolution: Z^{AGATA}=-252.3(17) mm. This value was used in the analysis presented along this thesis.

The second approach to measure the target position makes use of the ^{4}He ejectiles measured both in VAMOS and in the small gas chamber. The ejectile angle $\theta^{\mathrm{DCT}}_{^4\mathrm{He}}$, in the small drift chambers, was built back as a function of the detector position with respect to target (Z^{DCT}). From the observed shift between $\theta^{\mathrm{DCT}}_{^4\mathrm{He}}$ and $\theta^{\mathrm{VAMOS}}_{^4\mathrm{He}}$ upon the input Z^{DCT}, it is possible to determine the target position. The position of the target Z^{DCT} is obtained for the minimum value of mean($|\theta^{\mathrm{DCT}}_{^4\mathrm{He}} - \theta^{\mathrm{VAMOS}}_{^4\mathrm{He}}|$). The results are shown in Fig. 6.10. The proper distance from the target to the small gas chamber was found to be $Z^{\mathrm{DCT}}=148^{+12}_{-8}$ mm. The precision of the method is about 10 mm, that is less accurate than in the first method, of 1.7 mm.

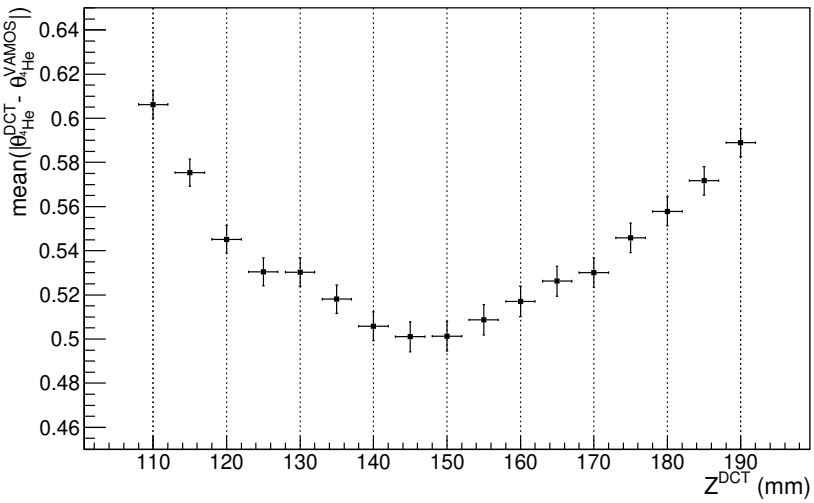

Figure 6.10: Evolution of the average difference between $\theta^{\mathrm{DCT}}_{^4\mathrm{He}}$ and $\theta^{\mathrm{VAMOS}}_{^4\mathrm{He}}$, written mean($|\theta^{\mathrm{DCT}}_{^4\mathrm{He}} - \theta^{\mathrm{VAMOS}}_{^4\mathrm{He}}|$), versus the small gas chamber position Z^{DCT} along beam direction. The minimum, for $Z^{\mathrm{DCT}}=148^{+12}_{-8}$ mm, is measured as the proper distance from the target to this detector.

The determined target position (and its precision) with respect to the detectors impacts the reconstructed Doppler angle θ_{DS}, the resulting uncertainties are of the order of the AGATA angular resolution ($\sim$1 deg).

The measurements of the target position are consistent between the two independent methods. The results are associated with a shift of the target position along the beam axis of 17 mm compared to the surveyor value. Similarly, the experimental β distributions were well in agreement with the simulated profiles for a target shifted by 17 mm.

- Target implatantion profile

We have shown with EVASIONS simulations that the two expected ^{3}He implantation profiles did not impact the γ-ray spectrum for the limit of AGATA energy resolution ($\delta E_\gamma \sim 2$ keV), see Sec.4.2.2. We have also derived the consequences of ^{3}He implanted ions in gold medium, resulting in $\leq$1 % change in stopping powers.

- Other sources of systematic uncertainties

There are other possible sources of systematic uncertainties. The γ-ray lineshape and the β distribution depend also on the beam dispersion, the intrinsic resolution of AGATA detector, the uncertainties of the reconstructed Doppler angle θ_{DS}, the stability of the AGATA energy calibration during the experiment which was correct down to 2 keV (see Fig. 3.21) . The EVASIONS code helped us at quantifying the sensitivity of the lifetime measurement to the different experimental parameters. Results are summarized in Table 6.6. Lifetime, last row, is among the most impacting parameters to the γ-ray and β observables.

Effect	$\frac{dE_\gamma}{E_\gamma}$ (%)	$\frac{d\beta}{\beta}$ (%)
Detector resolution (energy, angle)[a]	(0.064, 0.046)	(0.954, 0.740)
Beam dispersion (energy, transverse space)[a]	(0.029, 0.002)	(0.419, 0.017)
Depth profile[b] of ^{3}He	0.0277	0.389
Stopping powers in medium (1% uncertainties)	0.007	0.065
Uncertainties in reconstructed θ_{DS} of <1 deg	<0.065	<0.75
Energy calibration error of 2 keV along experimental time	0.015	0.23
Shift in τ of 1 fs	0.044	0.650

[a] From measured σ

[b] Between target entrance and maximum depth

Table 6.6: Quantification of the main experimental contributions to the γ-ray lineshape and to the reconstructed β at emission. Relative importances were derived from EVASIONS simulations for the ^{23}Mg state with (Ex=7.785 MeV, $E_{\gamma,0}$=7.333 MeV, τ=1 fs).

In conclusion, the AGATA resolutions in energy and angle are the two dominant contributions in systematic uncertainties for the lifetime measurements. They have an effect equivalent to a lifetime shift of about 1 fs.

6.2.6 Conclusion

Three methods were employed to access to lifetimes. If the experimental datasets used in the different approaches were independent, the resulting lifetime would be equal to the weighted average of the found values, and the uncertainty to the standard deviation of the weighted average. More details can be found in Sec.39.2 of Ref. [110]. If the same experimental dataset is used with different analysis methods, as it is the case in this study, the measured lifetimes are not independent and so, the final result is more complex to estimate. In principle, one would expect to obtain the same value for each approach since the experimental dataset is the same. However, the analysis methods convert the experimental data into physics distributions differing in statistics and sensitivity, from which the lifetimes are then estimated. In particular, one approach (DSAM) does not carry enough statistics for measuring lifetimes. However, wise calculations allowed us to gather the whole γ-ray dataset into either a single velocity distribution or a single Doppler-corrected γ-ray spectrum. Analysis were so done on dataset with higher statistics and improved sensitivity, contrary to the usual technique of decreasing the spectrum binning when one wants higher statistics per bin.

The different lifetime measurements of the identified states in ^{23}Mg* were observed consistent between the three methods and literature values, see Table 6.4. For the final values given in Table 6.7, we decided

to use the weighted average of the measured lifetimes with the βM and DCLM methods (plus DSAM if successful), and the smallest statistical uncertainties for the final uncertainties.

$$\tau = \frac{1}{\frac{1}{\sigma^2_{\beta\mathrm{M}}} + \frac{1}{\sigma^2_{\mathrm{DCLM}}}} \times \left(\frac{\tau_{\beta\mathrm{M}}}{\sigma^2_{\beta\mathrm{M}}} + \frac{\tau_{\mathrm{DCLM}}}{\sigma^2_{\mathrm{DCLM}}}\right) \qquad \pm \min(\sigma_{\beta\mathrm{M}}, \sigma_{\mathrm{DCLM}}) \tag{6.2}$$

		Present work	
Ex (MeV)	τ (fs) [55]	τ (fs)	Γ_{tot} (meV)
0.4514(1)	1.66(1.2) ps	$1.50^{+0.31}_{-0.25}$	$0.44^{+0.09}_{-0.08}$
2.0524(5)	94(17)	87(10)	$7.6^{+1.0}_{-0.8}$
2.9055(7)	15(3)	14^{+3}_{-2}	47(8)
3.7967(4)	41(6)	36.7^{+5}_{-2}	18^{+1}_{-2}
3.8617(8)	12(3)	16.3^{+2}_{-1}	40^{+3}_{-4}
4.3569(8)	<11	9.2^{+4}_{-2}	72^{+20}_{-22}
4.6825(9)	10(3)	12^{+4}_{-2}	55^{+11}_{-14}
5.2939(9)	5(2)	5(3)	132^{+197}_{-49}
5.6993(3)	⌀	26.5^{+2}_{-3}	25^{+3}_{-2}
6.1326(12)	⌀	18.9^{+2}_{-3}	35^{+7}_{-3}
6.1941(10)	17(3)	16.1^{+3}_{-1}	41^{+3}_{-6}

		Present work	
Ex (MeV)	τ (fs) [55]	τ (fs)	Γ_{tot} (meV)
6.2414(8)	<40	19.6(3)	34^{+6}_{-4}
6.7757(14)	⌀	14.4^{+4}_{-3}	46^{+12}_{-10}
6.9008(5)	<10	8.7^{+5}_{-2}	76^{+23}_{-28}
6.9834(3)	⌀	30.8(4)	21^{+3}_{-2}
7.1135(7)	⌀	9.6^{+1}_{-2}	69^{+18}_{-6}
7.4433(3)	<14	4.2(3)	157^{+392}_{-65}
7.583(6)	⌀	<2	>329
7.7689(20)	2(1)	2.6^{+3}_{-2}	253^{+844}_{-136}
7.7818(9)	<1	<2.5	>263
7.7845(9)	10(3)	$9.9^{+4.5}_{-2.0}$	66^{+17}_{-21}
7.8030(6)	⌀	<2.5	>263

Table 6.7: Experimental results in total widths from the measured lifetimes by combining the βM and DCLM methods (and DSAM if successful) of states in ^{23}Mg*. The excitation energies Ex were averaged between literature and our work from the measured $E_{\gamma,0}$.

6.3 Proton width

With the knowledge of the total width of the Ex=7.785 MeV state, the proton width could be estimated by measuring BR_p. Two methods have been proposed to extract BR_p, see Sec2.2.3. We start here with the first method.

- Identification of proton decays from states in ^{23}Mg*

The protons, emitted from the Ex=7.785 MeV state, have first to be identified through the coincidences between the measured excitation energies Ex^{VAMOS} (from the measured ^{4}He) versus Ex^{SPIDER} (from the measured protons). A background noise subtraction was prior applied, bin to bin, by using the similar (Ex^{VAMOS}, Ex^{SPIDER}) matrix measured with the pure gold target, shown in Fig. 6.11. The Fig. 6.12(a) presents the experimental matrix after this background noise subtraction. Red lines mark the expectation energies of the emitted protons to the ground state and the first Ex=0.583 MeV state in ^{22}Na*. The Ex^{SPIDER} was reconstructed assuming energy conservation. Hence, by missing energies, Ex^{SPIDER} is equal to the excitation energies in ^{22}Na*:

$$Ex^{VAMOS} - Ex^{SPIDER} = Ex(^{22}\mathrm{Na}) \tag{6.3}$$

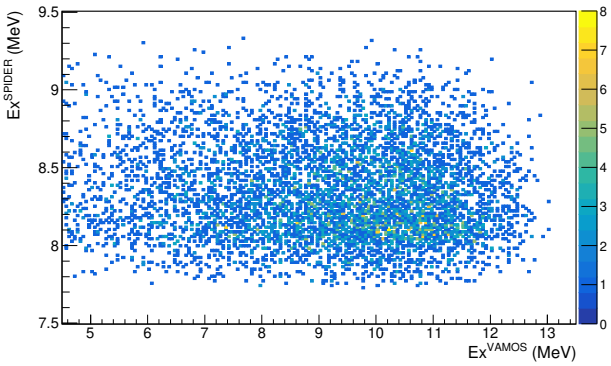

Figure 6.11: Measured (Ex^{VAMOS}, Ex^{SPIDER}) matrix with the pure gold target.

Without taking into account the energy straggling of the protons in target, the simulated (Ex^{VAMOS}, Ex^{SPIDER}) plot shown in Fig. 6.12(b) was obtained by considering the proton decays of the 10 states in $^{23}Mg^{*}$ given in Fig. 6.13. The states with excitation energies above 8.163 MeV decay by protons to both the ground state and the first excited state in $^{22}Na^{*}$. The Fig. 6.12(b) clearly shows that the parameter Ex^{VAMOS} is mandatory in order to avoid a mixing between protons emitted from states around Ex$\sim$7.8 MeV and from states around Ex$\sim$8.3 MeV which decay to the Ex=0.583 MeV state in $^{22}Na^{*}$. This idea obviously extends to higher excited states in $^{23}Mg^{*}$ able to populate higher lying states in $^{22}Na^{*}$. The simulated (Ex^{VAMOS}, Ex^{SPIDER}) matrix in Fig. 6.12(c) includes the proton energy straggling. This simulated 2D plot for the 10 states looks like the measured plot shown in Fig. 6.12(a). This good agreement between the two figures proves that protons emitted from unbound states in $^{23}Mg^{*}$ were detected. The expected protons from the Ex=7.785 MeV state are isolated in the simulated Fig. 6.12(d), shown then in the black square in Fig. 6.12(a). By a qualitative comparison with experimental data, the aimed protons seemed hardly visible above the noise level.

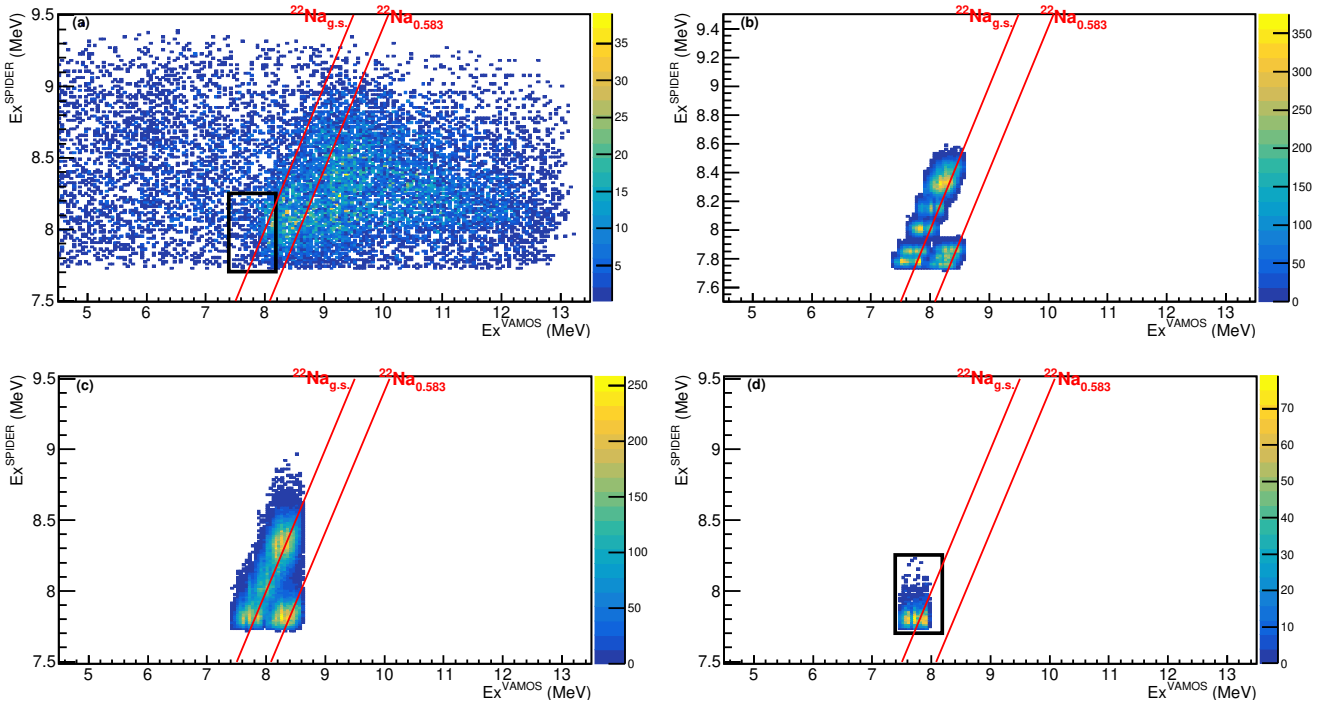

Figure 6.12: Analysis of coincidences between populated states and proton decays in ^{23}Mg* with the reconstructed (Ex^{VAMOS}, Ex^{SPIDER}) matrices. Red lines indicate the populations of the ground state and the first excited state in ^{22}Na*. Panel (a): experimental matrix after background noise subtraction. Panel (b): simulated matrix for proton decays from the 10 states in ^{23}Mg*, shown in Fig. 6.13, without straggling effect in gold. Panel (c): similar simulated matrix where straggling is implemented. The induced degradation in energy resolution agrees well with the experimental one in (a). Emitted protons from the first proton unbound states in ^{23}Mg* were thus identified. Panel (d): simulated matrix where only the Ex=7.785 MeV key state is considered for comparison with experimental matrix (a). The emitted protons from the key state are expected in the black square, they hardly appear above the background noise.

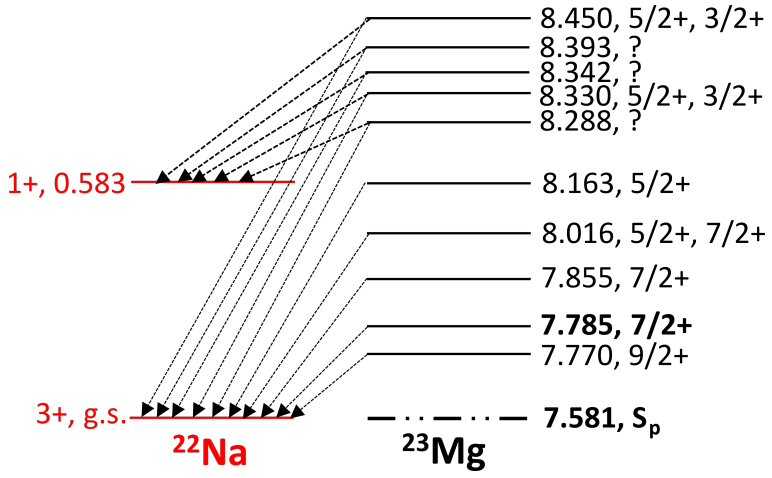

Figure 6.13: Proton decay scheme of states in ^{23}Mg*, up to 1 MeV above the proton threshold, used for the simulations shown in Fig.6.12. States were chosen according to their spins if known, allowing ℓ=0 or ℓ=2 proton emission, or to possible mixing with the Ex=7.785 MeV state.

A selection on the ^{22}Na ground state line with $|\mathrm{Ex}^{\mathrm{VAMOS}} - \mathrm{Ex}^{\mathrm{SPIDER}}| \leq 0.45$ MeV, justified by the resolution on $\mathrm{Ex}^{\mathrm{VAMOS}}$, was applied to obtain the $\mathrm{Ex}^{\mathrm{SPIDER}}$ spectrum shown in Fig. 6.14. It was done both on experimental data (black points) and on simulated states (colour histograms). The resolution is ∼100 keV FWHM. The key state is shown with the red histogram. Furthermore, the Ex=7.855 MeV (8.016 MeV) higher-lying state was well identified as the purple (cyan) curve. They allowed us to check the $\mathrm{BR_p}$ derivation. The total histogram (black curve) was derived by adding weighted state contributions, at the exception of the Ex=7.770 MeV state. This last one is well known: $\tau = 2(1)$[49], J=$\frac{9}{2}$[55], $\omega\gamma$<0.5 meV[46], its γ-ray decay channel was also observed in our experiment. Hence, its contribution was constrained according to $\mathrm{BR_p}$<0.2 %. The total histogram of simulations was associated with the lowest χ^2/ndf compared to experimental points. The χ^2/ndf was only derived within the astrophysical region ($\mathrm{Ex}^{\mathrm{SPIDER}} \in [7.65, 7.85]$ MeV).

The number of counts, derived for an aimed sate peak in Fig. 6.14, was corrected by the detection efficiency, the SPIDER intrinsic efficiency was assumed to be 100 % and the geometric efficiency was estimated through simulations with EVASIONS. The remaining background noise, apparent in Fig. 6.12(a), was estimated by looking at $\mathrm{Ex}^{\mathrm{SPIDER}}$ selected on the $\mathrm{Ex}^{\mathrm{VAMOS}}$ region below the ground state line of ^{22}Na. The resulting background noise spectrum for the Ex=7.785 MeV key state, given in Fig. 6.15, was noticed low. The absolute values $\mathrm{I_{Ex\&p}}$ were so got, this parameter was combined with the absolute number of observed γ-rays $\mathrm{I_{Ex\&\gamma}}$ in Eq. (2.6) to finally extract $\mathrm{BR_p}$.

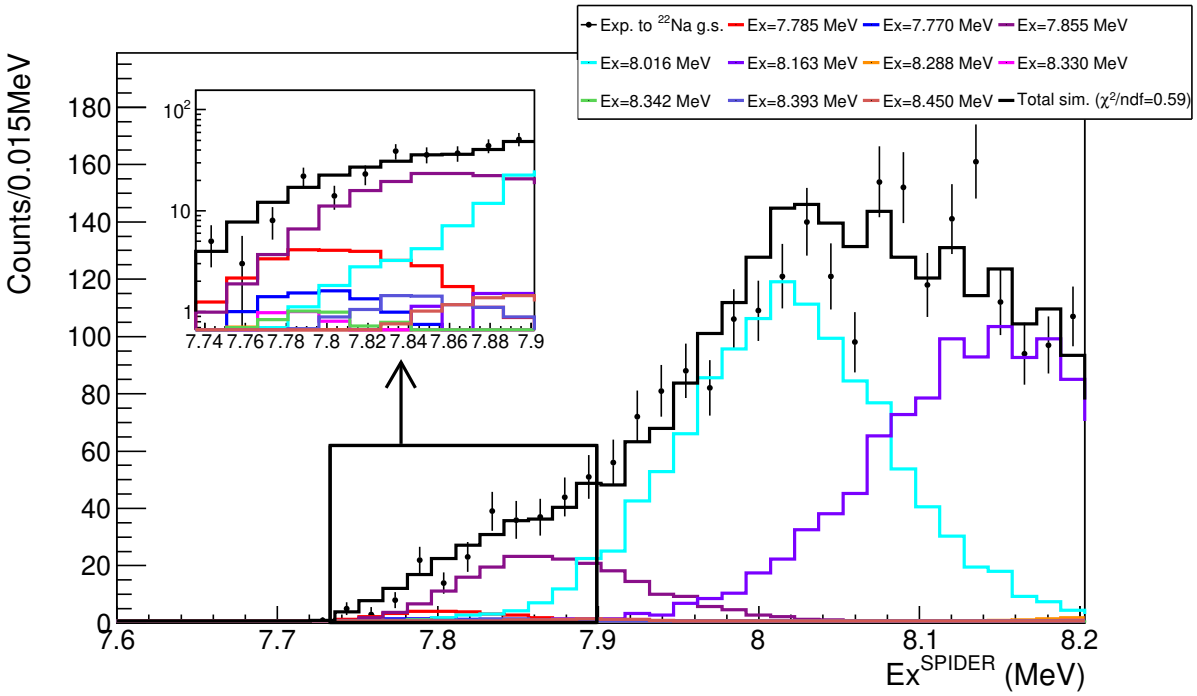

Figure 6.14: Analysis of the proton spectrum emitted from states in ^{23}Mg*. Experimental $\mathrm{Ex}^{\mathrm{SPIDER}}$ (black points) and simulated ones (colour lines) were selected on the populated ^{22}Na ground state line. The contributions of all known states in the region of interest were taken into account in the fit, the sum of all contributions is shown with the black curve. A zoom within the key state is presented in the upper caption. The Ex=7.785 MeV simulated contribution corresponds to the red curve. This plot demonstrates its population can not be large.

Effect	$\frac{dEx}{Ex}$ (%)
Detector resolution (energy, angle)[a]	(0.090, 0.014)
Beam dispersion (energy, transverse space)[a]	(0.319, 0.01)
Depth profile[b] of ^{3}He	0.255
Stopping powers in medium (1 % uncertainties)	0.192
Proton energy straggling in gold target+foil	0.372
Shift in τ of 1 fs	0.063

[a] From measured σ

[b] Between target entrance and maximum depth

Table 6.8: Quantification of the experimental uncertainties contributing to the determined Ex from observed protons. Relative importances derived from simulations for the ^{23}Mg state with (Ex=7.785 MeV, S_p=7.581 MeV, τ=1 fs).

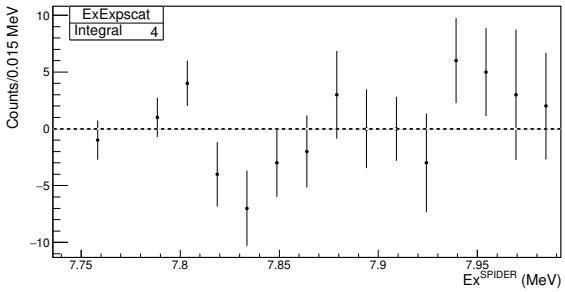

Figure 6.15: Experimental noise spectrum of Ex^{SPIDER}, after a selection on the events with -1.5 MeV $\leq Ex^{VAMOS} - Ex^{SPIDER} \leq$-0.5 MeV. The remaining noise contribution is seen low.

The main experimental uncertainties contributing to the determined Ex have been quantified with the EVASIONS code. They are summarized in Table 6.8: the proton energy straggling is noticed as the highest contribution.

- Results

From identified unbound states, BR_p have been investigated. The results are summarized in Table 6.9. In the case of the other two higher-lying states, the estimated BR_p are only lower limits since the γ-ray decays were not observed: $I_{Ex\&\gamma}$ were taken to be the background noise level of the γ-ray spectrum. With their $\omega\gamma$ (and J) values known, the proton branching ratios were also estimated by taking τ from shell-model calculations, see Sec.7.2, in order to check the measured limits in BR_p were coherent. From Table 6.9, a reasonable agreement is apparent for these two states, strengthening so the present analysis on BR_p. In the cases of states with Ex>8.5 MeV, the BR_p estimation was more complex since their emitted protons were not stopped in the SPIDER ΔE ring.

Ex MeV	BR_p (%)	BR_p (%) This study	BR_p (%) from ($\omega\gamma$, J) Ref. [46, 55], τ (shell model, Sec.7.2)
7.785	0.65(8)[48]	0.68(6)	/
7.855	∅	>40[a]	67
8.016	∅	>60[a]	50[b]

[a] $I_{Ex\&\gamma}$ taken at noise level in E_γ since γ-ray transitions not observed.

[b] $J=\frac{9}{2}$ from shell model (Sec.7.2).

Table 6.9: Results obtained on proton branching ratios BR_p to the ground state in ^{22}Na for three states in ^{23}Mg* of astrophysical interest. Main uncertainties in BR_p originate from remaining background noise. Since γ-ray transitions were not observed for the Ex=$\{7.855, 8.016\}$ MeV states, the BR_p represent only lower limits. The observed trend is expected: the higher the excitation energy, the greater the proton width and therefore the greater the ratio in general.

The second method to measure BR_p, presented in Sec. 2.2.3, was tried out. The main idea of the method is to quantify the number of emitted protons from the number of measured ^{4}He with and

without coincidence with γ-rays. However, the background noise contribution in the ^{4}He ejectile energy spectrum from fusion-evaporation reactions was very important. It induced large uncertainties for the estimated number of events of the Ex=7.785 MeV populated state. The branching ratio was estimated: $\mathrm{BR_p} = 15^{+16}_{-15}$ %. This poor sensitivity was expected since 10^3 counts were measured whereas $5{\times}10^4$ counts are needed to reach a sensitivity better than 1 %, see Fig. 2.4.

To conclude this part,

1. Protons emitted from unbound states in ^{23}Mg* close to threshold have been observed, including the ones from the key state.

2. For the key state, we measured $\mathrm{BR_p}$= 0.68(6) % associated with $\Gamma_\mathrm{p} = 0.45^{+0.16}_{-0.17}$ meV.

6.4 Spin

Our approach to access to the spin J of the Ex=7.785 MeV state was explained in Sec.2.2.4. It is based on the relative value of the compound nucleus cross sections, which is a function of the spin. The measured differential cross sections $(\frac{\mathrm{d}\sigma}{\mathrm{d}\Omega_\alpha}^{\mathrm{lab}})^{\mathrm{Exp}}$ were gathered in Fig. 6.16(a). They were then compared to the calculated $(\frac{\mathrm{d}\sigma}{\mathrm{d}\Omega_\alpha}^{\mathrm{lab}})^{\mathrm{Sim}}$ with TALYS [65, 66] in Fig. 6.16(b) for known J. Predictions from TALYS included both Ex and 2J+1 dependencies on the cross sections. The key state, surrounded in red, was preliminary taken as J=$\frac{7}{2}$ in the calculations. No real rule can be observed in this plot. Two trends were seen:

1. $(\frac{\mathrm{d}\sigma}{\mathrm{d}\Omega_\alpha}^{\mathrm{lab}})^{\mathrm{Exp}} \sim 3 \times (\frac{\mathrm{d}\sigma}{\mathrm{d}\Omega_\alpha}^{\mathrm{lab}})^{\mathrm{Sim}}$ for Ex<4.4 MeV, where additional reaction mechanisms, like transfer reactions, most likely contributed to the measured differential cross sections, similarly to [111],

2. $(\frac{\mathrm{d}\sigma}{\mathrm{d}\Omega_\alpha}^{\mathrm{lab}})^{\mathrm{Exp}} \sim 0.3 \times (\frac{\mathrm{d}\sigma}{\mathrm{d}\Omega_\alpha}^{\mathrm{lab}})^{\mathrm{Sim}}$ for Ex>4.4 MeV.

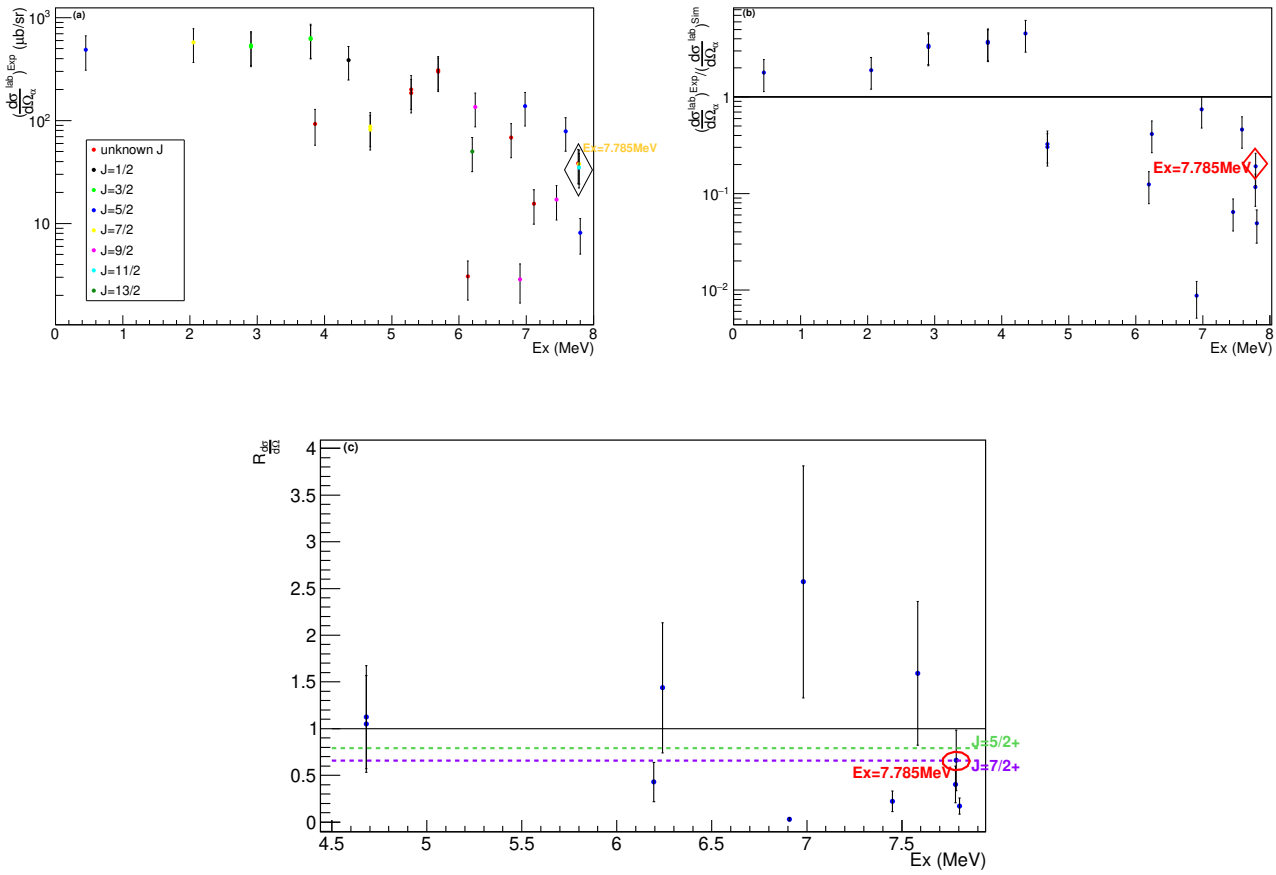

Figure 6.16: Analysis of differential cross sections $(\frac{d\sigma}{d\Omega_\alpha}^{lab})$ of states in $^{23}Mg^*$ in order to access to the spin J of the Ex=7.785 MeV state which is shown in the surrounded regions. Panel (a): the estimated $(\frac{d\sigma}{d\Omega_\alpha}^{lab})^{Exp}$ from experimental data as a function of Ex are separated in colors according to known J (or unknown in red). Panel (b): experimental values are compared to calculated $(\frac{d\sigma}{d\Omega_\alpha}^{lab})^{Sim}$ for the compound nucleus with TALYS [65, 66]. The key state spin was taken as J=$\frac{7}{2}$ in calculations. Two conducts observed: experiment higher than calculations for Ex<4.4 MeV and the opposite for Ex>4.4 MeV, see details in text. Panel (c): the ratio $R_{\frac{d\sigma}{d\Omega}}$ after renormalization of calculated values, from Eq. (6.4), is shown as a function of Ex above 4.4 MeV. Dotted lines mark $R_{\frac{d\sigma}{d\Omega}}$ values if the TALYS input J of the Ex=7.785 MeV state is either $\frac{7}{2}^+$ (purple) or $\frac{5}{2}^+$ (green). From past works on other nuclei, the calculated values were expected to reproduce experiment, up to a reasonable factor 2.

Using states above 4.4 MeV with well-known J, the reduction factor was found of $f^{sim}_{compound} = 0.29(22)$. The derived ratio $R_{\frac{d\sigma}{d\Omega}}$ calculated with Eq. (6.4), is shown as a function of Ex in Fig. 6.16(c).

$$R_{\frac{d\sigma}{d\Omega}} = \frac{(\frac{d\sigma}{d\Omega_\alpha}^{lab})^{Exp}}{f^{sim}_{compound} \times (\frac{d\sigma}{d\Omega_\alpha}^{lab})^{Sim}} \tag{6.4}$$

The dispersion of the points was observed up to a factor 5. From [111] among others, the dispersion was noticed of a factor 1.5. TALYS predictions for the key state are
- $R_{\frac{d\sigma}{d\Omega}} = 0.79$ if J= $\frac{5}{2}$ (green dotted line)
- $R_{\frac{d\sigma}{d\Omega}} = 0.66$ if J= $\frac{7}{2}$ (purple dotted line).

The difference between these two values is too weak and the statistical uncertainties on the evaluated cross section are too high to conclude anything about this state, see Fig. 6.16(c).

As a conclusion, even if we were able to predict the cross sections of these states precisely with the TALYS code, using other optical parameters for example, we would not be able to determine the spin of these states because the statistical uncertainties on the measured cross sections are too large, larger than the expected difference between two spins.

6.5 Conclusion

Among the spectroscopic parameters of the Ex=7.785 MeV state aimed in this experiment, two have been successfully measured by our experimental work. The new measurements in lifetime and in proton branching ratio are presented in Fig. 6.17 and compared to the other works. The measured total and proton widths are very narrow: $\Gamma_{\rm tot} = 66^{+17}_{-21}$ meV and $\Gamma_{\rm p} = 0.45^{+0.16}_{-0.17}$ meV. Is it expected for such high-lying state? Is there any hint from theoretical models with respect to the state spin? With these questions in mind, the next Chapter 7 presents the theoretical calculations undergone and the final compilation of all results to access to an unambiguous $\omega\gamma$.

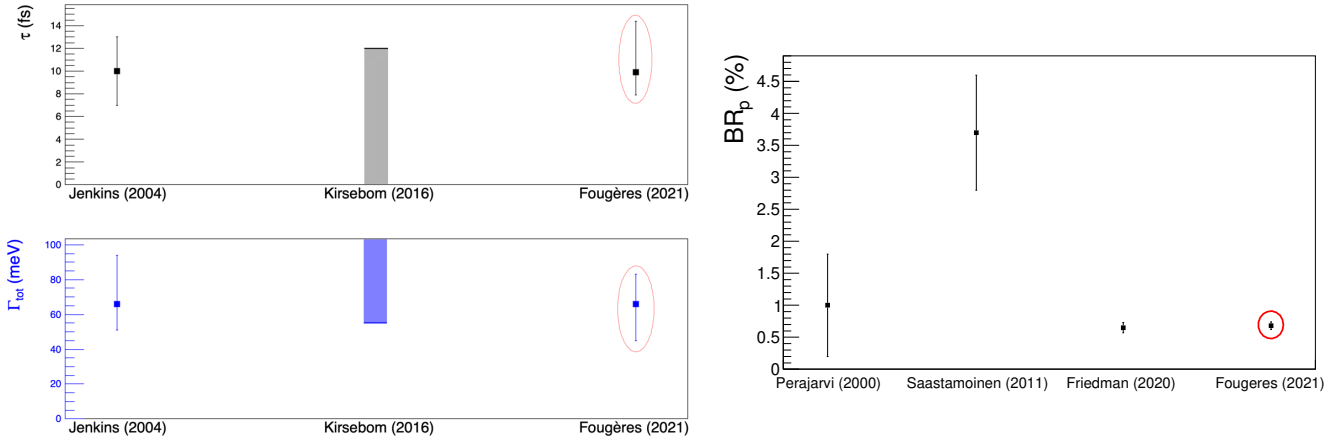

Figure 6.17: Current status of the lifetime (top left), the total width (bottom left) and the proton branching ratio (right) measurements for the Ex=7.785 MeV state in ^{23}Mg*. Present results of Fougères *et al* are shown in the red circles. The measured τ agrees with the past one from Jenkins *et al* [49]. The estimated $\rm BR_p$ agrees with the recent measurement of Friedman *et al* [48] and with Perajarvi *et al* [51].

CHAPTER 7

Determination of the resonance strength

7.1 Introduction

The aim of this work is to measure the resonance strength of the Ex=7.785 MeV excited state in ^{23}Mg*. The spin of this E_R=0.204 MeV resonant state being uncertain, we extended our approach by looking for predictions from theoretical tools. They also allowed us to examine our results on the widths (Γ_{tot}, Γ_p). The other resonance strengths of interest at peak nova temperatures were looked at, in order to verify the reliability of the theoretical results.

All that shell model can say about the spin of the resonant state is presented in Sec.7.2. In Sec.7.3, all information from experimental and theoretical works are gathered to determine an unambiguous new value of $\omega\gamma$ of the E_R=0.204 MeV resonance.

7.2 Spins of the ^{23}Mg resonant states from the perspective of shell model

7.2.1 Introduction

The shell-model diagram of the ^{23}Mg nucleus is drawn in Fig. 7.1. Shell model is perfectly relevant to study such light nuclei where the sd shells are involved. Reliable predictions for the states in ^{23}Mg* are expected.

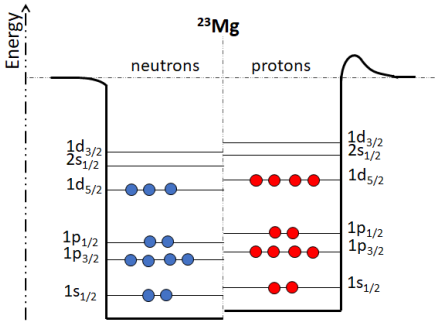

Figure 7.1: Scheme of ^{23}Mg nucleus in the shell-model frame.

Regarding the unbound states in ^{23}Mg*, four have been shown of interest for the s-wave proton capture on ^{22}Na within the nova Gamow window. They are presented in Table 7.1. The key state n_R=1 with

E_R=0.204 MeV is noticed close in energy to the state n_R=2, to only 18 keV. This later state is the Isobaric Analogue State (IAS) of the ground state in ^{23}Al, with T = $\frac{3}{2}$ and $J^\pi = \frac{5}{2}^+$. This energy proximity and the possibility that the key state has a spin $\frac{5}{2}^+$ have opened the question of a possible isospin mixing between the IAS and the key state.

n_R	Ex MeV	E_R=$E_p^{c.m.}$ MeV	J^π
1	7.785	0.204	$\frac{7}{2}^+$[49], $\frac{5}{2}^+$[63]
2 (IAS)	7.803	0.222	$\frac{5}{2}^+$
3	7.855	0.274	$\frac{7}{2}^+$
4	8.016	0.435	$\frac{5}{2}^+$, $\frac{7}{2}^+$
5	8.163	0.582	$\frac{5}{2}^+$

Table 7.1: Review of the possible $\ell = 0$ resonances in ^{22}Na+p capture, interesting at peak nova temperatures, that is to say within 0.6 MeV above the S_p=7.581 MeV threshold. Energies and spins are from [55] if not mentioned.

Along the next sub-sections, the outcome of the shell-model calculations is presented. Starting by explaining how the calculations were made in Sec.7.2.2, the resonant states with experimentally well-known spins were identified among the shell-model states with $J^\pi \in (\frac{5}{2}^+, \frac{7}{2}^+)$ in Sec.7.2.3. The candidates for the E_R=0.204 MeV state in the remaining shell-model states are described in Sec.7.2.4. For this key state, the mirror state in ^{23}Na* was also looked for but this was not conclusive, see Sec.7.2.5. From the calculated properties of the shell-model candidates, the implications of assigning $J^\pi = \frac{5}{2}^+$ or $J^\pi = \frac{7}{2}^+$ to the E_R=0.204 MeV state are studied in Sec.7.2.6. Finally, the spin for the state n_R=4 was assigned in Sec.7.2.7 by identifying the best shell-model candidate.

7.2.2 Shell-model calculations

The study of the targeted states within the shell-model frame was based on three main steps: the calculations of states in (Ex, J^π), their identifications to experiment and the derivations of their partial and total widths.

- States calculations

Shell-model calculations were achieved with the NUSHELLX code [112]. As shown in Fig. (7.1), the valence shells in ^{23}Mg are sd shells and the core ^{16}O. With $J^\pi = 3^+$ for the ground state in ^{22}Na, only positive parity states are of interest in s-capture. Two interactions (USDA, USDB) [113] were used with the valence sd space. They were completed by the charge dependent Coulomb part and the charge-asymmetric nuclear Hamiltonian published by Ormand and Brown for the sd shell [114]. From now on, these two calculations are referred as (USDAcpn, USDBcpn) for simplicity. The states properties (Ex, J^π) were directly computed.

Another valence space, the psd space with the core nucleons restricted in the $1s_{1/2}$ and $1p_{3/2}$ shells, was also looked at with the interaction PSDMKcpn. However, this was found to be in fairly strong disagreement with the other calculations (USDAcpn, USDBcpn).

- States identification

The observed states had to be identify among the calculated states. To do so, 4 spectroscopic properties were compared:
(1) the spin, if experimentally well-known, and Ex reasonably within 0.5 MeV
(2) the path of γ-ray transitions
(3) the probability and the nature of the ^{23}Al β^+ decay population, Fermi or Gamow-Teller transition

(4) the proton spectroscopic factors if experimentally well-known.

With regard to the point (2), the γ-ray transitions and the associated intensities were calculated with NUSHELLX from the overlaps between states in ^{23}Mg*.

In relation to the point (3), the ground state in ^{23}Al has $J^{\pi} = \frac{5}{2}^{+}$ which implies that only $J^{\pi} \in (\frac{3}{2}^{+}, \frac{5}{2}^{+}, \frac{7}{2}^{+})$ states in ^{23}Mg* are populated in the β^{+} decay (allowed transitions). The ^{23}Al β^{+} decay was computed to get the transition strengths (B(F), B(GT)), either Fermi or Gamow-Teller. Then the transition rates $\log_{10}$(ft), i.e. their probabilities of occurring, were derived as follow

$$\mathrm{ft} = \frac{\mathrm{k}}{\mathrm{B(F)} + (\frac{\mathrm{g_A}}{\mathrm{g_\nu}})^2 \mathrm{B(GT)}} \tag{7.1}$$

where k = 6144 $\pm$ 45, $\frac{\mathrm{g_A}}{\mathrm{g_\nu}}$ = -1.267$\pm$0.0035. When the transition is purely Fermi, the strength B(F) is equal to

$$\mathrm{B(F)} = |\mathrm{Z} - \mathrm{N}| \tag{7.2}$$

where (Z, N) are those of the father nucleus. In the present studied case, pure Fermi transitions give (B(F)=3, B(GT)=0) and the associated $\log_{10}$(ft)=3.311.

Regarding the last point (4), spectroscopic factors are proportional to the overlaps between states in ^{23}Mg* and the ground state in ^{22}Na.

- States widths

The proton width Γ_{p} is equal to the sum over the partial widths $\Gamma_{\ell,\mathrm{p}}$ associated with each ℓ-transfer momentum. Only ℓ=0 and ℓ=2 were considered in this case.

$$\Gamma_{\mathrm{p}} = \Gamma_{\ell=0,\mathrm{p}} + \Gamma_{\ell=2,\mathrm{p}} \tag{7.3}$$

As shown in Fig.7.1, ℓ=0 transfer corresponds to a proton on the $2s_{1/2}$ shell, and ℓ=2 on the $1d_{3/2}$ and $1d_{5/2}$ shells. The partial proton width $\Gamma_{\ell,\mathrm{p}}$ is defined by the proton spectroscopic factor $C^2S_{\ell,\,\mathrm{p}}$ and the single-particle proton decay width $\Gamma_{\ell,\mathrm{s.p.,\,p}}$ as

$$\Gamma_{\ell,\mathrm{p}} = C^2S_{\ell,\mathrm{p}} \times \Gamma_{\ell,\mathrm{s.p.,\,p}} \tag{7.4}$$

The single-particle widths $\Gamma_{\ell,\mathrm{s.p.,\,p}}$ were calculated with the DWU code. This code derives proton scattering wave functions on a Woods-Saxon potential. All results in $\Gamma_{\ell,\mathrm{s.p.,\,p}}$ associated with the studied states are given in the Annexes C.3.1. The $C^2S_{\ell,\mathrm{p}}$ were obtained from the NUSHELLX code. The proton widths may also be derived knowing $\mathrm{BR_p}$ and γ-ray width.

$$\Gamma_{\mathrm{p}} = \frac{\mathrm{BR_p} \times \Gamma_\gamma}{1 - \mathrm{BR_p}} \tag{7.5}$$

The γ-ray width Γ_γ is derived by summing on the partial γ-ray widths from γ-ray transitions found dominant (L$\leq$2). The partial γ-ray width $\Gamma_{\gamma,(\mathrm{L,\,i\to f})}$ associated with a transition of order L, from state i to state f, is given by

$$\Gamma_{\gamma,(\mathrm{L,\,i\to f})} = \frac{8\pi(\mathrm{L}+1)}{\mathrm{L}[(2\mathrm{L}+1)!!]^2} (\frac{\mathrm{E_\gamma}}{\hbar c})^{2\mathrm{L}+1} \mathrm{B_\gamma} \tag{7.6}$$

where $\mathrm{E_\gamma} = \mathrm{Ex^i} - \mathrm{Ex^f}$ in MeV, $\hbar c = 197.3$ MeV.fm, !! is the double factorial (2L+1)$\times$(2L+1-2)$\times$..$\times$1, $\mathrm{B_\gamma}$ the reduced transition probability either B(E2) in $\mathrm{e^2.fm^4}$ (1.44 MeV.fm.fm^4) or B(M1) in μ_{N}^2 ($(0.1052)^2 \times 1.44$ MeV.fm^3). Hence calculated (B(E2), B(M1)) were used to obtain Γ_γ. All results in (B(E2), B(M1), $\Gamma_{\gamma,(\mathrm{i\to f})}$) associated with the studied states are given in Annexes C.3.2.

The total width Γ_{tot} is obtained by adding the derived proton and γ-ray widths from Eq. (7.3) and (7.6):

$$\Gamma_{\mathrm{tot}} = \Gamma_{\mathrm{p}} + \Gamma_\gamma \tag{7.7}$$

7.2.3 Identification of the known-spin states

In this section, we will try to identify one by one the states predicted by the shell model.

- Identification of the IAS (n_R=2)

The IAS in ^{23}Mg* is experimentally well-known: two dominant γ-ray transitions were measured to the ground state (66 %) and the first excited state (30 %), see the brown lines on the left of Fig. 7.2. The shell-model state n_{SM}=9 with $J^\pi = \frac{5}{2}^+$ presents similar γ-ray transitions, shown with the brown lines when using USDAcpn (USDBcpn) on the middle (right) of Fig. 7.2.

Spectroscopic properties of the measured IAS and the shell-model candidates n_{SM}=9 are listed in Table 7.2. The $\log_{10}$(ft) was measured of 3.305(23)[53], in agreement with the expected value for the IAS (3.311, see Eq. 7.2). The shell-model state n_{SM}=9 with USDBcpn presents the highest B(F)=2.968 and $\log_{10}$(ft)=3.318, close to the experimental values. Furthermore, the calculated C^2S_p results in a negligible Γ_p=5 μeV. As expected, the IAS is found forbidden to proton decay. These results confirm the identification of the IAS as the n_{SM}=9 state among the calculated states with USDBcpn. The measured γ-ray width of the analog state in the mirror ^{23}Na [115] agrees with the calculated one using Eq. (7.6), see last column Table 7.2.

IAS n_R=2		Ex MeV, J^π	$\log_{10}$(ft)	B(F), B(GT)	C^2S_p ($\ell=0$, $\ell=2$)	Γ_p meV	Γ_γ eV
SM	USDAcpn	7.890, $\frac{5}{2}^+_9$	3.464	2.121, 0.333	(0.0073, 0.0173)	6.7	1.71
	USDBcpn	7.861, $\frac{5}{2}^+_9$	3.318	2.968, 0.222	(0.0000, 0.0007)	5 μeV	3.02
Exp.		7.803, $\frac{5}{2}^+$	3.305(23)[53]	(3.044, 0)[a]	(0.0056, /)[d]	5[c]	3.0(2)[b]

[a] From Eq. (7.1) with value of [53], assuming a pure Fermi transition.
[b] From Γ_γ[115] of the mirror T=$\frac{3}{2}$ state in ^{23}Na.
[c] From BR_p = 0.17 %[51] and mirror Γ_γ, using Eq. (7.5).
[d] Calculated from measured BR_p [51] and mirror Γ_γ.

Table 7.2: Comparison of the IAS properties between shell-model calculations, with USDAcpn or USDBcpn interaction, and experiment.

Shell-model calculations using USDAcpn give a different result: a strong mixing of the IAS state n_{SM}=9 with another $J^\pi = \frac{5}{2}^+$ state, as already obtained by Tripathi *et al* [116]. This explains the lower B(F)=2.121 than the value obtained with USDBcpn, for the n_{SM}=9 state. As a result of the isospin mixing, the proton decay from the IAS is allowed with a calculated width Γ_p=6.7 meV, 10^3 higher than the width without mixing. The experimental study of Perajarvi *et al* gives the only measured value of BR_p = 0.17 %[51] for the IAS. Later experiments [48, 50] did not observe the proton decay from IAS and rejected this BR_p value. The experimental proton width agrees with USDAcpn calculations.

To summarize, the IAS state is the state n_{SM}=9 in both shell-model calculations. Only one experimental study has observed an isospin mixing, in agreement with USDAcpn, all the other experimental studies have not observed mixing, in agreement with USDBcpn.

- Identification of the n_R=3 and 5 states

Calculated γ-ray transitions are compared with the observed transitions for the n_R=3 and 5 states in Fig. 7.2. The n_R=3 state, with $J^\pi = \frac{7}{2}^+$ and located 0.274 MeV above S_p, was identified without ambiguity as the state n_{SM}=8 thanks to the good agreement between the observed γ-ray transitions and the shell-model results. Its transitions are shown in purple. The n_R=5 state, with E_R=0.582 MeV, was also clearly identified among shell-model $J^\pi = \frac{5}{2}^+$ states: it is the state n_{SM}=10 with the γ-ray transitions shown with the red lines in Fig. 7.2.

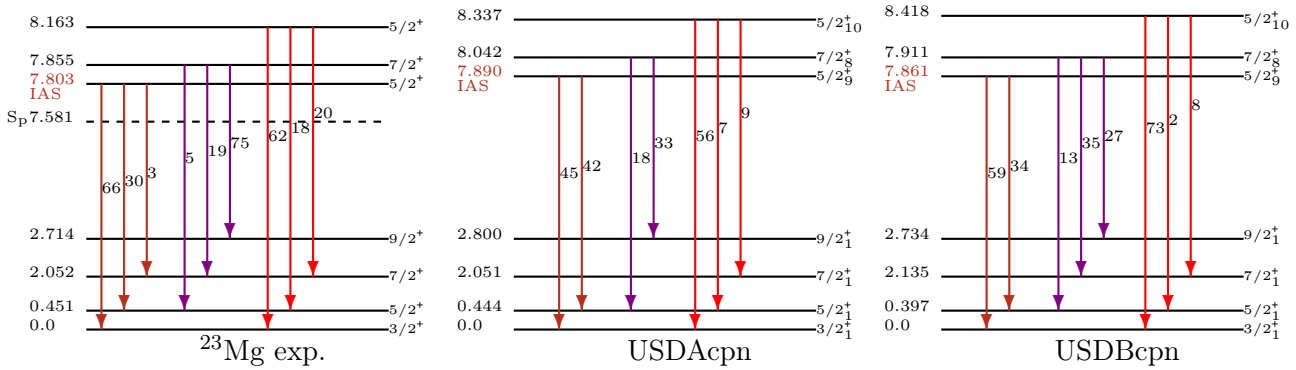

Figure 7.2: Experimental and theoretical levels schemes and γ-rays transitions emitted from 3 states in ^{23}Mg* are compared here. Calculated states were easily identified to these 3 experimental states located above the proton emission threshold S_p, in particular the IAS highlighted in brown color. The results of the 2 used interactions (USDAcpn, UDSBcpn) are consistent. Excitation energies Ex are given in MeV and γ-ray intensities (I_γ) in %, with measured ones from [55].

- Assessment of the n_R=2, 3 and 5 states

The spectroscopic properties of the three previously identified states are summarized in Table 7.3. Several observations can be made.
- All these states have a short predicted lifetime of < 1 fs.
- One can observe a factor up to 1.5 (and 3) differences between the different predicted Γ_p (and Γ_γ) when using the different interactions.

n_R	Ex MeV, J^π	Ex MeV, J^π		C^2S_p ($\ell=0$, $\ell=2$)		Γ_p		Γ_γ	
	Exp.	USDAcpn	USDBcpn	USDAcpn	USDBcpn	USDAcpn	USDBcpn	USDAcpn	USDBcpn
2 (IAS)	7.803, $\frac{5}{2}^+$	7.890, $\frac{5}{2}^+_9$	7.861, $\frac{5}{2}^+_9$	(0.0073, 0.0173)	(0.0000, 0.0007)	6.7 meV	5 μeV	1.71 eV	3.02 eV
3	7.855, $\frac{7}{2}^+$	8.042, $\frac{7}{2}^+_8$	7.911, $\frac{7}{2}^+_8$	(0.076, 0.158)	(0.104, 0.191)	667 meV	907 meV	88 meV	248 meV
5	8.163, $\frac{5}{2}^+$	8.337, $\frac{5}{2}^+_{10}$	8.418, $\frac{5}{2}^+_{10}$	(0.056, 0.251)	(0.033, 0.228)	223 eV	135 eV	1.02 eV	1.38 eV

n_R	τ fs	Γ_{tot} eV		τ fs	
	Exp.	USDAcpn	USDBcpn	USDAcpn	USDBcpn
2 (IAS)	< 3.5	1.72	3.02	0.38	0.21
3	∅	0.75	1.15	0.88	0.57
5	∅	1.24	1.52	0.53	0.43

Table 7.3: Calculated properties of the $\ell = 0$ resonances, within 0.6 MeV above the ^{22}Na+p threshold, with spins known from experiment, and of the IAS.

In conclusion, the three states with experimentally assigned spins were easily identified among the states predicted by the shell model.

7.2.4 Candidates for the key state

Two candidates of the observed E_R=0.204 MeV state were identified in the shell-model calculations, namely the (n_{SM}=7, $J^\pi = \frac{7}{2}^+_7$) and (n_{SM}=8, $J^\pi = \frac{5}{2}^+_8$) states. Close in energy to the IAS, they are

discussed now with respect to their γ-ray transitions and their spectroscopic properties.

- Comparing γ-ray transitions

In Fig. 7.3, the observed γ-ray transitions from the key state are given on the left, and the proposed shell-model candidates on the middle (right) for the interaction USDAcpn (USDBcpn). On the one hand, the transition to the first excited (Ex=0.451 MeV, $J^\pi = \frac{5}{2}^+$) state was measured dominant in our experiment, i.e. >97 % as in [49, 52]. This was also found true for the (n_{SM}=7, $J^\pi = \frac{7}{2_7}^+$) state with a predicted intensity of 67 % (58 %) with USDBcpn (USDAcpn). These transitions are shown in blue. On the other hand, the transitions shown in red from the (n_{SM}=8, $J^\pi = \frac{5}{2_9}^+$) state differ strongly from experiment regardless of the interaction. In particular, a γ-ray transition to the ground (n_{SM}=1, $J^\pi = \frac{3}{2_1}^+$) state is predicted with a high intensity of $\geq$30 % whereas such γ-ray has never been observed. It can be seen that this transition is stronger when isospin mixing is present: 73 % (USDAcpn) against 30 % (USDBcpn). The γ-ray transitions of the n_{SM}=8 state are alike the γ-ray transitions from the IAS, see brown lines in Fig. 7.2. Mixed states are indeed expected to present similar features. However, there are experimental counter examples such as the isospin mixing in ^{55}Ni [116]. There, the two γ-ray transitions from the IAS to the first two $J^\pi = \frac{3}{2}^-$ states were not observed in the mixed state. Furthermore, the shell-model calculations of the mixed states did not agree with experiment. Such counter-intuitive observation remains to be understood.

Overall, our study of the γ-ray transitions from the key state favors the first (n_{SM}=7, $J^\pi = \frac{7}{2_7}^+$) candidate without settling definitively the question of the spin.

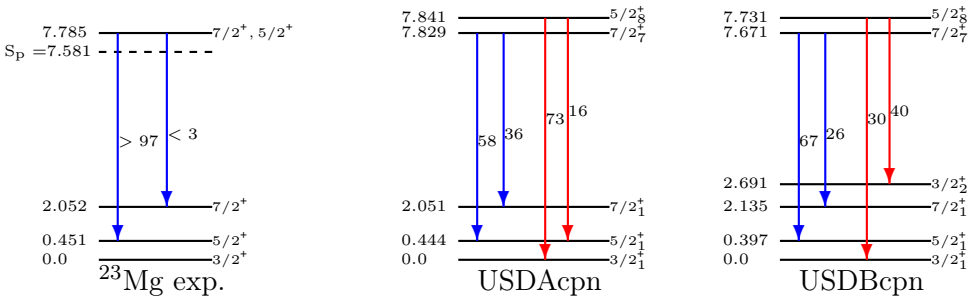

Figure 7.3: Comparison between the observed γ-ray transitions from the n_R=1 state with the ones from shell-model candidates: (n_{SM}=7, $J^\pi = \frac{7}{2_7}^+$) and (n_{SM}=8, $J^\pi = \frac{5}{2_8}^+$). There is a good agreement for the blue transitions, strengthening the n_{SM}=7 candidate with $J^\pi = \frac{7}{2_7}^+$ as the n_R=1 state. Energies are given in MeV and intensities in %. The experimental results are from the present experiment.

- Comparing β-decay strengths

Results of shell-model calculations are compared to experimental data of the E_R=0.204 MeV state in Table 7.4.

		Ex MeV	$J^\pi_{n_{SM}}$	$\log_{10}$(ft)	B(F), B(GT)	C^2S_p ($\ell=0$, $\ell=2$)	Γ_p meV[a]	Γ_γ eV	Γ_{tot} meV	τ fs
n_{SM}=7	USDAcpn	7.829	$\frac{7}{2}^+_7$	4.101	0, 0.303	(0.004, 0.060)	1.5	669	670	1.0
	USDBcpn	7.671	$\frac{7}{2}^+_7$	3.862	0, 0.526	(0.049, 0.058)	16.5	552	568	1.2
n_{SM}=8	USDAcpn	7.841	$\frac{5}{2}^+_8$	3.863	0.847, 0.002	(0.015, 0.084)	5.3	1779	1784	0.4
	USDBcpn	7.731	$\frac{5}{2}^+_8$	5.333	0.008, 0.030	(0.001, 0.020)	0.3	184	184	3.6
n_R=1	Exp.	7.785	$\frac{7}{2}^+$[49] / $\frac{5}{2}^+$[63]	3.85(5)[53]	(0.0, 0.54(6))[b] mixed B(F)/B(GT)[d]	/	$0.45^{+0.16}_{-0.17}$[c]	$65.5^{+17.2}_{-21.2}$[c]	66^{+17}_{-21}[c]	$9.9^{+4.5}_{-2.0}$[c]

[a] Calculated with single particle widths from experimental excitation energies.
[b] From $\log_{10}$(ft) of [53].
[c] From this study.
[d] With a reduction of the IAS B(F).

Table 7.4: Comparison of the measured spectroscopic properties of the n_R=1 (E_R=0.204 MeV) state, with those of the two shell-model candidates: (n_{SM}=7, $J^\pi = \frac{7}{2}^+_7$) and (n_{SM}=8, $J^\pi = \frac{5}{2}^+_8$).

First candidate (n_{SM}=7, $J^\pi = \frac{7}{2}^+_7$) has $\log_{10}$(ft)=3.98(12) in agreement with the β-delayed experimental value ($\log_{10}$(ft)=3.85(5)[53]). The present shell-model uncertainties have been defined from the two values obtained for the two interactions. This $\log_{10}$(ft) is a relatively low value for a Gamow-Teller transition, this contradicts the argument of Ref. [63, 116] that the low value must come from an isospin mixing and so a spin $J^\pi = \frac{5}{2}^+$. But calculations show here that spin $J^\pi = \frac{7}{2}^+$ also gives a low value. Second candidate (n_{SM}=8, $J^\pi = \frac{5}{2}^+_8$) has small $\log_{10}$(ft)=3.86 only when there is a strong isospin mixing.

- Comparing proton widths

The proton widths of the candidates differ, according to the interaction, by a factor more than 10, see Table 7.4. Shell model can be relied upon for proton spectroscopic factors (and so Γ_p) to predict real values within a factor 2 in general. A variation of a factor 1000 for the calculated Γ_p with respect to the interaction was also observed in the case of the IAS, see Table 7.3. The isospin mixing, predicted strong with USDAcpn, was most likely responsible for such dispersion in calculated Γ_p. The measured Γ_p and past BR_p [50, 48, 51], associated with the key state, were not found excluded by these theoretical considerations. Proton widths do not help to disentangle the candidates.

- Comparing lifetimes

Regarding the calculated lifetimes, they were found much shorter than our measurement, by a factor of ∼10, see Table 7.4. The dispersion due to the interaction choice does not explain the difference with experiment. As seen with the other resonant states, a high-lying state with a long lifetime τ ∼10 fs was unexpected from the theoretical point of view. For the candidate (n_{SM}=7, $J^\pi = \frac{7}{2}^+_7$), shell-model reduced probabilities are: B(M1)=6.4×10^{-2} (8.2×10^{-2}) W.u. and B(E2)=2.9×10^{-2} (4.0×10^{-2}) W.u. by using USDBcpn (USDAcpn), here in Weisskopf units. Typical values are B(M1)∼10^{-1} W.u. and B(E2)∼ 10^2 W.u.. In comparison, the measured reduced probability is B(M1)=1.3×10^{-2} W.u., assuming the γ-ray transition at $E_{\gamma,0}$ = 7.333 MeV to be pure M1. Being in the relatively low ranges for B(M1), B(E2) and at high excitation energies, theoretical uncertainties are important: $\pm6\times10^{-2}$ W.u. (0.1 μn^2), from [117]. These uncertainties may explained the observed difference between experimental and shell-model values. As an indication, the distributions of relative differences between shell-model and experimental B(M1) for the ^{21,23}Na isotopes are shown with the blue histograms in Fig. 7.4, with data from [118]. Shell-model calculations in [118] were achieved with USDB (on the left) and with USDA (on the right). The B(M1) differences in the case of the $E_{\gamma,0}$=7.333 MeV γ-ray transition are pointed out in

red. They are inside of the observed distributions. About 40 % of B(M1) values differ by more than 50 % between experiment and shell model.

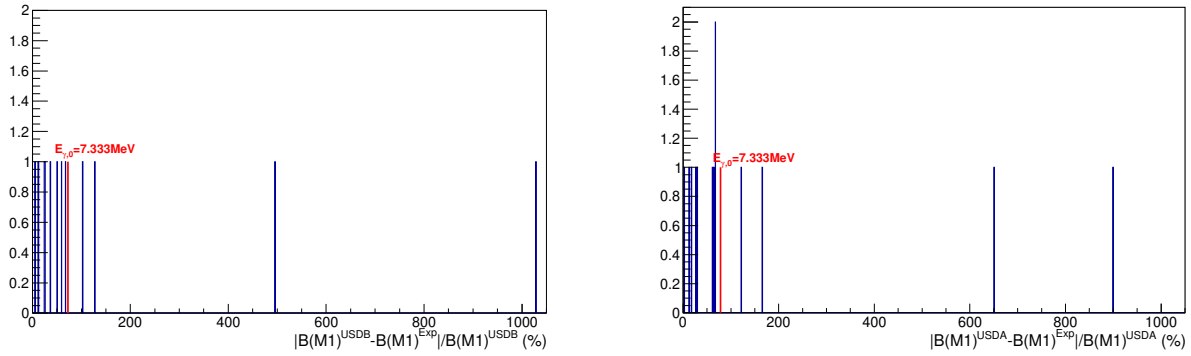

Figure 7.4: Distributions of relative differences of B(M1) between experimental and shell-model values: on the left when USDB is used and on the right with USDA. Blue histograms are associated to available data with ^{21,23}Na isotopes from [118] with states Ex$\leq$6 MeV. Red lines correspond to B(M1) of the $E_{\gamma,0}$=7.333 MeV γ-ray transition from the E_R=0.204 MeV state in ^{23}Mg*, with the shell-model candidate (n_{SM}=7, $J^\pi = \frac{7}{2}^+_7$). The difference observed in ^{23}Mg* is in the range of possible values.

In conclusion, shell model gives two possible candidates for the observed key state, either it is the state n_{SM}=7 with $J^\pi = \frac{7}{2}^+_7$ or it is n_{SM}=8 with $J^\pi = \frac{5}{2}^+_8$. These candidates, consistent in widths, differ in γ-ray transitions, making the first candidate more likely to correspond to the key state.

7.2.5 Search for the mirror state in ^{23}Na

The analog mirror state of the IAS has been identified to be the Ex=7.564 MeV state in ^{23}Na* which has a spin $J^\pi=\frac{5}{2}^+$, a lifetime τ=0.38 fs and a 70 % γ-ray transition to the ground state. Close to this state, there are two candidates for the mirror state in ^{23}Na* of the state n_R=1 in ^{23}Mg*:
(1) The Ex=7.477 MeV state with a 100 % γ-ray transition to the first Ex=0.440 MeV state in ^{23}Na* and unknown (τ, J^π).
(2) The Ex=7.451 MeV state with a 90 % γ-ray transition to the Ex=0.440 MeV state and (τ<4.3 fs, $J^\pi \in \{\frac{3}{2}^+, \frac{5}{2}^+\}$).

As discussed in Ref. [64], there is no straightforward assignment of the mirror state in ^{23}Na of the astrophysical state, and thus no help regarding the spin debate.

7.2.6 Consequences of a spin $\frac{5}{2}^+$ or $\frac{7}{2}^+$

A spin of the key state equal to $\frac{5}{2}^+$ has strong implications that are investigated now. First, it has been shown in that case that the predicted γ-ray transitions strongly disagree with experiment. Second, such a spin must result in a strong isospin mixing between the IAS and the key state due to:

1. The same spin and parity
2. The small energy gap between the two states, i.e. dE=18 keV from experiment, and the fact that the mixing between two states is inversely proportional to the energy separation [116]
3. The shell-model predictions

However, strong arguments are against such a high isospin mixing.

- The measured $\log_{10}$(ft)$\sim$ 3 for the IAS is in perfect agreement with a pure Fermi transition
- Its estimated γ-ray width $\Gamma_\gamma \sim$ 3 eV agrees with predictions when there is no strong mixing, see Table 7.2.
- The observed properties disagree with calculated ones in the case of strong mixing, in particular the γ-ray transitions paths.
- Shell model shows that spectroscopic properties are expected to be the same for the IAS and the resonant state if the isospin mixing is strong. Indeed, it was found, using USDAcpn, that:
  - Γ_p=6.7 meV (IAS) vs 5.3 meV (n_{SM}=8, $J^\pi = \frac{5}{2}^+_8$),
  - Γ_γ=1.7 eV (IAS) vs 1.8 eV (n_{SM}=8, $J^\pi = \frac{5}{2}^+_8$),
  - τ=0.4 fs (IAS) vs 0.4 fs (n_{SM}=8, $J^\pi = \frac{5}{2}^+_8$).
- The branching ratio was measured only once for the IAS, it was BR_p=0.17(8) %[51]. This is high for such state, and it was justified by a possible isospin mixing but the estimated $\omega\gamma$=2.2(10) meV[51] is at odds with the direct measurements [45, 46] where proton captures to the IAS were not observed. We argue that the proton decay measured in [51] originated from the key state and not from the IAS. Thus, as the β-branching to the IAS is higher than that of the key state, the derived BR_p corresponds to a lower limit for the key state, in agreement with all other measurements.

A strong isospin mixing could result in a longer lifetime for the mixed resonant state, in the direction then of the experimental value (τ=9.9 fs). However, the opposite was noticed in the shell-model calculations. Regarding the candidate (n_{SM}=8, $J^\pi = \frac{5}{2}^+_8$), the calculated lifetime is shorter with USDAcpn (with mixing) than with USDBcpn (without mixing): 0.4 fs vs 3.6 fs (Table 7.4).

The other candidate (n_{SM}=7, $J^\pi = \frac{7}{2}^+_7$) strongly agrees with the key state n_R=1 with respect to

- γ-ray transitions,
- probabilities in ^{23}Al β-delayed population.

As a conclusion, a spin of $J^\pi = \frac{5}{2}^+$ for the key state necessarily produces a strong isospin mixing. This has been found at odds with experiment. On the contrary, arguments have been put forward in favour of $J^\pi = \frac{7}{2}^+$.

7.2.7 Spin assignment of the state n_R=4

The spin of the n_R=4 state is unknown. There are two proposed values $J^\pi \in (\frac{5}{2}^+, \frac{7}{2}^+)$[55]. This state was hardly seen in the ^{23}Al β-delayed experiment [50]: no γ-ray clearly seen above background noise for $E_{\gamma,0} \in \{5.300, 5.965\}$ MeV, an absolute ^{23}Al β-proton branching of 0.02(1) %. In the more accurate experiment [48], this state was not indicated. A peak in the proton spectrum can be hardly distinguished at the expected energy $E_p^{c.m.}$ = 0.435 MeV, see Fig7.6(b). The proton decay from this state was well observed in our experiment, see Table 6.9. It was also measured in the direct experiments [45, 46]. Two γ-ray transitions dominate, to the low-lying states with $J^\pi \in \{\frac{9}{2}^+, \frac{7}{2}^+\}$, see on the left of Fig.7.5. To summarize, this state was found:
(1) weakly populated by β^+-decay of ^{23}Al,
(2) well populated by proton capture on the ground state $J^\pi = 3^+$ in ^{22}Na,
(3) highly decaying by proton ($BR_p \sim$80 %),
(4) mainly populating states with $J^\pi \in \{\frac{9}{2}^+, \frac{7}{2}^+\}$ by γ-ray transitions.

The point (4) favours a spin of $\frac{9}{2}^+$ or $\frac{7}{2}^+$, assuming dominant transitions to be M1. Considering L≤2 in proton capture and emission, the points (2, 3) give $^\pi \in [\frac{1}{2}^+, \frac{11}{2}^+]$.

Five candidates were found in shell model for six existing states with Ex∈ [7.918, 8.141] MeV states. Among these calculated states, one candidate with $J^\pi = \frac{5}{2}^+$ was excluded because of the poor matching with observed γ-ray transitions, and no candidate exists with $J^\pi = \frac{7}{2}^+$. Two candidates with $J^\pi = \frac{9}{2}^+$ are compared to experiment in Fig. 7.5.

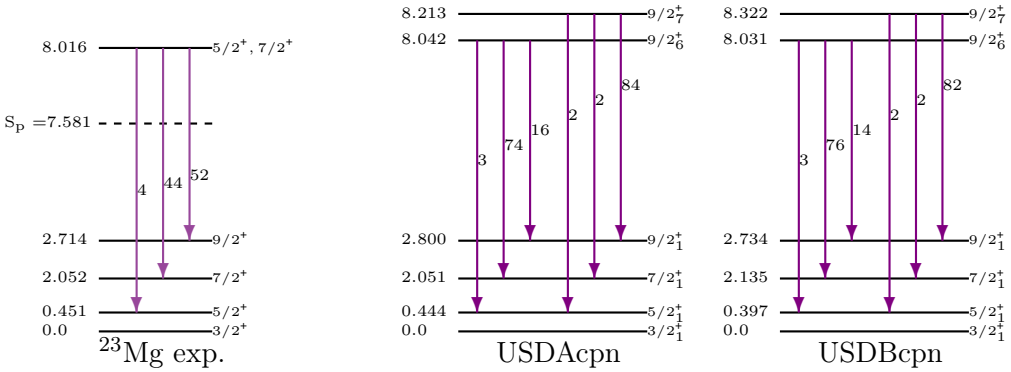

Figure 7.5: Comparison between experimental and shell-model γ transitions of the n_R=4 state. Candidates (n_{SM}=6, $J^\pi = \frac{9}{2}^+_6$) and (n_{SM}=7, $J^\pi = \frac{9}{2}^+_7$) appear in agreement with the measured state. Excitation energies Ex are given in MeV and γ-ray intensities (I_γ) in %, with measured ones from [55].

The candidate (n_{SM}=6, $J^\pi = \frac{9}{2}^+_6$) probably corresponds to the state n_R=4 state, due to its closest excitation energy and γ-ray branching. The comparison of spectroscopic properties is given in Table 7.5.

n_R=4		Ex MeV	J^π	Γ_p meV	Γ_γ meV	τ fs
SM	USDAcpn	8.042	$\frac{9}{2}^+_6$	163	488	1.0
	USDBcpn	8.031	$\frac{9}{2}^+_6$	164	608	0.9
Exp.		8.016	$\frac{5}{2}^+$, $\frac{7}{2}^+$	∅	∅	∅

Table 7.5: Comparison of the n_R=4 state properties between experiment and the shell-model candidate (n_{SM}=6, $J^\pi = \frac{9}{2}^+_6$).

Concluding this study, a spin $J^\pi = \frac{9}{2}^+$ has been proposed to the n_R=4 state after comparing experimental and shell-model data.

7.2.8 Conclusion

The present theoretical study was fruitful: strong hints towards $J^\pi = \frac{7}{2}^+$ assignment for the key state in ^{23}Mg* were pointed out. On the basis of evidences against an isospin mixing between this state and the IAS, we dismissed the other possible value $\frac{5}{2}^+$. Shell-model predicted spectroscopic properties are given for the five cases under review in Table 7.6.

n_R	Ex MeV	J^π	Γ_p	Γ_γ
1	7.785	$\frac{7}{2}^+$	9(7) meV	611(59) eV
2 (IAS)	7.803	$\frac{5}{2}^+$	3.4(33) meV	2.4(7) eV
3	7.855	$\frac{7}{2}^+$	787(120) meV	168(80) meV
4	8.016	$\frac{9}{2}^+$	163.5(5) meV	548(60) meV
5	8.163	$\frac{5}{2}^+$	179(44) eV	1.2(2) eV

Table 7.6: Overview of shell-model properties in spin and partial widths of the four resonant states, 0.6 MeV above the ^{22}Na+p threshold, and of the IAS. Uncertainties in partial widths are estimated from the different results obtained using different interactions, either USDAcpn or USDBcpn.

7.3 Compilation of ^{23}Mg spectroscopic properties

7.3.1 Resonance strengths

Thanks to shell-model calculations, we obtained or deduced all spectroscopic properties needed to estimate the important resonance strengths at peak nova temperatures. They were derived by using Eq. (7.8) with shell-model data in Table 7.6. These predictions are compared with the two direct measurements in Table 7.7. They were found to be consistent, shell-model predictions seem a little higher than the experimental results. Theoretical uncertainties were estimated based on the two interactions used in the calculations. Shell-model predictions were not useful for solving the observed systematic factor of 2.5 between the measurements [45] and [46] for E_R>0.210 MeV.

$$\omega\gamma = \frac{2J_{^{23}Mg}+1}{(2J_{^{22}Na}+1)(2J_{p+1})} \times \frac{\Gamma_\gamma\Gamma_p}{\Gamma_\gamma+\Gamma_p} \tag{7.8}$$

n_R	E_R MeV, J^π	$\omega\gamma$ meV		
		Measurements		SM[a]
		[45]	[46]	
1	0.204, $\frac{7}{2}^+$	1.4(3)[b]	$5.7^{+1.6}_{-0.9}$	5.1(39)
2	IAS 0.222, $\frac{5}{2}^+$	∅	≤ 0.67	1.5(14)
3	0.274, $\frac{7}{2}^+$	15.8(34)	39(8)	79(32)
4	0.435, $\frac{9}{2}^+$	68(20)	166(22)	90(3)
5	0.582, $\frac{5}{2}^+$	235(33)	591^{+103}_{-74}	511(86)

[a] Using Eq. (7.8) with calculated (Γ_γ, Γ_p) in Table 7.6.
[b] From I_γ observed in our experiment (Table 5.2).

Table 7.7: Comparison between measured and shell-model resonance strengths $\omega\gamma$ of interest for novae. Uncertainties associated with shell model have been estimated from the different interactions used.

7.3.2 Newly determined resonance strength for the E_R=0.204 MeV resonance

The required spectroscopic parameters of the E_R=0.204 MeV resonance state in ^{23}Mg* have been obtained. The measured lifetimes from past works and the present experiment, shown on the left of Fig. 6.17, were averaged to determine the final lifetime. The upper limit of Ref. [52] was also included, knowing that in the case of an upper limit the expected value is L/2 (±L/2) [119].

The measured proton branching ratios, shown on the right of Fig. 6.17, were also averaged to determine the final BR_p. The high BR_p=3.7(9) %, measured by Saastamoinen *et al* [50], disagrees with the other experiments [48, 51] and our work. We have chosen to reject it as a finite value and to consider it as an

upper limit $BR_p \leq 3.7(9)$ % because of the two arguments detailed now.
(i) The experiment from Ref. [50] relied on a large background noise subtraction, due to β particles, in order to obtain the proton spectrum in the low energy region, as shown in Fig. 7.6(a). This is well-known that a strong noise contribution is expected when a Si detector is used for the implantation and the measurement. On the contrary, the gaseous detector GADGET used by [48] allowed them to strongly mitigate the β background at low energies. This resulted in an improved proton spectrum, as shown in Fig. 7.6(b). Similarly to arguments presented in [48], we think that the required background subtraction in Ref. [50] increased the systematic uncertainties of the measured BR_p.
(ii) Pile-up events between protons and β particles contributed to distorting the Gaussian shape expected for the measured protons in the experiment [50] with Si detector. Due to wrong energy measurement, they induced a tail on the high-energy side for each proton peak. This is apparent in Fig. 7.6(a). The signals were so fitted with skewed Gaussian peaks. This effect was not seen in the case of the gaseous detector, see Fig. 7.6(b). The intensity of the right tail relatively to the Gaussian peak should not depend on the proton energy, since the tail came from fortuitous coincidences. But, this was seen decreasing with respect to the proton energy, in counts ratio: 50/350 at $E_p \sim 0.2$ MeV against 50/800 at $E_p \sim 0.6$ MeV, from Fig7.6(a). This is a strong hint that something was incorrect with the background in the low energy region of interest.

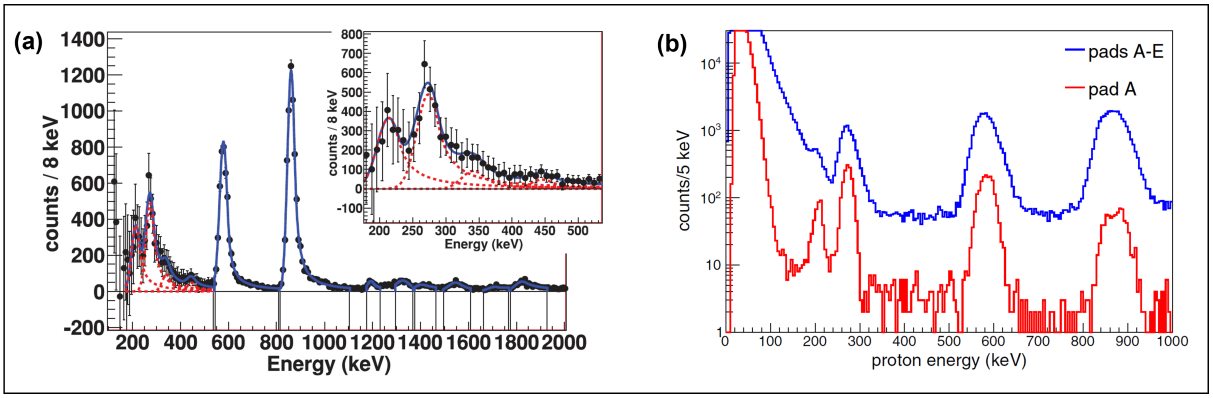

Figure 7.6: Panel (a) taken from Saastamoinen *et al* [50]: ^{23}Al β-delayed protons spectrum after background noise subtraction. Fits of the peaks, appearing as lines, were derived with a skewed Gaussian peak shape. Tails on the high-energy side originated from fortuitous coincidences between a proton and a β particle. We noticed that the tail contributions compared to Gaussian peaks were higher for the low energy protons (<5 MeV) than for the high energy ones. These contributions should be independent of the proton energy. Panel (b) taken from Friedman *et al* [48]: ^{23}Al β-delayed protons spectrum measured with GADGET, a gaseous detector, radius of pad A being smaller than radii of pads A-E.

From our shell-model study, the spin had been chosen equal to $J^\pi = \frac{7}{2}^+$. As a summary, the three spectroscopic parameters have been determined

- τ=9.5(21) fs
- BR_p=0.66(8) %
- $J^\pi = \frac{7}{2}^+$

The resonance strength of the E_R=0.204 MeV key resonance is finally obtained:

$$\omega\gamma = 0.26^{+0.11}_{-0.07} \text{ meV} \tag{7.9}$$

The new resonance strength has up to 40 % uncertainties. The value is 22 (5.5) smaller than the direct measurement [46] ([45]). How to explain such a discrepancy? First of all, these direct experiments are

very challenging, and the fact that the two direct measurements do not agree by a factor 2.5 demonstrates the difficulty of these measurements. The use of the ^{22}Na radioactive targets makes these measurements difficult. A deeper thought has been given around possible problems during these direct experiments which may induce such large systematic errors. In this approach, $\omega\gamma$ are measured from the measured γ-rays yields after normalization to: (1) the γ-ray detection response function, (2) the proton beam intensity and density where irradiation is assumed uniform over the target active area, (3) the target ^{22}Na density. Systematic errors may come from these three points that are examined now.

Detections in Ref. [46, 45] made use of HPGe instruments which are usual. In the work of [46], the targets were made by irradiating a copper substrate with a $^{22}Na^{+}$ beam at tens of keV. Sodium ions were thus deposited on surface: a thin Cr coat was added to protect from on-beam sputtering. There were two main problems with the targets: the on-beam sputtering and the natural diffusion/evaporation of ^{22}Na ions. The target integrity could not be directly monitored online, by measuring $E_{\gamma,0}$=1.275 MeV from ^{22}Na(β^{+}), due to a high background noise at E_{γ}<4 MeV. The target concentration in ^{22}Na were estimated by measuring the residual activity in the beam-line, after target being removed, and by using known ^{27}Al(p,γ)^{28}Si resonances. This allowed to evaluate potential sputtering. This resulted in <12 %[46] losses for Cr-coated targets. The density of beam on target was estimated by using the known ^{27}Al(p,γ)^{28}Si resonances and Monte-Carlo simulations. They estimated final uncertainties of 10 % due to potential non-uniformities in beam and target densities. With 30 % uncertainties in the measured $\omega\gamma$ [46], both target and beam characterizations were the main factors of uncertainty. An error of 95 % is required to agree with our measured $\omega\gamma$.

We first argue that taking known $\omega\gamma$ in the ^{27}Al(p,γ)^{28}Si reaction to measure the ^{22}Na target composition was not a method with 90 % accuracy. Indeed a different target, with implanted ^{27}Al ions, was used. One wonders why the target concentrations were not measured after irradiations. Moreover, the diffusion coefficient of $^{22}Na^{+}$ ions in solid is 0.9×10^{-6} cm^{2}s^{-1} for a temperature of 573 K (Ref. [120]). This is only an indicative calculation since diffusion is a function of the temperature. Nonetheless, the estimated diffusion after 1 hour being 0.3 mm^2, we also argue that uncertainties of $\sim$10 % in ^{22}Na density were underestimated since it is the usual value for standard targets and not for a radioactive target. Finally, the scattering of the protons at E_{beam} = 0.2(2) MeV is expected important in the 20 nm thick Cr coat [46], increasing the errors in beam energy and density.

The present value $\omega\gamma = 0.26^{+0.11}_{-0.07}$ meV for the E_R=0.204 MeV resonance is among the lowest ever obtained in direct measurement, it is the sensitivity limit of resonance strength measurements.

7.4 Conclusion

A comprehensive study of different experimental works, including ours, and theoretical calculations allowed us to determine an accurate strength $\omega\gamma$ of the E_R=0.204 MeV resonance. With this new value, 22 smaller than the latest measurement [46], a question arises. What is the impact of our unprecedented-low $\omega\gamma$ value on the ^{22}Na(p,γ)^{23}Mg reaction rate? This is the subject of the next Chapter.

Part V

On the astrophysical impact

CHAPTER 8

New thermonuclear rate for the ^{22}Na(p,γ)^{23}Mg reaction

8.1 Introduction

The present work provided a new value of the strength of the E_R=0.204 MeV resonance. Hence the need to reassess the thermonuclear rate of the ^{22}Na(p,γ)^{23}Mg reaction. This is the subject of the present Chapter where the focus is put on the peak nova temperatures, that is to say from 0.1 GK to 0.4 GK.

First, the contribution of the direct-capture reaction mechanism to bound states in ^{23}Mg* was re-evaluated at peak nova temperatures in Sec.8.2. Its cross section was compared to the resonant one. Then, the total reaction rate was derived in Sec.8.3, using a statistical approach to do so. The chosen Monte-Carlo method, now recurrent in evaluations of thermonuclear reaction rates, allowed us to quantify the uncertainties associated with the presently investigated rate.

8.2 Direct capture contribution

The direct radiative capture is a one-step non-resonant nuclear reaction which may strongly contribute inside the Gamow window if there are no resonances or weak ones. This reaction mechanism corresponds to the nucleus fusion with another particle accompanied by the emission of electromagnetic radiation. The contribution of the direct capture (DC) was thus investigated for the ^{22}Na(p,γ)^{23}Mg reaction since the main resonance strength with E_R=0.204 MeV has been measured small, less than 1 meV, in the present work.

The direct capture cross sections to the bound states in ^{23}Mg* depend on the overlap between the entrance wave function $<^{22}\mathrm{Na}_{\mathrm{g.s.}}+\mathrm{p}>$ and the exit one $<^{23}\mathrm{Mg}^* + \gamma>$. The Fortran code RADCAP from [121] was used to derive these cross sections, referred as σ_{DC}. The cross sections for the ground state and the three first excited states in ^{23}Mg* are shown as a function of energy on top of Fig. 8.1. A Woods-Saxon (WS) potential model was chosen, the parameters had first to be adjusted to reproduce the binding energy E_B of the considered state. To do so, the depth of the central potential V_0 was varied. The inputs used are given in Table 8.1. Then, the possible proton incident waves and γ-ray transition orders were determined with respect to the final state. For each state, E1 transitions were found dominant compared to (M1, E2) transitions by more than a factor 10^5. The proton spectroscopic factors were taken from shell-model calculations, as explained in Sec.7.2. The resulting cross sections are presented with the dashed lines in the top of Fig. 8.1. The total cross section is presented with the continuous black line. Direct capture cross sections quickly decrease with Ex, reason why higher-lying states were not considered.

Exit channel ^{23}Mg*+γ				
γ	total to $\frac{3}{2}^+$ g.s.	total to $\frac{5}{2}^+$ Ex=0.451 MeV	total to $\frac{7}{2}^+$ Ex=2.051 MeV	total to $\frac{1}{2}^+$ Ex=2.357 MeV
E1 1^-	$\frac{1}{2}^-$, $\frac{3}{2}^-$, $\frac{5}{2}^-$	$\frac{3}{2}^-$, $\frac{5}{2}^-$, $\frac{7}{2}^-$	$\frac{5}{2}^-$, $\frac{7}{2}^-$, $\frac{9}{2}^-$	$\frac{1}{2}^-$, $\frac{3}{2}^-$
M1 1^+	$\frac{1}{2}^+$, $\frac{3}{2}^+$, $\frac{5}{2}^+$	$\frac{3}{2}^+$, $\frac{5}{2}^+$, $\frac{7}{2}^+$	$\frac{5}{2}^+$, $\frac{7}{2}^+$, $\frac{9}{2}^+$	$\frac{1}{2}^+$, $\frac{3}{2}^+$
E2 2^+	$\frac{1}{2}^-$ to $\frac{7}{2}^-$	$\frac{1}{2}^-$ to $\frac{9}{2}^-$	$\frac{3}{2}^-$ to $\frac{11}{2}^-$	$\frac{3}{2}^-$, $\frac{5}{2}^-$

Entrance channel ^{22}Na+p			
ℓ^π	^{22}Na	p	total
s-wave 0^+	3^+	$\frac{1}{2}^+$	$\frac{5}{2}^+$, $\frac{7}{2}^+$
p-wave 1^-	3^+	$\frac{1}{2}^+$	$\frac{3}{2}^-$, $\frac{5}{2}^-$, $\frac{7}{2}^-$, $\frac{9}{2}^-$
d-wave 2^+	3^+	$\frac{1}{2}^+$	$\frac{1}{2}^+$, $\frac{3}{2}^+$, $\frac{5}{2}^+$, $\frac{7}{2}^+$, $\frac{9}{2}^+$, $\frac{11}{2}^+$
f-wave 3^-	3^+	$\frac{1}{2}^+$	$\frac{1}{2}^-$, $\frac{3}{2}^-$, $\frac{5}{2}^-$, $\frac{7}{2}^-$, $\frac{9}{2}^-$, $\frac{11}{2}^-$, $\frac{13}{2}^-$

Strongest direct capture		
Ex MeV	γ	proton
g.s.	E1	p-wave
0.451	E1	p-wave
2.052	E1	p-wave
2.357	E1	p-wave

Bound states ^{23}Mg = ^{22}Na$_{3^+}$ + p$_{\frac{1}{2}^+}$					
Ex MeV	J^π	single-particle configuration	C^2S_p [a]	E_B MeV	V_0 MeV WS potential
g.s.	$\frac{3}{2}^+$	($d_{5/2}$, $d_{3/2}$)	(0.56, 0.078)	7.58	(106.32, 121.43)
0.451	$\frac{5}{2}^+$	$s_{1/2}$	0.026	7.13	109.24
		($d_{5/2}$, $d_{3/2}$)	(0.424, 0.035)		(105.42, 120.58)
2.051	$\frac{7}{2}^+$	$s_{1/2}$	0.002	5.53	105.45
		($d_{5/2}$, $d_{3/2}$)	(0.211, 0.005)		(102.18, 117.48)
2.357	$\frac{1}{2}^+$	$d_{5/2}$	0.075	5.22	101.54

[a] From shell-model calculations (Sec.7.2).

Table 8.1: Summary of inputs used to estimate direct capture cross sections associated with the ground state and the first three excited states in ^{23}Mg*. Single-particle configurations and associated spectroscopic factors C^2S_p are determined from the state spin J^π. A Wood-Saxon WS potential was used with a central depth V_0 fitted to reproduce the binding energy E_B: E_B=Ex-S_p. Possible exit channels in the first table were found dominated by E1 transition multipolarity. The corresponding total angular momenta must equal the partial waves of the entrance channels given in the second table.

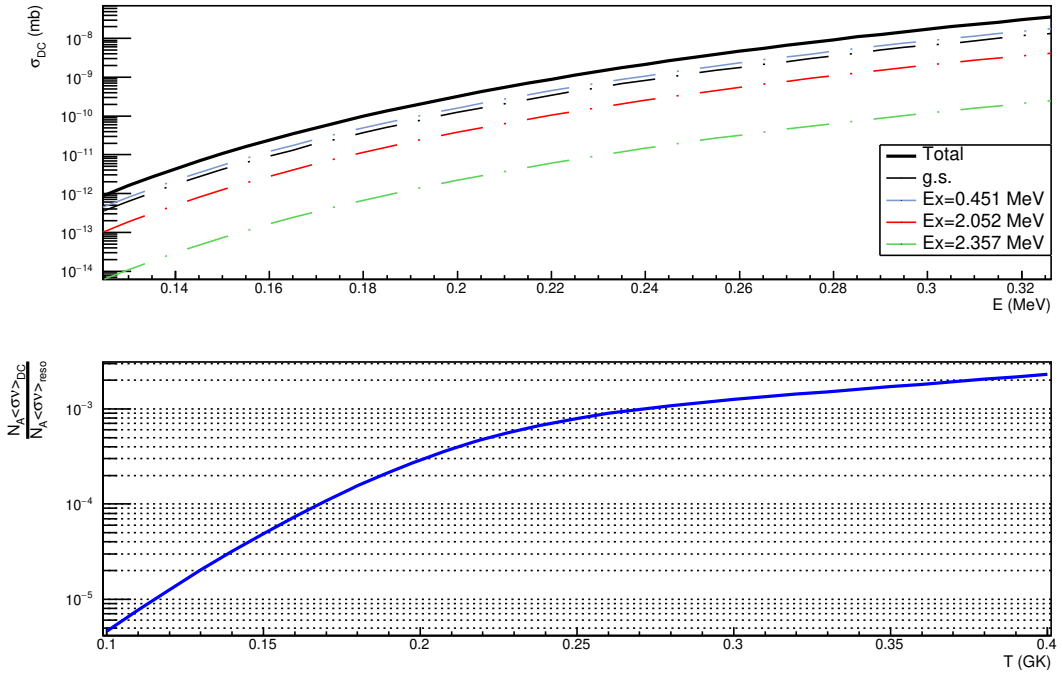

Figure 8.1: Top panel: evolution of the direct capture cross sections $\sigma_{\rm DC}$ along energy (E). The direct capture cross sections are calculated with the RADCAP code [121] for the first excited states in ^{23}Mg* (dashed lines) and the total cross section (continuous black line). Each cross section was normalized with proton spectroscopic factors C^2S_p, predicted from shell-model calculations. The cross sections quickly weaken with the state excitation energy Ex. Bottom panel: the ratio between the direct capture reaction rate $N_A < \sigma\nu >_{\rm DC}$ and the resonant reaction rate $N_A < \sigma\nu >_{\rm reso}$ including the four resonances ($E_R \in \{0.204, 0.274, 0.435, 0.582\}$MeV), as a function of temperature (T). The contribution of the direct capture is always lower than 0.3 %.

The direct capture reaction rate is compared to the resonant reaction rate at the bottom of Fig. 8.1. The ratio of the direct capture reaction rate $N_A < \sigma\nu >_{\rm DC}$ over the resonant reaction rate $N_A < \sigma\nu >_{\rm reso}$ is shown as a function of temperature. Two observations can be made. First, direct capture reaction rate represents less than 0.3% of the resonant reaction rate for T$\in$[0.1, 0.4] GK. Second, the direct capture contribution to the ^{22}Na(p,γ)^{23}Mg total reaction rate increases with temperature. This second point is consistent with the result of Stegmuller *et al* [45]: direct capture was derived and it was shown that this mechanism kicks up at high temperatures (T=2 GK). The ratio of the direct capture reaction rate from the present calculations over the one from Stegmuller *et al* [45] is shown in Fig. 8.2. Their calculations differed from ours in two ways. First, their results are not as good as the present rate since they took C^2S_p=0.1 for all bound states whereas present C^2S_p are within [0.002, 0.56] (Table 8.1). Thus, they overestimated C^2S_p according to our shell-model predictions. The second difference from our calculations is their inclusion of all bound states in ^{23}Mg, but it was not necessary since direct capture cross sections strongly decrease with Ex as shown on the top of Fig. 8.1.

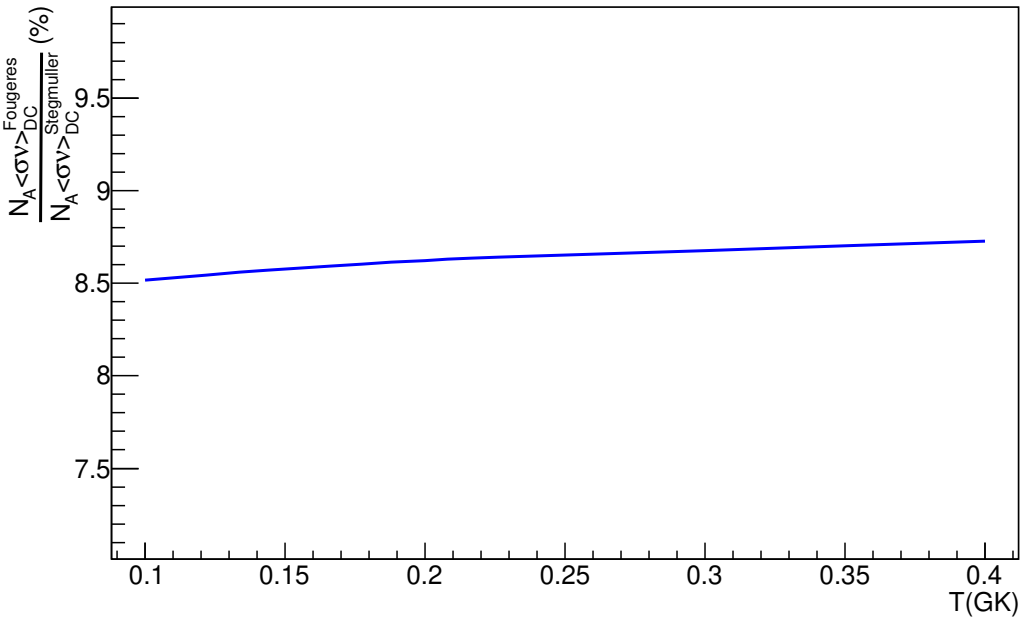

Figure 8.2: Evolution of the new direct capture rate of the ^{22}Na(p,γ)^{23}Mg reaction ($N_A < \sigma v >^{Fougeres}_{DC}$) divided by the direct capture rate of Stegmuller *et al* [45] ($N_A < \sigma v >^{Stegmuller}_{DC}$), as a function of temperature. The present rate is improved by taking into account the shell-model C^2S_p for each excited state, in comparison of the work of Stegmuller *et al* with a constant used C^2S_p=0.1.

As a conclusion, direct capture was found negligible at peak nova temperatures, contributing less than 0.3 % to the total reaction rate.

8.3 Derivation of the reaction rate by the Monte-Carlo method

Thermonuclear reaction rates can be derived as a function of temperature by adding each resonance rate in the analytic expression presented in Eq. (1.10). Each resonance carries uncertainties which need to be properly included in the rate derivation. A simple approach consists on analytically resolving the rate expression with the resonance uncertainties to obtain upper and lower limits. However, it is more pertinent and accurate to include simultaneously all uncertainties and to derive the associated rate statistical distribution: the Monte-Carlo method developed by Longland *et al* [47, 122] allows it. Detailed descriptions of its principle can be found for instance in [47, 122, 123]. In short, the principle of these calculations follows Monte-Carlo approaches. Each resonance parameter is randomly generated according to a probability density. This density is defined by a distribution among those presented in Ref. [47], its expected value and standard deviation must be equal to the user input values. The rate is then derived and these calculations are repeated. In the present calculations, three specific parameters were entered using the recommended distributions from [47]:

1. resonance energies E_R and uncertainties, following a Gaussian distribution,
2. resonance strengths $\omega\gamma$ and uncertainties, following a lognormal distribution,
3. upper limits in $\omega\gamma$, following a Porter-Thomas distribution.

From the calculated rate distribution at a given temperature, the recommended rate corresponds to the median value. Its limits are taken as usual at 1σ (CL 68 %).

The present derivation of the ^{22}Na(p,γ)^{23}Mg rate includes all resonances listed in Table 8.2 with their associated strengths and uncertainties. In addition to the $\omega\gamma$ obtained in the present study for the E_R=0.204 MeV resonance, the other measured strengths for the $E_R \in \{0.274, 0.435, 0.582\}$ MeV resonances were derived by reviewing the direct works of Stegmuller *et al* [45] and Seuthe *et al* [44], their results being in agreement. The work of Sallaska *et al* [46] was not included for these three resonance. The first references [45, 44] have been favoured for the present rate calculation since: (1) the $\omega\gamma$ values were found to be smaller than in [46], hence more consistent with our result on the E_R=0.204 MeV resonance, (2) the target profile in ^{22}Na was fully measured before the experiment in the transversal plane with respect to beam axis and the observed inhomogeneity of the target was compensated by a proper tuning of the proton beam, see details about the beam wobbling in [45]. Concerning the $E_R \in \{0.189, 0.201, 0.222\}$ MeV where only upper limits are known, the lowest value was looked for in the three works [46, 45, 44]. It happened to be found for the three resonances in the reference [46].

E_R MeV	Ex MeV	J^π	$\omega\gamma$ meV	Ref.
0.1894(8)	7.7704(20)	$\frac{9}{2}^+$	<0.51	lowest value in [46, 45, 44]
0.2008(11)	7.7818(9)	$\frac{11}{2}^+$	<0.40	lowest value in [46, 45, 44]
0.2035(11)	7.7845(9)	$\frac{7}{2}^+$	$0.26^{+0.11}_{-0.07}$	present
0.2220(8)	7.8030(6)	$\frac{5}{2}^+$	<0.67	lowest value in [46, 45, 44]
0.2745(9)	7.8555(7)	$\frac{7}{2}^+$	14.8(22)	average [45, 44]
0.4346(9)	8.0156(7)	$\frac{9}{2}^+$	68(20).	average [45, 44]
0.5821(14)	8.1631(12)	$\frac{5}{2}^+$	235(14)	average [45, 44]

Table 8.2: Summary of resonance inputs used to derive the ^{22}Na(p, γ)^{23}Mg reaction rate by using the Monte-Carlo method [47, 122]. Resonance energies E_R and associated Ex are given with their uncertainties from present study and [55]. The upper limits for the low resonances were taken by comparing all direct works [46, 45, 44].

The newly recommended rate is shown with the red curve on the left of Fig. 8.3 as a function of temperature. The ratios of the distributed reaction rates to the recommended one are given on the right of Fig. 8.3. The thick black lines show the 1σ limits, at temperatures higher than 0.15 GK it corresponds to less than 40 % uncertainties on the reaction rate. Such a strongly constrained rate was aimed by the present Ph.D. work. As a comparison, rates using past direct measurements were also derived: the purple curve is associated to [45] and the blue curve to [46]. Dashed lines correspond to the 1σ uncertainties. As expected from the new $\omega\gamma$ at E_R=0.204 MeV, our new rate is well below the rates derived with the strengths measurements, by a factor 10 for the recent measurement [46] and 3 for the older measurements [45]. For comparison, the NACRE 1996 rate [124] is pointed out with the green line: it is 13 times higher than the present rate, clearly overestimating the resonance contributions for $E_R \in \{0.189, 0.201, 0.222\}$ MeV by not taking the strengths as upper limits.

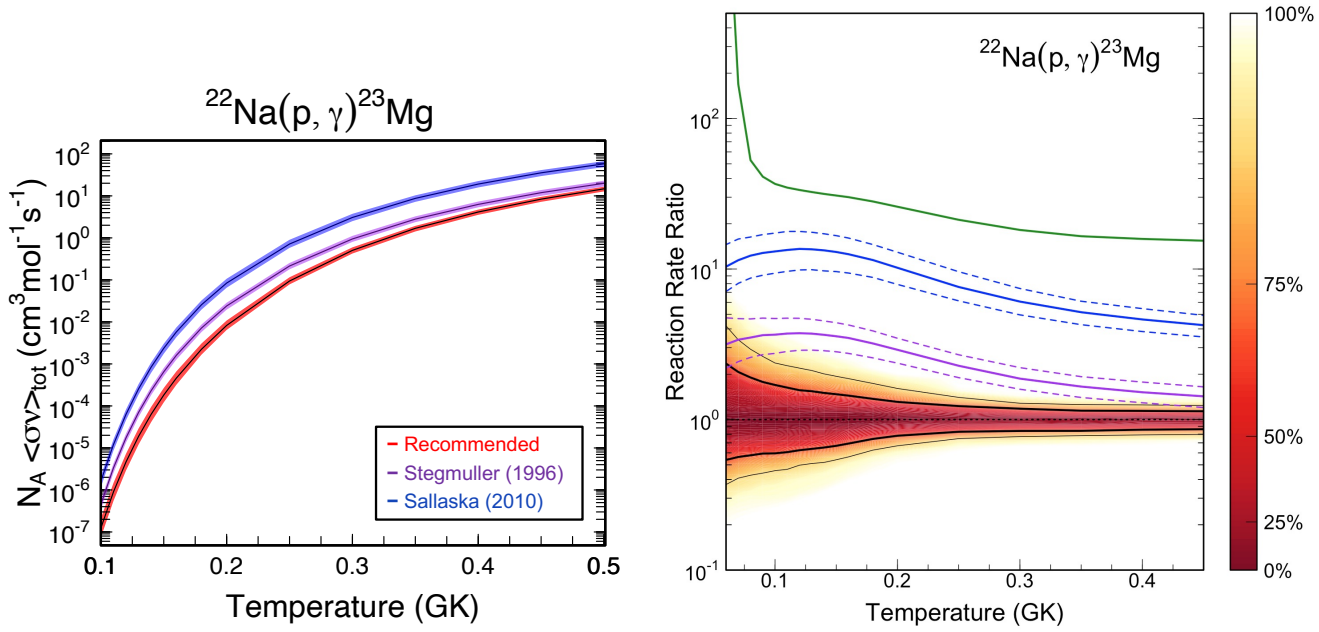

Figure 8.3: Left: the thermonuclear rates of the ^{22}Na(p,γ)^{23}Mg reaction are shown as a function of temperature. The rates were obtained with the Monte-Carlo method [47, 122]. Lines are associated to the recommended median values and shaded regions to the level confidence of 1σ. Red region is the recommended rate. The purple rate corresponds to the measurements [45], it converges to the present rate at high temperatures. On the contrary, the evaluated rate from the latest measurement [46], shown in blue, was found much higher. Right: the rates are normalized to the recommended rate. The green curve was calculated using the NACRE 1996 database [124]. Except for the recommended rate, the continuous coloured lines are median values and the dotted lines correspond to 1σ CL. The cumulative distribution from MC calculations associated with the present work is shown by the red-like color scale. The uncertainties on the rate were observed $<$40 % (for 1σ, thick black lines) within the classical nova temperatures, T$\sim$ [0.15, 0.35] GK. Higher uncertainties, i.e. $\geq$ 50%, are observed for low temperatures T$\leq$0.1 GK, due to the only known upper limits in $\omega\gamma$ for the low energy resonances.

Each resonance relative contribution was also re-evaluated as a function of the temperature as shown on the right of Fig. 8.4. The contributions obtained here differ from those before our experimental work, as shown on the left side. Within nova temperature range, the two resonances at E$_R$=0.204 MeV and 0.274 MeV are important now with the new rate, they contribute for more than 50%. In order to further reduce the rate uncertainties, it would be interesting to measure the strengths of the two low resonances with E$_R$=0.189 MeV and 0.201 MeV. Such an experiment would be challenging due to the required sensitivity, 0.1 meV at least. However, the results obtained here represent already a reliable and accurate destruction rate of ^{22}Na at peak nova temperatures.

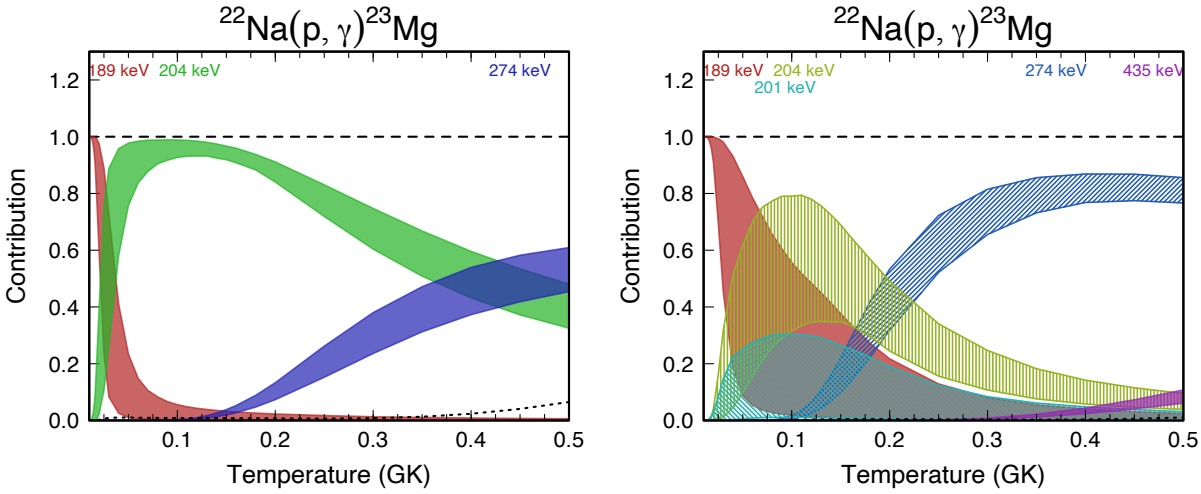

Figure 8.4: Relative contributions of the resonances to the rate of the ^{22}Na(p,γ)^{23}Mg reaction as a function of the temperature selected on the nova range. Only contributions above 5% are shown. Coloured regions represent the statistical uncertainties. Left: the different strengths $\omega\gamma$ of Sallaska *et al* [46] were used. Right: the contributions of the resonances are re-evaluated with the new strength of the E_R=0.204 MeV resonance and the reassessment of the other resonances. The E_R=0.204 MeV resonance (green) appears less dominant, up to 80 %. The higher E_R=0.274 MeV resonance (blue) contributes now for more than 60 % at temperatures above 0.2 GK. The contribution of the low energy resonances, with E_R=0.189 MeV and 0.201 MeV at low temperatures (<0.2 GK) is only an upper limit. For this reason, the contributions of the resonances remain rather uncertain around 0.1 GK.

In conclusion, our re-evaluation of the ^{22}Na(p,γ)^{23}Mg thermonuclear reaction rate has led to a new, accurate rate that was significantly reduced from the previous rates.

8.4 Conclusion

After deriving the strength of the E_R=0.204 MeV resonance, the main contributor to the destruction of ^{22}Na by proton capture in novae, the rate of the ^{22}Na(p,γ)^{23}Mg reaction was re-evaluated. In the first place, the direct capture was re-evaluated to confirm that this mechanism is indeed negligible compared to the resonances. The final thermonuclear reaction rate was calculated by using a Monte-Carlo statistical approach in order to determine the impact of the resonances uncertainties and the resulting rate uncertainties. In the temperature range of interest, the recommended rate has now less than 40 % uncertainties, a strong improvement with respect to the factor 2.5 discrepancy from previous reaction rate based on strengths measurements. It turned out to be more than 10 times smaller than before [46]. What are the consequences on the predicted amount of ^{22}Na produced during novae outburst? Chapter 9 will investigate this question as well as the part ^{22}Na can play in novae physics and gamma-ray astronomy.

CHAPTER 9

Production of ^{22}Na in novae

9.1 Introduction

The knowledge of the destruction rate of ^{22}Na by proton capture at peak nova temperatures is not sufficient. How many ejected ^{22}Na nuclei can be expected during a nova event? Will we be able to observe their γ-ray line with the next generation of space telescopes? Can such observations shed light on the mechanism of novae laying behind? These three burning questions will be addressed in the last Chapter of the present thesis.

With our reevaluated ^{22}Na(p,γ)^{23}Mg reaction rate, simulations of ONe novae were carried out in order to predict the amount of ejected ^{22}Na nuclei. This work is presented in Sec.9.2. Then in Sec.9.3, some parameters of the nova models were investigated with respect to the ejected amount of ^{22}Na. Finally in Sec.9.4, we have looked toward the future landscape of γ-ray astronomy: positive prospects for the radioelement ^{22}Na have been developed.

9.2 Predicting the amount of ^{22}Na ejected

9.2.1 MESA code

The simulation code MESA (Modules for Experiments in Stellar Astrophysics) of Paxton *et al* [40] has been used. This tool, freely available [125], allows us to calculate stellar evolutions from the youngest stars on the main sequence to black holes. We will briefly introduce the code principle and a short technical guideline in order to run novae simulations. MESA simulations of ONe novae have been well investigated by Denissenkov *et al* [126]. All tools built from their work are open source [127].

MESA code, based on Fortran-95, is made of modules *star* which are used to run specific stellar simulations in multi-zone processing, with spherical symmetry and hydrodynamics included. Pre-built modules and their associated Fortran script are found in the *star/test_suite* directory, there are in particular the codes for making white dwarf nova bursts and CO or ONe white dwarfs.

The inputs files *inlist* allow us to define and to control the simulation. Three main sections are of interest: *(i) star_job* to set the stellar evolution features, *(ii) controls* to define the used star module and *(iii) pgstar* to choose the plots display during the simulation. Before running, one has to ensure that the path of *mesa_dir* is properly defined in the *makefile* and *inlist* files. In our case of interest, simulations of novae, the initial white dwarf module is chosen at the start of *inlist_setup* file. The nuclear network, referred as *.net* file, can be adjusted, an example is available in [127]. For computing times saving, it is of interest to reduce the network to only the isotopes and reactions which mainly contribute to the stellar

thermodynamics, see [126]. The ^{22}Na(p,γ)^{23}Mg reaction rate we wanted to investigate is entered in the *data/rates_ data/rate_ tables* directory. All rates and reactions are listed in two specific text files. Then, the *inlist_ wd_ nova_ burst* file allows us to define:
- the accretion rate with *mass_ change*,
- the accreta isotopic composition with the possibility to use an external file.
The accreta composition was chosen here as 50% solar composition and 50% white dwarf matter, from [127]. This is of course a free parameter.

Once the simulation is completed, all results in the *LOGS* directory are pictures of the stellar system for different instants *profiles* of the simulated nova. Each picture includes arrays, indexed along the spatial zones, of all physics parameters defined by the user in the *history_ columns.list*. The main parameters of interest for us were the nuclei abundances, the temperature, the luminosity, the radius, the density, the pressure, the mass, the star age. The analysis of the outputs is easily handled with the Python open library dedicated to MESA: *mesa_ reader*. This can be found in [128].

Prior to simulate the nova outbursts, the white dwarf was built until the defined termination mass, and cooled down with another MESA script until the defined central temperature. The two scripts allow us to tune the initial parameters M_{WD} and T_{WD}.

In conclusion, simulations of novae with the MESA code are based on multi-zone processing to simulate the white dwarf evolution, from its core to its extended surface, along time.

9.2.2 Building ONe novae with MESA

Several aspects of the ONe novae simulations, run with the MESA code, are presented in the next paragraphs.

- White dwarf properties

In this binary system, the central star is a white dwarf composed mainly of stable oxygen and neon nuclei. We have built such a white dwarf with both fixed mass M_{WD}=1.2 $M_\odot$ and fixed isotopic composition, and we have let its mean central temperature free, referred as T_{WD}. The latter depends on the age of the white dwarf: the older the star, the cooler the star. The isotopic composition of the white dwarf is shown in Fig. 9.1. The abundances of stables ions, from ^{4}He to ^{24}Mg, are plotted against the radius (R) with the origin at the star center. The simulated white dwarf radius R_{DW}=5.2×10^{-3} $R_\odot$ agrees, within 50 %, with expectations from Eq. (1.4). The star is mainly composed of ^{20}Ne ions (50 %) and ^{16}O ions (40 %) in the inner parts. At the surface, lighter ions ^{16}O and ^{12}C are dominant by a factor of more than 90 %. The stable sodium ^{23}Na is present at less than 1 % in the whole star.

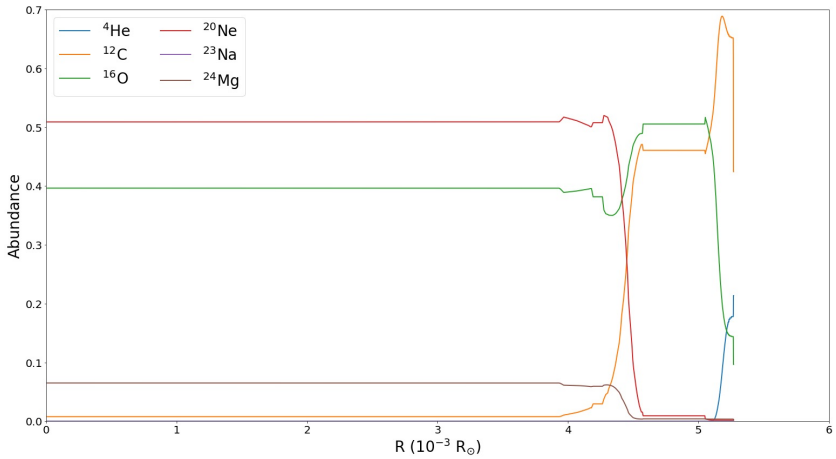

Figure 9.1: Isotopic abundances against the radius R, from a calculated ONe white dwarf with MESA. The isotopes presented are: ^{4}He (blue), ^{12}C (orange), ^{16}O (green), ^{20}Ne (red), ^{23}Na (purple), ^{24}Mg (brown).

The simulations show that the mixing of the accreted material with the inner layers of the white dwarf is important for the NeNaMg cycle. We remind that this cycle governs the production of ^{22}Na in ONe novae.

Then an explosion is triggered in the outer layers, lasting less than an hour.

- Outburst storyline

The first stage in the simulations of ONe novae is the long accretion of matter onto the outer layers of the white dwarf star. The radius of the white dwarf slowly increases over thousands of years. Then, an explosion is ignited in the outer layers lasting less than 1 hour. In this second stage, i.e. the outburst, the maximum temperature T_{max} increases until it reaches a maximum, and a fast increase of the surface luminosity $L_{surface}$ is observed. These temperature and luminosity profiles are shown in Fig. 9.2 with respectively the red and orange curves. The time has been defined to be 0 for the peak temperature. The associated maximum of the temperature T_{max} is called the peak nova temperature T_{peak}, in the present case it is 0.24 GK. It is observed that the luminosity after the outburst is constant, this corresponds to the constant bolometric luminosity stage (Sec.1.3). Here, L_{const} was found to be equal to $10^{4.4}$ $L_\odot$. The density of the zone associated with T_{max}, written $\rho_{T_{max}}$, is also shown with the green curve. Its fast decay suggests the ejection of outer layers. Before the outburst, the density was found to be $10^{3.25}$ g.cm^{-3}.

Our simulation of the ONe nova outburst has been compared to that performed with the SHIVA code in the 115ONe model with M_{WD}=1.15 $M_\odot$ and a 50 % pre-enrichment of the ONe white dwarf (Ref. [20]). The results obtained are T_{peak}=0.23 GK, $\rho_{T_{max}}$=7.45×10^3 g.cm^{-3} and L_{const} ∼10^4 $L_\odot$. Our results obtained with MESA agree well with the results of the simulations using SHIVA.

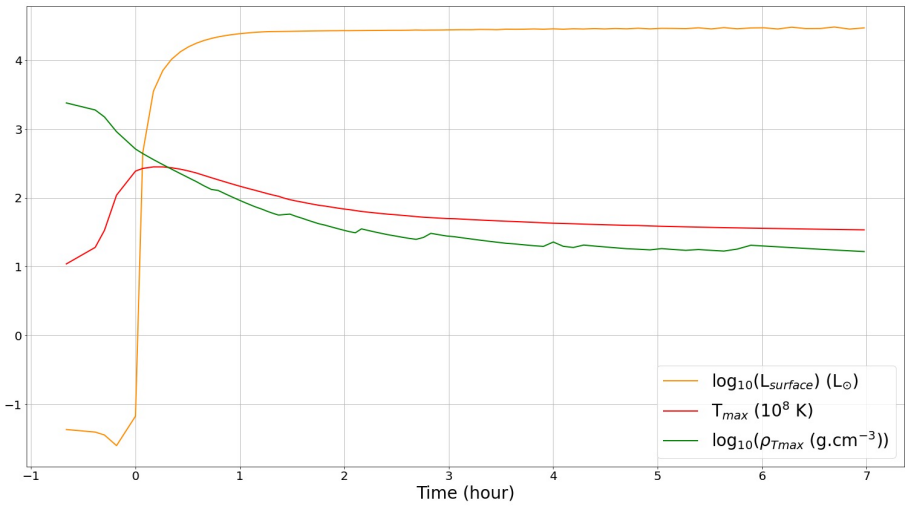

Figure 9.2: Set-up of the outburst during a ONe nova, simulated with MESA. Red curve: the maximum temperature T_{max} plotted along the time, put at 0 for the peak temperature. Orange curve: the surface luminosity ($L_{surface}$). Green curve: the density at T_{max} ($\rho_{T_{max}}$). The outburst appears with a peak in T_{max}, up to T_{peak}=0.24 GK, and a fast increase in $L_{surface}$, for less than 1 hour. This is followed by the constant bolometric luminosity stage ($L_{surface}$=$10^{4.4}$ $L_\odot$). Units in the legend.

- Ejecta properties

With MESA code, the ejecta is not automatically pointed out: we therefore have to determine which outer zones were ejected during the simulations. In Fig. 9.3(a) and (b), pressures are plotted against the radius for the instant respectively before and after the outburst . At the radius position of R=R_{WD}=5.2×10^{-3} $R_\odot$, the pressure goes up to [10^{19}, 10^{20}] dyn.cm^{-2}, indicating that the envelop can be ejected, see [34, 33]. A fast expansion of the outer zones after the outburst can be noticed: R$\geq$$8\times10^{-3}$ $R_\odot$ (Fig. 9.3(b)) compared to max(R)=6.5×10^{-3} $R_\odot$ (Fig. 9.3(a)) before the outburst. In Fig. 9.3(c), the evolution of the surface radius $R_{surface}$ which corresponds to the remotest zone from the star center, is normalized by R_{WD} and shown as a function of time during the nova event. We note that the surface layer expands well above the initial white dwarf radius, by more than a factor of 10. The radius of the zone is so a pertinent criteria to determine if the zone is ejected. Likewise Ref. [126], we assumed that each post-outburst zone with a radius above R_{WD} is ejected.

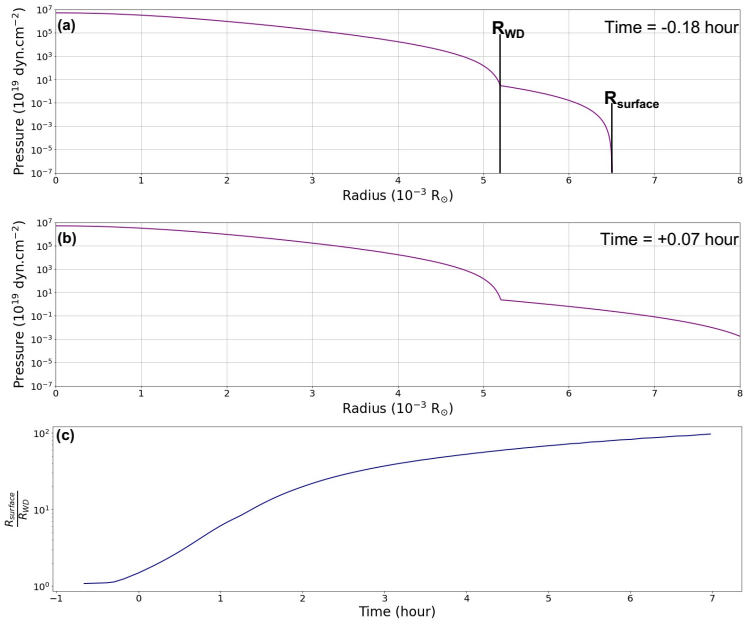

Figure 9.3: Panels (a, b): pressure is shown over the radius, 0.18 hour before the outburst (a) and 0.07 hour after the outburst (b). The white dwarf radius R_{WD} and the surface radius $R_{surface}$ are indicated with the black lines in (a). After the outburst, the outer layers expand. Panel (c): the ratio of the surface radius over the white dwarf radius, $\frac{R_{surface}}{R_{WD}}$, is presented as a function of the time. For few hours after the nova peak, the envelop surface is more than 10 times away from the white dwarf initial surface.

The luminosity of the zone is also a criteria to determine if the zone is ejected: if the luminosity is higher than the Eddington luminosity L_{Edd}, then the zone can be ejected as explained in Sec.1.3. In Fig.9.4, the normalized luminosity of the zone $\frac{L}{L_{Edd}}$ is presented along the normalized radius during a simulated ONe nova. The expanding envelop which has $\frac{R}{R_{WD}} \geq 10$ is observed with $L > L_{Edd}$ after the outburst at time=0 hour. This confirms that a zone with a radius larger than the initial radius of the white dwarf is ejected.

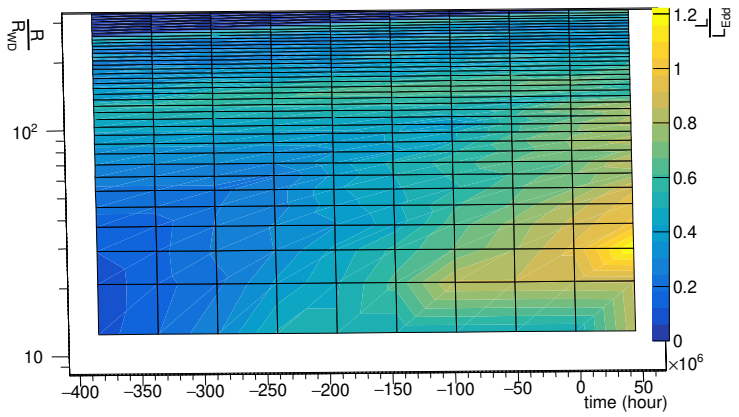

Figure 9.4: The luminosity L normalized by the Eddington luminosity L_{Edd} is shown as a function of the radius normalized by R_{WD} and of the time, during a simulated ONe nova with MESA. The expanding envelop with $\frac{R}{R_{WD}} \geq 10$ is observed with a luminosity higher than the Eddington limit after the outburst time (time=0 hour), this proves this region is being ejected.

Analyzing the velocity of the different zones may also help to determine which zones are ejected after the nova outburst. However, the calculated velocities, maximum for the expanding envelop, reached the values of [20, 30] km.s^{-1} whereas they are expected to be around 1000 km.s^{-1} [20, 33]. This known problem of MESA code which does not manage to reproduce real ejecta velocities, is currently unsolved.

To conclude on the simulations of ONe novae with MESA, we have highlighted that

1. The outburst can be identified by the evolution of three main parameters (temperature, density, luminosity).

2. It is assumed that the entire layer above the white dwarf initial radius is ejected after the outburst.

9.2.3 Determination of the ejected mass of ^{22}Na

From simulations of a ONe nova event, the ejected mass of ^{22}Na is easily derived by extracting the abundances of ^{22}Na in each ejected layer, i.e. R$\geq$R$_{WD}$. The abundances of ^{22}Na were converted into masses by multiplying with the associated zone mass. The ejected mass of ^{22}Na, $M_{ej}^{^{22}Na}$, is finally defined as the integrated masses of ^{22}Na in each ejected zone. In Fig. 9.5, the mass of ^{22}Na ($M^{^{22}Na}$) is presented as a function of the radius normalized by R$_{WD}$ and of the time. A peak of produced ^{22}Na is observed in the ejected zones with R$\geq$10$\times$R$_{WD}$ at the time of outburst (time=0 hour). The calculated ejected mass of ^{22}Na is $M_{ej}^{^{22}Na}$=3.51$\times$10^{-9} M$_\odot$.

The radioelement ^{22}Na is mainly produced around the time of the outburst when the temperature is higher than 1 GK, as shown in Fig. 9.2 and 9.7. The present ^{22}Na(p,γ)^{23}Mg reaction rate has main uncertainties ($\geq$ 50%) at low temperatures T$\leq$0.1 GK, due to the only known upper limits in $\omega\gamma$ for the low energy resonances (Sec.8.3). However, as shown here, it would only impact uncommon cold novae events.

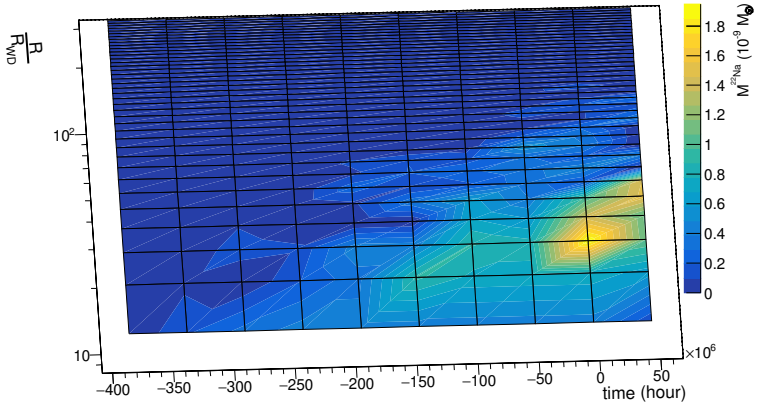

Figure 9.5: The mass of ^{22}Na, $M^{^{22}Na}$, as a function of the radius normalized by R$_{WD}$ and of the time, during a simulated ONe nova with MESA. A peak of ^{22}Na, seen with the yellow region, is observed around the time of the outburst (time=0 hour) in the expanding envelop with $\frac{R}{R_{WD}} \geq 10$.

The ejected mass of ^{22}Na obtained in the MESA simulations was compared to results of ONe models obtained with the SHIVA code in Table 9.1. The results are reasonably in agreement, within a factor 3, mainly due to the different ^{22}Na(p,γ)^{23}Mg reaction rates. The consistency between our results and the ones with the more realistic SHIVA code [33, 129], supports the present investigation on ONe novae simulations.

Code	ONe model		Ref	$M_{ej}^{^{22}Na}$ (10^{-9} $M_\odot$)
	Mixing	M_{WD} ($M_\odot$)		
MESA	50% ONe	1.2	present work	3.51
SHIVA	ONe2		[33]	1.11
	23% ONe	1.25		
	ONe3		[129]	1.01
	50% ONe	1.15		
	ONe5		[129]	1.34
	50% ONe	1.25		

Table 9.1: Comparison between the predicted ejected masses of ^{22}Na ($M_{ej}^{^{22}Na}$) from the present MESA simulations of ONe novae with the SHIVA simulations. The ONe models, presented in the 2nd and 3rd columns, are quite similar. The increases of M_{WD} and of ONe mixing were observed to increase also $M_{ej}^{^{22}Na}$. Among the codes inputs here, the ^{22}Na(p,γ)^{23}Mg reaction rate has by far the greatest impact on $M_{ej}^{^{22}Na}$.

In conclusion, the amount of ejected ^{22}Na by the nova outburst can be derived with the MESA code. It is in the order of $\sim 10^{-9}$ $M_\odot$ for a classical ONe nova with M_{WD} $\sim$1.2 $M_\odot$. This amount depends sensibly on the ^{22}Na(p,γ)^{23}Mg reaction rate.

9.3 Constraining ONe nova models

9.3.1 Sensitivity of ^{22,23}Na isotopes

The radioelement ^{22}Na is known to be a key astronomical observable of ONe novae, in order to improve our understanding of these cosmic events, see Chapter 1. Nevertheless, the stable isotope ^{23}Na is easier to detect with its atomic lines in the light curve of novae. The evolution of the total mass ratio of ^{22}Na over ^{23}Na, $\frac{M_{^{22}Na}}{M_{^{23}Na}}$, during the nova outburst is presented in Fig. 9.6(a). The isotope ^{23}Na is noticed 10^6 more abundant than the radioelement ^{22}Na. We therefore wondered whether the stable ^{23}Na could also contribute in the understanding of ONe novae. The relative variations of the total masses ($\frac{dM_{tot}}{dt \times M_{tot}}$) in ^{23}Na and ^{22}Na are shown during the outburst in respectively Fig. 9.6(b) and Fig. 9.6(c). The abundance of ^{23}Na is almost unchanged, $\frac{dM_{tot}}{dt \times M_{tot}}$ varying by only 0.05 %.hour^{-1}. This shows that the abundance of ^{23}Na hardly changed during the ONe nova outburst unlike the radioelement ^{22}Na highly produced at the time of the outburst.

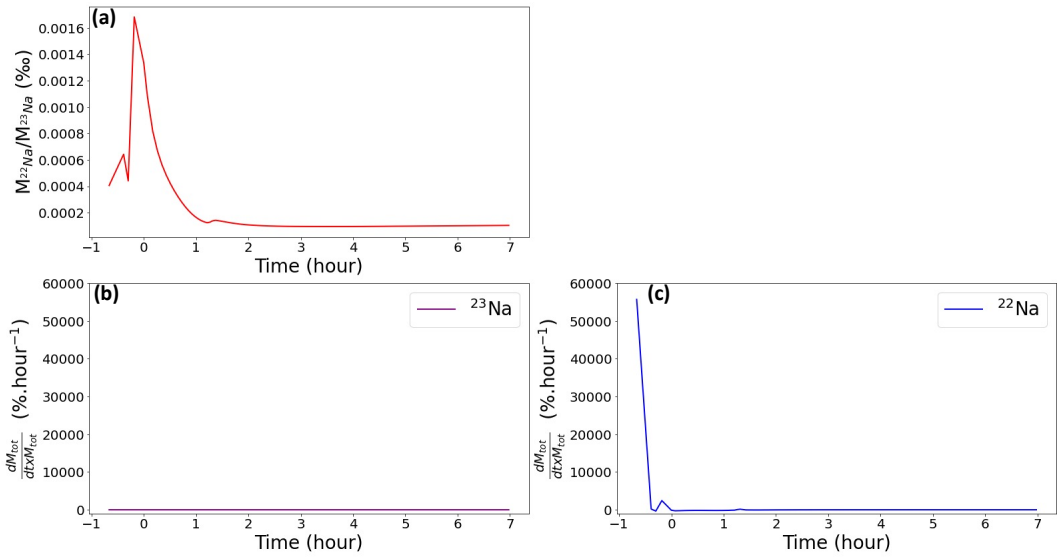

Figure 9.6: Panel (a): the total mass of ^{22}Na over the one of ^{23}Na, $\frac{M_{22_{Na}}}{M_{23_{Na}}}$, is presented during a simulated nova event with MESA. The radiolement ^{22}Na is negligible, i.e. 1 ion per 10^6 ions of ^{23}Na. Panels (b, c): the relative time derivatives ($\frac{dM_{tot}}{dt \times M_{tot}}$) of the total mass of ^{23}Na (b) and of ^{22}Na (c) are shown during the event. The amount of ^{23}Na appears unchanged as compared to the amount of ^{22}Na.

9.3.2 The free parameters investigated

The main open questions regarding the physics of novae have been raised in Sec.1.3. They result in uncertain parameters when nova models are built. These parameters are thus relatively free, the word relatively being employed since they are often restricted in limited ranges, sometimes partially constrained by observations. Some parameters have already been mentioned: the mixing ratio between the white dwarf material and the accreted material, the composition of the accreted material, etc. We have chosen to investigate two free parameters for the two stages before the outburst:
(1) the white dwarf initial central temperature T_{WD},
(2) the accretion rate, assumed constant.
The latter is expected to be within [10^{-10}, 10^{-9}] $M_{\odot}.yr^{-1}$. The parameter (1) was taken in [12, 18] MK, coming from MESA simulations of ONe white dwarfs and their associated cooling time. From now on, the other uncertain parameters are fixed: M_{WD}=1.2 $M_{\odot}$, a mixing of 50 % solar composition and 50 % ONe-rich material. In Fig. 9.7, the peak nova temperature T_{peak} is given as a function of the chosen T_{WD} and accretion rate. The peak nova temperature is indeed a function of the other parameters, i.e. it is not a free parameter.

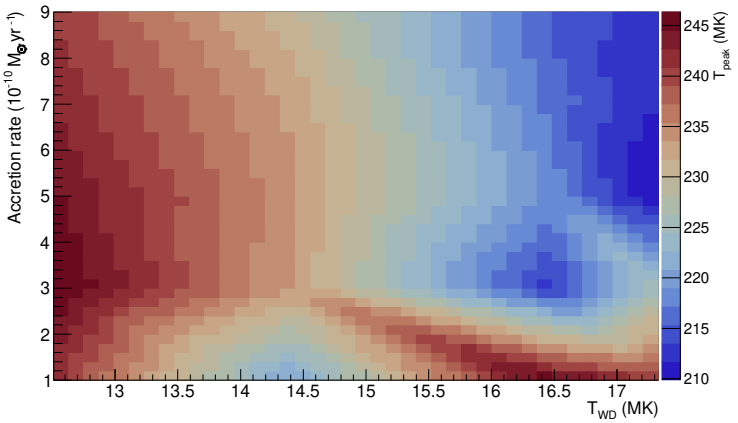

Figure 9.7: The peak nova temperature T_{peak} as a function of the white dwarf initial central temperature T_{WD} and the accretion rate, from MESA simulations of ONe novae.

9.3.3 Impact on the ejected mass of ^{22}Na

The impact of the two free parameters, i.e. T_{WD} and the accretion rate, on the ejected mass of ^{22}Na is now investigated. The ejected mass has been converted into the emitted γ-ray flux which represents the actual signal accessible from the γ-ray space telescopes. Knowing that the flux depends on the ejected mass of the radioelement ^{22}Na according to

$$\text{Flux } ^{22}\text{Na} = \frac{M_{ej}^{^{22}\text{Na}}}{M_{ion}^{^{22}\text{Na}}} \times \frac{\ln(2)}{4\pi d^2 \times \tau_{\frac{1}{2}}} \quad (\text{ph.cm}^{-2}.\text{s}^{-1}) \tag{9.1}$$

where $M_{ion}^{^{22}\text{Na}}$ is the mass of the ^{22}Na ion, d is the distance from Earth to the observed nova, and $\tau_{\frac{1}{2}}$ is the half-life of the radioelement ^{22}Na.

We present the expected flux from the ejected ^{22}Na ions during an ONe nova event located at 0.6 kpc in the left side of Fig. 9.8. This was obtained as a function of T_{WD} and the accretion rate. The minimum value of the flux shown in the left of Fig. 9.8 corresponds to the sensitivity of the e-ASTROGAM space spectrometer, a proposed ESA project for γ-ray astronomy [130]. From such a nearby nova, the ^{22}Na γ-ray line would be accurately observed. As an illustration, let's suppose we observe a flux of $8.5(5)\times10^{-6}$ ph.cm^{-2}.s^{-1}, then the underlying nova should have the values for the accretion rate and the white dwarf initial central temperature shown in the right side of Fig. 9.8. This confirms that the radioelement ^{22}Na indirectly gives informations related to the physical properties of the detected ONe nova, helping so to constrain the current models.

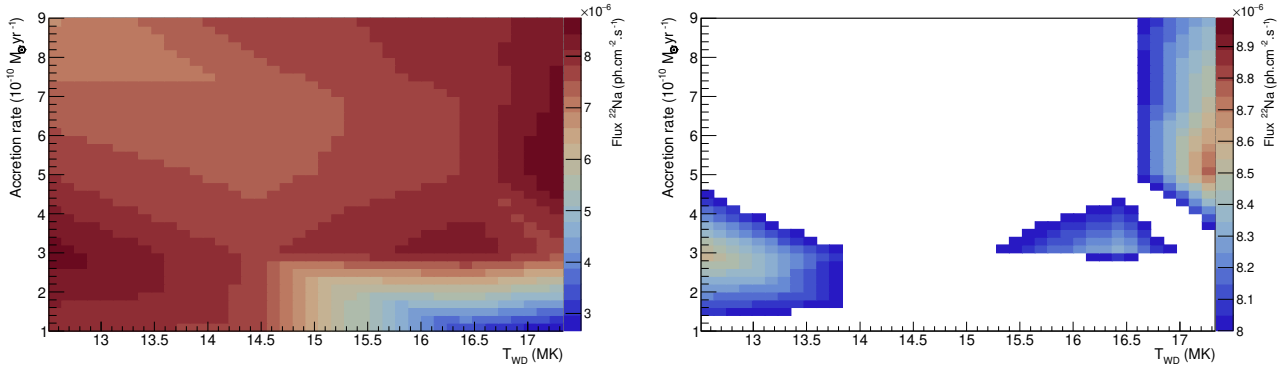

Figure 9.8: Left: the γ-ray flux from the ^{22}Na ions, ejected by a simulated ONe nova event at 0.6 kpc, is shown over the accretion rate and T_{WD}. The lower value of the flux corresponds to the sensitivity of e-ASTROGAM space telescope. Right: the flux is selected on the range $8.5(5)\times10^{-6}$ ph.cm^{-2}.s^{-1}, constraining the possible values in the accretion rate and T_{WD}.

In conclusion, the study of the influence of two physical parameters of the novae on the ^{22}Na γ-ray flux reinforced the idea that the observation of this flux from Earth could provide constrains on the nova.

9.4 Prospects for astronomy

9.4.1 Expectations in future γ-ray observation campaigns

New instruments for γ-ray astronomy are expected in the coming decade. In particular, two projects are currently pushed for supports from ESA and NASA, respectively: the enhanced e-ASTROGAM [130] and the COmpton Spectrometer and Imager COSI [8].

The proposed space mission e-ASTROGAM targets γ-rays ranging from 0.3 MeV to the GeV scale, fitting into the multi-messengers astronomy. The principle of the spectrometer is shown on the left side of Fig. 9.9, taken from [130]. The energy and cosmic source position of γ-rays are built back by tracking the Compton interactions and the pair productions in the active volume made of silicon detectors. Unprecedented capabilities are expected in terms of sensitivity, i.e. an improvement of a factor 30 compared to INTEGRAL for MeV γ-rays, of energy and angle resolutions, and of the possibility of polarimetric measurements. For MeV γ-rays, the aimed resolutions are 3 % for energies and $\leq$1.5 deg for angles. The Si tracker is made of layers of double-sided strip detectors DSSD to measure recoil electrons from Compton scattering and pair productions. A calorimeter would detect the secondary particles from pair productions. The crucial background noise issue of past missions, like INTEGRAL, is also supposed to be improved with an enveloping Anti-Coincidence system able to reject $\geq$99 % of noise. There are many interesting physics cases: gamma-ray bursts, nucleosynthesis of novae, supernovae, kilonovae with the radioelements (^{26}Al, ^{22}Na, ^{44}Ti, ...), active galactic nuclei, cosmic rays. A complete study is found in the white book [130].

The second spectrometer, COSI, would present a narrower γ-ray energy range, from 0.2 to 5 MeV. It is also expected with a much higher efficiency than the past INTEGRAL and COMPTEL missions. Presented in the right side of Fig. 9.9, the spectrometer should include a compact array of 16 cross-strip Germanium detectors which would be surrounded by BGO shields to improve SNR. The sensitivity around 1 MeV is higher than e-ASTROGAM, see Table 9.2. With an energy resolution of 0.5 %, the spatial resolution is expected the same as e-ASTROGAM. More details are given in [8].

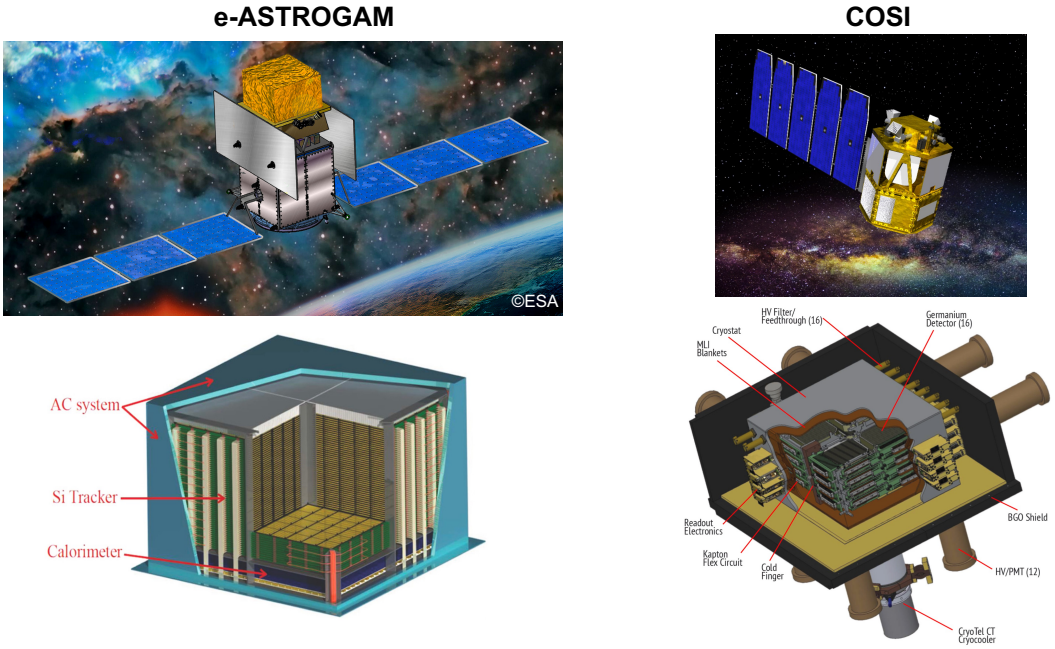

Figure 9.9: Left: layout of e-ASTROGAM with Si tracker made of silicon DSSD, calorimeter and anti-coincidence enveloping box. Images taken from De Angelis *et al* [130]. Right: structure of COSI, with in particular 16 Ge detectors ($8\times8\times1.5$ cm^3) and a BGO shield box. Images taken from Tomsick *et al* [8].

A compilation of surveys [131, 20] of the observed ONe novae over the past 60 years has been done. Eight ONe novae have been identified within 50 kpc from the Sun and with reliable derived distances. Indeed, distances of distant stellar events are difficult to estimate since the observed magnitudes may be wrong due to interstellar dusts and gases. These 8 events are represented on the map of the Milky Way with the red points, shown in Fig. 9.10. The expected γ-ray fluxes from ^{22}Na were used to normalize the color of points. The novae more distant than the galactic center are not bright enough to be visible. The areas of detectability for the two γ-ray space spectrometers are delimited by the colored circles, the orange (cyan) circle for e-ASTROGAM (COSI). These limits in distance are given in Table 9.2. They were calculated by using the expected sensitivities for 1 MeV γ-rays, and the ejected mass of $M_{ej}^{^{22}Na}=3.5\times10^{-9}$ $M_\odot$ from previous simulations of classical ONe novae.

In Fig. 9.10, three (one) ONe nova events are seen within the detectability range of COSI (e-ASTROGAM) for the γ-ray line from ^{22}Na. Thus, the next generation of γ-ray onboard space spectrometers should observe at least 1 ONe nova event during a twenty-year campaign.

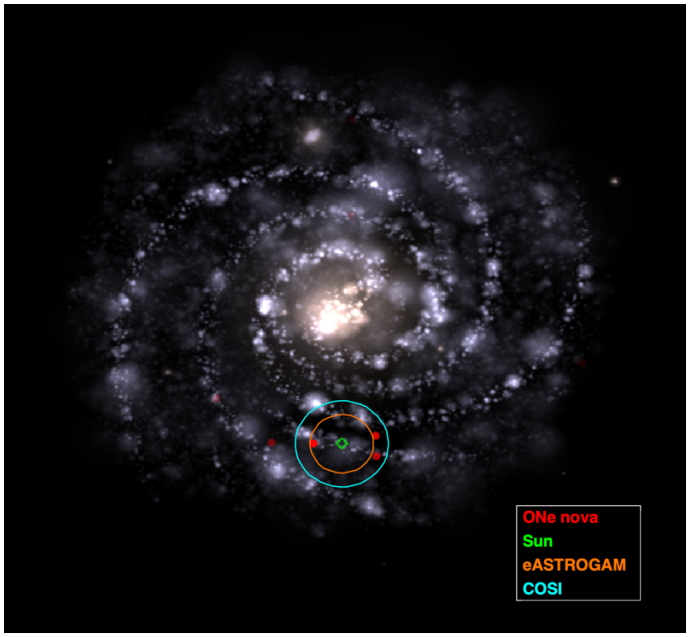

Figure 9.10: The Milky Way map with the observed ONe nova events in the last 60 years, shown as red points. The color of points is function of the emitted flux of ^{22}Na from simulated $M_{ej}^{^{22}Na}$=3.5×10^{-9} $M_{\odot}$. Only a few events would have been visible, novae further away are not visible. Green circle corresponds to the Sun position. The cyan and orange circles represent the limit in detection distance of COSI and e-ASTROGAM for the γ-ray line from ^{22}Na. The COSI instrument is so expected to detect the radioelement ^{22}Na from 1 ONe nova every 20 years, and e-ASTROGAM expectations are 1 ONe nova every 60 years.

Space γ-ray spectrometer	Ref	Sensitivity (ph.cm^{-2}.s^{-1}) for 1 MeV γ-rays	Detection distance limit[a](kpc) of ^{22}Na from ONe novae	Expected detection frequency[a] of ^{22}Na from ONe novae
e-ASTROGAM	[130]	3×10^{-6}	1.9	≥1 event every 60 years
COSI	[8]	1.7×10^{-6}	2.8	≥1 event every 20 years

[a] From a simulated ONe nova with $M_{ej}^{^{22}Na}$=3.5×10^{-9} $M_{\odot}$

Table 9.2: Overview of observation expectations for the proposed e-ASTROGAM and COSI telescopes. The focus is on the γ-ray line, from ^{22}Na ejected during ONe novae.

As a conclusion, we predict that the ^{22}Na γ-ray line produced in an ONe nova will be observed typically once every 20 years by the next generation of space telescopes.

9.4.2 Considerations on the Ne-E excess in presolar grains

The expected ejected ^{22}Na nuclei from the simulations of different ONe nova models may be converted into the trapped amount of daughter ^{22}Ne ions in presolar grains. To do so, its probability of crystallization is required. This parameter is similar between the ^{22,23}Na isotopes. Thus, analyzing the abundances of ^{23}Na and ^{22}Ne (daughter nucleus of ^{22}Na) in presolar grains and comparing these abundances with their predicted values in the ejecta could help to quantify the dust formation of ^{22}Na. The measured abundance ratio ^{22}Ne/^{20}Ne compared to the known value in the solar system could be used to constrain nova models.

9.5 Conclusion

ONe novae have been simulated using the MESA code. The initial thermal conditions of the white dwarf star and the accretion dynamics were varied. We have shown that these unknown physical parameters can be constrained by the measurement of the γ-ray flux of ^{22}Na ejected after the explosion. This observation could be carried out in nearby novae during long-term observation campaigns. This could be an important objective of the future γ-ray astronomy missions.

Part VI

Conclusion

Conclusion

Among the sites of explosive nucleosynthesis in our Galaxy, novae are the second most frequent events. We have shown that classical ONe novae can be investigated in the light of the radioelement ^{22}Na. The sensitivity of past space telescopes was not good enough to observe γ-rays from the β decay of ^{22}Na emitted during novae. Its destruction rate through the ^{22}Na(p,γ)^{23}Mg reaction remains the last important uncertainty from a nuclear point of view. We have seen that the uncertainties on this reaction rate impact the ^{22}Na abundance more than the differences of the nova models. The nuclear uncertainties originate from a high discrepancy in the published strengths of the E_R=0.204 MeV dominant resonance at peak nova temperatures. Due to the challenges of measuring cross section or strength for a such low energy resonance, we decided to access to the key resonance by indirectly measuring the spectroscopic properties of the corresponding excited state in ^{23}Mg*.

An experiment took place at GANIL to measure the lifetime, the proton branching ratio and the spin of the Ex=7.785 MeV excited state, populated by the ^{3}He(^{24}Mg,^{4}He)^{23}Mg* reaction. The ^{3}He ions, naturally in a gaseous state, were implanted near the surface of gold targets. Both γ-ray and proton decay channels were studied thanks to the set-up of four detectors, i.e. VAMOS, AGATA, SPIDER, DCTs. The analysis of γ-ray and proton lineshapes has relied on our own simulations tools with the newly developed EVASIONS code. We undertook a complete spectroscopic study of the astrophysical state as well as of 21 observed states in ^{23}Mg*. Facing the difficulties to measure a short lifetime for the high-lying Ex=7.785 MeV state, a new approach based on the profiles of the velocity at emission has been proposed, thus making the most of the state-of-the-art detectors used.

Our experimental work has successfully led to the measurement of the lifetime and the proton branching ratio of the Ex=7.785 MeV state, being to our knowledge only the second time that a femtosecond lifetime is determined by a γ-rays analysis with AGATA. These measured properties have been found consistent with some other results, confirming that the key state is an uncommon long-lived unbound state which decays weakly by proton emission. Beyond the experimental work, our theoretical calculations have provided some clues to the spin value. The first goal of my thesis was fulfilled with the measurement of a precise value for the E_R = 0.204 MeV resonance strength. Our result is $\sim$20 times smaller than in the latest measurement. The resonance strength thus determined is among the lowest ever obtained in direct measurements, i.e. at the sensitivity limit of direct measurements. This could explain the large differences observed between the different measurements.

We have re-evaluated the ^{22}Na(p,γ)^{23}Mg reaction rate at peak nova temperatures with a statistical Monte-Carlo approach. The rate is reduced by a factor 10 from the current rate. Our achieved uncertainties, up to 40 % of the rate, improve the nuclear inputs required for ONe novae. We have shown that the ^{22}Na γ-rays flux can be used as a fingerprint of the underlying novae physics. In particular, the

accretion dynamics and the stellar conditions prior to the outburst impact the amount of ^{22}Na ejected. The present results encourage long-lasting observation campaigns which would be sensitive to γ-rays from ^{22}Na produced in nearby novae events.

A critical look is taken at the work carried out. The reliable lifetime and proton branching ratio measurements highlight the pertinence of the high-resolution detectors and analysis processes used in this study. Assigning spin demands, however, either a larger angular coverage or higher compound nucleus cross sections. Our measured statistics and uncertainties can be improved by increasing the density of ^{3}He in target. Indeed, implanting several layers of ^{3}He ions at different depths has been thought of after the experiment. This could be done by varying the ^{3}He beam energy. Then, the reactions associated with each layer depth could be selected by the ejectiles energy measured in VAMOS if the resolution is sufficient. The analysis of γ-rays and protons would be implemented for the different ^{4}He energy slices. The (τ, BR$_{\rm p}$) parameters would be measured multiple times. It is worth mentioning that the lifetime of the key resonance will be soon remeasured in an experiment accepted at TRIUMF facility. This should obviously be in line with our value and will improve accuracy.

More generally, there is considerable interest in the experimental determination of resonant reaction rates. In addition to the work presented in this thesis, two other experimental methods were also investigated.

First, resonance strengths can be measured with angle-integrated transfer reactions reproducing the astrophysical reactions. I have shown that the resonance strength is proportional to the number of detected γ-rays from the resonant state populated directly by the transfer reaction. With the strong efforts made for the development of radioactive ion beams in worldwide facilities, this approach can be applied now to key astrophysical reactions. The details of this method are presented in the E825_21 proposal for GANIL PAC (2021). A simple experiment with γ-ray spectrometers, combined with particle detectors to improve SNR, would allow us to test this approach on known strengths: for instance, in TRIUMF where a ^{22}Na beam intensity of 10^{10} pps can be delivered and the DRAGON separator can be used to select the ^{23}Mg recoil nuclei of the transfer reaction d(^{22}Na,n)^{23}Mg*, the E$_{\rm R}$ = 0.204 MeV dominant strength may be measured by using a CD_2 target . This new method has been proposed recently at GANIL for measuring the strengths of the ^{25}Al(p,γ)^{26}Si reaction which impacts the production of ^{26}Al in novae.

Second, reaction rates may be measured directly by using a beam energy distribution reproducing the Maxwell Boltzmann energy distribution at stellar temperatures. The principle here is identical to the measurements of neutron capture rates done with thermal neutron flux. This new approach was the subject of A. Valente's internship under my supervision. Preliminary studies have shown that MB energy distributions can be obtained with beams passing trough degrader materials like gold. The estimated count rate was preliminary found too low to make such experiment realistic. The results obtained are not yet conclusive, but this original approach deserves to be developed further.

Our sensitivity study of nova models on ^{22}Na production should be extended to other astrophysical parameters. In particular, we would like to investigate the consequences of changing the composition of the accreted material and the mixing parameter. Simulations, done with the open source code MESA, failed to reproduce key parameters like the velocity of the ejecta. More realistic codes like SHIVA will improve confidence in predicting the mass of ^{22}Na ejected from novae, which may soon be detected in the next bright nova, in the celestial vault that intrigues us so much.

Appendices

CHAPTER A

Complements to the reconstruction processes

The derivation in the present experiment of the state excitation energy has relied on kinematics calculations which are explained in Sec.A.1. In particular, two reaction mechanisms were studied to extract Ex: the reactions ^{3}He(^{24}Mg,^{4}He)^{23}Mg* populating the states and the proton decays from states above the proton threshold. Additionally to the excitation energies determination, the differential cross sections of the states in ^{23}Mg* were obtained thanks in part to local background noise subtractions, presented in Sec.A.2. All state lifetime measurements were based on the Doppler effect, it is described in Sec.A.3.

A.1 Particle kinematics

A.1.1 Two-body reactions ^{3}He(^{24}Mg,^{4}He)^{23}Mg*

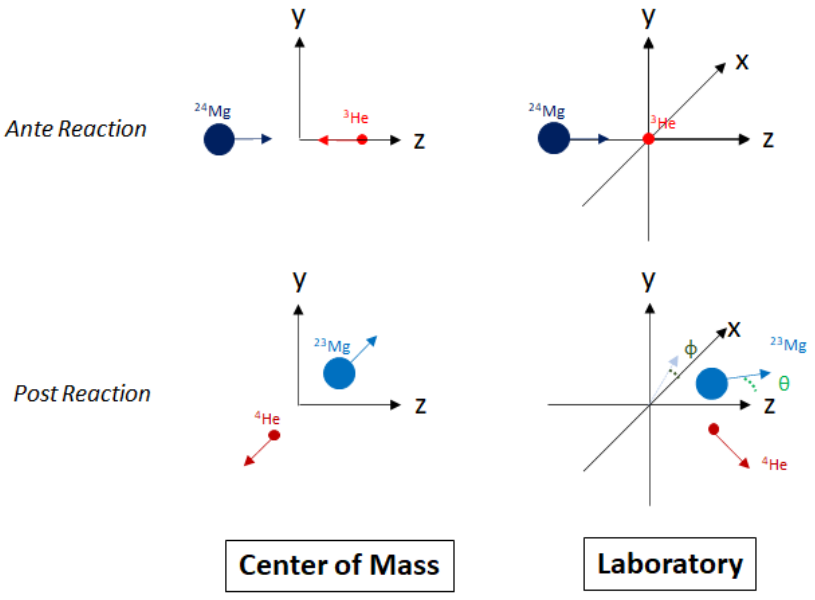

Figure A.1: Layout of the experimental reaction ^{3}He(^{24}Mg,^{4}He)^{23}Mg* in inverse kinematics, both in the center of mass and laboratory frames. Light ^{3}He nuclei were at rest in laboratory, angles (θ, ϕ) of ^{23}Mg recoil nuclei mentioned.

We recall that the change from the laboratory frame to the center-of-mass (CM) frame or inversely is achieved with matrix transformations

$$\begin{pmatrix} \mathrm{E} \\ \mathrm{p_z} \end{pmatrix}_{\mathrm{CM}} = \begin{pmatrix} \gamma & -\gamma\beta \\ -\gamma\beta & \gamma \end{pmatrix} \times \begin{pmatrix} \mathrm{E} \\ \mathrm{p_z} \end{pmatrix}_{\mathrm{lab}} \tag{A.1}$$

with $\vec{z}$ the beam axis. The angular parameters, used along the analysis, were the spherical angles
- θ with respect to $\vec{z}$
- ϕ associated to the vector projection in the ($\vec{x}$, $\vec{y}$) plan, with respect to $\vec{x}$.

The laws of energy and impulsion conservations in laboratory frame are for the reaction ^{3}He(^{24}Mg,^{4}He)^{23}Mg* as follow

1. $\mathrm{E}_{^{24}\mathrm{Mg}} + \mathrm{Q} = \mathrm{E}_{^{23}\mathrm{Mg}} + \mathrm{E}_{^4\mathrm{He}} + \mathrm{Ex}$, with E the kinetic energies, the Q value equal to the mass change ($\mathrm{Q} = \Delta\mathrm{m}$) and Ex the state excitation energy.
2. $\vec{\mathrm{P}}_{^{24}\mathrm{Mg}} = \vec{\mathrm{P}}_{^{23}\mathrm{Mg}} + \vec{\mathrm{P}}_{^4\mathrm{He}}$, with $\vec{\mathrm{P}}$ the impulsions.

From relativistic laws, the total nuclear energy is given by $\mathrm{E_{tot}} = \mathrm{E} + \mathrm{E}^0 = \gamma\mathrm{mc}^2$, with E^0=mc^2 the rest energy. The impulsion norm is equal to $\mathrm{E_{tot}^2}-\mathrm{P}^2\mathrm{c}^2 = \mathrm{m}^2\mathrm{c}^4$. Combining the two, the impulsion norm is derived as a function of (γ, E^0): P^2=(γ^2-1)$\frac{{\mathrm{E}^0}^2}{\mathrm{c}^2}$. By the impulsion conservation, the ^{23}Mg Lorentz factor γ is obtained

$$\gamma_{^{23}\mathrm{Mg}} = \sqrt{1 + \frac{1}{{\mathrm{E}^0_{^{23}\mathrm{Mg}}}^2} \times ({\mathrm{E}^0_{^4\mathrm{He}}}^2 \times (\gamma^2_{^4\mathrm{He}} - 1) + {\mathrm{E}^0_{^{24}\mathrm{Mg}}}^2 \times (\gamma^2_{^{24}\mathrm{Mg}} - 1) - 2 \times \cos(\theta_{^4\mathrm{He}})\mathrm{E}^0_{^{24}\mathrm{Mg}}\mathrm{E}^0_{^4\mathrm{He}} \times \sqrt{\gamma^2_{^4\mathrm{He}} - 1}\sqrt{\gamma^2_{^{24}\mathrm{Mg}} - 1})} \tag{A.2}$$

From Eq. (A.2), the kinetic energy is derived

$$\mathrm{E}_{^{23}\mathrm{Mg}} = \mathrm{E}^0_{^{23}\mathrm{Mg}} \times (\sqrt{1 + \frac{1}{{\mathrm{E}^0_{^{23}\mathrm{Mg}}}^2} \times ({\mathrm{E}^0_{^4\mathrm{He}}}^2 \times (\gamma^2_{^4\mathrm{He}} - 1) + {\mathrm{E}^0_{^{24}\mathrm{Mg}}}^2 * (\gamma^2_{^{24}\mathrm{Mg}} - 1) - 2 \times \cos(\theta_{^4\mathrm{He}})\mathrm{E}^0_{^{24}\mathrm{Mg}}\mathrm{E}^0_{^4\mathrm{He}} \times \sqrt{\gamma^2_{^4\mathrm{He}} - 1}\sqrt{\gamma^2_{^{24}\mathrm{Mg}} - 1})} - 1) \tag{A.3}$$

The impulsion of ^{23}Mg is defined as

$$\begin{pmatrix} |\mathrm{P}_{^{23}\mathrm{Mg}}| \times \sin(\theta_{^{23}\mathrm{Mg}}) \times \cos(\phi_{^{23}\mathrm{Mg}}) \\ |\mathrm{P}_{^{23}\mathrm{Mg}}| \times \sin(\theta_{^{23}\mathrm{Mg}}) \times \sin(\phi_{^{23}\mathrm{Mg}}) \\ |\mathrm{P}_{^{23}\mathrm{Mg}}| \times \cos(\theta_{^{23}\mathrm{Mg}}) \end{pmatrix} = \begin{pmatrix} -|\mathrm{P}_{^4\mathrm{He}}| \times \sin(\theta_{^4\mathrm{He}}) \times \cos(\phi_{^4\mathrm{He}}) \\ -|\mathrm{P}_{^4\mathrm{He}}| \times \sin(\theta_{^4\mathrm{He}}) \times \sin(\phi_{^4\mathrm{He}}) \\ |\mathrm{P}_{^{24}\mathrm{Mg}}| - |\mathrm{P}_{^4\mathrm{He}}| \times \cos(\theta_{^4\mathrm{He}}) \end{pmatrix} \tag{A.4}$$

with the norm of impulsion equals to $|\mathrm{P}| = \frac{1}{\mathrm{c}}\sqrt{\mathrm{E}^2 + 2\mathrm{E}^0\mathrm{E}}$. From Eq. (A.4), after projecting on the beam axis $\vec{z}$, $\theta_{^{23}\mathrm{Mg}}$ is obtained

$$\theta_{^{23}\mathrm{Mg}} = \mathrm{acos}(\frac{|\mathrm{P}_{^{24}\mathrm{Mg}}| - |\mathrm{P}_{^4\mathrm{He}}| \times \cos(\theta_{^4\mathrm{He}})}{|\mathrm{P}_{^{23}\mathrm{Mg}}|}) \tag{A.5}$$

The angle $\phi_{^{23}\mathrm{Mg}}$ is defined as $\mathrm{atan}(\frac{\mathrm{P}^{\mathrm{y}}_{^{23}\mathrm{Mg}}}{\mathrm{P}^{\mathrm{x}}_{^{23}\mathrm{Mg}}})$. The impulsion conservation implies that $\mathrm{P}^{\mathrm{x}}_{^{23}\mathrm{Mg}} = -\mathrm{P}^{\mathrm{x}}_{^4\mathrm{He}}$ and $\mathrm{P}^{\mathrm{y}}_{^{23}\mathrm{Mg}} = -\mathrm{P}^{\mathrm{y}}_{^4\mathrm{He}}$, hence

$$\phi_{^{23}\mathrm{Mg}} = \pi + \phi_{^4\mathrm{He}} \tag{A.6}$$

The level energy could be also extracted by combining Eq. (A.3) and the energy conservation

$$\mathrm{Ex} = \mathrm{E}_{^{24}\mathrm{Mg}} + \Delta\mathrm{m} - \mathrm{E}_{^{23}\mathrm{Mg}} - \mathrm{E}_{^4\mathrm{He}}$$

With the VAMOS algorithm in Fig. 3.7, $(E, \theta, \phi)_{^4He}$ were derived, after correction of energy losses in the {target + beam catcher} foils. Using $E_{^4He}$, the other parameters of Eq. (A.3) were derived as follow

1. $\gamma_{^4He} = \frac{E_{^4He}}{E^0_{^4He}} + 1$
2. norm $|P_{^4He}| = \frac{1}{c}\sqrt{E^2_{^4He} + 2E_{^4He} \times E^0_{^4He}}$

A.1.2 Proton decays from states in $^{23}Mg^*$

The measured protons properties (β_p^{lab},θ_p^{lab}) can be used to derive the proton center-of-mass velocity which then allowed us to determine Ex. The velocity is decomposed in the (x, y, z) frames (center of mass, laboratory) by angular projections

$$\begin{pmatrix}\beta^x\\ \beta^y\\ \beta^z\end{pmatrix}_p^{cm} = \begin{pmatrix}\beta_p^{cm}\sin(\theta_p^{cm})\cos(\phi_p^{cm})\\ \beta_p^{cm}\sin(\theta_p^{cm})\sin(\phi_p^{cm})\\ \beta_p^{cm}\cos(\theta_p^{cm})\end{pmatrix} \quad \text{and} \quad \begin{pmatrix}\beta^x\\ \beta^y\\ \beta^z\end{pmatrix}_p^{lab} = \begin{pmatrix}\beta_p^{cm,x}\frac{\sqrt{1-\beta^2}}{1-\beta_p^{cm,z}\beta}\\ \beta_p^{cm,y}\frac{\sqrt{1-\beta^2}}{1-\beta_p^{cm,z}\beta}\\ \beta_p^{cm,z}\frac{\beta_p^{cm,z}+\beta}{1+\beta_p^{cm,z}\beta}\end{pmatrix} \tag{A.7}$$

where β, the velocity of the center-of-mass in the decay reaction, is equal to the velocity of ^{23}Mg in the laboratory. The norm of the observable proton velocity β_p^{lab} depends on the β_p^{cm} and the angles.

$$\beta_p^{lab\,2} = (\beta_p^{cm}\sin(\theta_p^{cm}))^2\frac{(1-\beta^2)}{(1-\beta\beta_p^{cm}\cos(\theta_p^{cm}))^2} + (\beta_p^{lab}\cos(\theta_p^{lab}))^2 \tag{A.8}$$

Using the coordinate $\beta_p^{z,\,lab}$ in Eq. (A.7) to express $\beta_p^{cm}\cos(\theta_p^{cm}) = \beta_p^{z,\,cm}$ in laboratory coordinates ($\frac{\beta-\beta_p^{lab}\cos(\theta_p^{lab})}{\beta\beta_p^{lab}\cos(\theta_p^{lab})-1}$), Eq. (A.8) becomes

$$\beta_p^{lab\,2} = (\beta_p^{cm\,2} - (\frac{\beta-\beta_p^{lab}\cos(\theta_p^{lab})}{\beta\beta_p^{lab}\cos(\theta_p^{lab})-1})^2)\frac{1-\beta^2}{(1-\beta\frac{\beta-\beta_p^{lab}\cos(\theta_p^{lab})}{\beta\beta_p^{lab}\cos(\theta_p^{lab})-1})^2} + (\beta_p^{lab}\cos(\theta_p^{lab}))^2 \tag{A.9}$$

From previous Eq. (A.9), the proton center-of-mass velocity is derived from the measured (β_p^{lab},θ_p^{lab}). The β is determined as explained in Sec.A.1.1. Defining the ratio R=$\frac{\beta-\beta_p^{lab}\cos(\theta_p^{lab})}{\beta\beta_p^{lab}\cos(\theta_p^{lab})-1}$, the proton center-of-mass velocity is equal to

$$\beta_p^{cm\,2} = R^2 + (\beta_p^{lab}\sin(\theta_p^{lab}))^2\frac{(1-\beta R)^2}{1-\beta^2} \tag{A.10}$$

The proton center-of-mass energy is $E_p^{cm} = \frac{(Ex-S_p)E^0_{^{22}Na}}{E^0_{^{22}Na}+E^0_p}$ and its velocity $\beta_p^{cm} = \sqrt{1-\frac{1}{(\frac{E_p^{cm}}{E_p^0}+1)^2}}$. The dimensionless mass of the system p+^{22}Na$_{gs}$ is written $r_\mu = \frac{E^0_{^{22}Na}}{E^0_{^{22}Na}+E^0_p}$. By expressing E_p^{cm} as function of Ex in β_p^{cm} formula, one obtains $\beta_p^{cm} = \sqrt{1-(r_\mu Ex + 1 - r_\mu S_p)^{-2}}$. Finally the state excitation energy is expressed as a function of the proton center-of-mass velocity.

$$Ex = \frac{(1-\beta_p^{cm\,2})^{\frac{1}{2}} - 1 + r_\mu S_p}{r_\mu} \tag{A.11}$$

Combining Eq. (A.10) and (A.11), the $^{23}Mg^*$ state excitation energies are reconstructed from the emitted protons measured in SPIDER.

A.2 Background noise subtraction

The population of each identified state in ^{23}Mg* had to be quantified to determine the differential cross sections in coincidences with ^{4}He ejectiles measured in VAMOS. This was achieved by deriving the number of counts in the γ-ray Doppler-corrected peaks. The resolution in state excitation energies from ^{4}He ejectiles measured in VAMOS was determined. These two procedures required background noise subtractions for the observed peaks of interest, either in γ-rays or in $E^{VAMOS}_{^4He}$. The latter is presented in Fig. A.2 for the astrophysical state. The background noise was subtracted, i.e. the average spectrum from the lower and upper shaded energy regions (Fig. A.2(a)) which surround the γ-ray energy region of interest delimited by black continuous lines (Fig. A.2(a)). This averaged noise spectrum (black) and the $E^{VAMOS}_{^4He}$ spectrum (red) in coincidence with the ^{23}Mg* $E_{\gamma,0}$=7.333 MeV transition are shown in Fig. A.2(b). The resulting spectrum after the background noise subtraction is given in Fig. A.2(c).

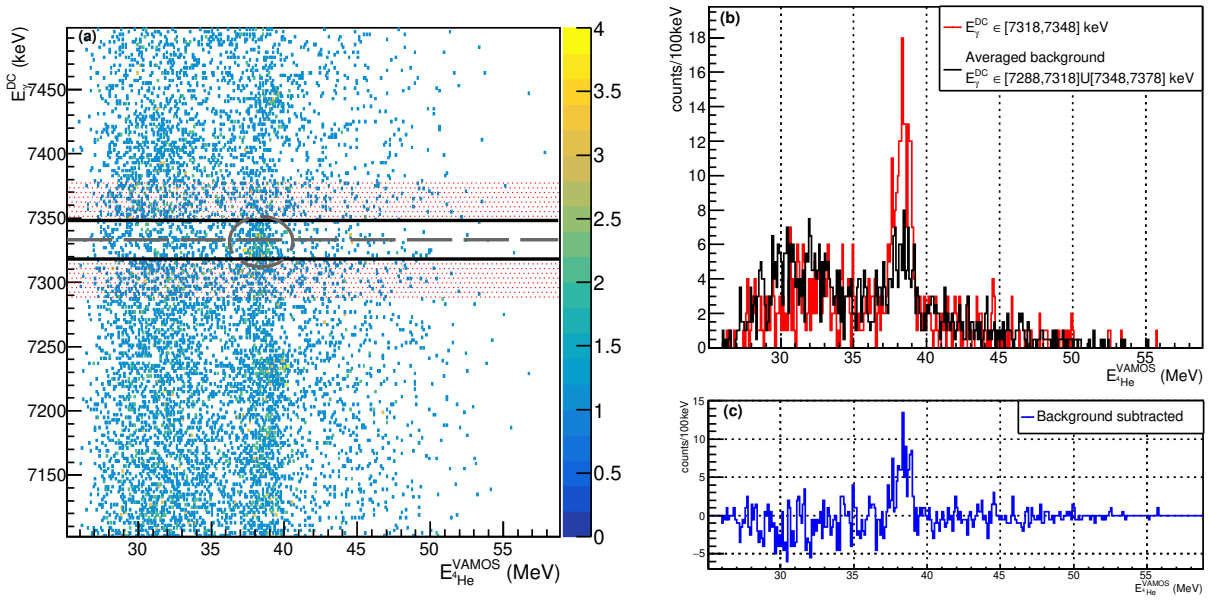

Figure A.2: Panel (a): matrix of the Doppler-corrected E^{DC}_{γ} versus the ^{4}He ejectile $E^{VAMOS}_{^4He}$. The grey dotted line indicates the $E_{\gamma,0}$=7.333 MeV γ-ray transition from the ^{23}Mg* Ex=7.785 MeV state. Three E^{DC}_{γ} regions, with a 30 keV range, are shown: (1) between the black continuous lines (E^{DC}_{γ}∈[7.318, 7.348] MeV), (2) and (3) red dashed areas with (E^{DC}_{γ}∈[7.288, 7.318] MeV, E^{DC}_{γ}∈[7.348, 7.378] MeV). Panel (b): red histogram is the projection onto $E^{VAMOS}_{^4He}$ of the selection E^{DC}_{γ}∈[7.318, 7.348] MeV, black histogram is the mean of the projections associated to the red dashed regions. Panel (c): the difference between the histograms in (b).

A.3 Doppler-Shift Attenuation Method

A.3.1 Doppler effect

The Doppler effect is presented in Fig. A.3 where the relative difference between rest and observed γ-ray energies is plotted as function of the ^{23}Mg recoil velocity (β) and the angle between γ-ray and ^{23}Mg* recoil nucleus (θ_{DS}). In order to experimentally observe the Doppler effect, the nucleus ^{23}Mg must be moving while γ-ray decaying, and the γ-ray detection away from [80, 90] deg where the Doppler shift would have been minimum as shown in the bottom of Fig. A.3).

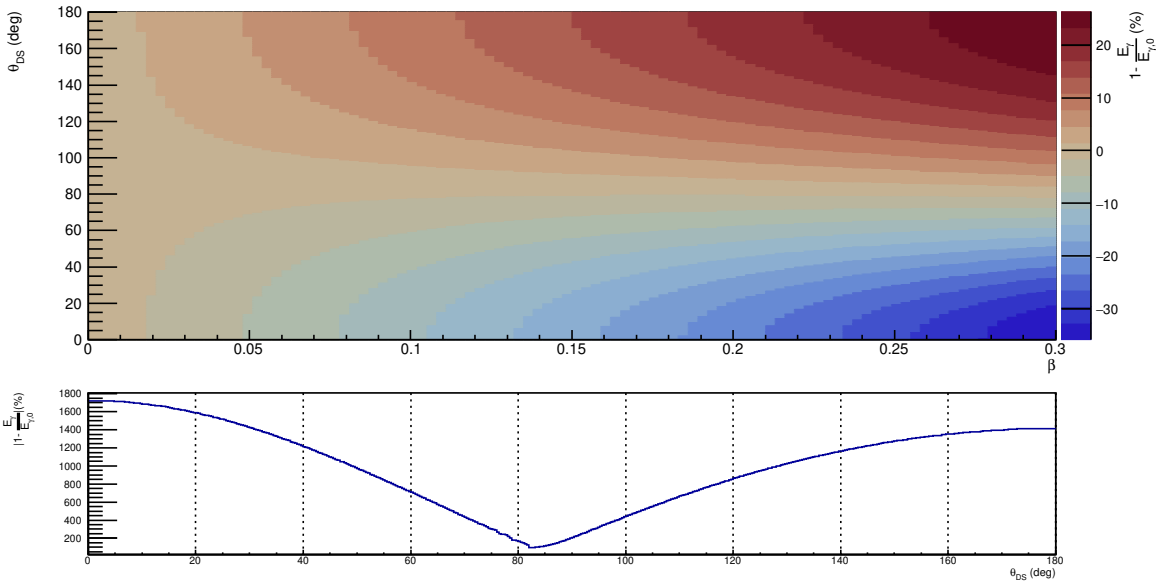

Figure A.3: What is the relativistic Doppler effect ? Top: the relative shift between the observed E_γ and rest $E_{\gamma,0}$ energies (Eq. (2.5)) is shown as a function of the emitter velocity (β) and of the emitter-and-γ-ray angle (θ_{DS}). At backward angles (>90 deg), redshift observed as lower energies than the rest energy, at forward angles a blueshift is inversely observed. Bottom: projection onto θ_{DS} is given with positive relative shift. The Doppler shift is maximum at 0 deg and 180 deg, minimum around 85 deg. One would expect no observation of Doppler effect at 90 deg, which is true in Newtonian physics but not in relativistic case as illustrated here.

A.3.2 Method principle

The principle of the DSAM approach to access to lifetimes is illustrated in Fig. A.4: the lifetime sensitivity is related to the γ-ray emitter slowing down in the absorber (a velocity degrading material). Measuring Doppler-shifted γ-rays, with energies depending on the velocities at emission, indirectly allows to detect these slowing down processes of the recoil nuclei. The choice of the absorber is of prime importance for the lifetime sensitivity. In Fig. A.5, it is shown that energy losses in gold of ^{23}Mg recoil nucleus, with kinetic energies at reaction in [50, 150] MeV, are decreased over time at the femtosecond scale. In contrary, energy losses in lead (dashed lines) appear to more slowly decrease over time.

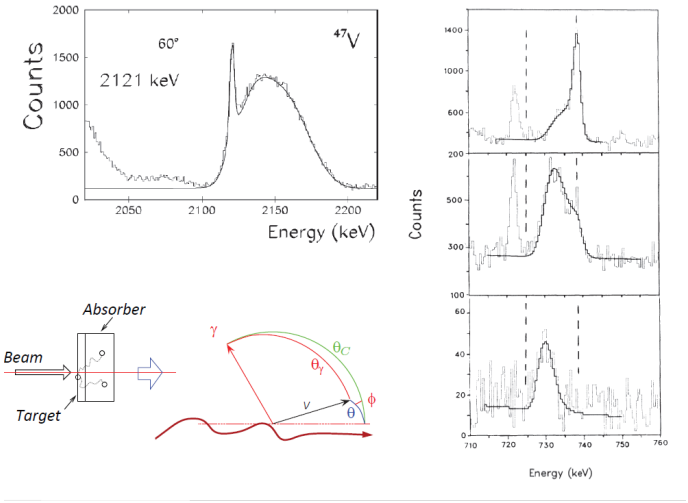

Figure A.4: Principle scheme of a DSAM experiment on the lower left and examples of measured γ-rays, source [58]. After nuclei slowing down in the absorber, γ-rays are emitted at different velocities with θ_γ the angle between γ-ray and emitter which has the (θ, ϕ) polar angles. Upper left: Doppler-blue-shifted γ-ray transitions from a state in ^{47}V* (τ=0.37(3) ps, $E_{\gamma,0}$=2.121 MeV) at forward angles. Right: γ-ray transitions from ^{166}Dy* at backward angles with three different absorbers, i.e. from top to bottom Au, Pb, Mg. The vertical dashed lines associated with the complete shift and the stopped peak.

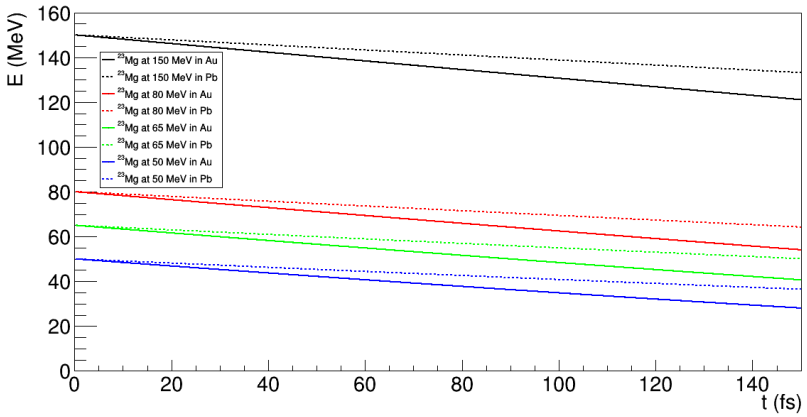

Figure A.5: Energy losses of ^{23}Mg in Au (solid lines) and Pb (dashed lines) upon the travelling time in medium, using SRIM stopping powers [76]. Four initial energies were taken: 150 MeV (black), 80 MeV (red), 65 MeV (green), 50 MeV (blue). The absorption in Au appears clearly higher than the one in Pb.

CHAPTER B

Complements to the detections

Some additional informations about the AGATA spectrometer and its data acquisition and characterization are presented in Sec.B.1. The complete calibration of the SPIDER ΔE strips is then given in Sec.B.2.

B.1 AGATA

B.1.1 Geometry

The geometry of the AGATA crystals is detailed in Fig. B.1. The 36 segments were divided into 6 column sectors and six rings. Depending on the front-end dimensions, there are three kinds of crystal (left side) gathered in a triple cluster which shares the same cryostat cooling system.

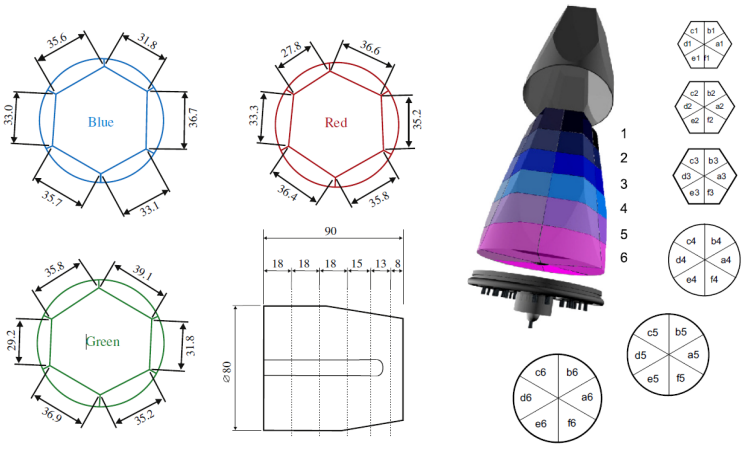

Figure B.1: Left: crystal shapes included in a triple cluster (all dimensions in mm). Right: presentation of the crystal segmentation with the external contact divided into 6 rings (1-6) each into 6 sectors (a-f). Pictures taken from [79].

B.1.2 Electronics

The replay of AGATA data is briefly outlined here, a comprehensive presentation is available in [58]. The Pulse Shape Algorithm PSA, a milestone in the determination of γ-ray interaction positions, is

explained in Fig. B.2: the interaction happens here in segment B4, noticed with the characteristic net signal, the transient signals in neighboring segments allow to improve the resolution on the derived position.

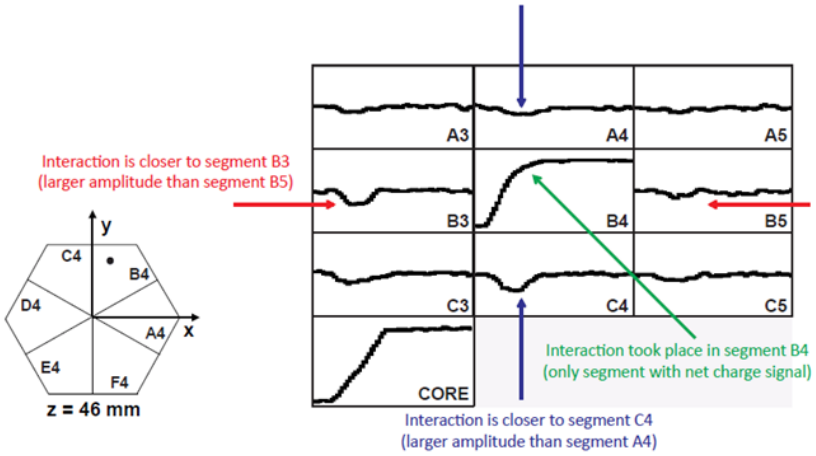

Figure B.2: Principle of PSA with net (B4) and transient (B3, B5, C4, A4) signals, from [79, 58].

At local level, the first encountered actor was the crystal producer which read traces from the front-end electronics and turned them into amplitude and time data for segments and cores. Then the preprocessing filter was in charge of a first energy-time calibration. The energy linear calibration parameters were obtained by using a source of ^{60}Co with the two γ-ray energies (1.1, 1.3) MeV. This actor properly prepared data for the PSA which relied on all segments working in the search of net and transient signals and all traces aligned with respect to time. Any segmented detector has cross-talks that is seen as shifts in the built back energies, and which affect the resolution. Cross-talk measurements in AGATA detectors were reported in [101], it was observed that energy shifts were proportional to the fired segment multiplicity. In case of high energy γ-rays >5 MeV like in this experiment, higher segment multiplicities were expected, up to 6 [58], hence increasing the cross-talk impact. The essential correction was achieved by applying on each segment the cross-talk matrix coefficients 36×36 which were determined by sorting the energy over the segment multiplicity. With PSA assuming same start event time for all traces, the time alignment was done by looking for shift coefficients to align segments with respect to the core signal. Some segments were observed "broken": the charges were not collected or too noisy at the FET+preamplifier stage. If only a few segments were broken per crystal, usually up to 3, the signals were recovered by the use of cross-talk effect and the core energy in principle equal to the sum of the segments energies. The extraction of interaction position was ensured after by the PSA filter with the calibrated data. The algorithm performances had to provide an efficient and fast processing of experimental traces and comparison with the references. It was based on Adaptive-Grid-Search AGS [105] with simulations of net and transient signals on a fine grid of points in the segments and evaluations over all grid points of the residues (sum of square differences between calculated and experimental signals). Minimal residue gave so the interaction position. In case of two interaction searches per segment, linear combinations of the two deposited energies were done. Higher multiplicity searches were not properly handled with such algorithm. To strongly decrease computing times, the grid search was adapted: first there were residue evaluations on a grid with high spacing of 6 mm, then position determinations on local fine grids of 2 mm.

An other important correction was applied at the PostPSA filter: the neutron damage. Radiations of fast neutrons generated negative charge traps in the detector volume, they did not affect the electrons drifting toward the central anode core but they trapped the positive charge carriers. They induced losses of charge collection efficiency at the outer cathodes and so reductions of measured currents at segment level. The segment energy resolution was degraded compared to the core signal, in the form of left side

tails for the γ-ray peaks. The correction was performed by computing coefficient grids 36×36, applying them on the "Hit" data and quantifying the peak FWHM and left tails (^{60}Co) in order to reach a set that minimized these last two. At PostPSA filter, the sum of segment energies was forced to be equal to the core one which enhanced the neutron damage correction. At PostPSA filter, the calibration coefficients for the core signals were tuned by using also a source of ^{152}Eu.

The last actor of LLP was the consumer GenericAFC which saved the calibrated results to disk files in order to be read by the event builder filter of global level. At this point, the data were selected according to close timestamps, a window of acceptable timestamp differences being chosen before the experiment. Local AGATA fired components (segments, cores) sent trigger requests, if satisfying the global trigger (GTS) they were validated, or if not, rejected. The global trigger processing of AGATA as well as the global front-end electronics are drawn in Fig. B.3. Online monitoring of the trigger validations and rejections was possible. The experiment was at low counting rate, the global trigger was chosen to validate all local triggers: trigger-less mode. Data were built into a global event sent to the merger actor where additional ancillary could participate in the trigger event, which was not the case in the experiment. The Compton tracking was implemented with the tracking filter to produce information at emission. Finally, the consumer GenericAFP converted the tracked data to root trees.

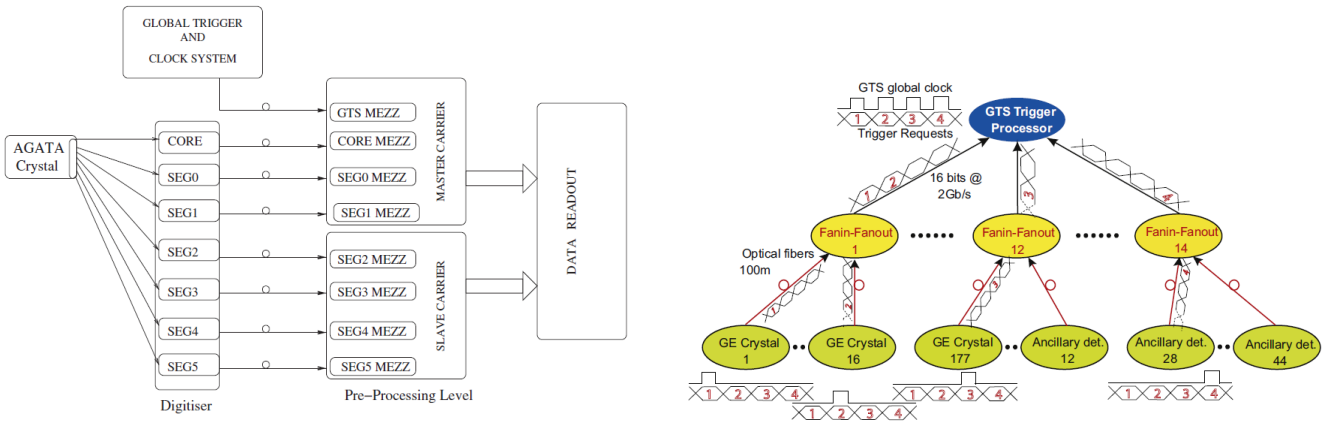

Figure B.3: Left: scheme of the crystal front-end electronics. Right: the GTS topology where any segment can transmit a trigger request labelled with the clock which then climbs the tree to the global trigger processor. Pictures From [79, 58].

B.1.3 Source calibrated spectra

The calibrated spectrum of the ^{152}Eu source, used prior to experiment, the background noise subtraction and the fit processes are shown in Fig. B.4. The ^{152}Eu ($\tau = 4.267 \times 10^8$ s) source has: an initial activity of 18755 disintegration.s^{-1}, an age of 6.127×10^8 s. The data taking to get spectra of Fig. B.4 lasted 5029 s. The calibrated spectrum of the AmBe(Fe) source is also presented with some identified γ-rays.

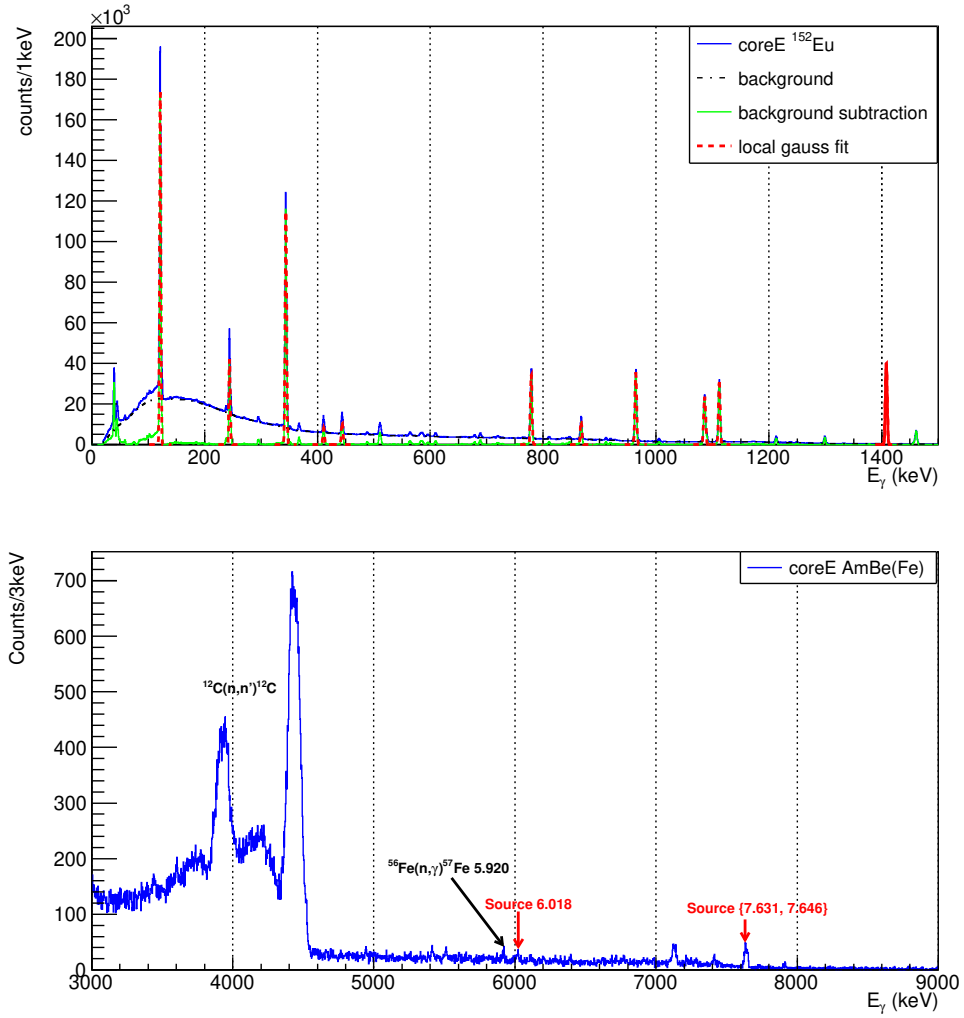

Figure B.4: Calibrated energy spectra from the sources used for AGATA calibration. Top: core signals from the ^{152}Eu source after calibration (blue histogram), and the derived background noise (black histogram). After its subtraction (green histogram), the highlighted peaks with a SNR$\geq$10 are fitted with Gaussian functions (red). Bottom: γ-rays measured from neutron captures by AmBe on Fe are marked by arrows. An example of another origin for the γ-rays is given with the neutron captures on carbon present in the paraffin support of the source.

B.1.4 Response function

The derivation of the energy resolution from online measurements on γ-ray transitions, emitted at rest, is presented in Fig. B.5.

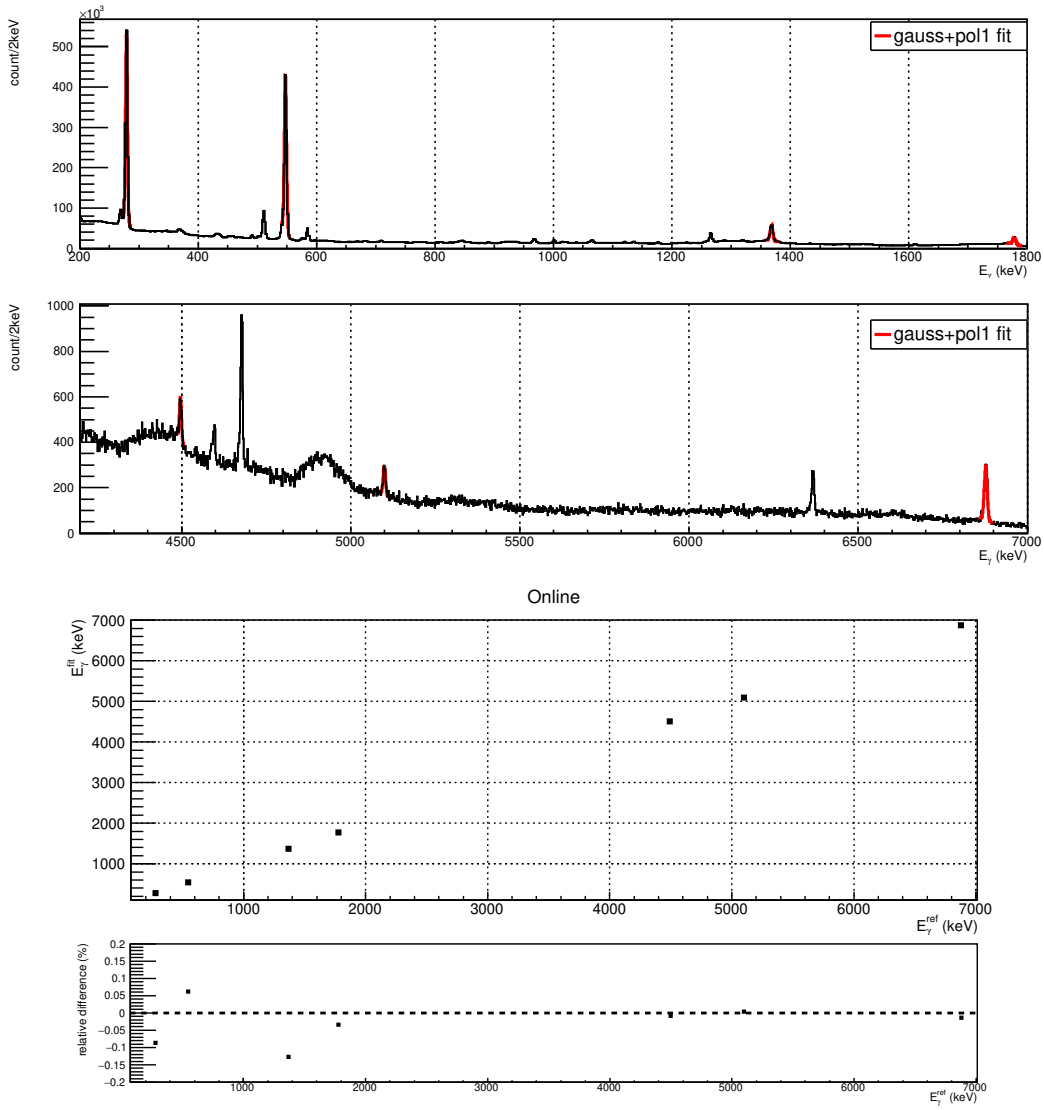

Figure B.5: The online determination of AGATA energy resolution. Two tops: energy tracked spectra at two energy ranges and Gaussian fits (red) of some observed unshifted peaks from known γ-ray emitters (Table B.1). Two bottoms: fit results along the peak centroids, with E_γ^{fit} the centroid energy and E_γ^{ref} the literature γ-ray rest energy from [55]. Relative differences between the two also shown. With differences $<$0.15 %, the calibration is proven good.

Source of γ-rays, Ref. [55]	$E_{\gamma,0}^{\text{ref}}$ (keV) Ref. [55]	Centroid (keV)	σ (keV)
^{197}Au, τ=18.6 ps	279	278.8 $\pm 2 \times 10^{-3}$	1.6 $\pm 3 \times 10^{-3}$
^{197}Au, τ=4.61 ps	547	547.3 $\pm 3 \times 10^{-3}$	1.8 $\pm 3 \times 10^{-3}$
^{24}Mg, τ=1.33 ps	1369	1368.3(0.1)	2.4(0.1)
^{28}Si, τ=475 fs	1779	1778.4(0.2)	2.6(0.2)
^{28}Si, τ=0.78 ps	4496	4496.6(3.1)	2.9(3.7)
^{28}Si, τ=1.9 ps	5099 (I_γ=28 %)	5099.2(3.4)	3.4(4.4)
^{28}Si, τ=1.9 ps	6878 (I_γ=72 %)	6877.0(1)	4.4(2.1)

Table B.1: Online energy resolution within the energy range [0, 7] MeV. Nuclei γ-ray emitters and their associated state (lifetime, γ-ray rest energy) are given. Gaussian fits results on the observed unshifted peaks are (centroid, σ).

The background noise along angles was determined by measuring the γ-ray matrices in energy and angle at different energy ranges. Two cases, i.e. low 1 MeV and high 7 MeV γ-rays, are shown in Fig. B.6. Angular noise distributions were obtained by projection, after energy selections where no γ-ray transition was observed, onto θ_γ and $\cos(\theta_\gamma)$, the latter to not depend on the angle solid efficiency.

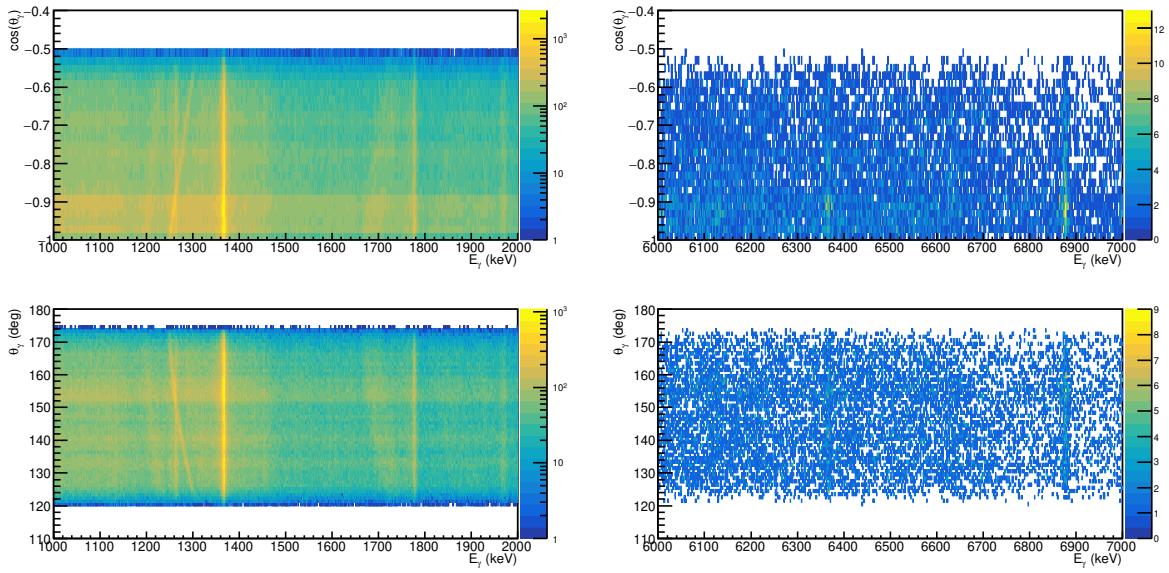

Figure B.6: AGATA matrices (E_γ, $\cos(\theta_\gamma)$ (top) and θ_γ (bottom)) to determine angular noise distribution and angular relative efficiency. Two energy ranges are illustrated: [1000, 2000] keV (left) and [6000, 7000] keV (right). Looking at $\cos(\theta_\gamma)$ allows us to be independent from the solid angle efficiency.

B.2 SPIDER calibration

The complete energy calibration of one quadrant of SPIDER 1st ring is illustrated in Fig. B.7. The 16 calibrated spectra from the triple-α source measurements were obtained by the linear equations between raw amplitudes measured in each strip and energies, they are listed for all strips of the four quadrants in Table B.2.

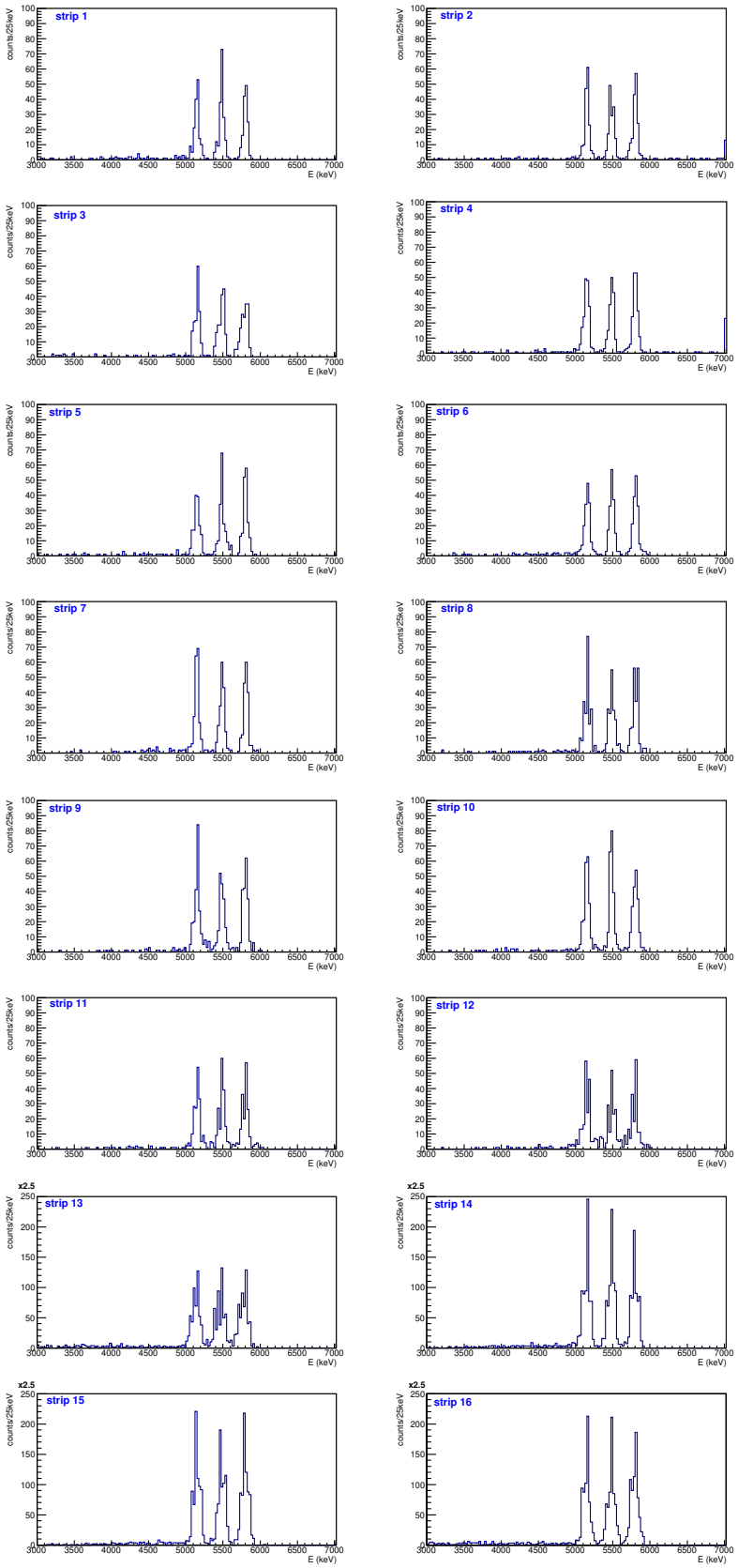

Figure B.7: Calibrated spectra of the Upper Right quadrant of SPIDER 1st ring (ΔE), obtained with the triple-α source. Detector is divided in 4 quadrants, each being stripped in 16 rings.

Strip	Linear calibration							
	keV quadrant				keV/a.u. quadrant			
	Q1	Q2	Q3	Q4	Q1	Q2	Q3	Q4
1	-392.5±32.71	-623.6±51.87	-854.8±108.70	-686.5±52.53	17.2±1.00	14.7±0.12	15.6±0.26	15.0±0.13
2	-296.1±26.86	-418.7±39.81	-374.4±83.57	-268.5±58.68	17.3±0.77	14.4±0.10	13.1±0.19	13.7±0.14
3	-108.9±44.63	-790.2±52.80	-886.3±125.50	-879.0±54.29	14.3±1.19	14.2±0.12	15.8±0.31	13.6±0.12
4	-457.5±32.71	-368.6±43.07	-288.9±144.70	-457.8±60.65	17.9±0.98	13.5±0.10	14.9±0.37	16.7±0.17
5	-737.6±70.44	-1024.0±63.39	-1016.0±285.30	-1205.0±35.28	10.6±0.12	14.7±0.14	14.0±0.59	18.0±0.09
6	-836.5±60.34	-559.2±40.46	-485.3±109.40	-833.7.q±42.29	16.0±0.15	12.3±0.08	14.1±0.26	17.6±0.12
7	-931.6±51.59	-812.6±35.20	-896.5±95.89	-1087.0±44.22	16.6±0.13	12.8±0.07	16.1±0.25	17.7±0.12
8	-984.0±19.70	-877.5±50.04	-1006.0±136.8	-972.2±48.81	19.3±0.59	16.5±0.13	16.7±0.39	18.4±0.14
9	-524.8±65.73	-602.7±38.78	-716.3±100.40	-972.9±61.13	12.3±0.13	10.7±0.07	14.4±0.23	18.2±0.17
10	-723.9±63.48	-467.9±54.56	-1101.0±150.00	-808.2±53.84	16.1±0.16	11.7±0.11	17.5±0.40	17.9±0.15
11	-222.2±28.71	-585.2±46.53	-502.5±88.60	-592.9±39.93	8.7±0.70	14.8±0.11	13.5±0.20	17.8±0.12
12	-593.4±56.93	-694.9±64.90	-705.8±92.64	-695.9±63.66	14.6±0.14	16.4±0.18	15.3±0.23	17.8±0.18
13	-468.8±87.72	-519.5±59.88	-496.2±128.40	-292.1±64.44	14.4±0.21	17.1±0.17	14.2±0.30	13.7±0.15
14	/	-583.8±48.55	-364.5±87.06	-435.5±59.76	/	17.9±0.14	14.7±0.22	13.9±0.14
15	-859.6±96.35	-876.7±53.02	-741.8±121.10	-709.5±63.43	14.3±0.22	18.0±0.15	15.1±0.29	15.6±0.16
16	-867.6±66.43	-1098.0±87.54	-1530.0±286.80	-927.6±90.32	16.6±0.18	19.1±0.26	20.4±0.81	13.7±0.19

Table B.2: Calibration of the whole SPIDER stripped ΔE 1st ring.

CHAPTER C

Complements to the calculations

Some details are provided along the present Annexes regarding calculations which support the experiment and theoretical analysis undergone in the thesis. First, the implantation profiles of the ^{3}He ions in gold are looked at in Sec.C.1. Then, distributions of expected β at reaction were estimated thanks to the LISE++ code, as presented in Sec.C.2. Finally, all calculated partial single-particle and γ-ray transition widths are listed in Sec.C.3.1. They were needed to derive the shell-model state widths.

C.1 Simulations of ^{3}He implantation profiles

The aimed reaction to populate states in ^{23}Mg* was ^{3}He(^{24}Mg,^{4}He)^{23}Mg*. The ^{3}He atoms are naturally in gaseous state, but gaseous targets with low densities were not enough compact and easy to handle for the experimental set-tup which combined AGATA, VAMOS, SPIDER and a small gas chamber. Furthermore, the lifetime sensitivity required that the target was also the degrader medium. It was thus required to trap the ^{3}He atoms into gold. As shown from SRIM calculations in Fig. C.1, this could be done by irradiating gold foils with a ^{3}He beam. Higher the beam energy is, deeper is the ^{3}He implantation profil is, see the peaked profile maximum around 250 Å for a beam at 5 keV (left) versus the profile maximum around 500 Å for a beam at 20 keV (right).

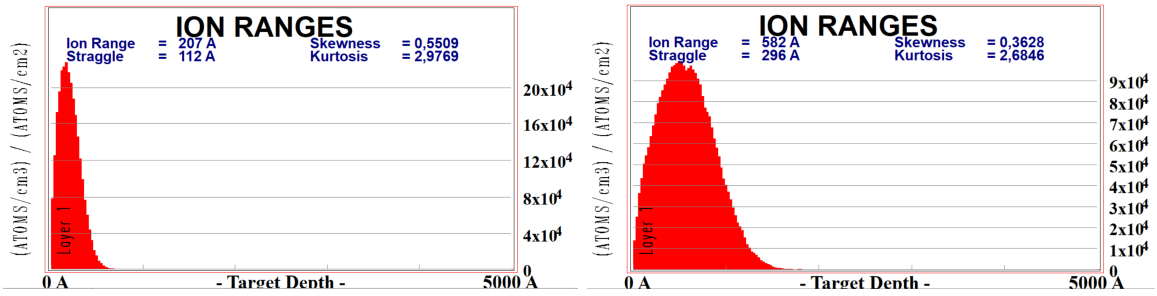

Figure C.1: SRIM simulation of ^{3}He implantation profiles in gold, left with a ^{3}He beam at 5 keV and right with a ^{3}He beam at 20 keV.

C.2 Velocities at reaction of states in ^{23}Mg*

Velocities of the recoil nuclei ^{23}Mg* were key both for lifetime measurements and proton decay measurements. Through the reconstruction of β-at-emission from the measured γ-rays with AGATA, it was

noticed that the β distributions depend on the state excitation energy Ex. This was confirmed with EVASIONS simulations. This is additionally strengthened here by simply calculating the velocities at reaction with LISE++ kinematics tools, as a function of Ex and of the target depth where reaction occur in Fig. C.2. We recall that the reaction ^{3}He(^{24}Mg,^{4}He)^{23}Mg* is associated with a ^{24}Mg beam energy of 110.83 MeV. As previously found out, β increases with Ex.

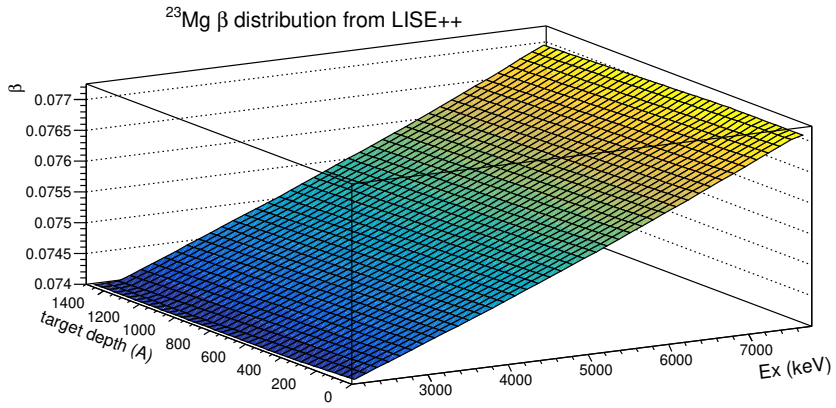

Figure C.2: Expected β at reaction of the populated state in ^{23}Mg* as a function of the excitation energy Ex and the target depth where the reaction happens. Calculations were done with LISE++ for the reaction ^{3}He(^{24}Mg, ^{4}He)^{23}Mg* at E_{beam}=110.83 MeV

C.3 Partial widths

C.3.1 Single-particle proton widths

Single-particle proton widths for each studied unbound state in ^{23}Mg* are summarized in the Table C.1. They were calculated with the experimental energies $E_p^{c.m.}$ and were used in Eq. (7.4) to determine the proton partial widths $\Gamma_{\ell,p}$.

n_R, Ex MeV	J^π	$E_p^{c.m.}$ MeV	$\Gamma_{\ell,s.p.,\,p}$ meV	
Experimental values			$\ell = 0$, 2s	$\ell = 2$, $1d_{3/2}$, $1d_{5/2}$
1, 7.785	$\frac{5}{2}^+$, $\frac{7}{2}^+$	0.204	332.4	2.5
2 (IAS), 7.803	$\frac{5}{2}^+$	0.222	900.0	6.6
3, 7.855	$\frac{7}{2}^+$	0.274	8640	59
4, 8.016	$\frac{5}{2}^+$, $\frac{7}{2}^+$	0.435	509 eV	3.04 eV
5, 8.163	$\frac{5}{2}^+$	0.582	8.736 keV	47.96 eV

Table C.1: Single-particle proton widths of proton unbound states in ^{23}Mg*, calculated with the code DWU.

C.3.2 Partial γ-ray widths

Partial γ-ray widths for each studied unbound state in ^{23}Mg* were determined by using the associated (M1, E2) reduced transition probabilities which were calculated with the NUSHELLX code, see Eq. (7.6). They allowed us then to derive the state γ-ray widths. The obtained values for the four resonant states and the IAS are shown in Tables C.2.

n_R=1	$E_{\gamma,0}$ MeV	SM γ transition	B(M1) μ_N^2, B(E2) $e^2.fm^4$		$\Gamma_{\gamma,(i\to f)}$ meV	
(E_R = 0.204 MeV)	Ref[55]		USDAcpn	UDSBcpn	USDAcpn	UDSBcpn
	7.333	$\frac{7}{2}^+_7 \to \frac{5}{2}^+_1$	0.1458, 0.1560	0.1140, 0.1117	668.6	522.6
	5.732	$\frac{7}{2}^+_7 \to \frac{7}{2}^+_1$	0.2007, 0.0038	0.1004, 0.0169	437.8	219.1
	7.785	$\frac{5}{2}^+_8 \to \frac{3}{2}^+_1$	0.2680, 0.1937	0.0306, 0.4412	1469	177.4
	7.333	$\frac{5}{2}^+_8 \to \frac{5}{2}^+_1$	0.0677, 0.0230	0.0013, 0.0133	309.6	6.165

n_R=2 (IAS)	$E_{\gamma,0}$ MeV	SM γ transition	B(M1) μ_N^2, B(E2) $e^2.fm^4$		$\Gamma_{\gamma,(i\to f)}$ meV	
(E_R = 0.222 MeV)	Ref[55]		USDAcpn	UDSBcpn	USDAcpn	UDSBcpn
	7.803	$\frac{5}{2}^+_9 \to \frac{3}{2}^+_1$	0.1529, 0.8863	0.337, 0.3866	862.1	1864
	7.351	$\frac{5}{2}^+_9 \to \frac{5}{2}^+_1$	0.1710, 0.7301	0.2266, 0.7441	799.4	1056
	5.751	$\frac{5}{2}^+_9 \to \frac{7}{2}^+_1$	0.0228, 0.2305	0.0438, 0.6131	51.40	99.61

n_R=3	$E_{\gamma,0}$ MeV	SM γ transition	B(M1) μ_N^2, B(E2) $e^2.fm^4$		$\Gamma_{\gamma,(i\to f)}$ meV	
(E_R = 0.274 MeV)	Ref[55]		USDAcpn	UDSBcpn	USDAcpn	UDSBcpn
	7.404	$\frac{7}{2}^+_8 \to \frac{5}{2}^+_1$	0.0086, 0.0500	0.0106, 0.0223	41.33	50.23
	5.803	$\frac{7}{2}^+_8 \to \frac{7}{2}^+_1$	0.0038, 0.0951	0.0634, 0.0731	91.00	143.9
	5.140	$\frac{7}{2}^+_8 \to \frac{9}{2}^+_1$	0.0498, 0.2298	0.0660, 0.2394	79.00	104.5

n_R=4	$E_{\gamma,0}$ MeV	SM γ transition	B(M1) μ_N^2, B(E2) $e^2.fm^4$		$\Gamma_{\gamma,(i\to f)}$ meV	
(E_R = 0.435 MeV)	Ref[55]		USDAcpn	UDSBcpn	USDAcpn	UDSBcpn
	7.564	$\frac{9}{2}^+_6 \to \frac{5}{2}^+_1$	0, 0.7355	0, 0.9254	14.69	18.48
	5.965	$\frac{9}{2}^+_6 \to \frac{7}{2}^+_1$	0.1595, 0.0073	0.2028, 0.0397	392.1	498.8
	5.300	$\frac{9}{2}^+_6 \to \frac{9}{2}^+_1$	0.0463, 0.4439	0.0511, 0.7574	81.34	90.67

n_R=5	$E_{\gamma,0}$ MeV	SM γ transition	B(M1) μ_N^2, B(E2) $e^2.fm^4$		$\Gamma_{\gamma,(i\to f)}$ meV	
(E_R = 0.582 MeV)	Ref[55]		USDAcpn	UDSBcpn	USDAcpn	UDSBcpn
	8.162	$\frac{5}{2}^+_{10} \to \frac{3}{2}^+_1$	0.1254, 0.1075	0.1919, 0.1479	792.9	1213
	7.712	$\frac{5}{2}^+_{10} \to \frac{5}{2}^+_1$	0.0149, 0.8001	0.0037, 0.6189	96.76	33.28
	6.110	$\frac{5}{2}^+_{10} \to \frac{7}{2}^+_1$	0.0448, 1.6520	0.0486, 0.9955	129.7	135.2

Table C.2: Calculated partial γ-ray widths from reduced probabilities B(M1) and B(E2) in Eq. (7.6) by using the NUSHELLX code [112], of each $\ell = 0$ resonance and IAS.

References

Synthèse de la thèse en français

Les enjeux et résultats de la présente thèse de l'Université française de Caen sont présentés le long de ce chapitre. Une description complète des démarches entreprises lors de l'expérimentation, de l'analyse et des simulations numériques est donnée dans la version anglaise de ce manuscrit.

Introduction

Des noyaux dans l'Univers

Un regard au ciel nocturne laisse songeur : quels spectacles se cachent derrière toutes ces étoiles si infimes dans ce sombre infini ? Les comprendre est facilité de nos jours par les différentes observables accessibles, à l'image des spectres lumineux des étoiles. Il a été prouvé que les noyaux, au coeur des atomes de matière, ont été en majorité produits dans les systèmes stellaires. Ces derniers sont principalement alimentés énergétiquement par les réactions nucléaires. La nucléosynthèse à l'œuvre peut être mise en évidence grâce aux spectres lumineux captés par nos télescopes, mais aussi par la composition des météorites où des poussières formées lors d'explosions stellaires ont été parfois piégées. Les abondances mesurées des noyaux dans notre système solaire (Fig. D.1) amènent de nouvelles interrogations. Pourquoi certains éléments (hydrogène, hélium, carbone, oxygène...) sont plus présents que d'autres ? Des indices se cachent ici sur les structures des noyaux. Le champ de l'astrophysique nucléaire s'intéresse principalement à expliquer où, quand et comment les éléments ont été synthétisés. Réciproquement, la nucléosynthèse et les abondances des noyaux observées au niveau des étoiles permettent de contraindre la physique stellaire.

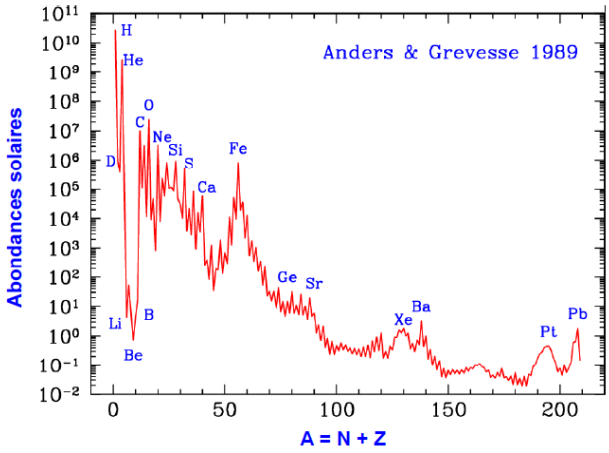

Figure D.1: Abondances mesurées dans le système solaire des noyaux selon leur masse.

L'objet de la présente thèse est le radioélément ^{22}Na qui est lié au système stellaire particulier que sont les novae.

Novae et ^{22}Na

Les novae sont avant tout des étoiles éphémères, visibles quelques mois dans le ciel nocturne. Elles sont parfois discernables à l'oeil nu (Fig. D.2(a)). Des duos d'étoiles sont prédits à l'origine de ces événements pendant lesquel une explosion se produit à la surface d'une étoile naine blanche qui préalablement accrétait la matière riche en hydrogène de sa compagne (Fig. D.2(c)). Si le scénario général semble être bien compris, il reste encore des incertitudes liées, entre autres, à la dynamique de l'accrétion, la quantité de matière éjectée, les conditions de la naine blanche ante et post explosion... De nouvelles observables astronomiques sont donc requises pour contraindre les modèles et mesurer précisément les propriétés physiques des novae détectées dans notre galaxie. Deux types de novae classiques sont rencontrées, selon la composition dominante de la naine blanche : carbone et oxygène CO ou oxygène et néon ONe. Pour ces dernières, le cycle de réactions nucléaires (Fig. D.2(d)) met en lumière un radioélément essentiel, le sodium 22 (^{22}Na), par sa durée de vie de 2,6 années. Celle-ci est suffisamment courte pour permettre une corrélation avec la source astrophysique, tout en étant suffisamment longue pour que le ^{22}Na survive à la phase opaque de quelques heures suivant l'explosion. Sa raie γ à 1,275 MeV n'a cependant pas été observée par les missions spatiales passées (INTEGRAL [13], COMPTEL [11]).

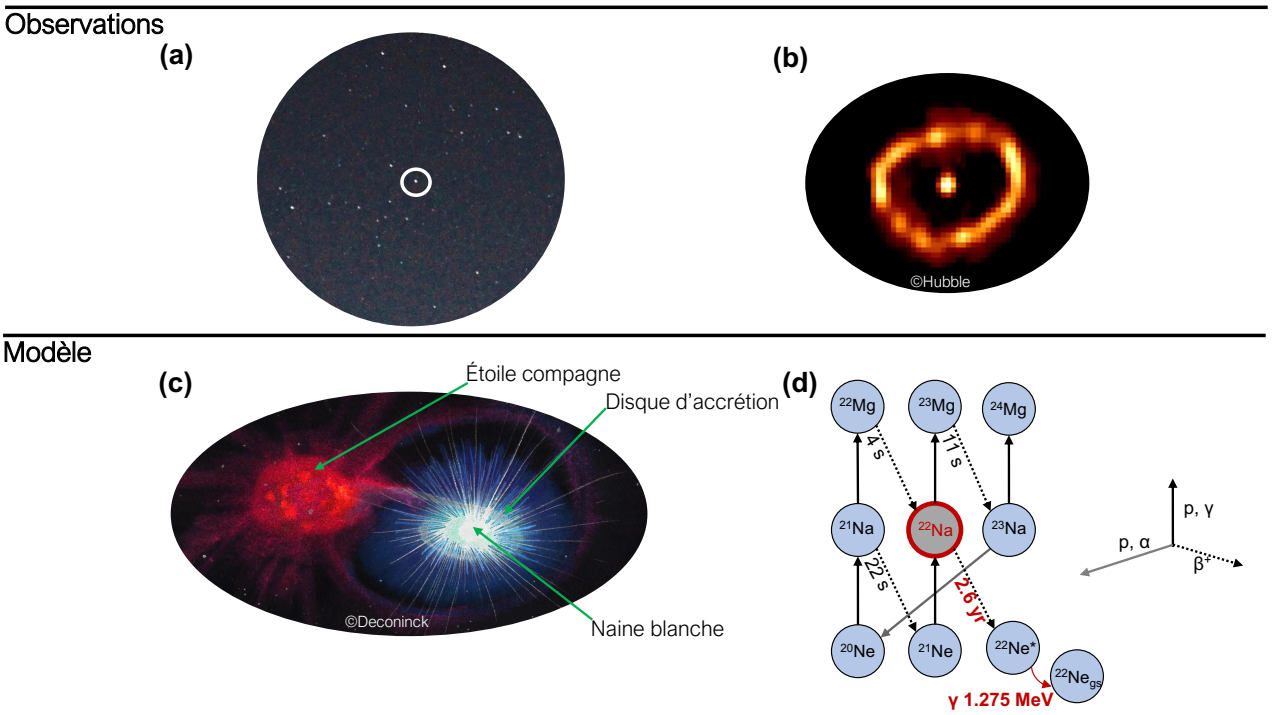

Figure D.2: (a) : photographie du ciel nocturne avec une nova visible dans la constellation du Dauphin (Normandie 2013). (b) : photographie avec la caméra FOC, embarquée dans le télescope Hubble, de la nova du Cygne 1992 où la matière éjectée après l'explosion forme un disque entourant la naine blanche. Source Paresce *et al*©Hubble [32]. (c) : aquarelle d'Aquarellia©Deconinck illustrant le modèle stellaire des novae, soit une naine blanche accrétant la matière riche en hydrogène de son étoile partenaire de type géante rouge. (d) : schéma de la nucléosynthèse impliquant les isotopes du neon, sodium et magnésium, qui se produit durant les novae ONe. Il y a principalement des réactions de capture proton et de décroissance β^+. Le radioélément phare ^{22}Na pour l'astronomie gamma des novae est montré avec le cercle gris.

Durant une nova, le radioélément ^{22}Na est détruit par la réaction de capture radiative ^{22}Na(p,γ)^{23}Mg, peuplant ainsi les états excités en ^{23}Mg* situés au-dessus du seuil proton (Fig. D.3 gauche). Les protons sont en mouvement selon la loi de Maxwell Boltzmann dans le plasma lors d'une nova. Selon la gamme de températures possibles de ce dernier ([0,1;0,4] GK), la probabilité qu'ils traversent la barrière coulombienne du noyau ^{22}Na, par effet tunnel, est maximale dans la fenêtre dite de Gamow. Dans l'intervalle d'énergies associé, la présence d'états excités du ^{23}Mg* génére des résonances dans la probabilité que la réaction ait lieu, à des énergies notées E_R. Le taux total de cette réaction est alors la somme des taux de chaque résonance. De plus, il a été montré que le taux de réaction associé à une résonance spécifique est proportionnel au paramètre $\omega\gamma$ appelé la force de résonance. A droite de la Figure D.3, nous montrons la contribution relative des taux de résonance par rapport au taux total de la réaction en fonction de la température dans le domaine des novae. Cela a été calculé en utilisant les forces de résonance mesurées par Sallaska *et al* [46]. La résonance à E_R=0,204 MeV (courbe verte), soit Ex=7,785 Mev en ^{23}Mg*, apparait clairement dominante sur une large gamma de températures.

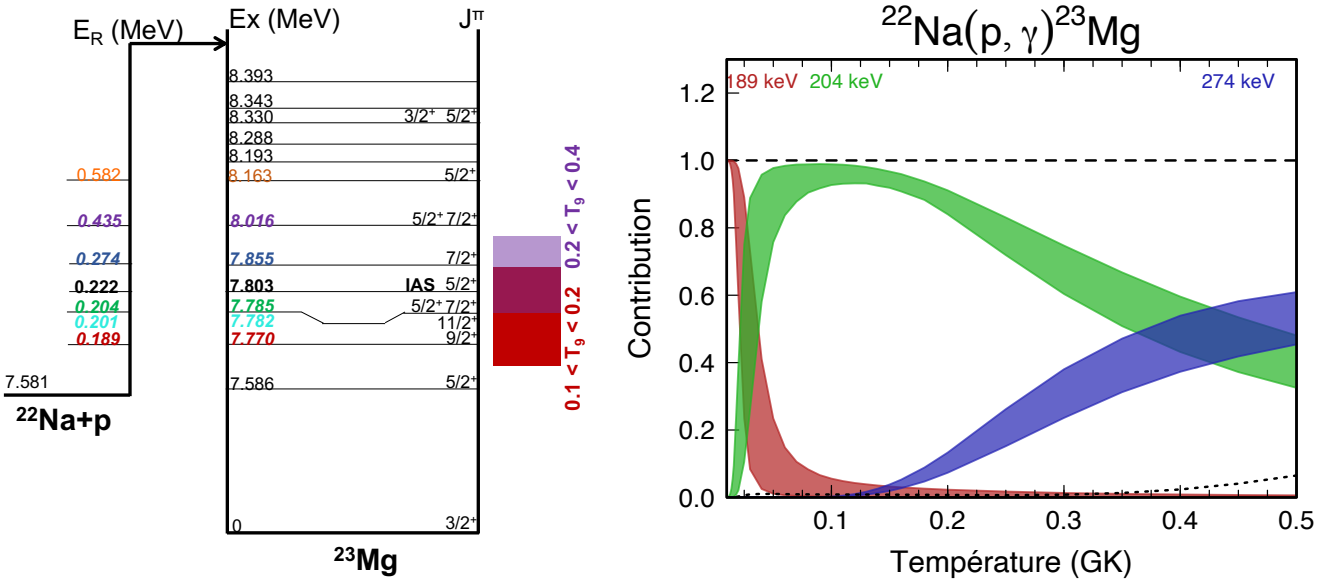

Figure D.3: Gauche : schéma des niveaux (Ex, J$^\pi$) en ^{23}Mg* présents dans la fenêtre de Gamow des novae ONe pour la réaction ^{22}Na(p,γ)^{23}Mg. Les énergies de résonance E_R correspondantes sont mentionnées. Droite : les contributions des résonances relatives au taux total de la réaction ^{22}Na(p,γ)^{23}Mg sont données en fonction de la température. Les résultats expérimentaux connus [46] montrent que la résonance à E_R=0,204 MeV (courbe verte) domine aux températures des novae ONe.

L'élément perturbateur de l'histoire du ^{22}Na entre maintenant en scène. Les différentes mesures de la force de résonance à E_R=0,204 MeV sont en désaccord à plus de 3σ (Fig. D.4 gauche). Cela résulte en plus d'un facteur 2 d'incertitudes dans la masse prédite de ^{22}Na éjecté durant les novae ONe (Fig. D.4 droite). A noter que pour toutes valeurs de $\omega\gamma$ de cette résonance, la masse prédite est bien inférieure aux limites obtenues par les campagnes d'observation gamma (lignes colorées). La force de résonance peut aussi être déterminée grâce aux propriétés spectroscopiques de l'état résonant situé à Ex=7,785 MeV :

$$\omega\gamma = \frac{2J_{^{23}\mathrm{Mg}}+1}{(2J_{^{22}\mathrm{Na}}+1)(2J_p+1)}\frac{\hbar}{\tau}\mathrm{BR_p}(1-\mathrm{BR_p}) \qquad (D.1)$$

où $J_{^{23}\mathrm{Mg}}$ est le spin de l'état résonant, τ sa durée de vie, $\mathrm{BR_p}$ son rapport d'embranchement proton, $J_{^{22}\mathrm{Na}}$=3 le spin de l'état fondamental du ^{22}Na et $J_p = \frac{1}{2}$ du proton.

Les valeurs connues de ($J_{^{23}\mathrm{Mg}}$, τ, $\mathrm{BR_p}$) pour l'état à Ex=7,785 MeV permettent de déterminer la force de résonance. Le résultat, ainsi obtenu, accentue la dispersion dans les estimations de la quantité ejectée

de ^{22}Na lors d'une nova (Fig. D.4 droite).

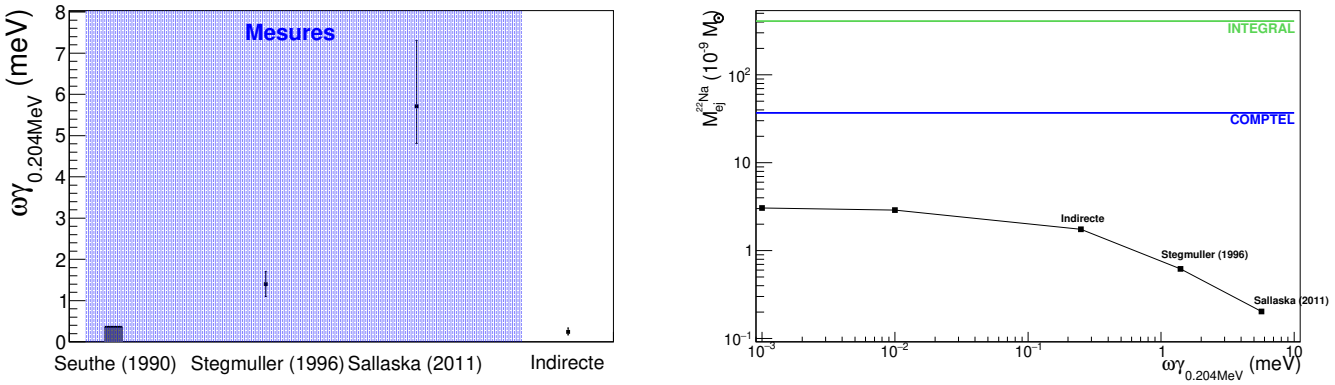

Figure D.4: Gauche : valeurs mesurées de la force de résonance à 0,204 MeV ($\omega\gamma_{0.204\mathrm{MeV}}$) et celle déterminée indirectement par les propriétés de l'état résonant en ^{23}Mg. Droite : évolution de la masse éjectée de ^{22}Na après l'explosion d'une nova ONe, prédite par des simulations avec le code MESA [40], en fonction de $\omega\gamma_{0.204\mathrm{MeV}}$. Les lignes colorées marquent les valeurs limites déduites des campagnes d'observation passées avec les instruments INTEGRAL et COMPTEL.

Dans cette thèse, une expérience a donc été menée au GANIL afin de résoudre la dispersion des données expérimentales liées à la force de la résonance dominante de la réaction ^{22}Na(p,γ)^{23}Mg. L'approche choisie fut de mesurer les propriétés de l'état résonant à Ex=7,785 MeV en ^{23}Mg*, soit sa durée de vie et son rapport d'embranchement proton. Un faisceau stable de ^{24}Mg, accéléré à 4,6 MeV/u, a été employé pour induire la réaction ^{3}He(^{24}Mg,α)^{23}Mg* et pour ainsi peupler l'état d'intérêt. La réaction fut étudiée avec les détecteurs de particules VAMOS et SPIDER, et avec le spectromètre gamma AGATA. Les cibles étaient constituées d'ions hélium 3 implantés dans de l'or afin de ralentir efficacement les noyaux ^{23}Mg* avant désexcitation. Les protons et alphas mesurés permirent de reconstruire les énergies d'excitation du ^{23}Mg. Après avoir sélectionné le peuplement direct des états, les spectres d'émissions de raies γ décalées Doppler ont été analysés afin de mesurer les durées de vie. La résolution souhaitée de 1 fs fut en particulier rendue possible par la qualité des mesures en énergie et position d'AGATA.

Résultats

Nouvelle méthode de mesure de durée de vie

Une nouvelle méthode de mesure des durées de vie d'états excités nucléaires a été développée au cours de l'analyse expérimentale. Elle a été validée sur 22 états excités en ^{23}Mg. Cette méthode repose sur :

1. La détection des émissions de raies γ issues de l'état excité du noyau qui est ralenti dans la cible. Les raies γ sont observées décalées en énergie par effet Doppler.

2. La sélection de l'état excité visé qui doit être directement peuplé en imposant une coincidence avec des particules α à la bonne énergie.

3. La reconstruction du profil de vitesse des noyaux au moment de l'émission à partir de la détermination de l'énergie et de l'angle des raies γ émises.

4. L'analyse χ^2 entre le profil de vitesse expérimental et les profils simulés selon la durée de vie de l'état.

Il s'agit donc d'une intégration dans un seul spectre de tous les angles de détection. La méthode nécessite un instrument de mesure de raies γ à grande ganularité pour reconstruire précisément la vitesse β à l'émission événement par événement. Ainsi, cette nouvelle approche agrée bien aux spectromètres γ à hautes résolutions et larges ouvertures angulaires que sont AGATA et GRETINA.

La méthode est implémentée dans le code EVASIONS qui intègre le montage expérimental de la thèse avec les instruments AGATA, VAMOS, SPIDER, DCTs. Les résultats obtenus pour deux états excités en ^{23}Mg sont montrés en haut de la Fig. D.5, à respectivement Ex=4,356 MeV et 7,785 MeV sur la gauche et la droite. Les durées de vie mesurées correspondent ici aux courbes rouges. Nos mesures de durée de vie s'étendent de 3 fs à 1.6 ps. L'obtention de durées de vie de quelques femtosecondes a ainsi été rendue possible. La durée de vie de l'état clé à Ex=7,785 MeV est mesurée à τ=11$^{+6}_{-4}$ fs (βM, Fig. D.5). Néanmoins, la sensibilité intrinsèque de cette nouvelle méthode ne nous semble pas limitée à la femtoseconde : cela est conditionnée ici par la statistique de l'état peuplé ainsi que les conditions expérimentales telles que la réponse instrumentale, la cinématique de réaction et la cible absorbante choisie.

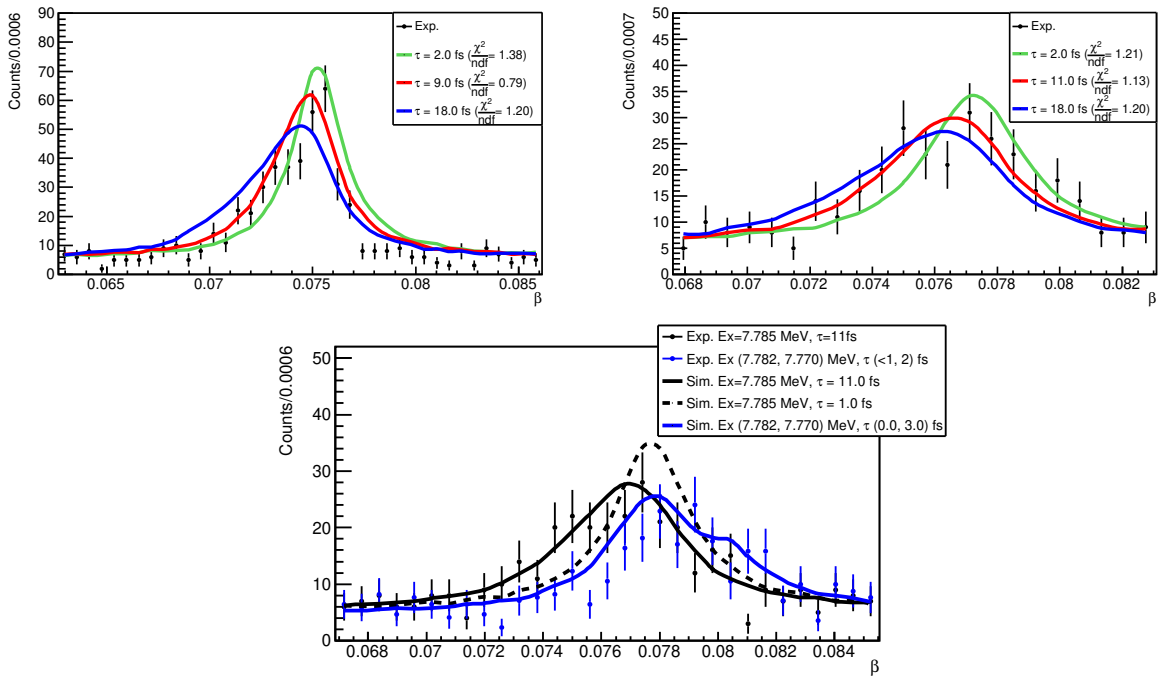

Figure D.5: Nouvelle méthode de mesure de durées de vie d'états nucléaires excités par reconstruction du profil de vitesse β à l'émission. Partie supérieure : les histogrammes β expérimentaux (points noirs) sont comparés à des profils simulés avec trois valeurs différentes de durée de vie τ pour l'état excité à Ex=4,356 MeV (gauche) et 7,785 MeV (droite) en ^{23}Mg*. La comparaison entre les distributions β expérimentale et simulées aboutit à un minimum en χ^2 correspondant aux courbes rouges. Partie inférieure : analyse de la sensibilité de la nouvelle méthode. Les histogrammes β expérimentaux (points) pour l'état à Ex=7,785 MeV (noir) et les états mélangés à Ex={7,782, 7,770} MeV (bleu) sont comparés à des profils simulés à : $\tau_{\beta M}$=11 fs (courbe noire continue), τ=1 fs (courbe noire en pointillés), et τ={0, 3} fs (courbe bleue continue). Le mélange des états à Ex={7,782, 7,770} MeV dont les durées de vie sont connues plus courtes, cause l'élargissement de la distribution β. Néanmoins le décalage observé entre ces deux distributions β montre que cette nouvelle méthode de mesure de durée de vie est capable de mesurer des durées de vie de l'ordre de 1 fs.

Les durées de vie mesurées ont été trouvées consistentes entre cette nouvelle approche βM et la méthode récente utilisant des spectres corrigés Doppler après integration angulaire (DCLM).

Spectroscopie de l'état résonant en ^{23}Mg à Ex=7,785 MeV

L'étude expérimentale de l'état résonant en ^{23}Mg à Ex=7,785 MeV a permis la mesure de la durée de vie associée, τ=9,9$^{+4,5}_{-2,0}$ fs, en contradiction avec la prédiction d'une valeur <1 fs selon le modèle en couches, et le rapport d'embranchement proton (BR$_p$=0,68(6) %) en bon accord avec la dernière mesure [48]). Notons que les protons émis par l'état clé et d'autres états non liés ont été observés avec SPIDER avec la possibilité de sélectionner l'état en ^{22}Na peuplé par la décroissance proton. Nos deux mesures sont comparées aux résultats passés (Fig. D.6) : l'accord observé entre toutes ces expériences indépendantes renforce les largeurs déduites pour l'état resonant en ^{23}Mg à E$_R$=0,204 MeV. Ainsi la dispersion observée entre les trois mesures de la force de résonance (Fig. D.4) nous semble résolue par l'approche indirecte où les propriétés spectroscopiques de l'état associé en ^{23}Mg* sont en accord d'une expérience à l'autre.

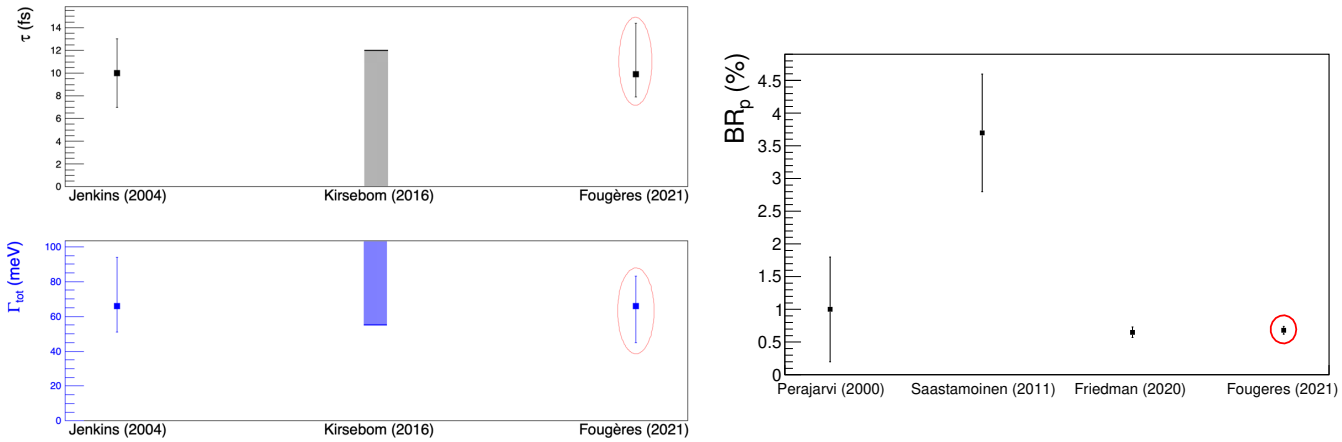

Figure D.6: Propriétés spectroscopiques mesurées de l'état astrophysique à Ex=7,785 MeV en ^{23}Mg*, à gauche la durée de vie τ et la largeur totale associée Γ_{tot} en bleu et à droite le rapport d'embranchement proton BR$_p$. Nos résultats Fougères *et al* (cercles rouges) sont en accord avec les expériences précédentes à l'exception de Saastamoinen *et al.* [50].

Les mesures des durée de vie et rapport d'embranchement proton associés à l'état astrophysique en ^{23}Mg (Fig. D.6) ont été moyennées. Une étude théorique basée sur le modèle en couches du noyau a donné des arguments forts pour que le spin de l'état clé soit égal à $J^\pi = \frac{7}{2}^+$. Finalement, la force de résonance à E$_R$=0,204 MeV a été déterminée.

$$\omega\gamma = 0.26^{+0.11}_{-0.07} \text{ meV} \tag{D.2}$$

Cette nouvelle valeur, avec 40 % d'incertitudes, est inférieure à la sensibilité des expériences de mesures directes des forces de résonance, typiquement 1 meV. Cela pourrait expliquer le désaccord avec ces mesures.

Conséquences astrophysiques

Réévaluation du taux de la réaction ^{22}Na(p,γ)^{23}Mg

Le taux de la réaction ^{22}Na(p,γ)^{23}Mg a été réévalué pour notre valeur déterminée de $\omega\gamma$ à E$_R$=0,204 MeV, avec la méthode statistique Monte-Carlo développée par Longland *et al* [47, 122]. Le taux ainsi recommandé est donné autour de la fenêtre de températures des novae sur la Fig. D.7, comportant <40 %

d'incertitudes. Les taux de Stegmuller *et al* [45] et Sallaska *et al* [46] sont aussi montrés pour comparaison : notre résultat est respectivement ∼3 et ∼10 fois plus petit.

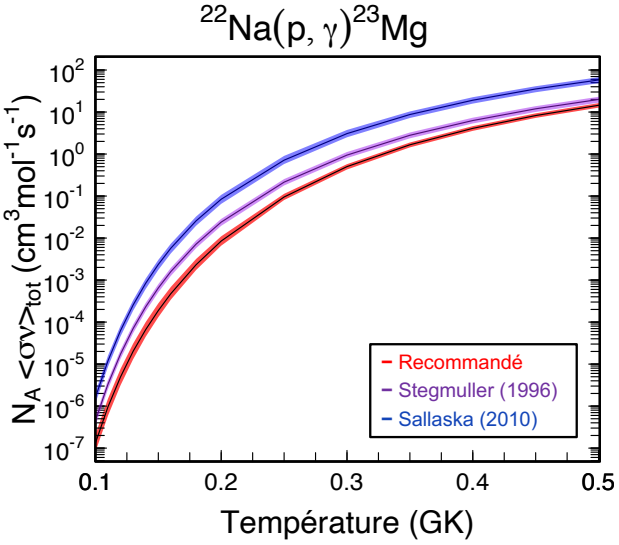

Figure D.7: Evolution du taux de la réaction ^{22}Na(p,γ)^{23}Mg en fonction de la température dans la région d'intérêt pour les novae. La région de confiance est prise à 1σ. Le taux recommandé (courbe rouge) est comparé aux précédents taux connus, basés sur des mesures directes de la force de résonance.

Contraindre certaines propriétés physiques des novae ONe

Grâce à l'outil de simulation stellaire MESA [40], nous avons pu prédire la quantité émise de ^{22}Na au cours d'une nova ONe, nos résultats pour le taux de la réaction ^{22}Na(p,γ)^{23}Mg étant intégrés. Deux paramètres physiques, que sont la vitesse d'accrétion avant l'explosion et la température initiale de la naine blanche, ont été variés. Il est montré (Fig. D.8) que le flux observable de la raie γ à 1,275 MeV issue du ^{22}Na, éjecté durant la nova, depend de ces deux paramètres. Pour une nova située ici à 0,6 kpc, ce flux pourrait être observé précisément avec les télescopes spatiaux e-ASTROGAM [130] ou COSI [8], des projets respectivement européen et américain dont les sensibilités sont attendues au moins 30 fois supérieures à celle d'INTEGRAL. Par exemple, si le flux de ^{22}Na est mesuré égal à 8,5(5)$\times 10^{-6}$ ph.cm^{-2}.s^{-1} alors la vitesse d'accrétion et la température initiale de la naine blanche pour la nova observée sont contraintes dans les trois possibles régions illustrées sur la Fig. D.8 droite. Nous confirmons ainsi que le radioélément ^{22}Na pourrait permettre de mieux comprendre la physique de ces explosions stellaires.

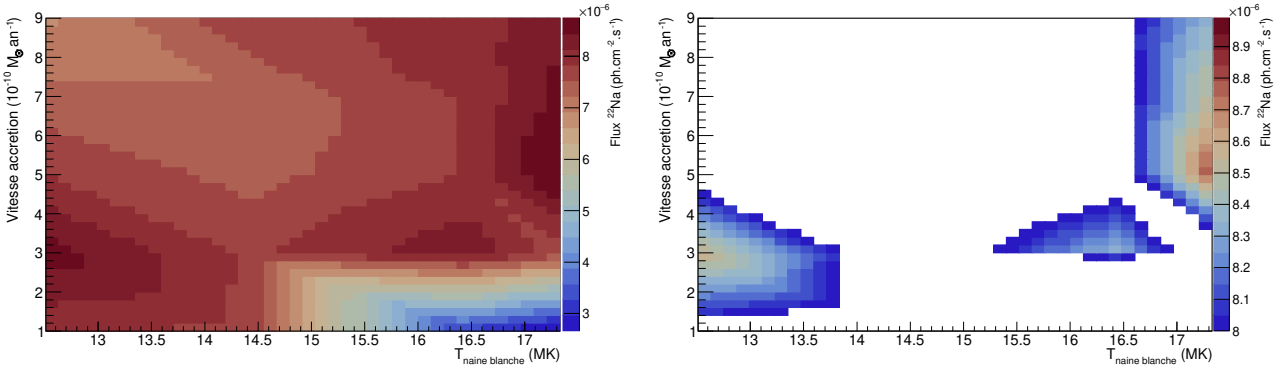

Figure D.8: Gauche : le flux prédit de photons émis par le ^{22}Na à 1,275 MeV est montré en fonction de la vitesse d'accrétion et de la température initiale de la naine blanche pour une nova ONe simulée et choisie à 0,6 kpc de la Terre. Droite : le flux est sélectionné autour de $8{,}5(5)\times10^{-6}$ ph.cm^{-2}.s^{-1}, dans la limite de sensibilité attendue pour le télescope spatial européen e-ASTROGAM à l'étude. Ainsi, l'observation de l'émission gamma issue du ^{22}Na devrait permettre de contraindre la nova sous-jacente.

Promesses pour les futures campagnes d'observation spatiale autour du ^{22}Na

De nouvelles missions d'observation spatiale autour des raies γ de basses énergies devraient être mises en place durant la prochaine décennie : les télescopes COSI et e-ASTROGAM proposés à la NASA et à l'Agence spatiale européenne, leurs performances instrumentales devant être fortement améliorées. Dans ce contexte prometteur, nous avons estimé la distance maximale d'une nova telle que les raies γ émises par le ^{22}Na soient détectables par ces instruments. La distance maximale est représentée par des cercles colorés sur la carte de la voie lactée (Fig. D.9). Il a été noté qu'au moins une nova ONe pourrait être détectée en ^{22}Na avec COSI tous les 20 ans. Nous nous sommes basés ici sur les événements observés au cours des 60 dernières années dans la voie lactée qui ont été identifiés comme des novae ONe. Seuls ceux dont la position fut précisément mesurée ont été considérés. Les 8 novae ainsi trouvées sont marquées par les points rouges, la couleur étant normalisée par le flux gamma de ^{22}Na attendu.

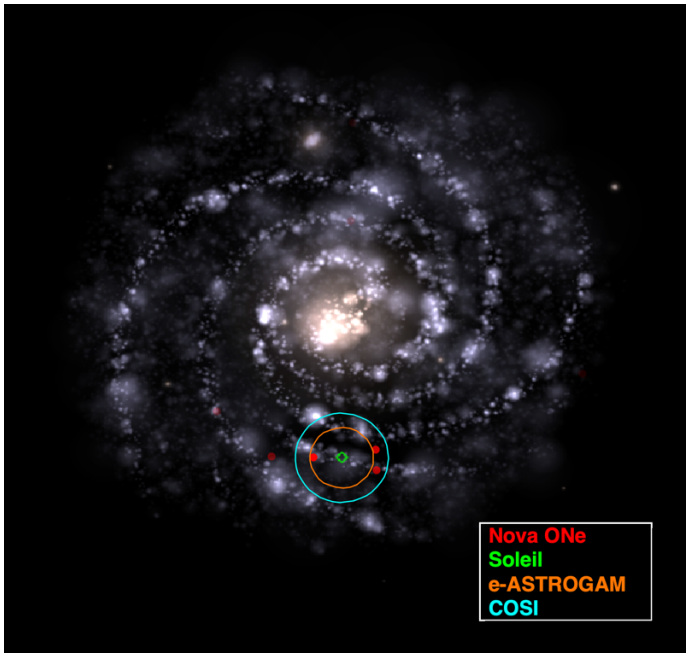

Figure D.9: Carte de la voie lactée où sont mentionées les distances limites de détection du flux de ^{22}Na par les projets de télescope spatial COSI et e-ASTROGAM (cercles colorés). Les novae ONe observées au cours des 60 dernières années sont marquées par les points rouges avec la couleur normalisée par le flux de ^{22}Na prédit.

Bibliography

[1] University of Illinois B. Fields. http://publish.illinois.edu/bdfields/multimedia/solareltabs/, 2021.

[2] E. Anders & N. Grevesse. Abundances of the elements: Meteoritic and solar. Geochimica and Cosmochimica Acta, 53, 1989.

[3] R.A. Alpher et al. The Origin of Chemical Elements. Physical Review, 73, 1948.

[4] C. E. Rolfs and W. S. Rodney. Cauldrons in the Cosmos. The University of Chicago Press, 1988.

[5] R. Diehl. Cosmic gamma-ray spectroscopy. Astronomical Review, 8, 2013.

[6] R. Dhiel et al. Astrophysics with Radioactive Isotopes, second edition. Springer, 2019.

[7] S. Pluschke et al. The COMPTEL 1.809 MeV survey. 4^{th} Integral Workshop: Exploring the Gamma-ray Universe, 2001.

[8] J.A. Tomsick et al. The Compton Spectrometer and Imager. Astro2020 APC White Paper, 2020.

[9] M. Renaud et al. The signature of ^{44}Ti in Cassiopeia A revealed by IBIS/ISGRI on INTEGRAL. The Astrophysical Journal, 647, 2006.

[10] European Space Agency. https://www.cosmos.esa.int/web/integral/instruments-spi, 2021.

[11] V. Schoenfelder et al. Instrument description and performance of the Imaging Gamma-Ray Telescope COMPTEL aboard the Compton Gamma-Ray Observatory. The Astrophysical Journal Supplements, 86, 1993.

[12] National Aeronautics and Space Administration. https://heasarc.gsfc.nasa.gov/docs/cgro/cgro.html, 2021.

[13] European Space Agency. https://www.cosmos.esa.int/web/integral/instruments, 2021.

[14] W. N. Johnson et al. The Oriented Scintillation Spectrometer Experiment - Instrument description. The Astrophysical Journal Supplements, 86, 1993.

[15] G. Vedrenne et al. SPI: The spectrometer aboard INTEGRAL. Astronomy & Astrophysics, 411, 2003.

[16] P. Ubertini et al. IBIS: The Imager on-board INTEGRAL. Astronomy & Astrophysics, 411, 2003.

[17] J. José et al. Nuclear uncertainties in the NeNa-MgAl cycles and production of ^{22}Na and ^{26}Al during nova outbursts. The Astrophysical Journal, 520, 1999.

[18] J. José et al. Nucleosynthesis in classical novae. Nuclear Physics A, 777, 2006.

[19] R.D. Gehrz et al. Nucleosynthesis in Classical Novae and Its Contribution to the Interstellar Medium. Pub. Astron. Soc. Pac., 110, 1998.

[20] J. José. Stellar Explosions - Hydrodynamics and Nucleosynthesis. CRC Press, 2020.

[21] D.D. Clayton et al. Gamma-ray lines form novae. The Astrophysical Journal, 187, 1974.

[22] S.M. Kent et al. Galatic structure from the Spacelab infrared telescope. II- Luminosity models of the Milky Way. The Astrophysical Journal, 378, 1991.

[23] M. Hernanz. Novae: gamma-rays from radioactivities and from particle acceleration. 2^{nd} e-ASTROGAM Workshop, 2017.

[24] A.F. Iyudin et al. COMPTEL search for ^{22}Na line emission from recent novae. Astronomy & Astrophysics, 300, 1995.

[25] National Aeronautics and Space Administration. `https://heasarc.gsfc.nasa.gov/docs/heasarc/missions/solarmax.html`, 2021.

[26] `http://cococubed.asu.edu/`, 2019.

[27] T. Siegert et al. Gamma-ray observations of Nova Sgr 2015 No. 2 with INTEGRAL. Astronomy & Astrophysics, 615, 2018.

[28] S. Amari et al. Presolar grains from novae. Nucl. Phy. A, 688, 2001.

[29] S. Amari et al. Presolar grains from novae: their isotopic ratios and radioactivities. New Astronomy Review, 46, 2002.

[30] M. Bose et al. Condensation of SiC Stardust in CO Nova Outbursts. The Astrophysical Journal, 873, 2019.

[31] D.C. Black. On the origins of trapped helium, neon and argon isotopic variations in meteroites- II. Carbonaceous meteorites. Geochimica et Cosmochimica Acta, 36, 1972.

[32] NASA F. Paresce, R. Jedrzejewski (STScI) and ESA. `https://esahubble.org/images/opo9406a/`, 2021.

[33] J. José et al. 123-321 models of classical novae. Astronomy & Astrophysics., 635, 2020.

[34] M. Y. Fujimoto. A theory of hydrogen shell flashes on accreting white dwarfs. I - Their progress and the expansion of the envelope. II - The stable shell burning and the recurrence period of shell flashes. The Astrophysical Journal, 257, 1982.

[35] B. Paczyński. Evolution of Single Stars. IV. Helium Stars. Acta. Astron., 21, 1971.

[36] European Space Agency. `https://sci.esa.int/web/education/-/35616-stellar-distances?section=apparent-and-absolute-magnitude`, 2021.

[37] M. Livio. Classical novae and the extragalactic distance scale. The Astrophysical Journal, 393, 1992.

[38] The FERMI-LAT collaboration. Fermi establishes classical novae as a distinct class of gamma-ray sources. Science, 345, 2014.

[39] A. Tajitsu et al. Explosive lithium production in the classical nova V339 Del (Nova Delphini 2013). Nature, 518, 2015.

[40] B. Paxton et al. Modules for Experiments in Stellar Astrophysics (MESA): Planets, Oscillations, Rotation, and Massive Stars. The Astrophysical Journal Supplement, 208, 2013.

[41] F. Matteuci et al. Modelling the nova rate in galaxies. Astronomy & Astrophysics, 405, 2003.

[42] J. Isern et al. Synthesis of radioactive elements in novae and supernovae and their use as a diagnostic tool. New Astronomy Reviews, 92, 2021.

[43] A. Parikh et al. Classical novae and type i X-ray bursts: Challenges for the 21st century. AIP Advances, 4, 2014.

[44] S. Seuthe et al. Resonances in the ^{22}Na(p,γ)^{23}Mg reaction. Nuclear Physics A, 514, 1990.

[45] F. Stegmuller et al. ^{22}Na(p,γ)^{23}Mg resonant reaction at low energies. Nuclear Physics A, 601, 1996.

[46] A.L. Sallaska et al. Direct Measurements of ^{22}Na(p,γ)^{23}Mg Resonances and Consequences for ^{22}Na Production in Classical Novae. Physical Review Letters, 105, 2010.

[47] R. Longland et al. Charged-particle thermonuclear reaction rates: I. Monte Carlo method and statistical distribution. Nuclear Physics A, 841, 2010.

[48] M. Friedman et al. Low-energy ^{23}Al β-delayed proton decay and ^{22}Na destruction in novae. Physical Review C, 101, 2020.

[49] D.G. Jenkins et al. Reevaluation of the ^{22}Na(p,γ)Reaction Rate : Implications for the detection of ^{22}Na Gamma Rays from Novae. Physical Review Letters, 92, 2004.

[50] A. Saastamoinen et al. Experimental study of β-delayed proton decay of ^{23}Al for nucleosynthesis in novae. Physical Review C, 83, 2011.

[51] K. Perajarvi et al. Measurement of the IAS resonance strength in ^{23}Mg. Physical Review B, 492, 2000.

[52] O.S. Kirsebom et al. Measurements of lifetimes in ^{23}Mg. Physical Review C, 93, 2016.

[53] Y. Zhai. The structure of ^{23}Al and astrophysical consequences. Ph.D. thesis, Texas AM University, 2007.

[54] V.E. Iacob et al. β decay of proton-rich nucleus ^{23}Al and astrophysical consequences. Physical Review C, 74, 2006.

[55] R.B. Firestone. `https://www.nndc.bnl.gov`, 2021.

[56] P.J. Nolan et al. The measurement of the lifetime of excited nuclear states. Reports on Progress in Physics, 45, 1979.

[57] E.K. Warbuton et al. The Measurement of Short Nuclear Lifetimes. Annual Review of Nuclear Science, 19, 1968.

[58] C. Michelagnoli. The lifetime of the 6.79 MeV state in ^{15}O as a challenge for nuclear astrophysics and γ-ray spectroscopy: a new DSAM measurement with the AGATA Demonstrator array. Ph.D. thesis, Padova University, 2013.

[59] A. Dewald et al. The differential plunger and the differential decay curve method for the analysis of recoil distance doppler-shift data. Zeitschrift fur Physik A Hadrons and Nuclei, 334, 1989.

[60] W.M. Currie. A Monte Carlo programme for Doppler shift analysis. Nuclear Instruments and Methods, 73, 1969.

[61] AGATA collaboration. `https://www.agata.org/`, 2021.

[62] Berkeley Laboratory GRETINA collaboration. `http://gretina.lbl.gov/`, 2021.

[63] M.S. Kwag et al. Spin assignmens for ^{23}Mg levels and the astrophysical ^{22}Na(p,γ)^{23}Mg reaction. European Physical Journal A, 56, 2020.

[64] D.G. Jenkins et al. γ-ray spectroscopy of the A=23, T=1/2 nuclei ^{23}Na and ^{23}Mg: High-spin states, mirror symmetry, and applications to nuclear astrophysical reaction rates. Physical Review C, 87, 2013.

[65] A.J. Koning et al. TENDL: Complete Nuclear Data Library for Innovative Nuclear Science and Technologys. Nuclear Data Sheets, 155, 2019.

[66] A.J. Koning et al. Modern Nuclear Data Evaluation With The TALYS Code System. Nuclear Data Sheets, 113, 2012.

[67] LLNL I. Thompson. `www.fresco.org.uk`, 2021.

[68] F. Boulay. Mesure dans le ^{19}Ne des résonances d'intérêt pour l'étude des novae par une nouvelle méthode de diffusion inélastique. 2015.

[69] L.C. Haun et al. A study of the low-lying states of ^{23}Mg. Nuclear Physics A, 140, 1970.

[70] H. Nann et al. Energy levels in ^{23}Mg from ^{25}Mg(p,t)^{23}Mg reaction. Physical Review C, 23, 1981.

[71] J. Kallne et al. Studies of (p,d) reactions in ^{24}Mg, ^{32}S and ^{40}Ca at 185 Mev. Phys. Scr., 11, 1975.

[72] D.W. Miller et al. Hole states excited by the ^{24}Mg(p,d)^{23}Mg reaction at 95 Mev. Phys. Scr., 11, 1975.

[73] S. Schmidt et al. ^{22}Na(^{3}He,d)^{23}Mg reaction studies of states near the proton threshold and hydrogen burning of ^{22}Na. Nuclear Physics A, 591, 1995.

[74] L.G. Svendsen et al. Corrosion inhibition by ion implantation of Al or Mg in Cu, investigated by RBS. Nuclear Instruments and Methods in Physics Research, 191, 1981.

[75] W. Moller. The behaviour of hydrogen atoms implanted into metals. Nuclear Instruments and Methods in Physics Research, 209-210, 1983.

[76] J.F. Ziegler et al. SRIM - The Stopping and Range of Ions in Matter. SRIM Co., United States of America, 6^{th}, 2013.

[77] W.R. Leo. Techniques for Nuclear and Particle Physics Experiments. Springer-Verlag, 1994.

[78] H. Ejiri et al. Gamma-ray and electron spectroscopy in nuclear physics. United Kingdom: Clarendon Press, 1989.

[79] AGATA collaboration et al. AGATA– Advanced GAmma Tracking Array. Nuclear Instruments and Methods in Physics Research A, 668, 2012.

[80] C.R. Alvarez. The GASP Array. Nuclear Physics News Europe, 2, 1993.

[81] LNL I.N.F.N homepage GASP. `https://npgroup.pd.infn.it/GASP/`, 2021.

[82] C.W. Beausang et al. Measurements on prototype Ge and BGO detectors for the Eurogam array. Nuclear Instruments and Methods in Physics Research A, 313, 1992.

[83] J. Simpson. The EUROBALL spectrometer. Zeitschrift fur Physik A Hadrons and Nuclei volume, 358, 1997.

[84] I.Y. Lee. The GAMMASPHERE. Nuclear Physics A, 520, 1990.

[85] Argonne N.L. homepage GAMMASPHERE. `https://www.phy.anl.gov/gammasphere/`, 2021.

[86] C.E. Svensson et al. TIGRESS: TRIUMF-ISAC gamma-ray escape-supressed spectrometer. Journal Physics G, 31, 2005.

[87] F. Azaiez et al. EXOGAM: γ-ray spectrometer for nuclear structure studies at SPIRAL. Nuclear Physics News, 7, 1997.

[88] U. Rizwan et al. Characteristics of GRIFFIN high-purity germanium clover detectors. Nuclear Instruments and Methods Physics Research A, 820, 2016.

[89] GANIL homepage ACTAR TPC. `https://www.ganil-spiral2.eu/scientists/ganil-spiral-2-facilities/instrumentation/actar/`, 2021.

[90] R.E. Horstman et al. Recoil-distance measurement of the g-factor $^{22}\mathrm{Ne}(2_1^+)$. Nuclear Physics A, 275, 1977.

[91] T.W. Bonner et al. Cross Section and Angular Distribution of the $\mathrm{he}^3(d,p)\mathrm{he}^4$ Nuclear Reaction. Physical Review, 88, 1952.

[92] H.S. Bosch et al. Improved formulas for fusion cross-sections and thermal reactivities. Nuclear Fusion, 32, 1992.

[93] R. Brun et al. ROOT - An Object Oriented Data Analysis Framework. Nuclear Instruments and Methods in Physics Research A, 389, 1997.

[94] S. Pullanhiotan. Characterization of a large acceptance spectrometer and its application to spectroscopy of exotic nuclei. Inter University Accelerator Centre (New Delhi) and Andhra University (Visakhapatn), 2008.

[95] F.D. Becchetti et al. Response of plastic scintillator detectors to heavy ions, Z $\leq$ 35, E $\leq$ 170 Mev. Nuclear Instruments and Methods, 138, 1976.

[96] F. Méot. The ray-tracing code Zgoubi. Nuclear Instruments and Methods A, 427, 1999.

[97] D. Bazzacco. The Advanced Gamma Ray Tracking Array AGATA. Nuclear Physics A, 746, 2004.

[98] A Lopez-Martens et al. γ-ray tracking algorithms: a comparison. Nuclear Instruments and Methods in Physics Research Section A, 533, 2004.

[99] NIST Germanium. `https://physics.nist.gov/PhysRefData/XrayMassCoef/ElemTab/z32.html`, 2021.

[100] A. Wiens et al. The AGATA triple cluster detector. Nuclear Instruments and Methods in Physics Research Section A, 618, 2010.

[101] B. Bruyneel. Characterization of Segmented Large V, High Purity Germanium Detectors. 2006.

[102] V.T. Jordanov et al. Digital techniques for real-time pulse shaping in radiation measurements. Nuclear Instruments and Methods in Physics Research Section A, 353, 1994.

[103] Advanced Telecommunication Computing Architecture. 2012.

[104] X. Grave. NARVAL a Modular Distributed Data Acquisition System with Ada 95 and RTAI. 14^{th} IEEE-NPSS, 1, 2005.

[105] R. Venturelli et al. Adaptive Grid Search as Pulse Shape Analysis Algorithm for γ-Tracking and Results. LNL Annual Report 2004, 43, 2005.

[106] Laboratoire National Henri Becquerel. Nucléide. `http://www.nucleide.org/Laraweb/index.php`, 2019.

[107] AGATA collaboration. `http://npg.dl.ac.uk/svn/agata/`, 2021.

[108] C. Stahl et al. APCAD - Analysis program for the continuous-angle DSAM. Computer Physics Communications, 214, 2017.

[109] F. James et al. Monte Carlo Phase Space. CERN 68-15, 1968.

[110] C. Patrignani et al. Particle Data Group. Review of Particle Physics, Chinese Physics C, 40, 2016.

[111] Y. Parpottas et al. Astrophysically important ^{26}Si states studied with (^{3}He, n) reaction and the ^{25}Al(p,γ)^{26}Si reaction rates in explosive hydrogen burning environments. Physical Review C, 70, 2004.

[112] B.A. Brown and W.D.M. Rae. The Shell-Model Code NuShellX@MSU. Nuclear Data Sheets, 120, 2014.

[113] B.A. Brown and W.A. Richter. New USD Hamiltonians for the sd shell. Physical Review C, 74, 2006.

[114] W.E. Ormand and B.A. Brown. Empirical isospin-nonconserving hamiltonians for shell-model calculations. Nuclear Physics A, 491, 1989.

[115] P.M. Endt. Energy levels of A = 21-44 nuclei (VII). Nuclear Physics A, 521, 1990.

[116] V. Tripathi et al. Split Isobaric Analog state in ^{55}Ni : Case of Strong Isospin Mixing. Physical Review Letters, 111, 2013.

[117] N. Smirnova. Discussions on γ transition probabilities between shell model and experiment of the Ex=7.785 MeV state in ^{23}Mg*. Private communication, 2021.

[118] A.K. Hasan et al. Positive Parity Levels of ^{21,23}Na Isotopes by Using the Nuclear Shell. Ukrainian Journal of Physics, 65, 2020.

[119] Bureau International des Poids et Mesures. Evaluation of measurement data - Supplement 1 to the Guide to the expression of uncertainty in measurement - Propagation of distributions using a Monte Carlo method. JCGM 101, 2008.

[120] X. Lei et al. Amorphous $Na_2Si_2O_5$ as a fast Na^{+} conductor: an *ab initio* molecular dynamics simulation. Journal of Materials Chemistry A, 3, 2015.

[121] C.A. Bertulani. RADCAP: A potential model tool for direct capture reactions. Computer Physics Communications, 156, 2003.

[122] R. Longland et al. Charged-particle thermonuclear reaction rates: III. Nuclear physics input. Nuclear Physics A, 841, 2010.

[123] A. Meyer. Etude expérimentale des réactions ^{13}N(α,p)^{16}O et ^{13}N(α,p)^{16}O, et impact sur les abondances isotopiques extrêmes en ^{13}C, ^{15}N et ^{31}Si dans les grains pré-solaires. Ph.D. thesis, Paris-Saclay University, 2020.

[124] C. Angulo et al. A compilation of charged-particle induced thermonuclear reaction rates. Nuclear Physics, A 656, 1999.

[125] MESA community. `http://mesa.sourceforge.net`, 2021.

[126] P. Denissenkov et al. MESA and NuGrid simulations of classical novae: CO and ONe nova nucleosynthesis. Monthly Notices of the Royal Astronomical Society, 442, 2014.

[127] P. Denisenkov. `http://www.astro.uvic.ca/~dpa/MESA_NuGrid_Tutorial.html`, 2021.

[128] Python library for MESA outputs. `https://github.com/wmwolf/py_mesa_reader`, 2021.

[129] J. José et al. Nucleosynthesis in classical novae: CO versus ONe white dwarfs. The Astrophysical Journal, 494, 1998.

[130] A. De Angelis et al. Science with e-ASTROGAM A space mission for MeV-GeV gamma-ray astrophysics. Journal of High Energy Astrophysics, 19, 2018.

[131] I. Hachisu et al. A Light-curve Analysis of 32 Recent Galactic Novae: Distances and White Dwarf Masses. The Astrophysical Journal Supplement Series, 242:18, 2019.

Acronyms

AGATA Advance GAmma Tracking Array
AGS Adaptive-Grid-Search
ATC AGATA Triple Cluster

β**M** β Method

CERN Conseil Européen pour la Recherche Nucléaire
CGRO Compton Gamma Ray Observatory
CL Confidence Level
CM Center-of-Mass
COMPTEL COMpton TELescope Level
COSI COmpton Spectrometer and Imager
CSS1 GANIL Cyclotron at Separated Sector

DC Doppler-corrected γ-rays
DCT Drift Chamber Target
DCLM Doppler-Corrected Lineshape Method
DRAGON Detector of Recoils And Gammas Of Nuclear reaction
DSAM Doppler-Shifted Attenuation Method

ESA European Space Agency
EVASIONS Experimental Vamos Agata Spider Implementation On Nuclear Spectroscopy

FET Fast Electronic Transistor
FWHM Full Width at Half Maximum

GANIL Grand Accélérateur National d'Ions Lourds
GLP Global Level Processing
GTS Global Trigger System

HF High Frequency
HPGe High Purity Germanium

IAS Isobaric Analogue State
IBIS Imager on Board of the Integral Satellite
IR Infra-Red
INTEGRAL International Gamma-Ray Astrophyscis Laboratory
ISM InterStellar Medium

LAT Large Area Telescope
LISE++ Ligne d'Ions Super Epluchés ++
LLP Local Level Processing

MB Maxwell-Boltzmann
MC Monte Carlo
MESA Modules for Experiments in Stellar Astrophysics

NASA National American Space Agency

OSSE Oriented Scintillation Spectrometer Experiment

PAC Program Advisory Committee
PL Plastic lighter
PM Photomultiplier
PSA Pulse Shape Analysis

ROOT Rapid Object Oriented Technology

SM Shell Model
SMM Solar Maximum Mission
SNe SuperNovae
SNR Signal Noise Ratio
SPI SPectrometer on INTEGRAL
SPIDER Silicon Particle Identification DEtector Ring
SRIM Stopping and Range of Ions in Matter

TOF Time of Flight
TRIUMF TRI-University Meson Facility

UV Ultra-Violet

VAMOS VAriable MOde Spectrometer

WD White Dwarf
WS Wood Saxon

Understanding the cosmic abundance of ^{22}Na

Simulations of explosive nucleosynthesis in novae predict the production of the radioelement ^{22}Na, a key astronomical observable by its short half-life to constrain nova models. It can also help to explain the observed ^{22}Ne excess in presolar grains and in cosmic rays. At peak novae temperatures, the dominant E_R=0.204 MeV resonance of the reaction ^{22}Na(p,γ)^{23}Mg has a highly debated strength. An experiment was performed at GANIL to measure the lifetime, spin and proton branching ratio of the Ex=7.785 MeV resonant state in ^{23}Mg*. The reaction ^{3}He(^{24}Mg,α)^{23}Mg*, populating the state of interest, was studied with particle detectors (VAMOS++, SPIDER) and the gamma tracking spectrometer AGATA. Alpha particles allowed us to reconstruct the excitation energies. By selecting the populated states, Doppler shifted γ-ray spectra were analyzed with several Doppler-based methods, including a new one, to measure lifetimes at 1 fs resolution. This led to the development of a new simulation code called EVASIONS. Protons emitted from unbound states were identified and proton branching ratio deduced. A shell-model study gave us clues on the spin of the key state which has a disputed experimental value. The resonance strength $\omega\gamma=0.26^{+0.11}_{-0.07}$ meV was obtained, it is below the sensitivity limit of the direct measurement experiments. A reevaluation of the ^{22}Na(p,γ)^{23}Mg rate was obtained with the Monte-Carlo approach. The amount of ^{22}Na ejected during novae was determined with the stellar simulation code MESA. It was shown that ^{22}Na can be used as a tool for quantifying some properties of the underlying novae. We finally estimate the detectability limit of ^{22}Na from novae and the observation frequency of such events with the next generation of gamma-ray space telescopes.

Keywords: Nuclear astrophysics, Novae, Gamma-ray astronomy, ^{22}Na, Resonance strength, ^{23}Mg, Femtosecondes lifetimes, Doppler γ-ray transitions, GANIL, AGATA, VAMOS, Proton branching ratios, SPIDER, EVASIONS code, MESA, NUSHELLX.

De la compréhension de l'abondance cosmique de ^{22}Na

Les simulations de la nucléosynthèse dans les novae prédisent la production du radioélément ^{22}Na, une observable astronomique clé, par sa courte demi-vie, pour contraindre les modèles de novae. Cette nucléosynthèse peut aussi expliquer l'excès mesuré de ^{22}Ne dans certains grains présolaires et rayons cosmiques. La résonance à 0,204 MeV, dominant la réaction ^{22}Na(p,γ)^{23}Mg aux températures des novae, a une force discutée. Une expérience a été menée au GANIL afin de mesurer la durée de vie, le spin et rapport d'embranchement proton de l'état résonant à Ex=7,785 MeV dans le ^{23}Mg. La réaction ^{3}He(^{24}Mg,α)^{23}Mg* a été mesurée avec des détecteurs de particules (VAMOS++, SPIDER) et avec le spectromètre gamma AGATA. Les particules alpha ont permis de reconstruire les énergies d'excitation. Sélectionnant les états peuplés, les spectres de raies γ décalées Doppler ont été analysés avec plusieurs méthodes, dont une nouvelle, pour mesurer les durées de vie à une résolution de 1 fs. A cette fin, le code de simulation EVASIONS a été développé. Des protons issus d'états non liés ont été identifiés, cela a permis de mesurer le rapport d'embranchement proton de l'état clé. Une étude du modèle en couches permit de déterminer son spin, qui était aussi discuté expérimentalement. La force de résonance clé, $\omega\gamma=0.26^{+0.11}_{-0.07}$ meV, a été obtenue, elle est inférieure à la sensibilité des expériences de mesure directe. Le taux de la réaction ^{22}Na(p,γ)^{23}Mg a été réévalué avec la méthode Monte-Carlo. En utilisant le code de simulation stellaire MESA, nous avons pu montrer que la quantité éjectée de ^{22}Na pendant les novae peut être utilisée comme un outil permettant de quantifier certaines propriétés des novae sous-jacentes. Finalement, nous avons estimé la distance limite de détection de ^{22}Na durant des novae et la fréquence d'observation de tels événements en utilisant la prochaine génération de télescopes spatiaux à raies γ.

Mots clés : Astrophysique nucléaire, Novae, Astronomie gamma, ^{22}Na, Force de résonance, ^{23}Mg, Durées de vie à la femtoseconde, Emissions de raies γ décalées Doppler, GANIL, AGATA, VAMOS, Rapports d'embranchement proton, SPIDER, Code EVASIONS, MESA, NUSHELLX.